HIGH RESOLUTION X-RAY SINGLE CRYSTAL DIFFRACTION

Eduardo Carmelo Escudero Adán

UNIVERSITAT ROVIRA i VIRGILI

HIGH RESOLUTION SINGLE CRYSTAL X-RAY DIFFRACTION

EDUARDO C. ESCUDERO ADÁN

DOCTORAL THESIS
2018

UNIVERSITAT ROVIRA I VIRGILI
HIGH RESOLUTION X-RAY SINGLE CRYSTAL DIFFRACTION
Eduardo Carmelo Escudero Adán
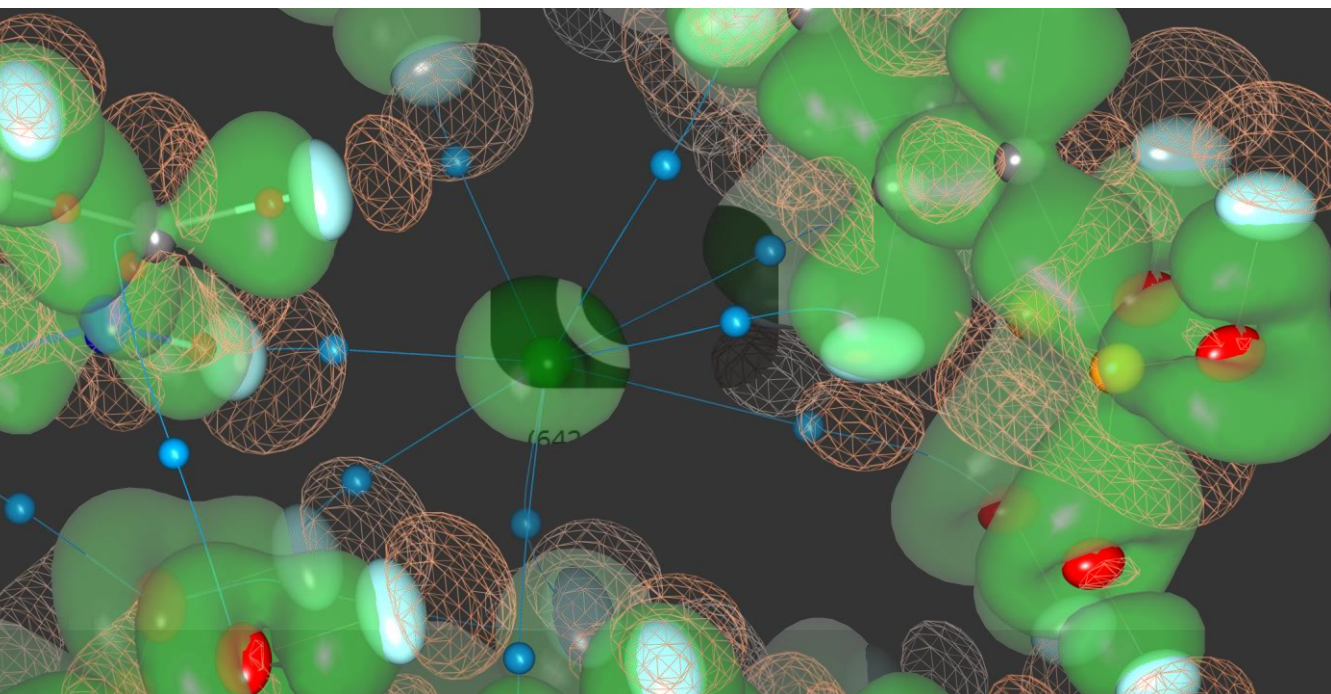
DOCTORAL THESIS

Eduardo Carmelo Escudero Adán

High-resolution X-ray Single Crystal Diffraction.

Supervised by Dr. Pablo Ballester Balaguer and Dr. Jordi Benet Buchholz

UNIVERSITAT
ROVIRA i VIRGILI

Tarragona 2018

FEM CONSTAR que aquest treball, titulat "High-resolution X-ray Single Srystal Diffraction", que presenta el Sr. Eduardo Carmelo Escudero-Adán per a l'obtenció del títol de Doctor, ha estat realitzat sota la nostra direcció al Institut Català d'Investigació Química, centre associat a aquesta universitat.

HACEMOS CONSTAR que el presente trabajo, titulado "High-resolution X-ray Single Srystal Diffraction", que presenta Sr. Eduardo Carmelo Escudero-Adán para la obtención del título de Doctor, ha sido realizado bajo nuestra dirección en el Institut Català d'Investigació Química, centro asociado a esta universidad.

WE STATE that the present study, entitled "High-resolution X-ray Single Srystal Diffraction", presented by Mr. Eduardo Carmelo Escudero-Adán for the award of the degree of Doctor, has been carried out under my supervision at the Institute of Chemical Research of Catalonia, a research center associated to this university.

Tarragona, 4 de gener de 2018

El/s director/s de la tesi doctoral

El/los director/es de la tesis doctoral

Doctoral Thesis Supervisor/s

Pablo Ballester Balaguer   Jordi Benet-Buchholz

"La historia de las ciencias nos demuestra que las teorías son perecederas. Con cada nueva verdad revelada, tenemos una mejor comprensión de la naturaleza y nuestras concepciones, y nuestros puntos de vista, se modifican."

Nicola Tesla

Acknowledgements

Ha habido y hay muchas personas a las que agradecer el trabajo que aquí se presenta. Hace ya unos cuantos años que la investigación se cruzó en mi camino, al principio tímidamente, a modo de experiencia, finalmente como principal ocupación (al menos en términos laborales).

A mi director de tesis, **Pablo Ballester**, por invitarme a hacer este trabajo de forma totalmente desinteresada. Tengo que agradecerle su visión de la química, sus charlas sobre ciencia, pero, sobre todo, el haberme enseñado a entender las cosas en profundidad.

A mi co-director de tesis, **Jordi Benet**, con quien, en Leverkusen, comencé mi andadura en la investigación. De aquella estancia en Bayer surgieron algunas ideas que han sentado base a parte del trabajo aquí expuesto.

Gracias también a mis compañeros de laboratorio, Marta y Eddy.

A Eva Casco y a Bea

Al personal del ICIQ que se ha interesado por mi trabajo y que han aportado ideas. A Carlos Rodríguez, a Fernando Bozoglian por sus conversaciones y sugerencias.

A Kilian Muñiz por estar siempre dispuesto a echar una mano.

A **Carmelo Giacovazzo**, que siempre ha respondido a mis consultas sobre cristalografía.

Special thanks to **Simon Parsons** for its help in the editing of the article of absolute configuration.

To the director of the crystallography team of the University of Lorraine, **Dominink Schaniel** for allowing me the stay at its group. Special thanks to **Christian Jelsch** for its interest in all the projects I have discussed with him and for its inestimable help. A **Enrique Espinosa**, por atender mis preguntas y sugerirme nuevas ideas. To **Claude**

Lecomte, for its help and its predisposition to explain share ideas and experience. To **Paul Allé** for sharing with me its deep knowledge of the X-ray detector technologies.

Thank also to **Rolad Boese** for sharing your knowledge every time we meet.

Gracias también a **Fernando Lahoz**, primero por organizar "The Charge Density School" y segundo por acogerme en su laboratorio para compartir su experiencia en el campo. A **Ignasi Mata**, con quien me inicié en la densidad electrónica de carga.

A Jordi Aguilera, a Albano Galán, a Alejandro Díaz, a Gemma Aragay, a Claudio Martínez, por su ayuda a la hora de buscar compuestos, disolventes, síntesis, etc.

A **Toni Frontera** por interesarse en los proyectos que le he propuesto, realizar los cálculos y por sugerir líneas de investigación que contribuyesen a mi trabajo. Gracias también a Antonio Bauzá.

To **Vladimir Grushin** and Andrey Konovalov for its intense debates about the trifluromethyl group.

Thank you to R. Hooft for his comments on the absolute structure determination.

Al ICIQ por permitirme realizar esta tesis.

Finalmente quiero agradecer a mi mujer **Laura** por tu ayuda en el día a día y por tu comprensión. A **Mario** y a **Paula** perdón por todo el tiempo que os he robado y gracias por darme fuerza cuando ya no queda.

Table of contents

Aims of the thesis

In recent years, interesting developments in X-ray diffraction techniques have taken place. With respect to the equipment, diffractometers benefit from more intense and stable radiation sources. Nowadays, X-ray sources are more intense owing to improved optics. The new sources can provide higher radiation fluxes with less nominal power. The use of more accurate and precise goniometers helps increasing the reliability of the measured intensities. The software used for data correction and structure refinement are executed on computers equipped with very efficient and fast processors. The advancement in computer hardware dramatically reduces the calculation time of complex refinements in comparison with the standards of the beginning of XXI century. Finally, it is worth to stressing the enhancement experienced by X-ray detectors. Implementation of photon counting detectors or hybrid pixel detectors represents the most exciting breakthrough experienced by the X-ray diffraction technology in the present decade. The possibility of combining a direct measurement of the X-ray photons with the ability of filtering non-desirable radiation, using an energy threshold, allows the detection of weak intensities with high accuracy and precision for its subsequent use in structure solving and refinement protocols. In particular, diffraction experiments that take advantage from the aforementioned advancements are those based on high-resolution measurements since at high resolution the X-ray diffraction intensities decay significantly.

Among the different high-resolution X-ray diffraction techniques, the X-ray charge density determination is a methodology allowing the experimental determination and quantification of inter- and intra-molecular interactions in the solid state of a single crystal. The methodology is based on the analysis of the charge density distribution in the crystal. In many cases, this methodology is applied as an experimental validation of theoretical calculations. In the last years, many research groups focused their attention in the study of non-covalent interactions owing to their critical role in many chemical fields. They play a key role in molecular recognition in biological processes and in supramolecular chemistry. Intermolecular interactions control crystallization of compounds and are used in material science to improve physical and chemical

properties. A better understanding of the nature of these weak interactions is important to gain further insight in some chemical and biological processes, as well as to pinpoint the key factors of their functioning and possible enhancement.

Chapter 1

Introduction
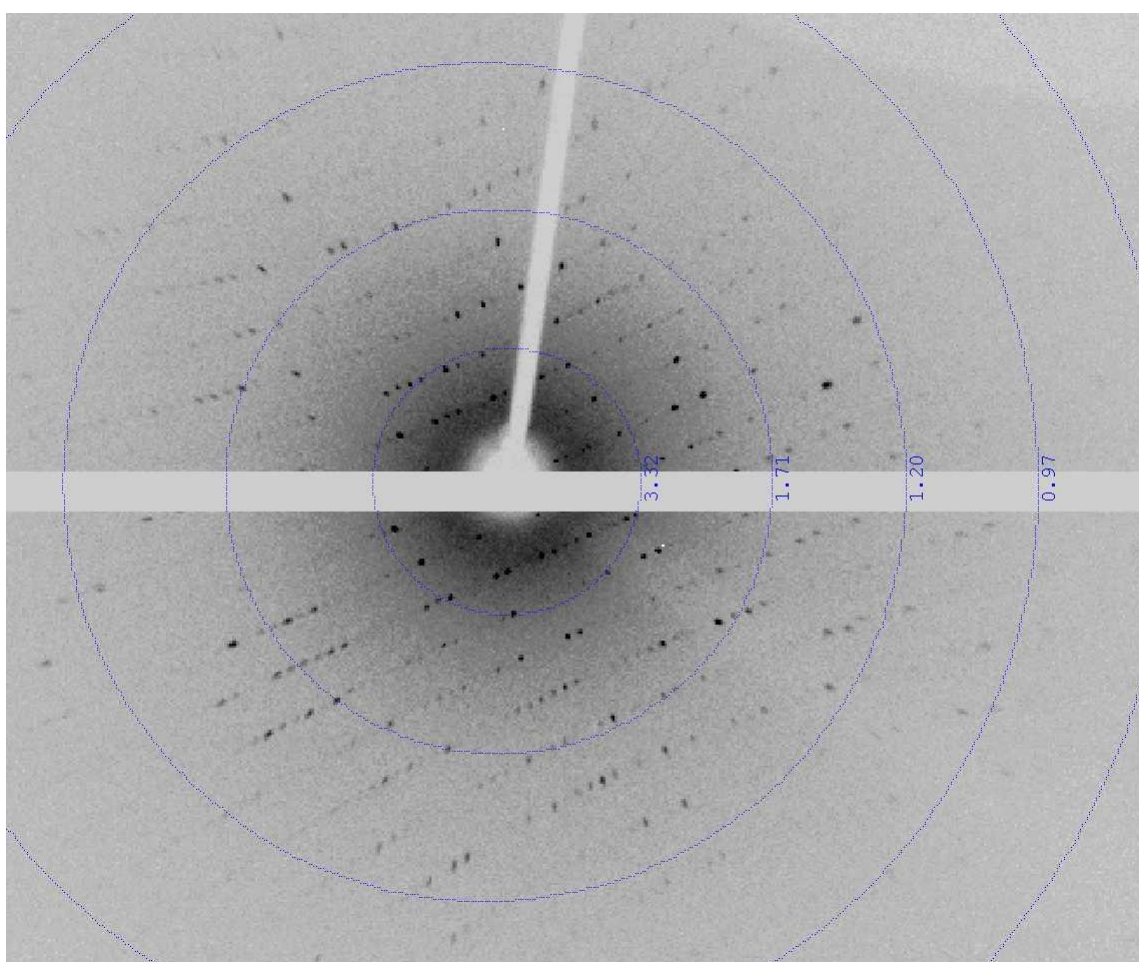
General aspects.

One of the most popular techniques for determining the atomic and molecular structure of a single crystal is X-ray diffraction. Since the first published structures by William Henry Bragg and his son, William Lawrence Bragg in 1913 (The Structure of Some Crystals as Indicated by their Diffraction of X-rays". Proc. R. Soc. Lond. A89 (610): 248–277) this technique has experienced significant improvements. Nowadays, there is a variety of X-ray sources available for in-house experiments; sealed tubes, micro-sources, rotating anodes or liquid anodes that provide stable intensities and a well-focused beam for Cu, Mo, Ag, Cr, Ga, Ga-In… anodes. In addition, the possibility of performing single crystal diffraction experiments using synchrotron radiation also exists. This latter type of radiation provides monochromatic and collimated beams with huge intensity and at multiple different wavelengths. One of the most exciting advancements for the technique of X-ray diffraction of single crystals was the development of new detectors. Nowadays, we are far from the first ionization gas detector used by Bragg. In the digital era, the two-dimensional charge-coupled device (CCD) detectors were rapidly overcame by hybrid pixel or complementary metal-oxide-semiconductor (CMOS) detectors. The state of the art of these latter detectors accumulate less noise and feature a higher dynamic range. As a direct consequence of the gained detector performances, it is now possible to obtain improved realistic values of diffraction intensities and therefore, to achieve a better determination of the phase.[1-3] These improvements invite to revisit the high-resolution X-ray single crystal diffraction technique in order to take advantage of the better-quality data that can be acquired.[4]

The interaction of X-ray radiation with the electronic clouds of the atoms generates the single-crystal diffraction pattern. Hence, the information that is extracted from the mathematical solution of the X-ray diffraction pattern is directly related to the electron distribution in the crystal structure. In short, through X-ray diffraction of a single crystal, it is possible to reconstruct its electron distribution and the positioning of the atomic components. Moreover, the determined electronic distribution is associated not only with the chemical bonding and the supramolecular interactions that are

established between the atomic components but also with the macroscopic properties of the single crystal as a solid material i.e. conductivity.
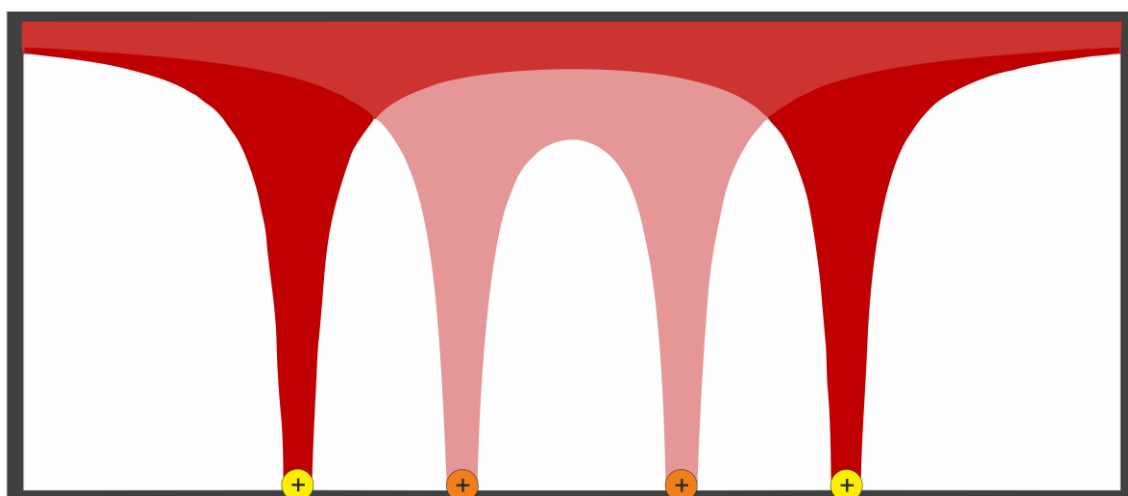
Figure 1. The red and the pink shapes represent 2D cuts of two Coulomb potentials. The closer the potential wells are the thicker is the path between them, and therefore, the deformation of the electronic clouds with respect to the spherical symmetry of the isolated potential becomes larger.

As mentioned above, using the Fourier transform of the diffraction pattern it is possible to replicate the electronic distribution between atoms in the crystal. For doing so, it is necessary to create a theoretical model of the crystal lattice, from which its calculated theoretical diffraction pattern accurately reproduces the experimentally measured counterpart. The simplest theoretical model that is used to reproduce the pattern produced by the electron diffraction of the X-rays is the spherical model also known as *independent atom model* (IAM). In this model, it is assumed that the atoms are spherical and independent entities. This is a very useful approximation that works very well for the structure determination of small molecules. The atomic position of each atom can be very precisely determined in the crystal matrix. This approach provides relevant information for determining the structural properties of the molecules and the intermolecular contacts defining the crystal lattice. The spherical model of the atoms justifies the large majority of the electron density causing the X-ray diffraction pattern. However, it is well know that the intra and inter-molecular interactions that are present between the atoms of the lattice provoke a distortion of the electron distribution of the atoms away from the simple spherical model, Figure 2. The stronger electron interactions between the atoms result in the covalent bonds. This type of bonds induces the most important deformations of the electron spherical

models for the atoms involved. The deformation of the spherical electron distribution of the atoms becomes visible in the significant residual maps of electron density resulting from the use of the spherical model in predicting the diffraction pattern, Fig. 2. To describe in more detail the distribution of the electronic density in the crystals, Stewart[5] and then Hansen and Coppens[6] proposed the use of a theoretical model for the electron distribution in the atoms that takes in account the deformation provoked not only for their involvement in covalent bonds but also for their participation in much weaker interactions i.e. hydrogen bonds. Using this more elaborated model and with the help of theoretical calculations it is possible to describe the electron density distributions resulting from interatomic interactions as weak as weak hydrogen bonding. A nice example of a well-known intermolecular interaction that was experimentally characterized by means of the calculated electron density distribution is halogen bonding. [7]
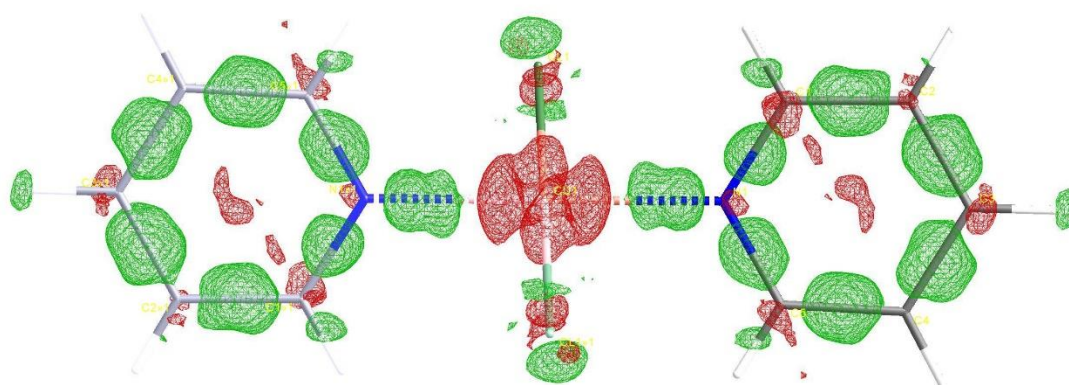
Figure 2. Residual Fourier maps observed after refinement of the structure of the complex $CuCl_2(Py)_2$ using an independent atoms model, IAM. Green areas, which are concentrated between the atomic nuclei involved in covalent bonds, represent regions with excess electron density. On the other hand, electron deficient regions are shown in red and are mainly centered in the Cu atom and to a reduced extent in some carbon atoms of the pyridines.

Although the charge density (CD) analysis is typically associated with small molecules, the future challenges of the technique point to its implementation in the analysis of X-ray diffraction patterns of macromolecules.[8,9]

1. The interference phenomena

The interference of an electromagnetic wave is the direct result of the superposition of two or more electromagnetic waves. As a result of the wave interaction, the final amplitude can be greater, identical or smaller than those of the components. To explain the interference phenomena occurring in an X-ray diffraction experiment of a single crystal it is worth to establish different interference levels. The sum of all the interference levels will result in the total effect of interference produced by the crystal.

1.1 X-ray scattering by a charged particle.
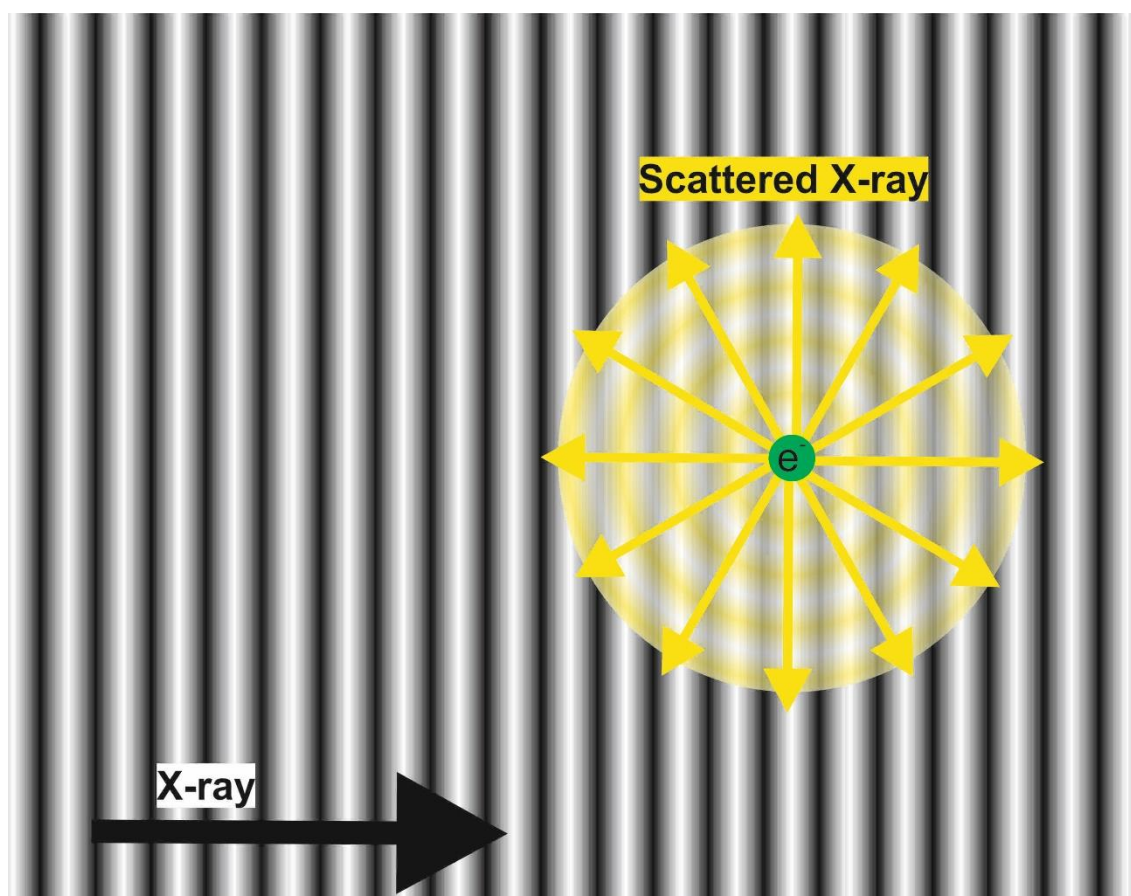
Figure 3. X-ray scattering produced by a charged particle. The incident x-ray wave is a plane wave, grey waves. When scattered by the charged particle it originates a spherical wave front, yellow waves.

The interaction of the x-ray with the charged particles of the crystal can be divided in two types, *inelastic scattering* or *Compton* and *elastic scattering* or *Thomson*. In the

21

Compton scattering, part of the energy of the incident photons is transferred to the electrons. Consequently, the scattered radiation must have a smaller energy (a bigger wavelength). In contrast, for the Thomson or elastic scattering the energy is conserved. The elastic scattering is responsible of the diffraction pattern used in the X-ray diffraction techniques. When the X-ray radiation interacts with a charged particle i.e. an electron, the scattered radiation produces a spherical wave, Figure 3. This means that, when a single crystal is exposed to an X-ray source, every electron will become a spherical source of scattered X-rays. At this point, the intensity of the scattered X-rays by any charged particle is identical in all directions. In a crystal, the scattered spherical waves will interfere with one another leading to the diffraction phenomena. The interference already happens in a single atom with multiple electrons. The atomic electron distribution cloud (electron configuration) produces a spatial distribution of electrons originating different wave fronts by interacting with X-ray radiation. These wave fronts interfere with one another. As a result, this interaction gives an intensity pattern, known as the atomic scattering factor. Moreover, the arrangement of the atoms in molecules causes a new interference phenomenon, which is the basis of the molecular structure factor. Eventually, the ordered arrangement of molecules, making up the crystal; is responsible of additional interferences between the scattered radiations of their electrons. The experimentally determined diffraction pattern is the sum of all the interferences.

Note that the scattering of the electromagnetic waves is caused by any charged particle. It means that the atomic nuclei are also scattering centers. However, the amplitude of the scattered waves produced by the atom centers are thousands of times smaller than the one originated by an electron. The intensity of the scattered wave is inversely proportional to the square of the mass of the charged particle[10]. Since the smaller mass of an atomic nucleus is that of a hydrogen atom, and the m_p (hydrogen atom mass) is $\approx 1836 m_e$ (mass of an electron), the intensities of the scattered waves originated by the nucleus of the atoms can be considered as negligible compared to those of the electrons.

22

1.2 Interference in the atom.

At the scale of the X-ray wavelengths used in crystallography, the approximation of considering an atom as a single point is not valid anymore. The volume of an atom is mainly the volume of its electron cloud. Quantum physics describe the atomic electron distribution through wavefunctions, atomic orbitals. These describe regions with high probability of containing electrons around the atomic nucleus. The shape of this electron distribution is the origin of the *atomic scattering factor (*ASF). From the atomic orbitals, squaring its amplitude, it is possible to calculate the probability of finding an electron in a volume around the nucleus, probability radial functions, Fig. 4. As mentioned above, the electrons forming the electron cloud are the origin of spherical sources of scattering radiation produced by an incident x-ray source. These spherical waves interfere with one another giving as final result the scattering factor of the full atom, X-ray *atomic scattering factor* (ASF).
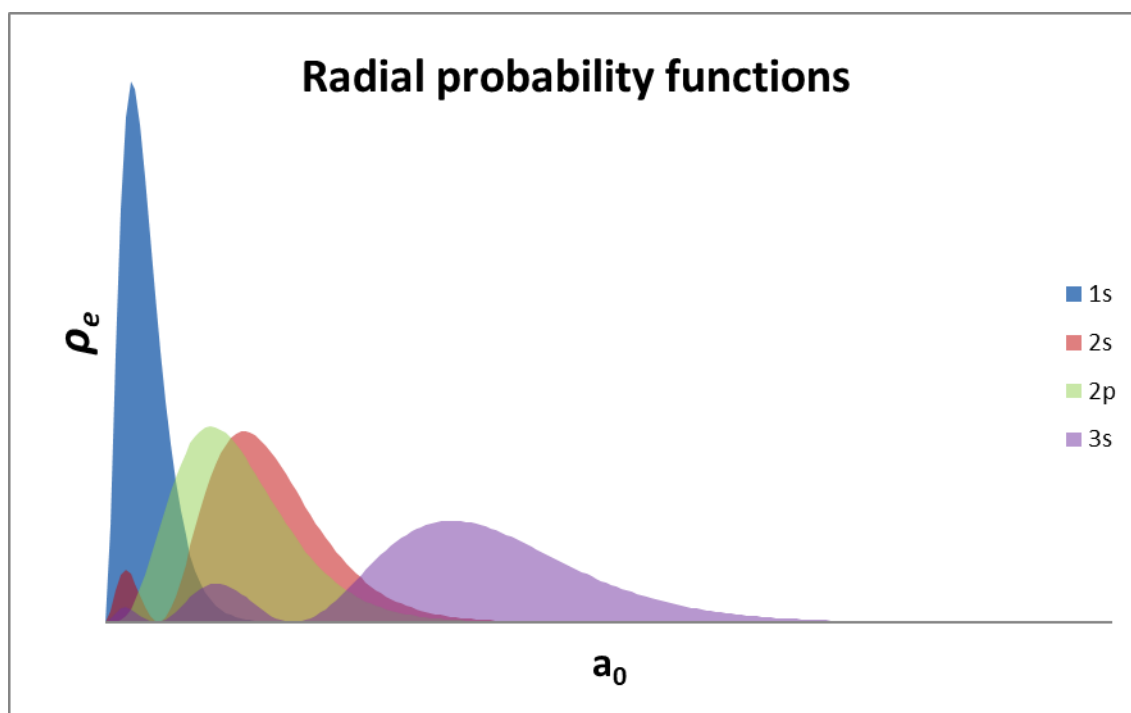
Figure 4. Radial distribution for 1s, 2s, 2p and 3s for a hydrogen like atom.

Formally, the X-ray ASF is defined as the Fourier transform of the electron distribution of the atom:

$$f(r^*) = \int_v \rho(r) exp\,(2\pi i r^* r) dr \quad (1.1)$$

Where $\rho(r)$ is the electron density (ED) or electronic charge density integrated over the atomic volume and r^* is a vector of the reciprocal space, Figure 5.
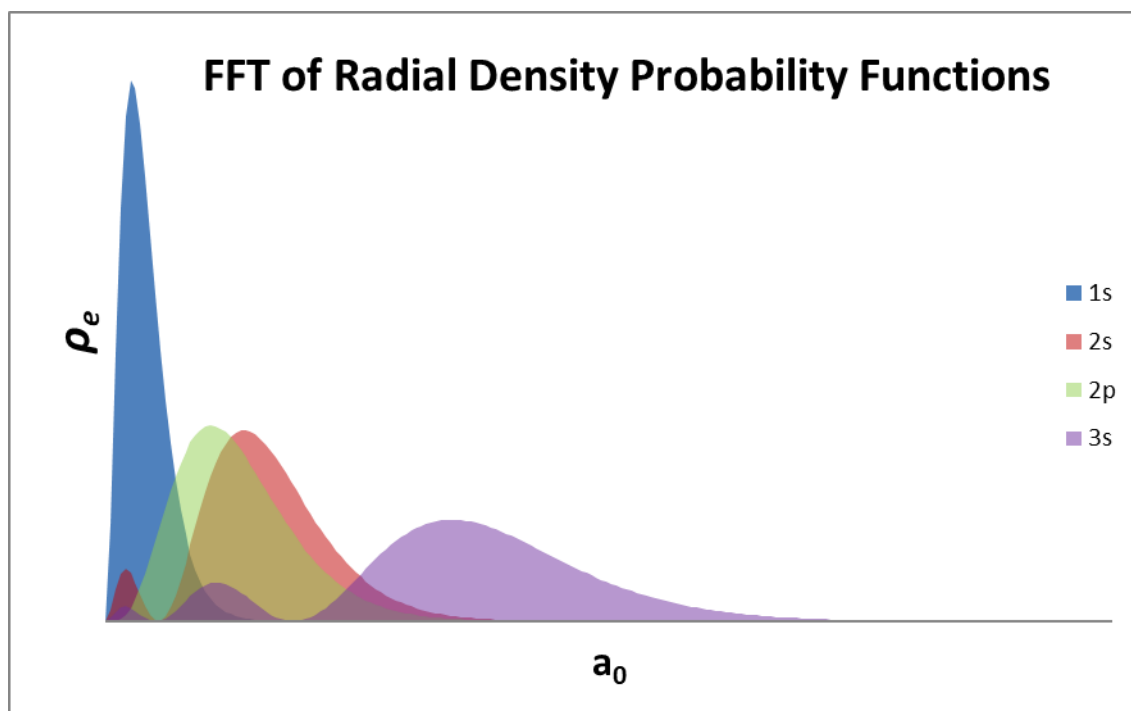
Figure 5. Fourier transform for the 1s, 2s, 2p and 3s radial functions (Slater functions). They are the basis of the atomic scattering factor.

After scaling and correcting processes, the FTs provide a theoretical intensity power. After normalization, this intensity is directly related to the number of electrons in the electron cloud of the atom. The ASF decays with the resolution, making that at high resolution the intensities become much weaker, Fig. 6. This is nothing but the result of the interference at angles different from zero. When the interference angle increases, the phase change of the scattered waves increases thus reducing the intensity.
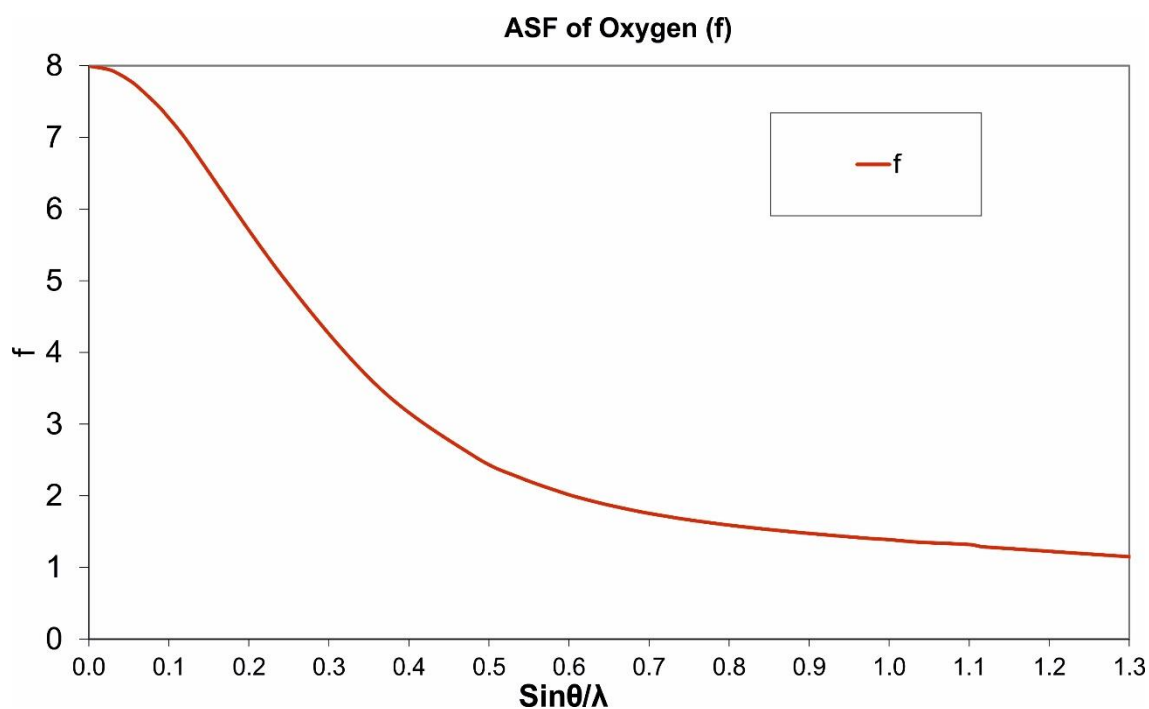
Figure 6. X-Ray atomic scattering factor (ASF) of an isolated oxygen atom versus resolution. The ASF predicts the intensity originated by a single atom owing to the scattering of the x-ray by the electron cloud of this atom.
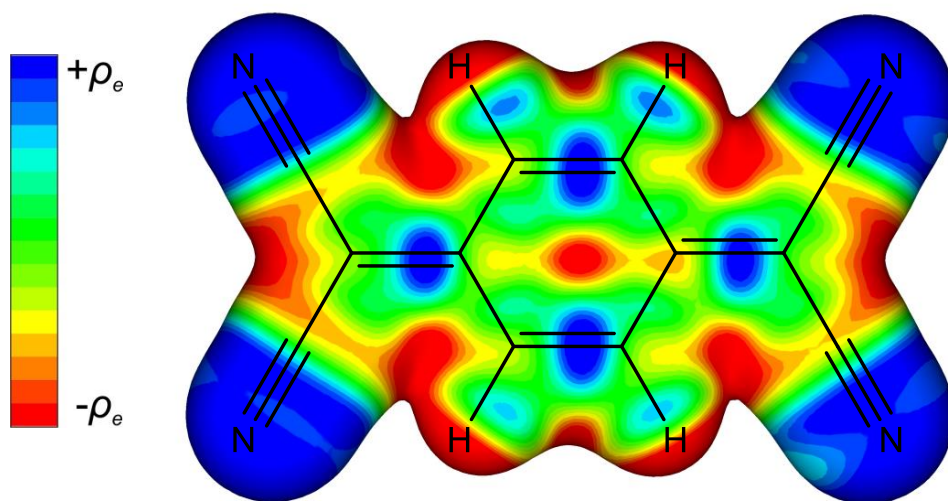
Figure 7. Surface exhibiting the electron density at 0.1 $e/Å^{-3}$ of the structure model of tetracyanoquinodimethane, TCNQ, using spherical atoms, IAM. The isosurface map was colored according to the difference with the multipolar model. It can be seen an increase of the electron density between the atoms involved in the double bonds as well as in the triple bond of the cyano groups and the lone pair of the nitrogen atoms.

1.3 Scattering by a molecule (unit cell).

A crystal is made up of single atoms, ions, molecules, proteins or even viruses. The contribution of the molecule to the diffraction pattern is the result of a second level of interference due to the arrangement of the atoms forming the molecules. In a crystal, we need to identify the minimum repeated entity, the asymmetric unit. With this entity, we would be able to build the unit cell including the information of the symmetry operations. If we calculate the scattering produced by all the atoms contained in the unit cell, and its interference, we obtain the *structure factor*. If the ASF was the Fourier transform of the atomic electron distribution, the *structure factor* is the Fourier transform of the electron distribution of the molecules contained in the unit cell.

$$F(\mathbf{h}) = \sum_j f_j exp(2\pi i \mathbf{h} \mathbf{r}_j) \quad (1.2)$$

As a first approximation, it is possible to build up the unit cell considering the atoms as isolated entities, *independent atom approximation* (IAA). At this level of theory, the atoms preserve its spherical symmetry, IAM. This approximation is very useful for small molecule crystallography allowing the identification of the molecular geometry of crystalline compounds and its supramolecular packing. However, the aim of this work is to go one step further. We are interested in analyzing how the spherical symmetry of the atom electron densities is deformed owing to the intra and inter-molecular interactions present in the crystal. The deformation electron density map is the difference between the "actual" electron density and the theoretical electron density if the crystal was composed of non-interacting atoms, Fig. 7. The "actual" electron density can be calculated using an experimental electron density map derived from X-ray diffraction experiments (crystallography). An approximation providing a more accurate model of the "actual" electron density is the *multipolar charge density model* or *Hansen-Coppens model*[6] . This model considers the deformations of the electron density map due to the interactions between atoms in the crystal structure. It includes deformations of the spherical atom according to the spherical harmonics. It also assigns a valence population to each atom. With this model, we can analyze deformations of the electron density maps, caused by strong atom interactions, i.e.,

covalent bonds, as well as those resulting from weak interatomic interactions, i.e., hydrogen bonds, halogen bond interactions, σ-hole interactions, etc. In addition, the accurate or "actual" electron distribution map of the molecule or molecules forming the crystal can be used to derive their physicochemical properties i.e. dipole, quadrupole values or MEP potentials.

1.4 Scattering by a crystal

In agreement with the interference phenomena described in 1.2 and 1.3, the interaction of the scattered X-rays produced by the array of ordered molecules in a crystal results in an additional "new" interference phenomena, commonly called diffraction.
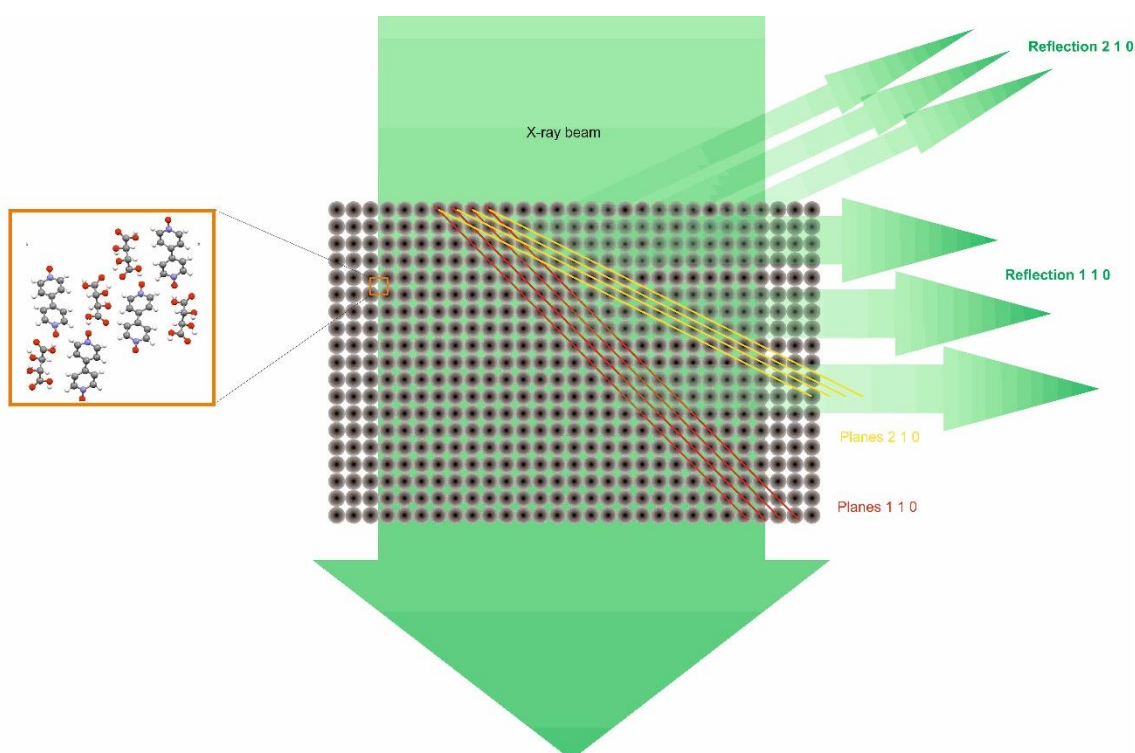
Figure 8. Planes defined by the unit cells, represented by the motifs, along the crystal. The inter-planar distance or resolution varies depending on the plane definition. It is not possible to collect reflections beyond a resolution limit. This theoretical resolution limit depends on the used wavelength and is $\frac{\lambda}{2}$.

In relation to the 3D arrangement of the molecules along the crystal structure, it is possible to define different families of planes, parallels to one another, which are the

origin of interference phenomena producing the diffraction pattern, Figure 8. The distances that exist between the different families of planes provoke that at certain angles (Fig. 9, Eq. 1) the interference phenomena becomes constructive. Therefore, a constructive interference phenomenon will take place when the angle at which one reflection occurs is directly related to the interplanar distance. The condition for having in phase wave fronts from a family of planes is described by the Bragg's law, Eq. 1.3.

$$2d \sin \theta = n\lambda \qquad (1.2)$$
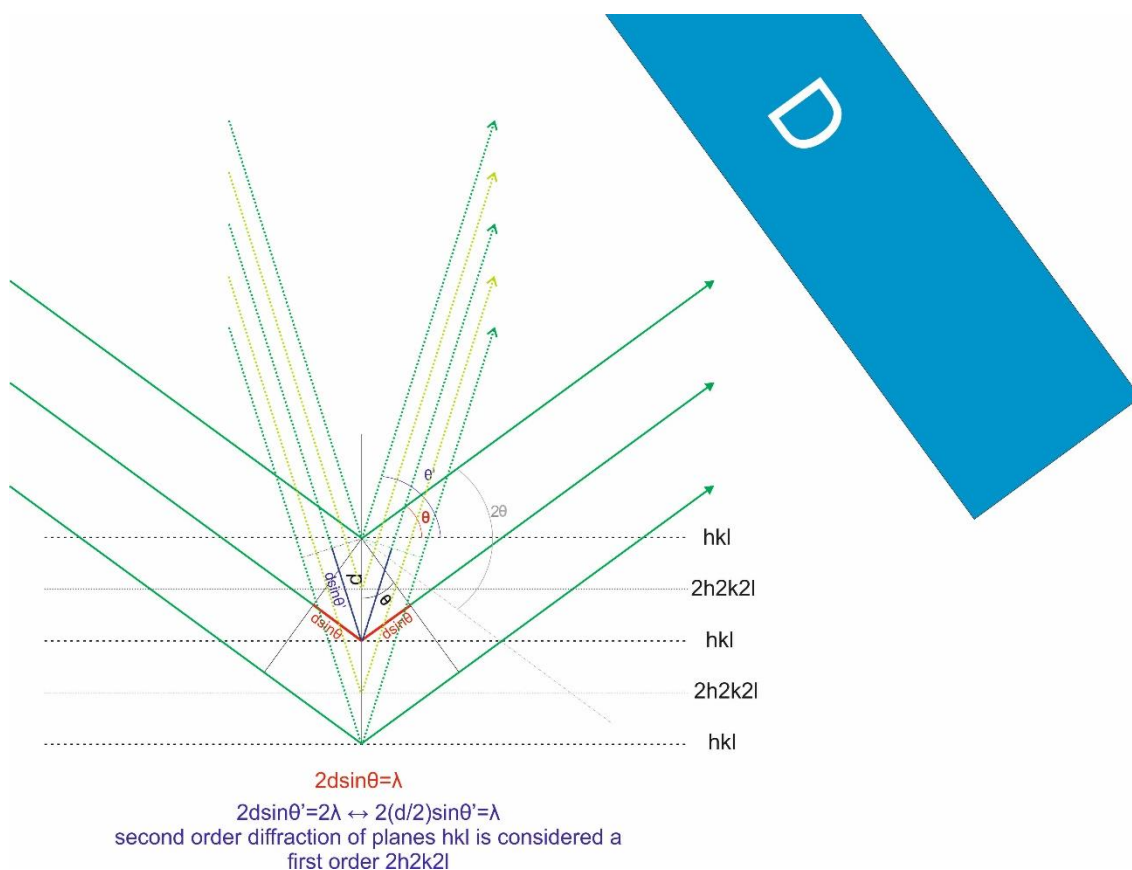
Figure 9. Geometric scheme of the interference phenomena occurring in two selected families of planes. Green lines represent the X-ray beam fulfilling the constructive interference condition for the hkl planes. The analogous representation for a second order interference condition is represented by the dotted lines.

The front waves go through different paths when reflected by the different planes that are parallel one to another. The difference in the paths provokes a change in the phase of the reflected waves. The condition for having a constructive interference is that the path-length difference must be an integer multiple of the X-ray wavelength, Figure 9.

2. Structural models

2.1 The Independent Atom Model, IAM.

After the collected diffraction data has been properly corrected, it is necessary to find the atomic arrangement that is responsible of the diffraction pattern, the phase problem. Once identified, the phase needs to be refined through the theoretical model. The first theoretical model is the Independent Atom Model, IAM. This model is able to unequivocally identify the atom species and its arrangement inside the crystal. In this model, the atoms forming the molecule are considered independent one from the others. The shape of the atoms is approximated to be a sphere. The accuracy of this model is maximal for high order reflections.

2.2 Virtual and Real Spherical Atoms Model

An improvement of the spherical atom model led to the *virtual and real spherical atoms model* (VRSAM)[11,12]. In the VRSAM the atoms are considered as spheres, real spherical atoms, but contain two extra parameters, with respect to the SAM model, that are also optimized in the refinement of the X-ray structure. These parameters are: the valence population P_{val} and the expansion/contraction of the spherical valence shell, k. In addition, the electron density located outside of the atom sphere (outer shell) , i.e., electron density in covalent bonds and lone pairs, is also taken in consideration during the structure refinement by considering a virtual spherical atom having only its corresponding P_{vir} and k_{vir} parameters.

$$\rho(r) = \sum_{atom} \rho_{core} + P_{val} k^3 \rho_{val}(kr) + P_{vir} k^3 \rho_{vir}(kr) \qquad (1.4)$$

2.3 Multipolar model; the Hansen-Coppens model.

This model is based on applying deformations to the spherical atom model. This is done by including spherical harmonic functions. The spherical harmonic functions are in fact the solutions of the Schrödinger equation for an isolated hydrogen-like atom. The *Hansen-Coppens model*[6] treats the electron density around an atomic nucleus considering an spherical electron density part for the inner shell that is analogous to the VRSAM. The part of the equation for the outer-shell electron density implies the use of fixed spherical functions combined with spherical harmonics. Both types of functions are centered in the atomic nucleus, Figure 10.

Mathematically, this model considers the expansion/contraction of the spherical distribution and its deformations as follows:

$$\rho(r) = \rho_{core} + P_{val}k^3\rho_{val}(kr) + \sum_{l=0}^{l_{max}} k'^3 R_l(k'r) \sum_{m=-l}^{+l} P_{lm}Y_{lm}(\theta,\varphi) \qquad (1.5)$$

The first two components are spherical densities corresponding to the core and the valence densities, respectively. The origin of these two densities is in Hartree-Fock (HF) or relativistic HF atomic wave functions. The parameter P_{val} assigns electrons to the valence shell while the parameter k expands or contracts the spherical valence shell. The third term includes the radial functions R_l, taken as Slater functions, which expansion/contraction is modulated by k' and the spherical harmonics functions multiplied by the parameter P_{lm} that assigns electronic population to the corresponding projections of the spherical harmonics. This term does not present a spherical symmetry serving to simulate the non-spherical anisotropic charge deformation.
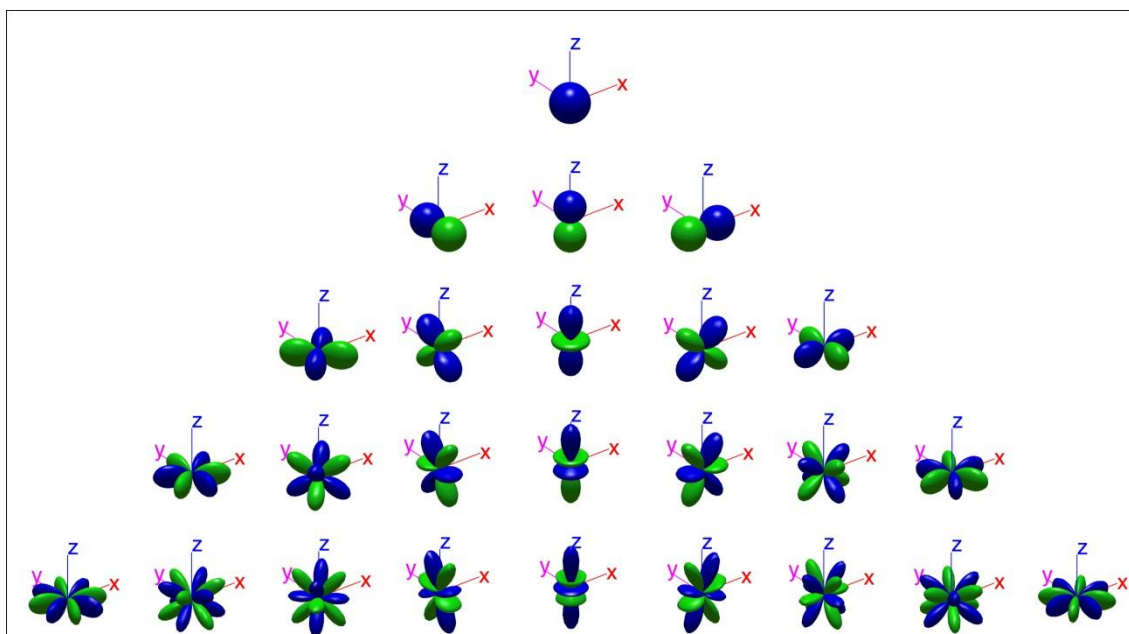
Figure 10. Representation of the Spherical Harmonics functions. First row corresponds to l=0, Y_{00}, second row to l=1, Y_{1-1}, Y_{10}, and Y_{11}. Successive rows are representations of the l=2, l=3 and l=4 projections.

2.4 Database models.

This structure model uses the deformations obtained in multipolar refinements to develop an aspherical model of electron density without performing a multipolar refinement[13]. To this end, it is necessary to use the information of the atom and its neighbors, in particular the ones that are covalently bonded. The power of this model increases as the database of atom scattering factors (ASF) corrected with multipolar refinements grows. The use of this model in the refinement of subatomic resolution protein structures allows the experimental description of their electrostatic properties.[13] Examples of databases are ELMAM, ELMAM2[14], UBDB[15] or Invariom.[16]

31

3 Important corrections to the structure factors in high resolution refinements

In a regular single crystal experiment, many corrections of the crude data are required in order to extract the useful contained information. There are corrections of the beam due to its polarization, corrections of the reflections due to is shape, due to the detector's shape, etc. Due to the special characteristics of the crystals needed for high order refinements some corrections become crucial to obtain realistic results.

3.1 Thermal motion

The atoms forming a crystal do not remain in rest due to their thermal motion. The vibration of the atoms in the crystal modulates the theoretical intensities predicted by the static structure factor. In this way, the ASF, f, decays as the thermal motion increases. It is possible to analyze the effect of the isotropic thermal motion of atoms in an X-ray diffraction experiment. Under these conditions, the ASF is defined by equation 3.1.

$$f' = f \exp(-\beta \frac{\sin^2 \theta}{\lambda^2}) \quad (3.1)$$

In Eq. 3.1, the atomic vibration weakens the intensity of the ASF following an exponential function. The β factor is called the *Debye-Waller factor* and is nothing but the isotropic thermal parameter multiplied by a constant, $8\pi^2 U_{iso}$. Moreover, β is multiplied by the square of the resolution, $\frac{\sin^2 \theta}{\lambda^2}$. This means that the weakening of the ASF intensity due to the atomic thermal motion is larger for high resolution reflections (high angle), Figure 11.

An accurate estimation of the vibrational parameters is crucial for obtaining reliable results. In Coppens own words: "no reasonable estimate of the charge density parameters can be obtained without an adequate description of the thermal

motion"[17]. Large thermal vibrations parameters produce serious disadvantages when performing X-ray charge density studies. On the one hand, the lower intensity of the high resolution ASF data decreases the number of observable reflections and the precision of the ones that are observed. On the other hand, thermal motions make electronic deformations more diffuse. Therefore, the best estimation of the thermal parameters is done at low temperatures. In fact, high order reflections contain accurate information on the thermal parameters and the atomic positons (hydrogen atom excluded).[18]
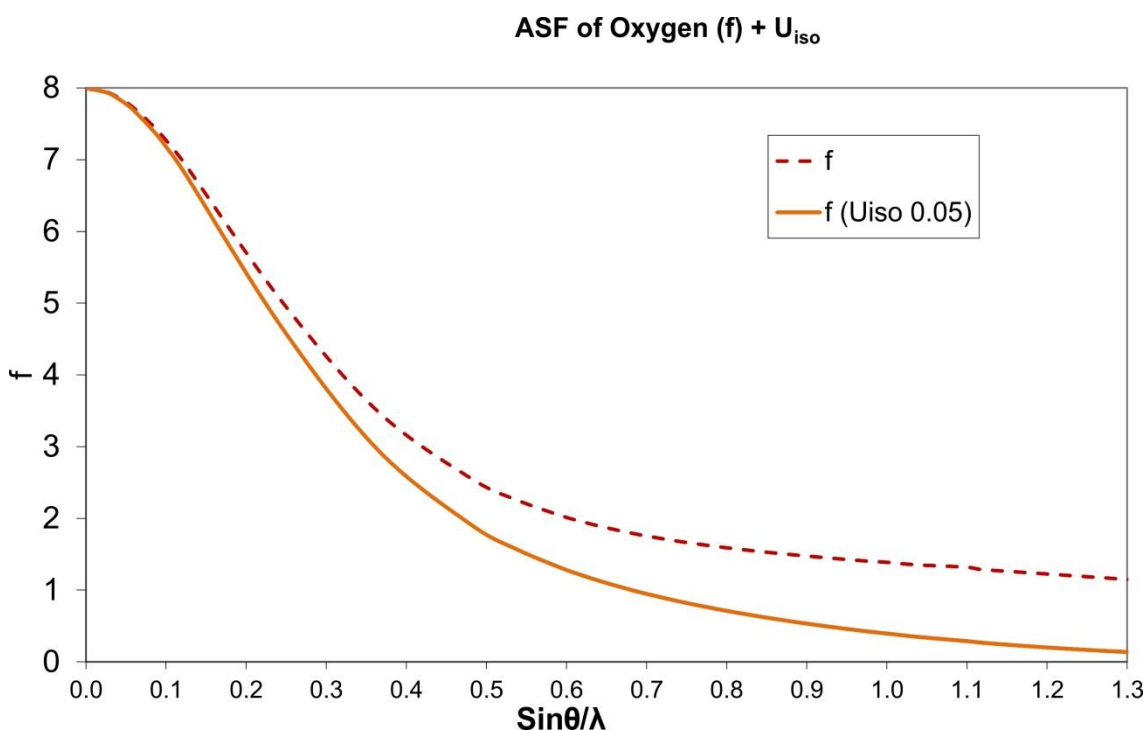
Figure 11. Plot of the ASF of an isolated oxygen atom versus resolution (Å^{-1}). The red dotted line represents the no thermal motion case and the orange line an isotropic thermal motion parameter of 0.05 Å^2.

Formally, the thermal motion must be modeled with parameters included in the refinement of the structure. It should not be dealt with a simple correction of the experimental diffracted data.

3.2 Harmonic and Anharmonic thermal motion

In the IAM model and in most multipolar refinements the atomic thermal motion follows a Gaussian distribution, harmonic thermal motion. However, in highly accurate high order data collections this harmonic model cannot be enough to describe the atomic thermal motion in the crystal.[19,20] The most common statistical approaches to treat the anharmonic motion of the atoms within a crystal are the Gram-Charlier coefficients.[21] Using the high resolution reflections, these parameters can clean residual densities that cannot be correct with the usual thermal motion parameters.

3.3 Absorption correction

A very important correction of the diffracted data is called *absorption correction*. It consists in correcting the absorption effects caused by the material that the X-ray passes through. It would depend on the compound and on the path of the X-ray through the crystal, the crystal shape. There are two main methodologies for this type of correction. Within the *semi-empirical* methods, the *multi-scan method* of Blessing[22] is of most use when there is a large redundancy in the data-set. Nowadays most of the single crystal diffractometers benefits of this methodology since they are equipped with 2D detectors that allows large redundancies of data. Equivalent reflections should have identical intensities. These equivalent reflections are analyzed in terms of a multipolar spherical harmonic expansion. This method is implemented in several programs like the widespread SADABS[23] or SORTAV[22]. The multi-scan absorption correction works remarkably well for crystals with small absorption coefficients, μ, light absorbers.

When the absorption of the crystal is large, $\ll \mu$, it would be necessary to apply complementary corrections. The so-called *numerical methods* require that the crystal faces can be accurately indexed and measured. In this way, it is possible to determine empirically the crystal shape. The measurement of the crystal faces can be complicated when crystals with irregular faces need to be corrected. In cases of severe

absorption however, numerical methods are essential in order to obtain well-corrected data sets. A particular case are cylindrical corrections that can also provide numerically accurate corrections for crystals whose morphology are cylinders, as the crystals grown inside capillaries.

3.4 Extinction

The diffraction process has been described in section one, explaining the origin of the so-called reflections. Crystallographic planes are the cause of the reflections when the primary X-ray beam goes through the crystal. This theory is assuming that the crystal has a degree of imperfection that neglects the fact that the reflections can be successively dispersed along the crystal. However, it certain crystal samples, the diffracted beam can be successively diffracted. The outcome of this new diffraction is to decrease the intensity of the affected reflections.[24,25] There are three main potential extinction processes:

- *Primary extinction*. The extinction is due to the reflection of the reflected beam, Figure 12a.

-*Secondary extinction*. The beam, when going through the crystal, decrease its intensity due to the successive reflections suffered along the crystallographic planes, Fig. 12b.
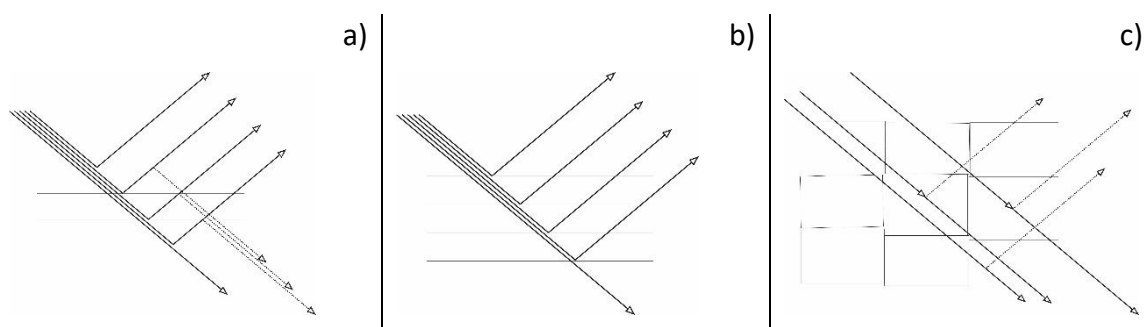
Figure 12. Schemes of the three extinction process happening in crystals. a) primary extinction due to a perfect crystal. b) secondary extinction, where the beam is progressively extinct when going through the crystal. c) extinction due to mosaicity.

-*Mosaicity extinction*. The beam, when going through the different perfect crystal domains forming the single crystal, Fig. 12c.

3.5 Renninger effect.

When the diffraction is very intense and comes from a quasi-perfect crystal, the reflections can be reflected in another family of planes, Figure 13. This effect can be significant in big crystals containing heavy atoms. The most affected reflections would be the most intense and would appear at low resolutions. These reflections are critical when refining charge density models of compounds containing heavy atoms.
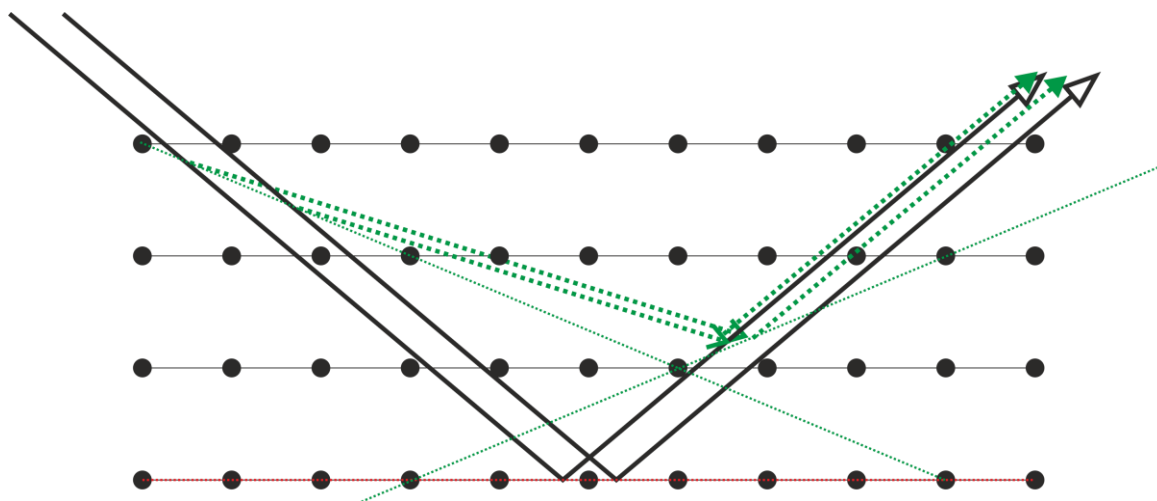
Figure 13. The Renninger effect occurs when reflections are reflected by a different family of crystallographic planes. Black lines representing a family of planes where occurring a reflection. Green dotted lines represent tw different families of planes where secondary reflections overlap direct beam reflections.

4   Experimental methodology

4.1 Low temperature is mandatory

For reducing the effects of the vibrational thermal motion it is necessary to cool down the crystal sample to the lowest achievable temperature. In this way one can minimize the extra reduction in the scattering diffraction intensity that is more intense at high resolutions as showed in section 3.1 (Figure 11). There is a double benefit in the use of low temperature in single crystal experiments. First, the low temperature improves the signal to noise ratio of the high resolution reflections, what makes that more reflections are available for refining the structure. Second, high resolution reflections mainly contain information of the position and thermal motion parameters what leads to a more accurate estimation of these parameters without being altered by other effects.

In the current days the cooling of the crystal sample is performed using a gas stream of nitrogen, for temperatures until 80K or helium, that can reach 15K in open gas streams. Cryostats can reach temperatures up to 4K.

Additionally, low temperatures reduce the vibration of the crystal lattice, the thermal diffuse scattering (TDS). These lattice vibrations produce a diffuse background and affect the intensity of the reflections. It can be significant, especially at high angles.

4.2 High redundancy and completeness.

In order to minimize errors in the data collection it is important to increase the redundancy. The redundancy, in crystallography, is the times that one reflection is collected. If one reflection is collected 10 times with a good $I/\sigma(I)$ ratio, it has more chances for being correctly estimated than one reflection 2 times collected. On the one hand, the absorption correction methods benefit of the redundancy. On the other hand, it is more likely to identify outlier data. In the same manner, collect all the

possible reflections helps in the absorption correction and in the absolute structure determination.

4.3 Higher exposure times for collecting frames at high resolution

As shown in section 1.2 and 2.1, at higher resolutions the reflections intensity decay dramatically because of the ASF decay combined with the atomic thermal motion. Other facts like mosaicity also decrease the intensity at high resolution. Though the low temperature helps in the detection of the high-resolution reflections, it is necessary to increment the data collection exposure times in the high resolution ranges, Fig. 14. Moreover, even using high exposures times it is usual to obtain less reliable data at ultra-high resolution ($\sin\theta/\lambda > 1.0$ Å^{-1}).
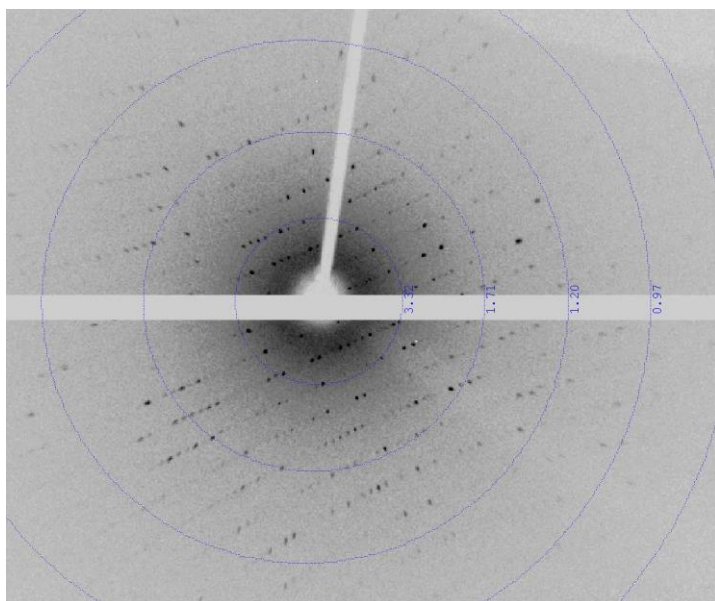
Figure 14. Frame showing reflections at different resolutions. Values of the resolution, d, are displayed in Å. Reflections inside the 1.71 Å resolution circle are obvious while reflections beyond a resolution of 0.97 Å are difficult to observe.

Paradoxically the exposure time can become a problem for the low-resolution ranges. The combination of long exposure times and with very strong reflections, leads to the risk of getting overflows if the detector achieves its count limit. (Even if the exposure time is minimum, one can get overflows depending on the counts per second detection limit of the detector). A detailed check of the intense low-resolution

reflections is therefore recommended. Though a single crystal experiment can provide thousands of data, every data becomes important if we want to detect for example the electronic deformation that can be a small fraction of the total electronic density even in organic compounds. Moreover, if one looks for the deformation of the electronic charge density, the low-resolution reflections become critical since they contain the information of this deformation. Additionally, the number of reflections increase with the resolution in a cubic potential factor. It means that at low resolutions there are fewer reflections available. This is critical for heavy atoms where only a few reflections contain information of the deformation electron density related with wide spread orbitals.[26]

4.4 High order refinement.

As stated before, the information of the deformation of the electronic density is contained in the low resolution reflections. When speaking about low resolution it depends of the type of atoms forming the crystal and even on the orbitals. For example, for the 4s orbitals of 3d transition metal only a few reflections at very low resolution contain this information.[27] For organic molecules containing oxygen as heaviest atom, this deformation of the electronic cloud is noticeable until resolutions of 0.9 $Å^{-1}$. When high-resolution data are available it is recommendable to perform a high order refinement. It consists in a refinement of the IAM position and thermal parameters of the non-hydrogen atoms using only the high-resolution data, i.e., reflections with resolutions over 0.9 $Å^{-1}$ for pure organic molecules. The resulting parameters of such a refinement are 'free' of the influence of the deformation densities, what allows obtaining more accurate and precise position and thermal parameters for non-hydrogen atoms.[18,28]

4.5 Hydrogen location.

Hydrogen atoms are a particular case in the X-ray diffraction data. Its only electron is involved in a bond. As pointed out in section 1.1 this electron is the only source of information we can obtain from a hydrogen atom in an X-ray experiment. For a good crystal and with the current diffractometers is not difficult to identify the position of these electrons. However, these electrons have larger vibrational and librational amplitudes than in other atoms. Additionally, the multipolar model needs to establish the position of the atomic nucleus in order to assign population to the spherical harmonics projections. Experimentally, the hydrogen nucleus can be determined through a neutron diffraction experiment. Contrary to the X-ray case, the neutron scattering factor of the hydrogen nucleus is quite intense. Unfortunately, single crystals neutron data collections are not routine experiments and have serious limitations. A shortcut to estimate the proton position of the hydrogen atom is to use averaged neutron-determined distances[29,30] or use they together with theoretical calculations[31,32]. In the same way, the thermal motion parameters of the hydrogen atoms cannot be properly estimated in an X-ray diffraction experiment. Again, theoretical calculations based on experimental neutron data can be used to approximate these vibrational parameters[33].

There is an alternative to the use of calculated hydrogen thermal motion parameters. It is possible to refine the hydrogen vibrational parameters using databases as ELMAM[8], UBDB or Invariom[16].

4.6 Selection of the axis in a Multipolar Model.

Due to the geometry of the spherical harmonics functions, it is very important to choose a system of coordinates in each atom that afford to justify the electron density deformation. Moreover, the axis selection allows to "switch off" some projections of the spherical harmonics due to the incompatibility of certain projections with the geometry of the deformation. In this way, one can reduce the number of refined

parameters and get reliable convergence minima[34]. Typical examples of the use of proper axis that allow the spherical harmonics functions to accommodate electronic deformations due to covalent bond are sp^2 hybridization systems. For this particular bond geometry is usual, taking the origin in the sp^2 hybridized atom, to choose the *Z* axis perpendicular to the plane formed by the three bonded atoms and the *Y* axis in the direction of one of the bonds. In this manner, the P_{33} SH function increase the charge density in the direction of the three involved covalent bonds and reduce it in the in between regions, Figure 15.
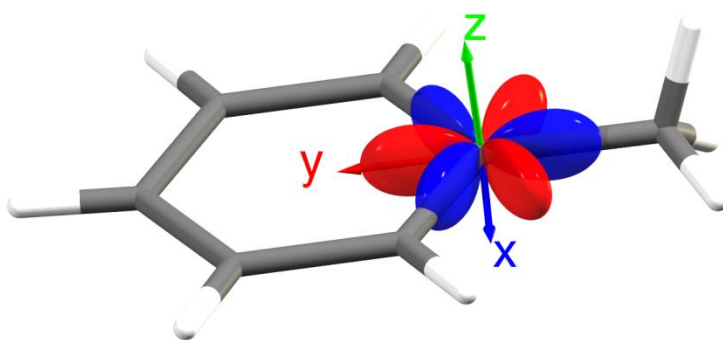
Figure 15. Example of a deformation happening in an aromatic ring, corresponding to a sp^2 hybridization. Three blue lobs of the spherical harmonic function P_{33} increase the electron density along the bond paths while the 3 red lobs decrease the electron density.

Another deformation that should take place on a sp^2 hybridization is a reduction of the electronic density over the z axis, corresponding to the pi orbitals. This deformation is well justified with the help of the SH function P_{20} that turns to be negative, Figure 16.
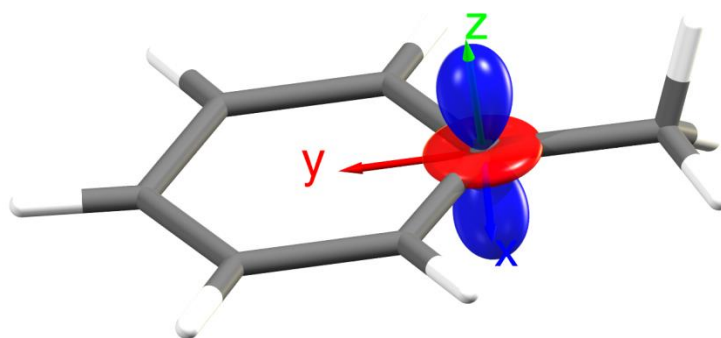
Figure 16. In the P_{20} SH function, blue lobs represent an increase in the electronic density, contrary to what one expects in a sp^2 hybridization, therefore P_{20} will take negative values.

Particular cases for the axis selection are again the hydrogen atoms. Its expansion is generally limited to the P_{10} multipolar term, i.e., one dipole oriented in the direction of the bond (z axis). Only in strong hydrogen bonds it was suggested the use of quadrupole moments for hydrogens[35]. Nevertheless, other groups claim that the deformation of the hydrogen atoms involved in hydrogen bonds is in better agreement with the theoretical calculations when using only one dipolar term[36]. The deformation of the electronic density is described through the SH. It is worth to stress that the SH projections are not equivalent to the atomic orbitals/molecular orbitals, MO. For example, Fig. 15 shows how the electronic deformation of a sp^2 hybridized carbon can be described with the help of the P_{33} SH projection. It has nothing to do with the electronic orbitals but its shape, Fig. 17. Despite there are some works claiming the observation of molecular orbitals,[37-43] these assertions are not free of controversy due to its limitations or even their consistency.[44,45] In a X-ray charge density experiment, the observable from which the information is extracted is the electron density distribution that is not the same that the wave functions that define the atomic or molecular orbitals.[17]
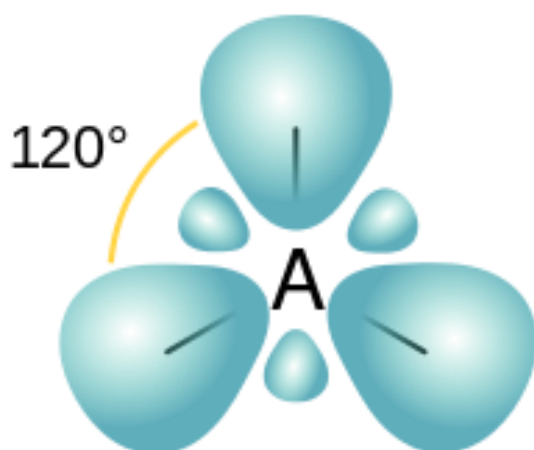
Figure 17. Representation of the three hybridized sp2 orbitals of a carbon atom (A).

4.7 Restrains and constrains. Reducing the number of parameters.

Imposing a constrain into a parameter fix the value of the parameter. However, a restrain allows to refine the parameter with a standard deviation around a target value. In the previous section 4.3 it was commented the possibility of, through a proper selection of axis for the spherical harmonics, considerably reducing the number of parameters, favoring determined projections of the SH. Imposing certain symmetry operations on the deformation geometry makes that some SH projections are forbidden. The associated P_{lm} parameters of this forbidden SH functions remain as zero and don't need to be included in the least square minimization matrix. In some cases, this can be essential to maintain an acceptable ratio data to parameters. Moreover, for non-centrosymmetric structures the local symmetry constrains can became critical for retrieving physically meaningful results[46,47].

5 Interpretation of results

5.1 Topology

After obtaining a model of the charge density distribution, it is time to analyze its shape in order to extract information. For example, in the *Atoms in Molecules* theory (AIM) the analysis of the derivate (gradient) and the second derivate (Laplacian) of the electronic distribution can give advices of the interaction strength, bond type, hybridization, etc.[48,49]

The points were the gradient of a function becomes cero are called critical points. The gradient vectors define a gradient vector field. This vector field define gradient paths. A gradient path always originates and terminates at critical points. In the present case, the function is the charge density of the electronic distribution, $\rho(r)$.

$$\nabla\rho(\mathbf{r}) = \left(\frac{\partial\rho}{\partial x}, \frac{\partial\rho}{\partial x}, \frac{\partial\rho}{\partial x}\right) \qquad (5.1)$$

$$\nabla^2\rho(\mathbf{r}) = \begin{pmatrix} \frac{\partial\rho^2}{\partial x^2} & \frac{\partial\rho^2}{\partial x\partial y} & \frac{\partial\rho^2}{\partial x\partial z} \\ \frac{\partial\rho^2}{\partial y\partial x} & \frac{\partial\rho^2}{\partial y^2} & \frac{\partial\rho^2}{\partial y\partial z} \\ \frac{\partial\rho^2}{\partial z\partial x} & \frac{\partial\rho^2}{\partial z\partial y} & \frac{\partial\rho^2}{\partial z^2} \end{pmatrix} \qquad (5.2)$$

$$\nabla^2\rho(\mathbf{r}) = \frac{\partial\rho^2}{\partial x^2} + \frac{\partial\rho^2}{\partial y^2} + \frac{\partial\rho^2}{\partial z^2} \qquad (5.3)$$

In a second derivative, calculating the eigenvalues of the Hessian matrix, it is feasible to identify the nature of those critical points. Mathematically, the gradient of a three dimensional function is a three coordinates vector, Eq. 5.1. The second derivative is a symmetric 3x3 matrix, the Hessian matrix, Eq. 5.2. After diagonalization, the three eigenvalues of the Hessian matrix (curvatures) determine the kind of critical point. If all three eigenvalues are non-zero, the *rank* (ω) of the critical point is 3. These critical points are topologically stable. The *signature* (σ) is the algebraic sum of the signs of the eigenvalues. The critical points can be then classified attending to their rank and

signature (ω, σ). Let us call the eigenvalues λ_1, λ_2 and λ_3. There will be four types of critical points, Table 1.

Table 1. The four types of critical bond defined by the sing of the 3 eigenvalues or curvatures.

Notation (ω, σ)	curvatures	N maxima	N minima	Type	Abbreviation
(3, +3)	$\lambda_i > 0$	0	3	Minimum-Cage	CCP
(3, +1)	λ_1, $\lambda_2 > 0$, $\lambda_3 < 0$	1	2	Saddle-Ring	RCP
(3, -1)	$\lambda_1 < \lambda_2 < 0$, $\lambda_3 > 0$	2	1	Saddle-Bond	BCP
(3, -3)	$\lambda_i < 0$	3	0	Maximum-Nucleus	NCP

The critical points where all three curvatures have negative values, (3, -3) indicates that ρ has a maximum. They are typically nuclear atomic position. All the surrounding gradient lines terminate at these type of critical points. That defines the *topological atom*, that is the region of space, *basin*, where the sets of trajectories defined by the gradient of ρ terminating at the nucleus or attractor[48].
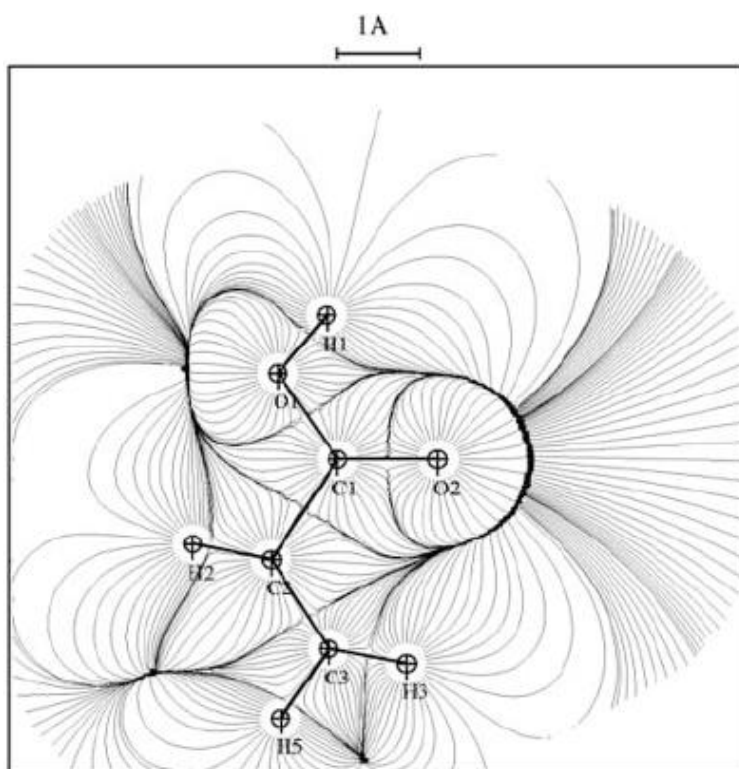
Figure 18. Gradient lines defining the atomic basins defining the topological atom.

When only one of the critical points is positive, (3, -1), the ρ function has a saddle point. In two directions, the charge density presents a maximum while in the third it has a minimum, corresponding with the positive curvature. This charge accumulation takes place between nuclei and is a necessary condition for bond formation in Bader's theory. Attending to the electron density in these type of critical points Bader establish a *bond order*, assigning a covalence to each bond, that improves the one defined by Pauling based on the bond distance. Currently, there are more complex and accurate bond orders, like the topological bond orders (n_{topo}), as defined by Howard et al.[50] Furthermore, regarding at the geometry of the charge density distribution at the critical point vicinity, one can define the *ellipticity* of the critical point. The *ellipticity*, ϵ, of a BCP is defined as:

$$\epsilon = \left|\frac{\lambda_1}{\lambda_2}\right| - 1 \qquad (5.4)$$

Where λ_1 and λ_2 are the negative curvatures of the (3, -1) cp. In principle, the bond, ϵ, could be a descriptor of the covalent *bond order*. However, has the well-known behavior of increasing to a maximum value for a 'perfect' double bond, and then decreasing to zero in the range of double–triple bonds as the bond approaches cylindrical symmetry. In other words, the bond order is not a single-valued function of, so is not suitable as a statistical descriptor of bond orders between atoms which can form triple bonds, e.g. C—C, C—N, C—P and so on.

An important function to analyze is the Laplacian, that is, the second derivative of the scalar function. It is equivalent to the sum of trace of the Hessian matrix, eq. 5.3. The Abramov expression associates the Laplacian with the energy[51], Eq. 5.5.

$$\frac{\hbar}{4m}\nabla^2\rho(r) = 2G(r) + V(r) \qquad (5.5)$$

This expression has been shown to be very consistent, for some weak interactions, with the experimental X-ray CD studies reported.[52-55]

5.2 Deformation maps

The residual maps of the electronic density are necessary tests to evaluate both the data before the charge density analysis and how the final model fits with the charge density.

Iso-surfaces plots of deformation densities around the molecules illustrate:

(a) the theoretical deformation ρ - ρ_{sph} (from periodic DFT/B3LYP)

(b) the static model deformation ρ_{stat} - ρ_{sph}

It exhibits the deformations between the multipolar model and the spherical model. This deformation, of two theoretical model but based on experimental data, is the easiest to interpret because of its soft shapes.

(c) dynamic model deformation F_{mult} - F_{sph}

It serves to compare the deformation obtained from the model with the observed deformation on the Fourier maps.

(d) the experimental deformation F_{obs} - F_{sph}

Similarly to the dynamic deformation map, it gives an idea of the deformation observed with respect to the spherical model. However, this deformation does not require a multipolar model and can be used to test the potential use of the collected data in a multipolar refinement.

5.3 Properties derived from the multipolar model

5.3.1 Electrostatic potential

Electrostatic interactions extend their effect in a long range. This long-range influence affects solvation, nucleation or chemical reactions within other chemical processes. An interesting point to take into account is that, the electrostatic potential derived from

the X-ray structure models include the effect of the crystal packing. One expects that the arrangement of the molecules organizes the molecules in the way that nucleophilic fragments point to positive electrostatic potential regions. Conversely, electrophilic regions will point to negative electrostatic potentials. This causes an effect into the electrostatic potential that should be taking into account when comparing it with theoretical calculations of the MEP.

The electrostatic potential, as usually defined, has a maximum in the atomic nucleus and decays with distance, being zero at infinite. When calculating the *molecular electrostatic potential* (MEP), it is usual to show it as an iso-surface at values of the electronic density iso values of 0.001 u.a., i.e. 6.75 e/$Å^{-3}$. This iso-surfaces values corresponds to separated regions from the atomic nucleus that are regions where the electrostatic molecular interactions are important.

5.3.2 Electrostatic moments

The calculation of the electrostatic moments form the pseudo-atoms model obtained from a multipolar refinement is well known. Even than Spackman and Byrom[56] note an overestimation in the quadrupole moments obtained through CDS, the results are consistent when comparing them with theoretical studies. As in the case of the electrostatic potential, it is expected an influence in the electrostatic molecular momentums due to the crystal packing that may provoke polarization effects. For a reliable electrostatic moment determination it is essential an accurate estimation of the multipolar parameters avoiding over-parametrization.[57]

6 Validation tools

The refinement of a pseudo-atoms model is a complex task. After a least squares refinement there are a few indices that, like in the IAM model, are indicators of the validity of the refinement. One of the best know factor of how well a model fits with the experimental data is the *R-factor*, Eq. 5.6. It is the most popular index, present in all published structure. However, the factor that is directly related with the quantity that is minimized in the least squares refinement is the *weighted R-factor*, Eq. 5.7.

$$R = \frac{\sum_{hkl} ||F_o| - Sc|F_c||}{\sum_{hkl} |F_o||} \qquad (5.6)$$

$$wR_2 = \sqrt{\frac{\sum_{hkl} w(F_o^2 - (ScF_c^2)^2}{\sum_{hkl} w(F_o^2)^2}} \qquad (5.7)$$

A full set of indicators of how well a structure was refined is found in the program PLATON. It is well known by all crystallographers the *check-cif* validation tool implemented in this program. Within others, PLATON checks the *rigid bond test* (RBT) and the residual Fourier map, two indicators of if the model is sound or not.

There are other analysis that are complementary to the usual ones commonly used in standard IAM refinements. In CDS, one of the most important analysis is to verify that, after the refinement of the model, the residual electron density than cannot be justified with such a model does not present an organized structure, i.e., behaves as Gaussian noise[58,59], Figure 19.

Other data analysis can take care of the scaling of the data. It is important that the collected data have the same scale factor along all the resolution ranges, Figure 20. There are many factors influencing the correct scaling of the data. Software, detector, radiation source, optics or cooling system within others, are potential distorters of the intensities collected.[60]
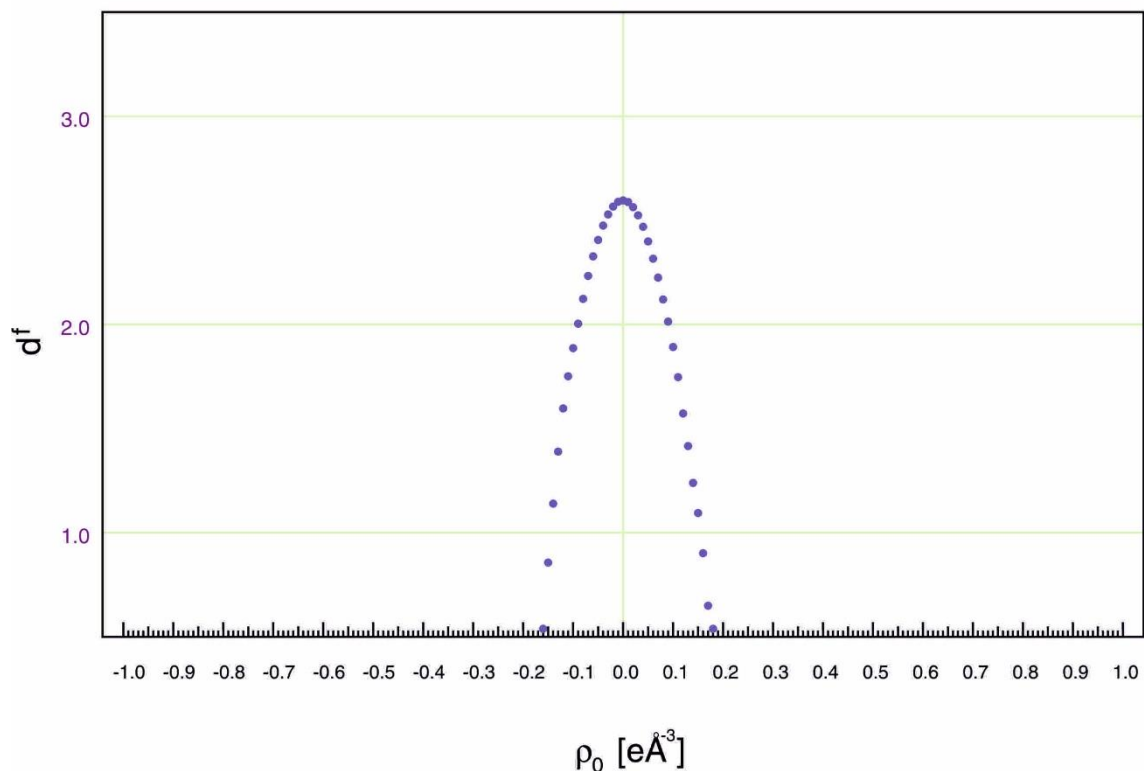
Figure 19. Analysis of the residual density. A Gaussian distribution of the residual electron density should display a parabolic curve in the Fractal dimension test developed by Meindl & Henn[59]
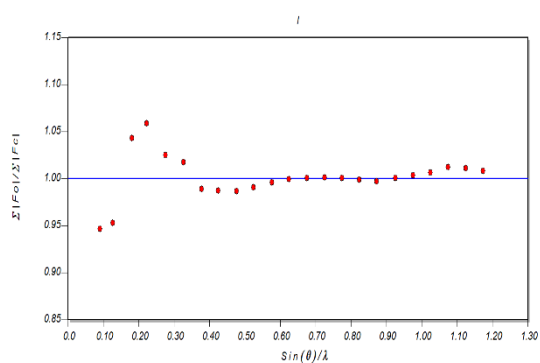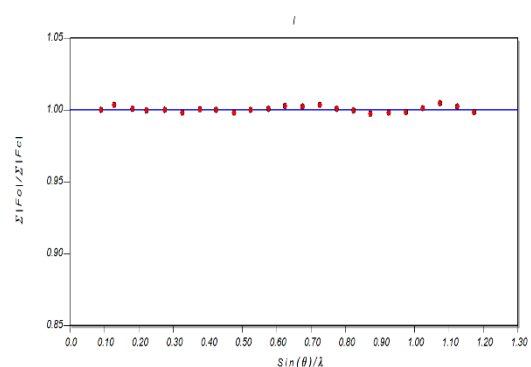
Figure 20. Comparison of the behavior of the scaling factor, $\sum|F_o|/\sum|F_c|$, at different resolution ranges using de program XDRKplot[60]. Scheme a) shows problems at low resolution while b) exhibits a correct flat shape demonstrating a stable scaling factor.

7 Limitations of the charge density analysis, AIM theory.

The QTAIM theory has been useful for the CDS performed during the las decades. The limitation of the multipolar models was well known but the accuracy of the data was not sufficient to notice them. Nowadays, state of the art instrumentation allows data that are much more accurate. This is pushing the researchers of the field to facing these inexactitudes for improving the model in order to extract the maximum allowed information of the data.

One of the best know limitation of any x-ray model is the impossibility to detect the hydrogen atoms. This is not completely true; the limitation of the x-ray diffraction is that only the electron density participating in the bond of the hydrogen can be detected. In reality, this happens in every atom but, for non-hydrogen atoms, there is electron density associated with the core of the atom that enables the correct positioning of the atomic nucleus.

The molecular orbitals are not accounted for.[61] Even though the orbitals are the result of two or more atoms, the QTAIM treat them as a product of the orbitals of the individual atoms. Moreover, the atomic orbitals are not implemented in the QTAIM but the atomic electron density is a sum of atomic terms.

The truncation of the spherical harmonics expansion for describing the atomic electron density. A perfect description requires an expansion in infinite terms what is not feasible.

The electron density of the atomic core is approximated to the one of the isolated atom. However, the distortion of the core of the atoms can happen affecting the diffraction in a perceptible manner.[62]

8 Anomalous dispersion

When the arrangement of the molecules of a crystal makes it non-centrosymmetric, it is possible to distinguish the orientation of the molecules trough this arrangement, its

absolute structure. The reflections of a centrosymmetric crystal structure will respect the Friedel law that says that the reflections hkl and $\overline{hkl}$ will have the same intensity; $F(hkl) = F(\overline{hkl})$, Figure 21. The anomalous dispersion is a non-elastic scattering that is always present when interacting electromagnetic waves with atoms. It is the responsible of the differences in the Friedel pairs. The anomalous dispersion corrections to the ASF are named *f'* and *f''*. While the effect of *f'* is to decrease the ASF, *f''* provokes a variation in the ASF accompanied by a phase change. This phase change is the responsible of the breaking of the Friedel law, $F(hkl) \neq F(\overline{hkl})$, in non-centrosymmetric structures.
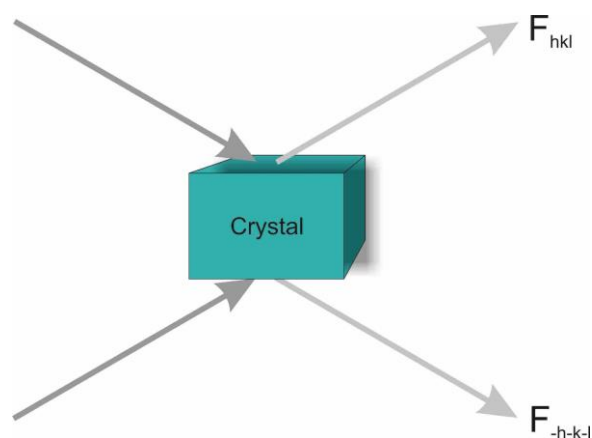
Figure 21. Friedel pairs, reflections $F(hkl)$ and $F(\overline{hkl})$ and their equivalents, are identical for centrosymmetric structures but different for non-centrosymmetric structures.

The intensity of the anomalous dispersion effects depends on the atomic number and the wavelength. Near the atomic species characteristic absorption edge, these effects are more noticeable, Figure 22.

For enantiopure compounds it is mandatory that the arrangement is chiral, a subgroup of the non-centrosymmetric group. When the compounds are a mixture of the two possible non-centrosymmetric structures, racemic twin, the effects of the anomalous dispersion are then counteracted and a new parameter evaluating the proportion of the two structures is necessary, the *Flack parameter*.[63]
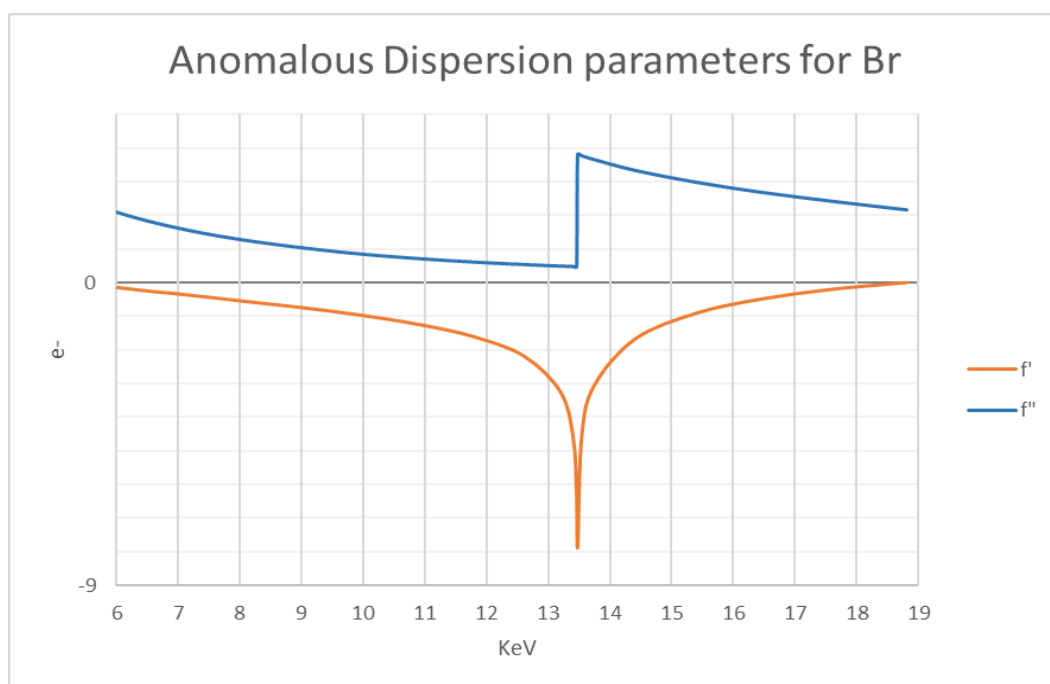
Figure 22. f' and f'' anomalous scattering factors (e⁻) for Bromide versus radiation source energy (KeV). The correction provoked by f'' is especially intense in the range of 12.5 to 19 KeV, more than 2 e⁻ for a normalized ASF of 26 e⁻ at θ=0. It means that, for the Bromide atom, for a Cu $K\alpha$ source, the correction is less intense than for a Mo $K\alpha$ radiation source.

It is noteworthy to stress that the nature of f'' makes it independent on the scattering angle what means that, for high-resolution reflections, its effect is more significant with respect to the elastic scattering.

9. References

(1)   Stalke, D. *Acta Crystallographica Section B-Structural Science Crystal Engineering and Materials* **2014**, *70*, 781.

(2)   Wenger, E.; Dahaoui, S.; Alle, P.; Parois, P.; Palin, C.; Lecomte, C.; Schaniel, D. *Acta Crystallographica Section B* **2014**, *70*, 783.

(3)   Allé, P.; Wenger, E.; Dahaoui, S.; Schaniel, D.; Lecomte, C. *Physica Scripta* **2016**, *91*, 063001.

(4)   Herbst-Irmer, R.; Stalke, D. *Acta Crystallographica Section B* **2017**, *73*, 531.

(5)   Stewart, R. *Acta Cryst. A* **1976**, *32*, 565.

(6)   Hansen, N. K.; Coppens, P. *Acta Cryst. A* **1978**, *34*, 909.

(7)   Bui, T. T. T.; Dahaoui, S.; Lecomte, C.; Desiraju, G. R.; Espinosa, E. *Angew Chem Int Edit* **2009**, *48*, 3838.

(8)   Jelsch, C.; Guillot, B.; Lagoutte, A.; Lecomte, C. *J. Appl. Cryst.* **2005**, *38*, 38.

(9)   Hirano, Y.; Takeda, K.; Miki, K. *Nature* **2016**, *534*, 281.

(10)   *International Tables of Crystallography. Mathematical, physical and chemical tables*; Prince, E., Ed., 2004; Vol. C.

(11)   Dadda, N.; Nassour, A.; Guillot, B.; Benali-Cherif, N.; Jelsch, C. *Acta Cryst. A* **2012**, *68*, 452.

(12)   Nassour, A.; Kubicki, M.; Wright, J.; Borowiak, T.; Dutkiewicz, G.; Lecomte, C.; Jelsch, C. *Acta Crystallographica Section B-Structural Science Crystal Engineering and Materials* **2014**, *70*, 197.

(13)   Lecomte, C.; Guillot, B.; Muzet, N.; Pichon-Pesme, V.; Jelsch, C. *Cellular and Molecular Life Sciences CMLS* **2004**, *61*, 774.

(14)   Domagala, S.; Fournier, B.; Liebschner, D.; Guillot, B.; Jelsch, C. *Acta Crystallographica Section A* **2012**, *68*, 337.

(15)   Volkov, A.; Li, X.; Koritsanszky, T.; Coppens, P. *The Journal of Physical Chemistry A* **2004**, *108*, 4283.

(16)   Dittrich, B.; Hubschle, C. B.; Messerschmidt, M.; Kalinowski, R.; Girnt, D.; Luger, P. *Acta Cryst. A* **2005**, *61*, 314.

(17)   Koritsanszky, T. S.; Coppens, P. *Chem. Rev. (Washington, DC, U. S.)* **2001**, *101*, 1583.

(18)   Parsons, S.; Flack, H. D.; Wagner, T. *Acta Cryst. B* **2013**, *69*, 249.

(19)   Kuhs, W. F. *Acta Cryst. A* **1992**, *48*, 80.

(20)   Herbst-Irmer, R.; Henn, J.; Holstein, J. J.; Hübschle, C. B.; Dittrich, B.; Stern, D.; Kratzert, D.; Stalke, D. *The Journal of Physical Chemistry A* **2013**, *117*, 633.

(21)   *International Tables for X-Ray Crystallography.* ; Johnson, C. K. L., H. A., Ed.; Kynoch Press: Birmingham, 1974; Vol. 4.

(22)   Blessing, R. H. *Acta Cryst. A* **1995**, *51*, 33.

(23)   Sheldrick, G. M.; University of Göttingen: Göttingen, Germany, 2008: 2008.

(24)   Becker, P. J.; Coppens, P. *Acta Crystallographica Section A* **1974**, *30*, 129.

(25)   Le Page, Y.; Gabe, E. J. *Journal of Applied Crystallography* **1978**, *11*, 254.

(26)   Farrugia, L. J.; Mallinson, P. R.; Stewart, B. *Acta Crystallographica Section B-Structural Science* **2003**, *59*, 428.

(27)   Martin, M.; Rees, B.; Mitschler, A. *Acta Cryst. B* **1982**, *38*, 6.

(28)   Ruysink, A. F. J.; Vos, A. *Acta Cryst. A* **1974**, *A 30*, 503.

(29)   Allen, F. H.; Kennard, O.; Watson, D. G.; Brammer, L.; Orpen, A. G.; Taylor, R. *Journal of the Chemical Society-Perkin Transactions 2* **1987**, S1.

(30)   Allen F.H., W. D. G., Brammer L., Orpen A.G., Taylor R. *International Tables for Crystallography* **2006**, *C*, 790.

(31)   Lusi, M.; Barbour, L. J. *Cryst. Growth Des.* **2011**, *11*, 5515.

(32)   Lusi, M.; de Villiers, D.; Esterhuysen, C. *Cryst. Growth Des.* **2014**, *14*, 3480.

(33)   Madsen, A. O. *J. Appl. Cryst.* **2006**, *39*, 757.

(34)   Domagala, S.; Jelsch, C. *J. Appl. Cryst.* **2008**, *41*, 1140.

(35)   Overgaard, J.; Schiott, B.; Larsen, F. K.; Iversen, B. B. *Chem-Eur J* **2001**, *7*, 3756.

(36)   Mata, I.; Espinosa, E.; Molins, E.; Veintemillas, S.; Maniukiewicz, W.; Lecomte, C.; Cousson, A.; Paulus, W. *Acta Cryst. A* **2006**, *62*, 365.

(37)   Itatani, J.; Levesque, J.; Zeidler, D.; Niikura, H.; Pépin, H.; Kieffer, J. C.; Corkum, P. B.; Villeneuve, D. M. *Nature* **2004**, *432*, 867.

(38)   Pascual, J. I.; Gómez-Herrero, J.; Rogero, C.; Baró, A. M.; Sánchez-Portal, D.; Artacho, E.; Ordejón, P.; Soler, J. M. *Chemical Physics Letters* **2000**, *321*, 78.

(39)   Weber-Bargioni, A.; Auwärter, W.; Klappenberger, F.; Reichert, J.; Lefrançois, S.; Strunskus, T.; Wöll, C.; Schiffrin, A.; Pennec, Y.; Barth, J. V. *ChemPhysChem* **2008**, *9*, 89.

(40)   Repp, J.; Meyer, G.; Stojković, S. M.; Gourdon, A.; Joachim, C. *Physical Review Letters* **2005**, *94*, 026803.

(41)   Villagomez, C. J.; Zambelli, T.; Gauthier, S.; Gourdon, A.; Stojkovic, S.; Joachim, C. *Surface Science* **2009**, *603*, 1526.

(42)   Guo, J.; Meng, X.; Chen, J.; Peng, J.; Sheng, J.; Li, X.-Z.; Xu, L.; Shi, J.-R.; Wang, E.; Jiang, Y. *Nature Materials* **2014**, *13*, 184.

(43)   Puschnig, P.; Boese, A. D.; Willenbockel, M.; Meyer, M.; Lüftner, D.; Reinisch, E. M.; Ules, T.; Koller, G.; Soubatch, S.; Ramsey, M. G.; Tautz, F. S. *The Journal of Physical Chemistry Letters* **2017**, *8*, 208.

(44)   Mulder, P. *Hyle : International Journal for Philosophy of Chemistry* **2011**.

(45)   Scerri, E. R. *Journal of Chemical Education* **2000**, *77*, 1492.

(46)   Kampermann, S. P.; Ruble, J. R.; Craven, B. M. *Acta Cryst. B* **1994**, *50*, 737.

(47)   ElHaouzi, A.; Hansen, N. K.; LeHenaff, C.; Protas, J. *Acta Cryst. A* **1996**, *52*, 291.

(48)   R.F.W., B. *Atoms in molecules : a quantum theory*; Oxford University Press, 1990.

(49)   Kumar, P. S. V.; Raghavendra, V.; Subramanian, V. *J. Chem. Sci.* **2016**, *128*, 1527.

(50)   S. T. Howard, O. L. *J. Phys. Org. Chem* **2003**, *16*, 133.

(51)   Abramov, Y. A. *Acta Cryst. A* **1997**, *53*, 264.

(52)   Brezgunova, M. E.; Aubert, E.; Dahaoui, S.; Fertey, P.; Lebègue, S.; Jelsch, C.; Ángyán, J. G.; Espinosa, E. *Crystal Growth & Design* **2012**, *12*, 5373.

(53)   Mata, I.; Alkorta, I.; Molins, E.; Espinosa, E. *Chemistry – A European Journal* **2010**, *16*, 2442.

(54)   Farrugia, L. J.; Kočovský, P.; Senn, H. M.; Vyskočil, Š. *Acta Crystallographica Section B* **2009**, *65*, 757.

(55)   Espinosa, E.; Lecomte, C.; Molins, E. *Chem. Phys. Lett.* **1999**, *300*, 745.

(56)   Spackman, M. A.; Byrom, P. G. *Acta Cryst. B* **1996**, *52*, 1023.

(57)   Poulain-Paul, A.; Nassour, A.; Jelsch, C.; Guillot, B.; Kubicki, M.; Lecomte, C. *Acta Cryst. A* **2012**, *68*, 715.

(58)   French, S.; Wilson, K. *Acta Crystallographica Section A* **1978**, *34*, 517.

(59)   Meindl, K.; Henn, J. *Acta Cryst. A* **2008**, *64*, 404.

(60)   Zhurov, V. V.; Zhurova, E. A.; Pinkerton, A. A. *Journal of Applied Crystallography* **2008**, *41*, 340.

(61)   Macchi, P.; Gillet, J. M.; Taulelle, F.; Campo, J.; Claiser, N.; Lecomte, C. *Iucrj* **2015**, *2*, 441.

(62)   Bentley, J.; Stewart, R. F. *Acta Crystallographica Section A* **1974**, *A 30*, 60.

(63)   Flack, H. D. *Acta Cryst. A* **1983**, *39*, 876.

57

Abbreviations.

AIM	Atoms in Molecules
ASF	Atomic scattering factor
IAA	Independent atoms approximation
IAM	Independent atom model
BCP	Bond Critical Point
BP	Bond Path
CDS	Charge Density Studies
CP	Critical Point
La	Lewis Acid
Lb	Lewis Base
Lp	Lone Pair
MEP	Molecular Electrostatic Potential
QTAIM	Quatum Theory of Atoms in Molecules
RBT	Rigid Bond Test
SED	Static Electron Deformation Density
Tr	Tetrel
VdW	Van der Waals
VRSAM	Virtual and real spherical atoms model

59

Nature of Noncovalent Carbon-Bonding Interactions Derived from Experimental Charge-Density Analysis
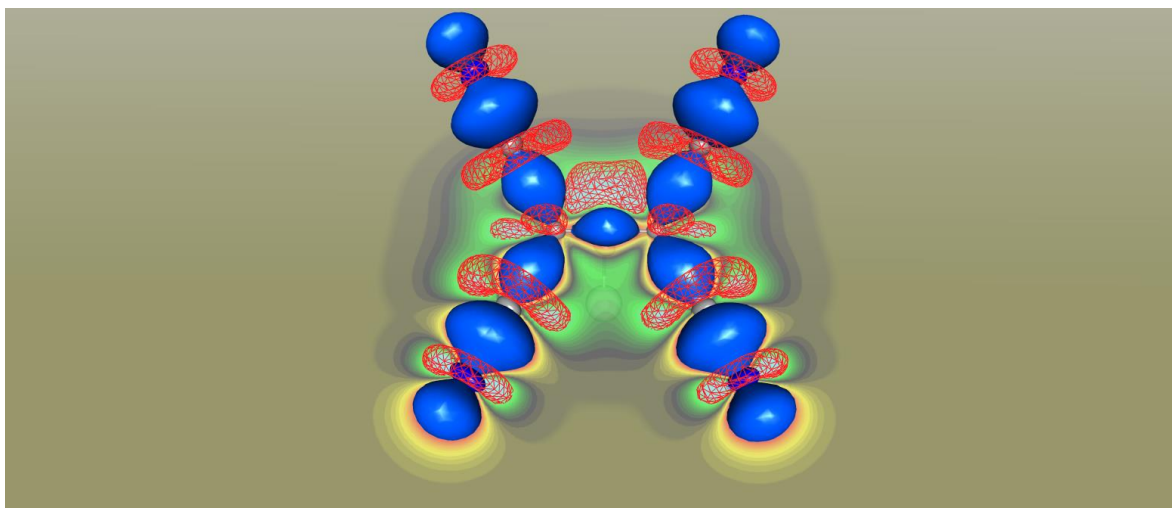
1. Introduction

In an effort to better understand the nature of non-covalent carbon bonding interactions, we undertook the accurate high-resolution X-ray diffraction analysis of single crystals of 1,1,2,2-tetracyanocyclopropane. We selected this compound to study the fundamental characteristics of carbon bonding interactions because it provides accessible σ-holes. The study required accurate experimental diffraction data because the interaction of interest is weak. The electron-density distribution around the carbon nuclei, as shown by the experimental maps of the electrophilic bowl defined by $(CN)_2C–C(CN)_2$ unit, was assigned as the origin of the interaction. This fact was also evidenced by plotting the $\Delta\rho(r)$ distribution. Taken together, the obtained results clearly indicated that non-covalent carbon bonding can be explained as an interaction between confronted oppositely polarized regions. The interaction is thus electrophilic–nucleophilic (electrostatic) in nature and unambiguously considered as attractive.

Attractive intermolecular electrostatic interactions encompass electron rich and electron poor regions of two molecules that complement each other.[1] Electron rich entities are typically anions or lone-pair electrons and the most well known electron poor entity is the hydrogen atom. Consequently, hydrogen bonding is undoubtedly the most exploited supramolecular interaction.[2] Nowadays, another very common electron poor entity is attracting increasing attention in the literature. It is the 'σ-hole' that can be defined as an electron deficient antibonding orbital of a covalent bond.[3-13] Such regions of positive electrostatic potential have been largely studied for atoms of groups V, VI, and VII (pnicogen,[14,15] chalcogen[16-18] and halogen[19-22] bonding respectively[23]).

Many reviews have described the halogen bonding in detail, which is the best-known σ-hole interaction.[11,19,21,22] More recently, σ-hole complexes with atoms of group IV –the tetrel (Tr) atoms–, have been described[24-29] and mostly focus on the heavier Tr atoms as tetrel-bond donors, leaving 'noncovalent carbon bonding' much less studied.[30-32] In an sp^3-hybridized electron deficient C atom, there is only a limited space available for the electron rich guest molecule to nest itself.[30,32] To exemplify this, we have represented in Figure 1 (right) the MEP surface of 1,1,2,2-tetracyanoethane (staggered conformation). The σ-hole is small and it is surrounded by the

negative belts that hinder the interaction with any concentration of negative charge (lone pair or anion). However, if the MEP surface is computed in the eclipsed conformation (C_{2v}), the resulting σ-hole is more exposed and the electrostatic potential is considerable more positive. As a matter of fact, it has been recently demonstrated that the $(CN)_2C–C(CN)_2$ motif of 1,1,2,2-tetracyanocyclopropane is an excellent carbon bond donor because the σ-hole is very exposed.[33] Moreover, it is synthetically accessible and the N≡C– is a poor leaving group thus preventing the SN_2 reaction. Therefore, it is an ideal motif for studying noncovalent carbon bonding. Recently, it has also been demonstrated that four membered rings substituted with electron deficient groups are also good σ-hole donors. As a matter of fact, perfluorocubane has six σ-holes symmetrically distributed in the middle of six faces of the cube. Moreover, noncovalent carbon bonding interactions have been found crucial to explain the solid state architecture of nitrocubanes, where the σ-holes are also very exposed.[34]

The aim of this communication is to gain experimental insights into the nature of tetrel interactions focusing our attention to non-covalent carbon bonding (N···C) interactions. To achieve this, we carried out the accurate high-resolution X-ray diffraction analysis of 1,1,2,2-tetracyanocyclopropane (see Figure 2). Compound 1 was selected to study the fundamental directionality characteristics of carbon bonding interactions because it is an excellent carbon bond donor (vide supra). For one of the polymorphic forms that were found of compound 1 we have obtained high-quality experimental data to derive reliable results. Atomic multipolar expansions[35-37] were used to reconstruct the experimental electron density $\rho(r)$. Dipole, quadrupole and octupole parameters are the most relevant terms to recover the experimental anisotropic $\rho(r)$ features of the crystal structure of 1A. Fig. 3 shows the aspherical static deformation of electron density obtained by subtracting a theoretical spherical model from the aspherical multipolar terms $\Delta\rho_{as}(r) = \rho_{aspherical}(r) - \rho_{spherical}(r)$.
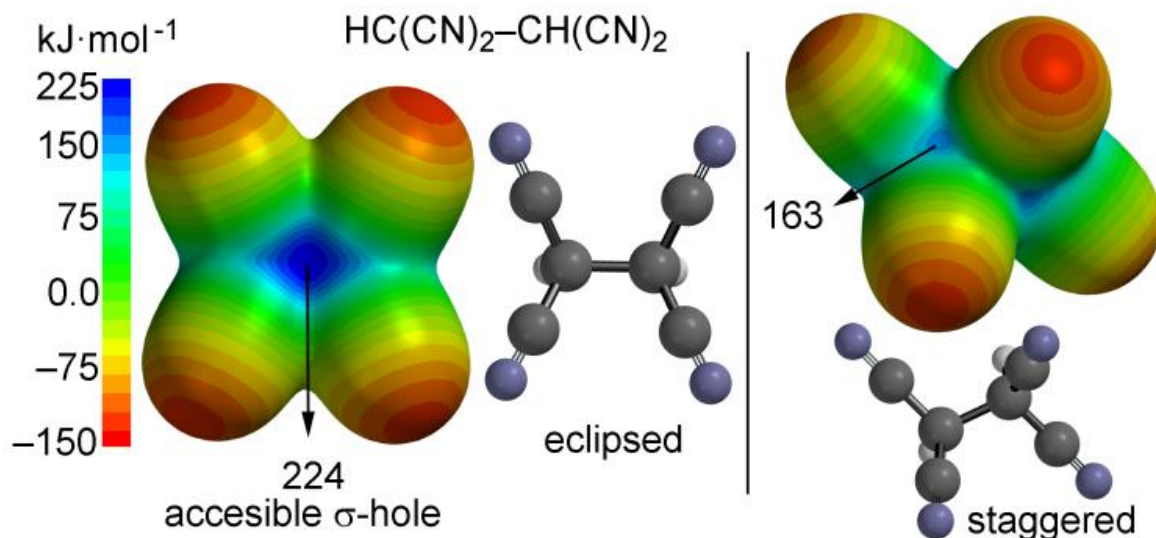
Figure 1. Electrostatic potential maps of 1,1,2,2-tetracyanoethane in the eclipsed (left) and staggered (right) conformations. Selected potential energies at the σ-holes are indicated. Energies in kcal·mol^{-1}.

2. Results and discussion

The results of the topological analysis provide valuable information on chemical bonding which, in fact, enhances the value of such a multipole model. Since the bond topological properties give a quantitative characterization of chemical bonds,[38] it is important to compare the properties derived both from experiment and from wave functions. An immediate consequence of a bonding interaction is the existence of a bond path between the atoms and the concomitant bond critical point (BCP) along this direction, where ρ(r) exhibits a saddle topology. The observation of BCPs is thus distinctive of interatomic bonding interactions and the topological properties of ρ(r) at BCP permit a characterization of the interaction. The examination of the crystal packing of 1 reveals the presence of multiple carbon bonding interactions (see Figure 4) ranging from 3.02 to 3.17 Å (considerably shorter than the sum of the VdW radii, 3.25 Å)[39] in both polymorphs, confirming the ability of this molecule for form noncovalent carbon bonding interactions. We have computed the lattice energy for both polymorphs using a supercell of 16 molecules and periodic boundary conditions (see ESI). The resulting lattice energies are very similar, that is E$_{lattice}$ = 117.5 and 118.7 kJ·mol^{-1} for 1A and 1B respectively; where $-E_{lattice} = E_{crystal}/n - E_{molecule}$.[40] In addition, the computed interaction energies of the dimer of 1A and 1B represented in Figure 2 are −33.8 and 36.4 kJ·mol^{-1}, respectively at the MP2/def2-TZVP level of theory.[41,42] These binding energies are significant taking into account the small basicity of the sp–hybridized nitrogen atom of the cyano group. In

65

order to study if orbital contributions are important to explain the noncovalent carbon interactions observed in the dimer of **1A**, we have performed Natural Bond Orbital (NBO)[43] calculations at the MP2/def2-TZVP level of theory focusing our attention on the second order perturbation analysis.[44] It is very useful to study donor acceptor interactions.[45] Interestingly, we have found that the lone pair of N1 interacts with both C1–C2 and C1–C3 antibonding orbitals with a concomitant second order stabilization energy of 1.42 kJ mol^{-1} for each interaction and the energetic difference between the lp and σ* antibonding orbitals is 1.22 a.u. Therefore, the stabilization energy that can be attributed to orbital effects (2.84 kJ·mol^{-1}) is very small compared to the total interaction energy (−33.8 kJ·mol^{-1}) computed for this dimer. Consequently, the interaction is likely dominated by electrostatic effects instead of orbital effects.
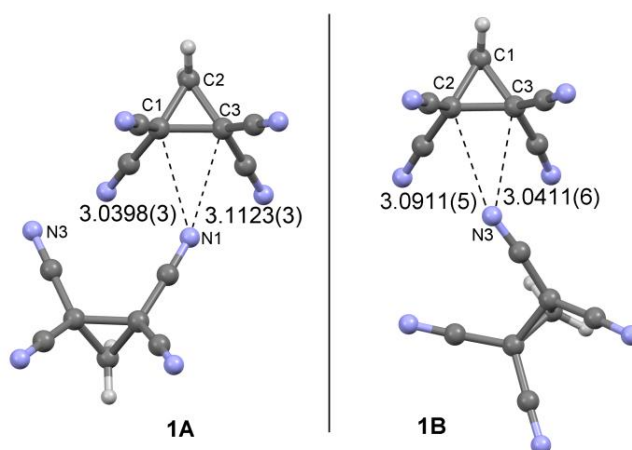
Figure 2. X-ray structure of both polymorphs of compound **1** exhibiting the potential σ-hole interaction with the lone pair at the nitrogen.

Table 1. Kinetic energy G(r) and the potential energy V(r) at the CP points[a] of the trimer represented in Figure 5.

	ρ(r)	∇^2ρ(r)	G(r) (kJ·mol^{-1})	V(r) (kJ·mol^{-1})
cp1 (C1–N3)	**0.047 (0.042)**	**0.62 (0.62)**	**13.1 (13.6)**	**-9.4 (-9.7)**
cp2 (C2–N1)	**0.066 (0.062)**	**0.88 (0.94)**	**19.4 (21.0)**	**-14.8 (-16.5)**
cp3 (N2–N3)	0.016 (0.017)	0.27 (0.22)	4.2 (4.5)	-2.6 (-2.6)
cp4 (N1–N3)	0.027 (0.027)	0.37 (0.41)	7.4 (8.1)	-4.9 (-5.0)

[a] RI-MP2/def2-TZVP theoretical values in parenthesis

Using polymorph **1A**, we have computed the experimental and theoretical (MP2/def2-TZVP wavefunction) distribution of bond critical points and bond paths in one selected trimer retrieved from the solid state. The results are shown in Fig. 5. Four independent BCPs characterize the intermolecular complex. Remarkably, two are associated with the carbon bonding interactions (cp1 and cp2). One of them connects the nitrogen atom with one sp^3–carbon atom of the $(CN)_2C–C(CN)_2$ motif and the other one connects the nitrogen atom with the carbon atom of the $–CH2–$ group. The magnitudes of both the electron density $\rho(r)$ and the Laplacian $\nabla^2\rho(r)$ are shown in Table 1 and they fall within the range of weak hydrogen bonds[46]. There is an excellent agreement between the theoretical and experimental distribution of BCPs, bond paths and their topological properties, including local kinetic energy G(r) and the potential energy density V(r)[47] (see Table 1). These energetic values indicate that the carbon bonding C2···N1 (cp2) is energetically more favored, in agreement with the MEP analysis. Interestingly the other σ-hole based carbon bond interaction (cp1) is also energetically favored over the other two interactions characterized by cp3 and cp4, corresponding to the alternate electron rich- electron poor regions at the cyano groups.
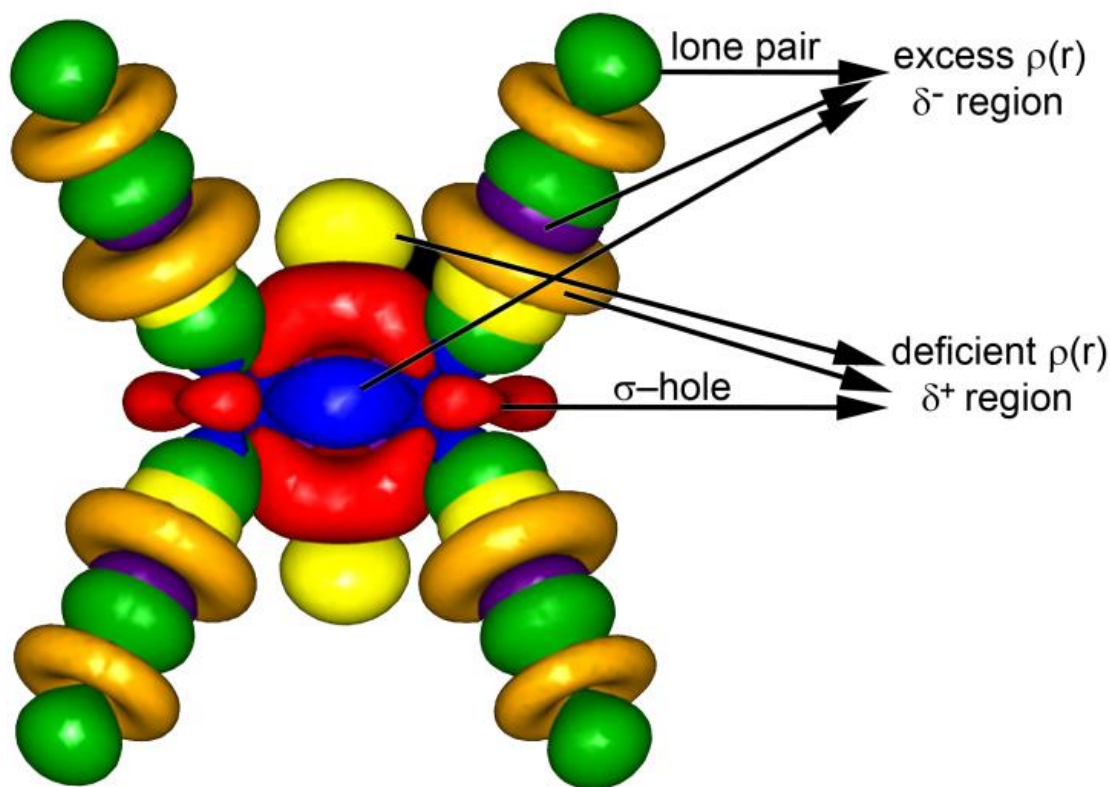
Figure 3. Map of $\Delta\rho(r)$ for **1A**. The $\Delta\rho(r)$ iso-surfaces are drawn at ±0.1 eÅ³. Electron rich (δ⁻) and electron deficient (δ⁺) regions of octupole, quadrupole and dipole terms are color coded. Blue and red for the octupoles, green and orange for the quadrupoles, violet and yellow for the dipoles.
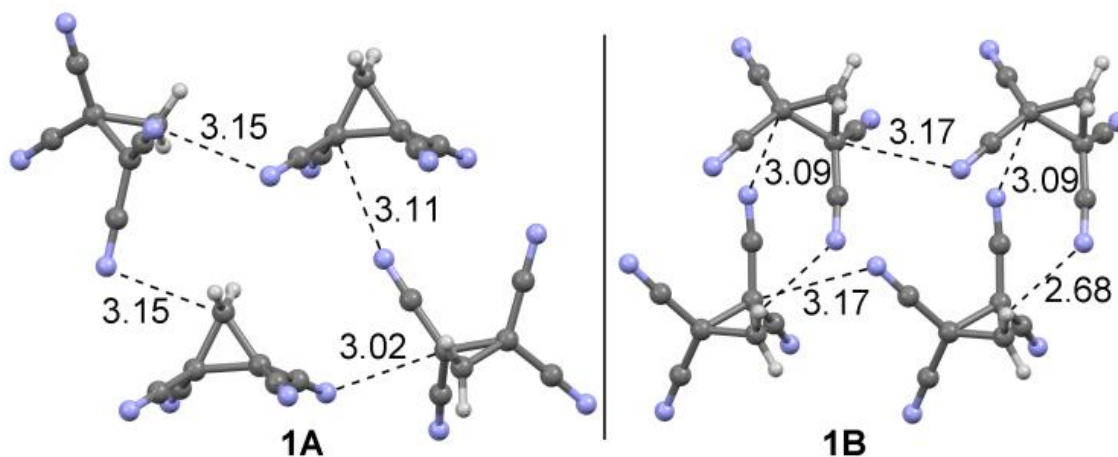
Figure 4. Carbon bonding networks observed in the solid state structure of **1**. The intermolecular N···C distances listed are in Å.

Finally, we have also obtained the theoretical and experimental molecular electrostatic potential surface (MEPS) for compound 1A. In Figure 6 we show the representation of both surfaces using two different electron density isovalues. In Figure 6A and 6B we show the MEPS representation using the Van der Waals surface (isovalue for the electron density 0.001 a.u. according to the Bader's definition[38]). It can be observed that there is a very good agreement between both surfaces including the blue region defining the σ-hole. The experimental MEPS exhibits a lower potential energy value (130 kJ/mol) than the theoretical one (180 kJ/mol) at the σ-hole. This significant difference can be also considered as an experimental confirmation of the carbon bonding interaction. That is, the theoretical MEP is computed using the electronic density of an isolated molecule and the experimental one is obtained using the X-ray diffraction data where the molecules are interacting with the neighboring ones in the crystal packing. In **1A** the σ-hole of one molecule is interacting with the nitrogen atom of the adjacent molecule, thus receiving electron density from the N lone pair and reducing the positive potential at the σ-hole. As a matter of fact, if the MEPs is computed using a smaller surface (96.6% of the total electron density, isovalue = 0.01 a.u.) instead of the van der Waals surface (99.6%, isovalue = 0.001 a.u.) the experimental value at the σ-hole significantly increases from 130 to 250 kJ/mol because the influence of the lone pair of the adjacent molecule is reduced. The theoretical value at the σ-hole also increases upon resizing the surface resulting in identical theoretical and experimental MEP values.
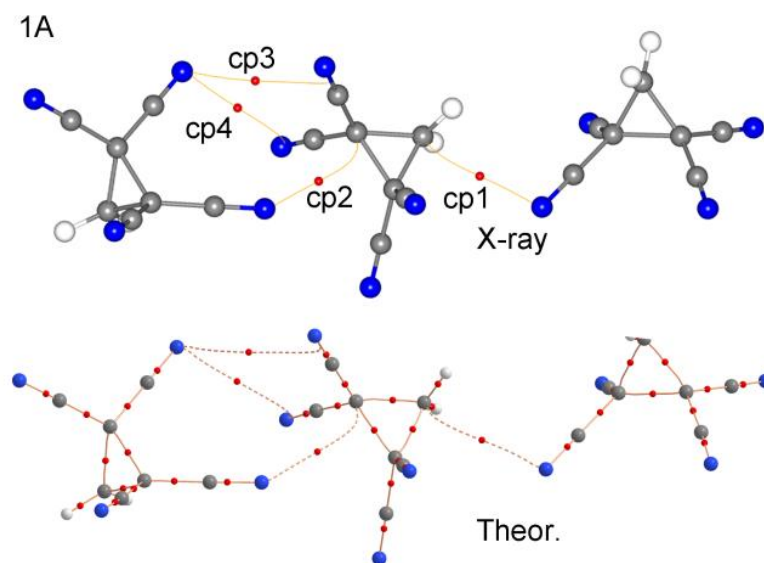
Figure 5. AIM distribution of critical points and bond paths in a selected trimer retrieved from the solid state structure of **1A**.
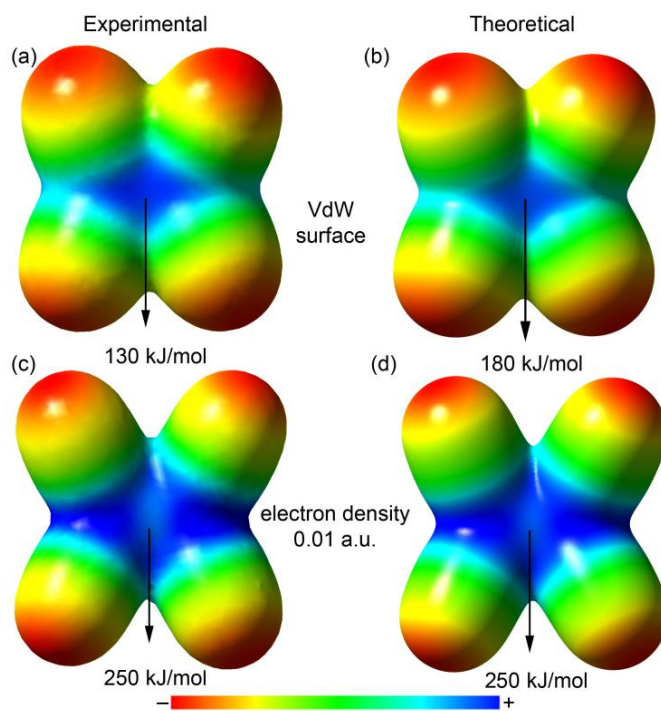
Figure 6. Experimental (a and c) and theoretical (b and d) Molecular Electrostatic Potential (MEP) surfaces calculated for **1A**. For each surface, the red color represents the more negative energy potential value (located at the lone pair of the N atoms) and the dark blue color corresponds to the highest positive potential value (located at the carbon atoms). The van der Waals (VdW) surface (a and b) corresponds to a density isovalue of 0.001 a.u. (1 a.u. = 6.748 e/Å^3). The surface for c and d relates to a density isovalue of 0.01 a.u.

3. Conclusions

We report a combined experimental and calculated molecular orbital electron density study of 1A accompanied with the corresponding accurate topological analyses to characterize qualitatively the non-covalent carbon bonding in 1A. The N···C intermolecular bond can be classified as a closed-shell interaction and its electrostatic nature is demonstrated by the mapped $\Delta\rho$(r) distribution for 1A. The interaction occurs between a nucleophilic (or Lewis base) region (δ^-) of a nitrogen atom and an electrophilic (or Lewis acid) region (δ^+) of the carbon atoms in the $(CN)_2C$–$C(CN)_2$ motif of the three-membered ring in 1A. The region of positive electrostatic potential (σ-hole) is readily accessible making non-covalent 'carbon-bonding' a viable supramolecular interaction between molecules of 1A in the solid-state. This finding is in sharp agreement with a recent thorough CSD analysis[33] providing strong support to carbon-bonding interactions in $(CN)_2C$–$C(CN)_2$ motifs. The interaction is highly directional in structures having (CN)CC(CN) dihedral angles of ≤ 15°. The experimental demonstration of the existence of a σ-hole in **1A** by means of the representation of the static deformation of the electron density iso-surface is very relevant and [35,36]gives reliability to the theoretically proposed existence of σ-hole based interactions involving carbon, the lighter tetrel atom.

4. Experimental section

Single crystals of **1A** and **1B** grew from a solution of **1** in ethanol heated at 45 °C. High-resolution X-ray diffraction data were carried out at 100K on a Rigaku XtaLab P200 Mo $K\alpha$ rotating anode equipped with a Pilatus 200K detector (a hybrid pixel detector recommended for charge density studies[48,49]). IAM was refined using SHELXL 2014.[50] The multipolar ρ(r) model was expanded up to the dipolar order (l = 1) for the H atoms and up to octupolar order (l = 3) for the C and N atoms, applying the corresponding geometrical constrains using the program MOPRO[35,36,51]. Molecular graphics of the multipolar model and deformation maps have been obtained using MOPRO and MoProViewer.[35,36] An optimization of the used restrains based on free R factors[52,53] has been performed. CCDC 1062475 and 1062476 contain the supplementary crystallographic data for this chapter.

5. References

(1)   *Intermolecular Interactions: Physical Picture, Computational Methods and Model Potentials*; John Wiley & Sons Ltd.: Chichester, 2006.

(2)   *Hydrogen Bonding - New Insights*; Springer Netherlands: Dordrecht, 2006.

(3)   Legon, A. C. *Phys. Chem. Chem. Phys.* **2010**, *12*, 7736.

(4)   Clark, T. *Wires Comput Mol Sci* **2013**, *3*, 13.

(5)   Clark, T.; Hennemann, M.; Murray, J. S.; Politzer, P. *Journal of Molecular Modeling* **2007**, *13*, 291.

(6)   Clark, T.; Politzer, P.; Murray, J. S. *Wires Comput Mol Sci* **2015**, *5*, 169.

(7)   Erdelyi, M. *Chemical Society Reviews* **2012**, *41*, 3547.

(8)   Murray, J. S.; Lane, P.; Clark, T.; Politzer, P. *Journal of Molecular Modeling* **2007**, *13*, 1033.

(9)   Murray, J. S.; Lane, P.; Politzer, P. *Int. J. Quantum Chem.* **2007**, *107*, 2286.

(10)   Murray, J. S.; Politzer, P. *Wires Comput Mol Sci* **2011**, *1*, 153.

(11)   Parisini, E.; Metrangolo, P.; Pilati, T.; Resnati, G.; Terraneo, G. *Chemical Society Reviews* **2011**, *40*, 2267.

(12)   Politzer, P.; Murray, J. S.; Clark, T. *Phys. Chem. Chem. Phys.* **2010**, *12*, 7748.

(13)   Scholfield, M. R.; Vander Zanden, C. M.; Carter, M.; Ho, P. S. *Protein Sci* **2013**, *22*, 139.

(14)   Scheiner, S. *Accounts of Chemical Research* **2013**, *46*, 280.

(15)   Sundberg, M. R.; Uggla, R.; Vinas, C.; Teixidor, F.; Paavola, S.; Kivekas, R. *Inorg. Chem. Commun.* **2007**, *10*, 713.

(16)   Sanz, P.; Mo, O.; Yanez, M. *Phys. Chem. Chem. Phys.* **2003**, *5*, 2942.

(17)   Sanz, P.; Yanez, M.; Mo, O. *Chem.--Eur. J.* **2002**, *8*, 3999.

(18)   Sanz, P.; Yanez, M.; Mo, O. *New J. Chem.* **2002**, *26*, 1747.

(19)   Cavallo, G.; Metrangolo, P.; Pilati, T.; Resnati, G.; Sansotera, M.; Terraneo, G. *Chem. Soc. Rev.* **2010**, *39*, 3772.

(20)   Grabowski, S. J. *Physical Chemistry Chemical Physics* **2013**, *15*, 7249.

(21)   Metrangolo, P.; Resnati, G. *Chem.--Eur. J.* **2001**, *7*, 2511.

(22)   Riley, K. E.; Murray, J. S.; Fanfrlik, J.; Rezac, J.; Sola, R. J.; Concha, M. C.; Ramos, F. M.; Politzer, P. *Journal of Molecular Modeling* **2013**, *19*, 4651.

(23)   Politzer, P.; Murray, J. S.; Clark, T. *Physical Chemistry Chemical Physics* **2013**, *15*, 11178.

(24)   Alkorta, I.; Elguero, J.; Fruchier, A.; Macquarrie, D. J.; Virgili, A. *J. Organomet. Chem.* **2001**, *625*, 148.

(25)   Alkorta, I.; Rozas, I.; Elguero, J. *J. Phys. Chem. A* **2001**, *105*, 743.

(26)   Bauza, A.; Mooibroek, T. J.; Frontera, A. *Angew. Chem., Int. Ed.* **2013**, *52*, 12317.

(27)   Bauza, A.; Ramis, R.; Frontera, A. *Comput Theor Chem* **2014**, *1038*, 67.

(28)   Bundhun, A.; Ramasami, P.; Murray, J. S.; Politzer, P. *Journal of Molecular Modeling* **2013**, *19*, 2739.

(29)   Grabowski, S. J. *Physical Chemistry Chemical Physics* **2014**, *16*, 1824.

(30)   Bauza, A.; Mooibroek, T. J.; Frontera, A. *Chem. Commun.* **2014**, *50*, 12626.

(31)   Mani, D.; Arunan, E. *Physical Chemistry Chemical Physics* **2013**, *15*, 14377.

(32)   Thomas, S. P.; Pavan, M. S.; Row, T. N. G. *Chem. Commun.* **2014**, *50*, 49.

(33)   Bauza, A.; Mooibroek, T. J.; Frontera, A. *Chem-Eur J* **2014**, *20*, 10245.

(34)   Bauza, A.; Mooibroek, T. J.; Frontera, A. *Physical Chemistry Chemical Physics* **2014**, *16*, 19192.

(35)   Guillot, B.; Viry, L.; Guillot, R.; Lecomte, C.; Jelsch, C. *J. Appl. Cryst.* **2001**, *34*, 214.

(36)   Jelsch, C.; Guillot, B.; Lagoutte, A.; Lecomte, C. *J. Appl. Cryst.* **2005**, *38*, 38.

(37)   Hansen, N. K.; Coppens, P. *Acta Cryst. A* **1978**, *34*, 909.

(38)   Bader, R. F. W. *Atoms in Molecules-a Quantum Theory*; Univ. Press: Oxford, 1990.

(39)   Bondi, A. *J. Phys. Chem.* **1964**, *68*, 441.

(40)   Perger, W. F.; Pandey, R.; Blanco, M. A.; Zhao, J. J. *Chem. Phys. Lett.* **2004**, *388*, 175.

(41)   Moller, C.; Plesset, M. S. *Phys Rev* **1934**, *46*, 0618.

(42)   Weigend, F.; Ahlrichs, R. *Phys. Chem. Chem. Phys.* **2005**, *7*, 3297.

(43)   Reed, A. E.; Curtiss, L. A.; Weinhold, F. *Chem. Rev. (Washington, DC, U. S.)* **1988**, *88*, 899.

(44)   Weinhold, F.; Landis, C. R. *Discovering Chemistry with Natural Bond Orbitals*; John Wiley & Sons: New Jersey, 2012.

(45)   Glendening, E. D.; Landis, C. R.; Weinhold, F. *Wires Comput Mol Sci* **2012**, *2*, 1.

(46)   *An Introduction to Hydrogen Bonding*; Jeffrey, G. A., Ed.; OUP: New York, 1997.

(47)   Abramov, Y. A. *Acta Cryst. A* **1997**, *53*, 264.

(48)   Stalke, D. *Acta Crystallographica Section B-Structural Science Crystal Engineering and Materials* **2014**, *70*, 781.

(49)   Herbst-Irmer, R.; Stalke, D. *Acta Crystallographica Section B-Structural Science Crystal Engineering and Materials* **2017**, *73*, 531.

(50)   Sheldrick, G. M. *Acta Crystallographica Section C-Structural Chemistry* **2015**, *71*, 3.

(51)   Domagala, S.; Jelsch, C. *J. Appl. Cryst.* **2008**, *41*, 1140.

(52)   Brünger, A. T. *Nature* **1992**, *355*, 472.

(53)   Paul, A.; Kubicki, M.; Jelsch, C.; Durand, P.; Lecomte, C. *Acta Crystallographica Section B* **2011**, *67*, 365.

(54)   Ahlrichs, R.; Bär, M.; Häser, M.; Horn, H.; Kölmel, C. *Chem. Phys. Lett.* **1989**, *162*, 165.

(55)   Boys, S. F.; Bernardi, F. *Mol. Phys.* **1970**, *19*, 553.

(56)   M. J. Frisch, G. W. T., H. B. Schlegel, G. E. Scuseria, M. A. Robb, J. R. Cheeseman, G. Scalmani, V. Barone, B. Mennucci, G. A. Petersson, H. Nakatsuji, M. Caricato, X. Li, H. P. Hratchian, A. F. Izmaylov, J. Bloino, G. Zheng, J. L. Sonnenberg, M. Hada, M. Ehara, K. Toyota, R. Fukuda, J. Hasegawa, M. Ishida, T. Nakajima, Y. Honda, O. Kitao, H. Nakai, T. Vreven, J. A. Montgomery, Jr., J. E. Peralta, F. Ogliaro, M. Bearpark, J. J. Heyd, E. Brothers, K. N. Kudin, V. N. Staroverov, R. Kobayashi, J. Normand, K. Raghavachari, A. Rendell, J. C. Burant, S. S. Iyengar, J. Tomasi, M. Cossi, N. Rega, J. M. Millam, M. Klene, J. E. Knox, J. B. Cross, V. Bakken, C. Adamo, J. Jaramillo, R. Gomperts, R. E. Stratmann, O. Yazyev, A. J. Austin, R. Cammi, C. Pomelli, J. W. Ochterski, R. L. Martin, K. Morokuma, V. G. Zakrzewski, G. A. Voth, P. Salvador, J. J. Dannenberg, S. Dapprich, A. D.

Daniels, Ö. Farkas, J. B. Foresman, J. V. Ortiz, J. Cioslowski, and D. J. Fox.; Gaussian, Inc.: Wallingford CT, 2009.

(57)   Keith, T. A.; TK Gristmill Software: Overland Park KS, USA, 2014.

(58)   Delley, B. *The Journal of Chemical Physics* **1990**, *92*, 508.

(59)   Delley, B. *The Journal of Physical Chemistry* **1996**, *100*, 6107.

(60)   Delley, B. *The Journal of Chemical Physics* **2000**, *113*, 7756.

(61)   Spek, A. *Acta Crystallographica Section D* **2009**, *65*, 148.

6. Supporting information

6.1. Computational methods:

Single point energy calculations have been performed using the crystallographic X-ray coordinates by means of the TURBOMOLE 6.5 software at the RI-MP2/def2TZVP level of theory.[54] The interaction energies were calculated with correction for the basis set superposition error (BSSE) by using the Boys-Bernardi counterpoise technique.[55] The MEPS and NBO analysis were computed at the MP2/def2TZVP by means of Gaussian 09 B.01 calculation package.[56] AIM analysis was performed at the same level of theory using AIMall software.[57] For crystal lattice energies, all calculations were performed in the frame of DFT with the DMol3 program package, using double numerical with polarization (DNP) basis sets and Perdew–Burke–Ernzerhof (PBE) exchange-correlation functional with Grimme's correction for dispersion.[58-60] The results obtained were calculated by applying the $-E_{lattice} = E_{crystal}/n - E_{molecule}$ formula.

Table S 1. Crystallographic table of **1A**

	Spherical	Multipolar
Identification code	TCCP	
Empirical formula	$C_7 H_2 N_4$	
Formula weight	142.13	
Temperature	100(2) K	
Wavelength	0.71073 Å	
Crystal system / Space group	Orthorhombic / $P2_12_12_1$	
Friedif$_{stat}$	2.94	
Unit cell dimensions	a = 6.14530(10)Å α= 90°.	
	b = 6.83430(10)Å β = 90°.	
	c = 15.9758(2)Å γ = 90°.	
Volume	670.965(17) Å^3	
Z	4	
Density (calculated)	1.407 Mg/m^3	
Absorption coefficient	0.094 mm^{-1}	
F(000)	288	
Crystal size	0.3 x 0.2 x 0.2 mm^3	
Reflections collected	33917	
Absorption correction	Multi-scan	
Max. and min. transmission	0.981 and 0.755	
Refinement model	Spherical	Multipolar
Theta range	3.24 to 66.55°	3.24 to 55.53°
Index ranges	-11≤h≤15,-16≤k≤14,-37≤l≤31	-13≤h≤13,0≤k≤15,0≤l≤36
Independent reflections	8362[R_{int} = 0.0125]	
Completeness to theta =55.53°	92.7%	
Data / restraints / parameters	8362/ 0/ 108	7762/330/312
Goodness-of-fit on F^2	1.108	1.002
Weigthing scheme	$1/[\sigma^2(F_o^2)+(aP)^2+bP]$ (a=0.055, b=0)	$1/[a\sigma^2(I)]$ (a=3.4)
Final R indices [I>2sigma(I)]	R1 = 0.0233, wR^2 = 0.0696	
R indices (all data)*	R1 = 0.0237, wR^2 = 0.0698	R1 = 0.0087, wR^2 = 0.0079
Hooft/Parsons parameter**	y =0.03(11)/z=0.00(10)	y =0.02(10)
Largest diff. peak and hole	0.59 and -0.25 eÅ^{-3}	0.11 and -0.11 eÅ^{-3}
RBT (non hydrogen atoms)	4.8×10^{-4}	1.8×10^{-4}

* I/σ(I)=0.1 for the multipolar refinement.

** Values obtained with PLATON.[61]

6.2. Experimental 2D residual electron density maps and Laplacian.

a)

b)
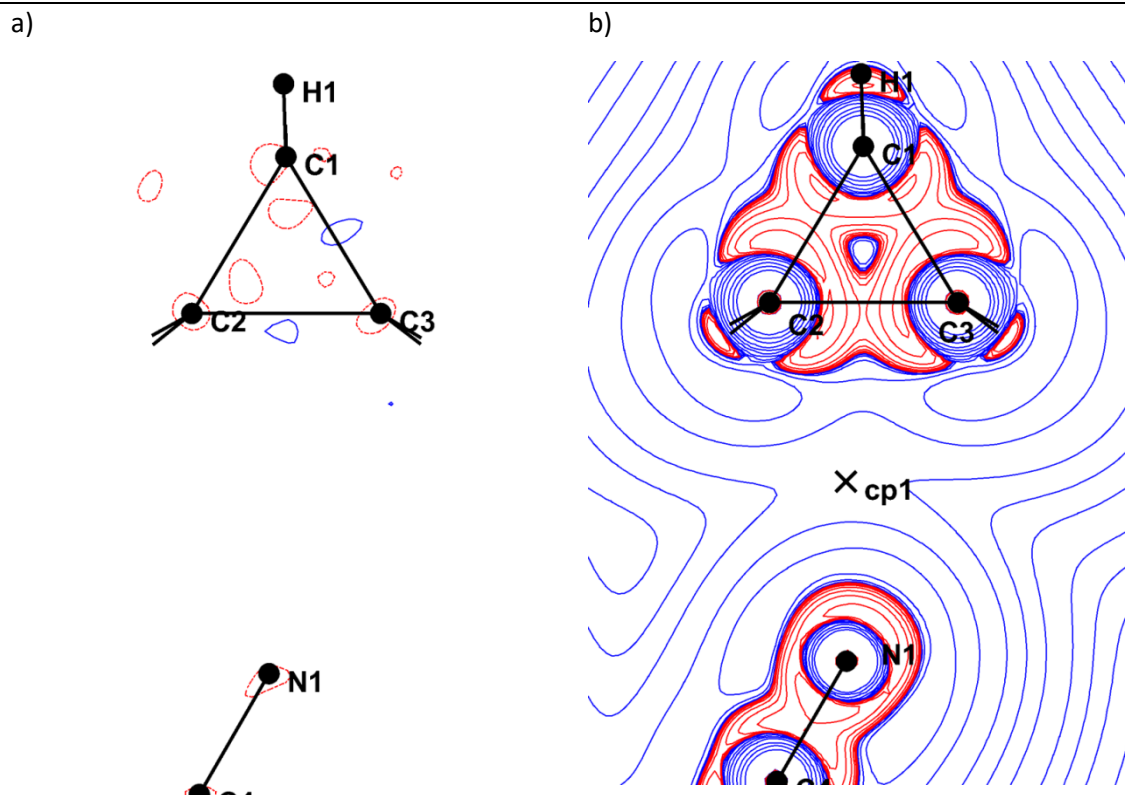
Figure S 1. a) 2D residual electron density map after the multipolar refinement up to the octupolar level. Positive and negative contours are in blue and red, respectively. Contours are drawn at ±0.05 eÅ^{-3} b) 2D Laplacian map showing, cp1 (3,-1), the intermolecular critical point between N1 and C2. Contours, in eÅ^{-5}, are drawn in logarithmic scale. 2D plane defined by C2, C3 and N1.

6.3. Experimental 2D electron density deformation and static electron density maps
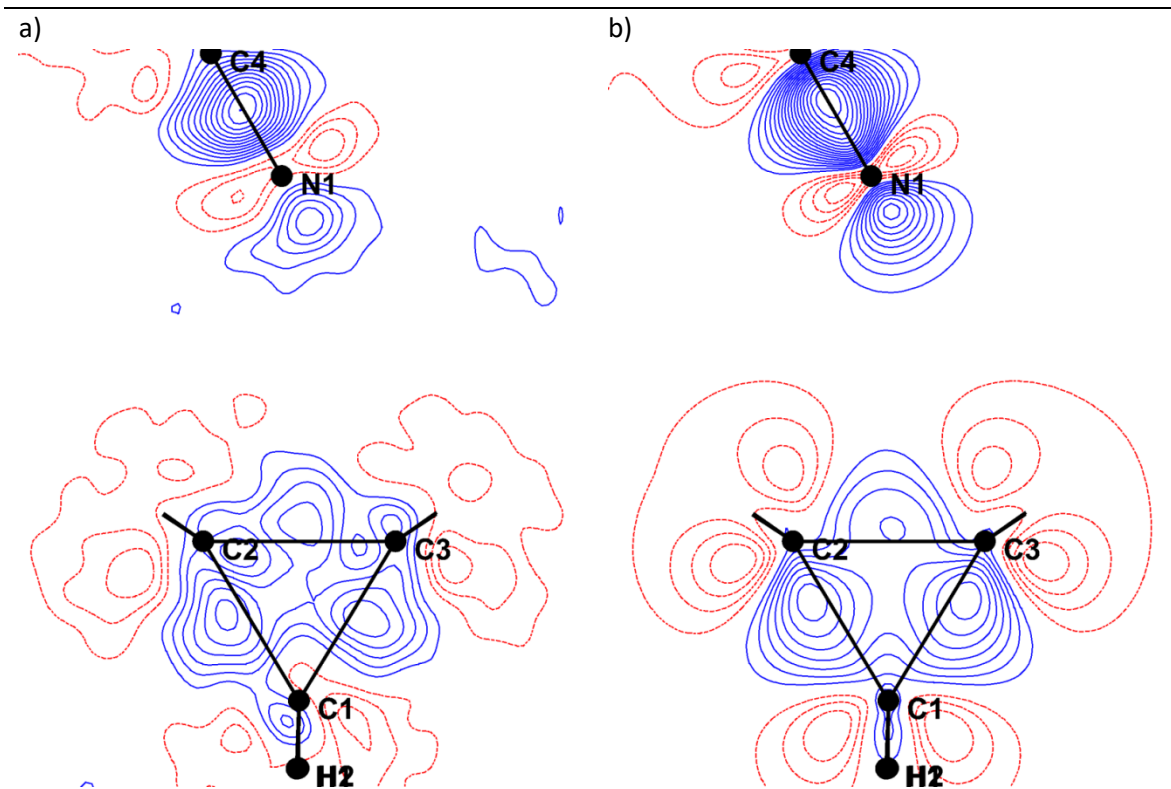
Figure S 2. Figure S2: a) 2D experimental electron density deformation map and b) static electron density map (right). Positive and negative contours are in blue and red, respectively. Contours are drawn at ±0.05 eÅ^{-3}. 2D plane defined by C1, C2 and C3.

6.4. Electron density parameters and topological features at bond BCPs

Table S 2. Refined multipolar parameters for the charge density study of **1A.**

ATOM	KP1	KP2	Pval	P00	P11	P1-1	P10	P20	P21	P2-1	P22	P2-2	P30	P31	P3-1	P32	P3-2	P33	P3-3
C1	1.004(2)	0.954(11)	4.03(3)	-	-	-	-0.073(5)	-0.012(5)	-	-	-0.125(5)	-	0.092(6)	-	-	0.283(9)	-	-	-
C2	0.9997(16)	0.947(7)	3.997(17)	-	0.019(4)	-	0.026(4)	-0.002(4)	0.056(4)	-	-0.041(4)	-	0.108(5)	0.020(4)	-	0.311(7)	-	0.028(4)	-
C3	1.0016(16)	0.950(7)	3.996(17)	-	0.025(4)	-	0.028(4)	0.001(4)	0.055(4)	-	-0.039(4)	-	0.116(5)	0.006(4)	-	0.310(6)	-	0.028(4)	-
C4	1.0145(14)	0.883(6)	4.117(12)	-	-	-	0.228(6)	0.395(7)	-	-	-	-	-0.053(5)	-	-	-	-	-	-
C5	1.0132(14)	0.875(6)	4.106(12)	-	-	-	0.239(6)	0.391(7)	-	-	-	-	-0.053(5)	-	-	-	-	-	-
C6	1.0142(14)	0.881(6)	4.124(12)	-	-	-	0.233(6)	0.396(7)	-	-	-	-	-0.054(5)	-	-	-	-	-	-
C7	1.012(7)	0.872(6)	4.113(12)	-	-	-	0.241(7)	0.389(7)	-	-	-	-	-0.055(5)	-	-	-	-	-	-
H1	1.138(7)	1.184(4)	0.806(11)	-	-	-	0.151(5)	-	-	-	-	-	-	-	-	-	-	-	-
H2	1.2158(10)	1.188(4)	0.833(12)	-	-	-	0.173(6)	-	-	-	-	-	-	-	-	-	-	-	-
N1	0.9999(10)	0.928(8)	4.967(11)	-	-	-	-0.038(4)	0.213(4)	-	-	-	-	0.037(4)	-	-	-	-	-	-
N2	0.9954(10)	0.930(8)	4.966(11)	-	-	-	-0.047(4)	0.212(4)	-	-	-	-	0.048(4)	-	-	-	-	-	-
N3	0.9958(10)	0.925(8)	4.973(11)	-	-	-	-0.025(4)	0.221(4)	-	-	-	-	0.024(4)	-	-	-	-	-	-
N4	0.9936(11)	0.929(8)	4.972(11)	-	-	-	-0.042(4)	0.218(4)	-	-	-	-	0.041(4)	-	-	-	-	-	-

Table S 3. Topological features at intramolecular bond critical points.

Critical Point	atom1	atom2	D12	D1cp	D2cp	RHOtotρ	Δρ	3 Hessian Eigenvalues			Ellipt
cp1	C1	C2	1.510	0.724	0.786	1.57	-6.18	-11.19	-6.05	11.06	0.85
cp2	C1	C3	1.514	0.726	0.788	1.56	-5.8	-11.13	-5.83	11.16	0.91
cp3	C1	H1	1.090	0.749	0.341	1.77	-18.35	-17.26	-16.71	15.61	0.03
cp4	C1	H2	1.090	0.714	0.376	1.88	-18.02	-17.78	-17.18	16.94	0.03
cp5	C2	C3	1.559	0.778	0.785	1.40	-2.56	-10	-3.35	10.78	1.98
cp6	C2	C4	1.442	0.707	0.735	1.88	-13.82	-13.36	-12.35	11.89	0.08
cp7	C2	C5	1.443	0.711	0.731	1.86	-13.58	-13.2	-12.2	11.82	0.08
cp8	C3	C6	1.445	0.710	0.735	1.87	-13.66	-13.34	-12.3	11.98	0.08
cp9	C3	C7	1.444	0.715	0.730	1.86	-13.56	-13.22	-12.19	11.84	0.08
cp10	C4	N1	1.152	0.417	0.735	3.40	-23.51	-27.02	-27.02	30.52	0
cp11	C5	N2	1.154	0.416	0.738	3.38	-22.23	-26.69	-26.69	31.14	0
cp12	C6	N3	1.155	0.418	0.738	3.39	-23.61	-26.68	-26.68	29.75	0
cp13	C7	N4	1.153	0.414	0.739	3.37	-20.42	-26.61	-26.61	32.79	0
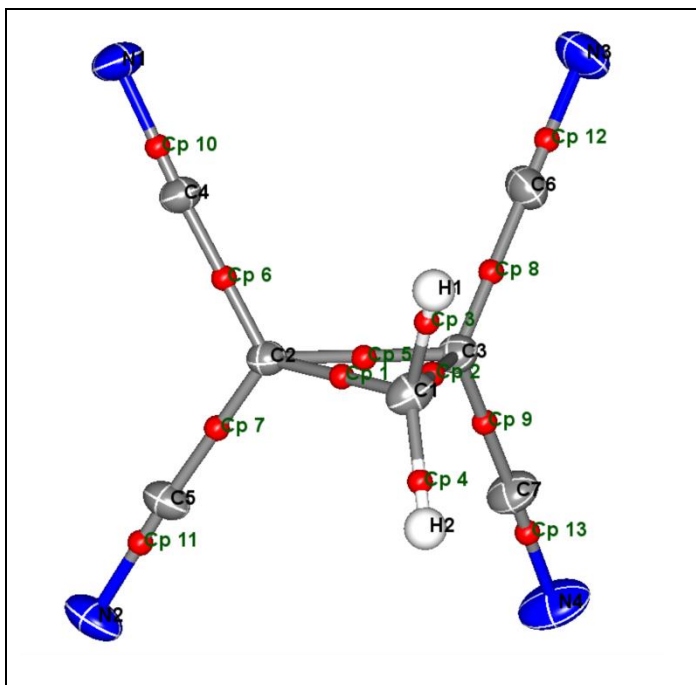
Figure S 3. Ortep view (thermal ellipsoids drawn at 50% probability level) and intramolecular bond critical points (red dots).

Chapter 3

Hidden interactions through Bader analysis.
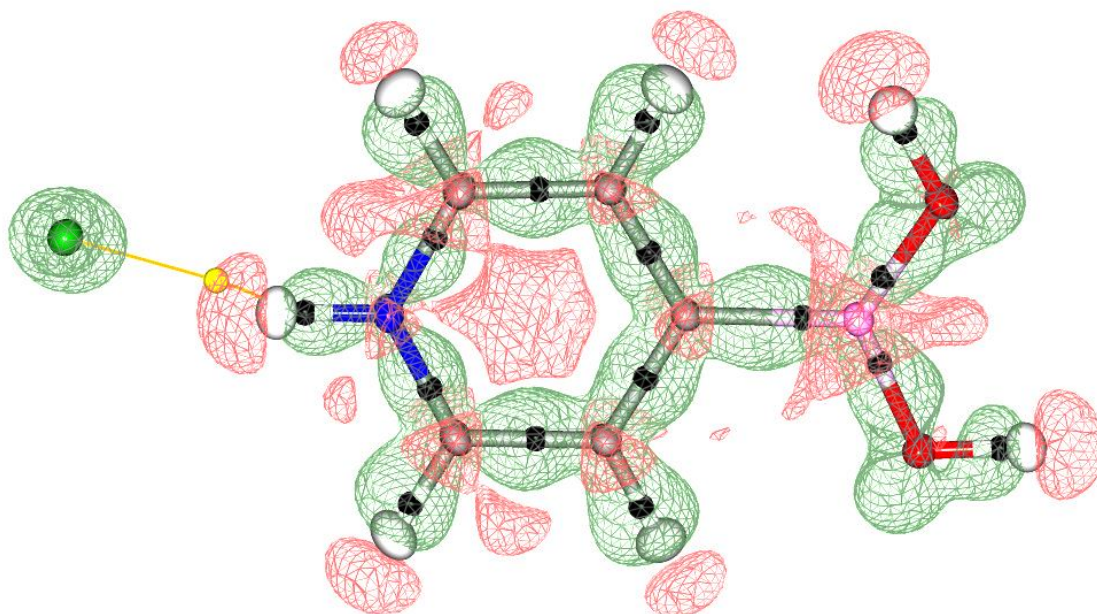
1. Introduction

Weak intermolecular interactions have been widely studied through Bader's Quantum theory of Atoms in Molecules (QTAIM) among other theories. From strong to weak hydrogen bonds, halogen bonds, σ-hole bonds, etc., QTAIM theory is suitable for describing these interactions. X-ray charge density studies are an excellent tool for providing experimental support to theoretical studies though the QTAIM theory. In the recent years, certain cases of the aforementioned σ-hole interactions have been successfully predicted and validated by both, theoretical and experimental data through the QTAIM point of view. In the present work, we would like to show that, even though the QTAIM has demonstrated its usability, in certain cases the presence of the interaction can be missed using this theory. We have compare three different π-hole interactions occurring in three types of functional groups (BO_2H_2, NO_2 and COOH). In the BO_2H_2, the bond path as well as the bond critical point between an electron rich site and the electron hole at the boron atom were not detected. In contrast, we rapidly found one example of such interactions involving NO_2 and COOH functional groups. The interaction was readily characterized by the QTAIM theory.

The detailed study of weak interactions is essential to expand the opportunities for new applications in supramolecular chemistry across a variety of fields. For example, explaining the role of the solvent in the formation of crystals or co-crystals is a challenging matter. A recent study is able to demonstrate that the formation of different type of co-crystals is related with the nature of the solvent, by comparing the strength of hydrogen bonds and halogen bonds in the involved solvents.[1] Molecular entities forming crystals can be understood as irregular "bricks" that build an ordered structure. Inhomogeneities in the electronic distribution of the molecules are the origin of attractive and repulsive electrostatic intermolecular forces (IMFs). In order to minimize the energetic cost of the

molecule arrangement, intermolecular electrostatic interactions encompass electron rich and electron poor regions of two molecules that complement each other. The electron rich entities include: anions, lone-pair electrons, equatorial regions of halogen atoms, double and triple bonds interatomic regions. Examples of electron poor moieties are cations, hydrogen atoms or σ-holes. A particular case of σ-hole interactions are π-hole interactions, that are the focus of the study presented here. A σ-hole can be defined as an electron deficient antibonding orbital of a covalent bond.[2,3] Such regions often lead to positive electrostatic potentials. They have been largely studied and have been classified as tetrel (group IV), pnicogen (group V), chalcogen (group VI) and halogen (group VII) bonding respectively.[4] In analogy to the σ hole, a π-hole can be seen as an electropositive potential located on an unpopulated π*-orbital. The best-known π-hole interactions involve carbonyl compounds. In terms of the Lewis acid-Lewis base (La-Lb) description, a σ-hole is a Lewis acid (La) where the La are atoms from the IV, V, VI, and VII groups. Atoms from the III group, triel atoms, when sp^2 hybridized, have electron deficient areas or La. These La are candidates to attract Lewis bases, Lb, as lone pairs or anions. Some theoretical examples of boron as a triel center with strong affinity to electrons have been reported.[5] In particular, boronic acids are anticipated to follow the same trend. In this functional group, the boron atom is a strong La center that would attract Lb center. Recently we have reported a X-ray charge density study where a σ-hole interaction, carbon tetrel bond, have been characterized trough both experimental and theoretical analysis.[6] The parallelism of this interaction with the triel bond makes sensible to analyze the nature of the later using the same methodologies.
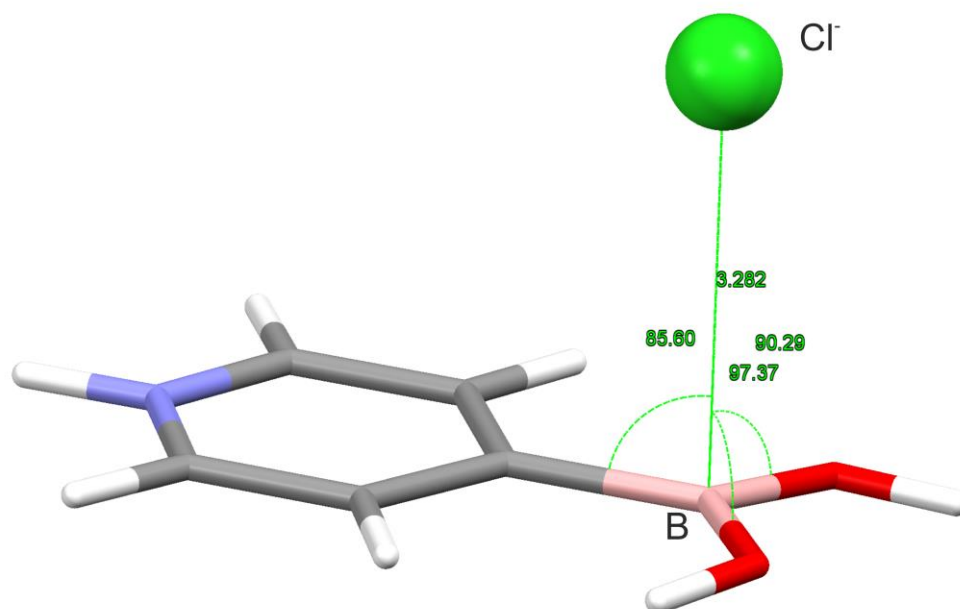
Figure 1. Crystal structure showing the arrangement of the anion with respect to the boron atom, lying over the π hole at the boron atom.

2. Results and discussion.

For studying the triel interaction, we initially choose molecules containing a boronic acid group substituted with an aliphatic chain containing a double bond. In the crystal structure of this compound the dimer showed a double carbon-carbon bond pointing towards the triel atom, as theoretically described by Grabowski[7]. A recent experimental example of the above described interaction has been reported. [8] The reported crystal structure reveals that the electron rich site at the C=C bond lies over the boron atom, as performed on the crystal did not produce evidence of bond expected for a triel bond interaction. However, the experimental charge density study paths or critical points between the C=C bond and the boron atom, as might be expected for the corresponding π-hole interaction. This finding made us reconsider our candidates for the experimental observation of the triel bond. In an attempt for making the interaction more detectable

using the QTIAM theory, we crystallized a salt containing a boronic acid group where the electronic rich component is a Cl⁻ anion.
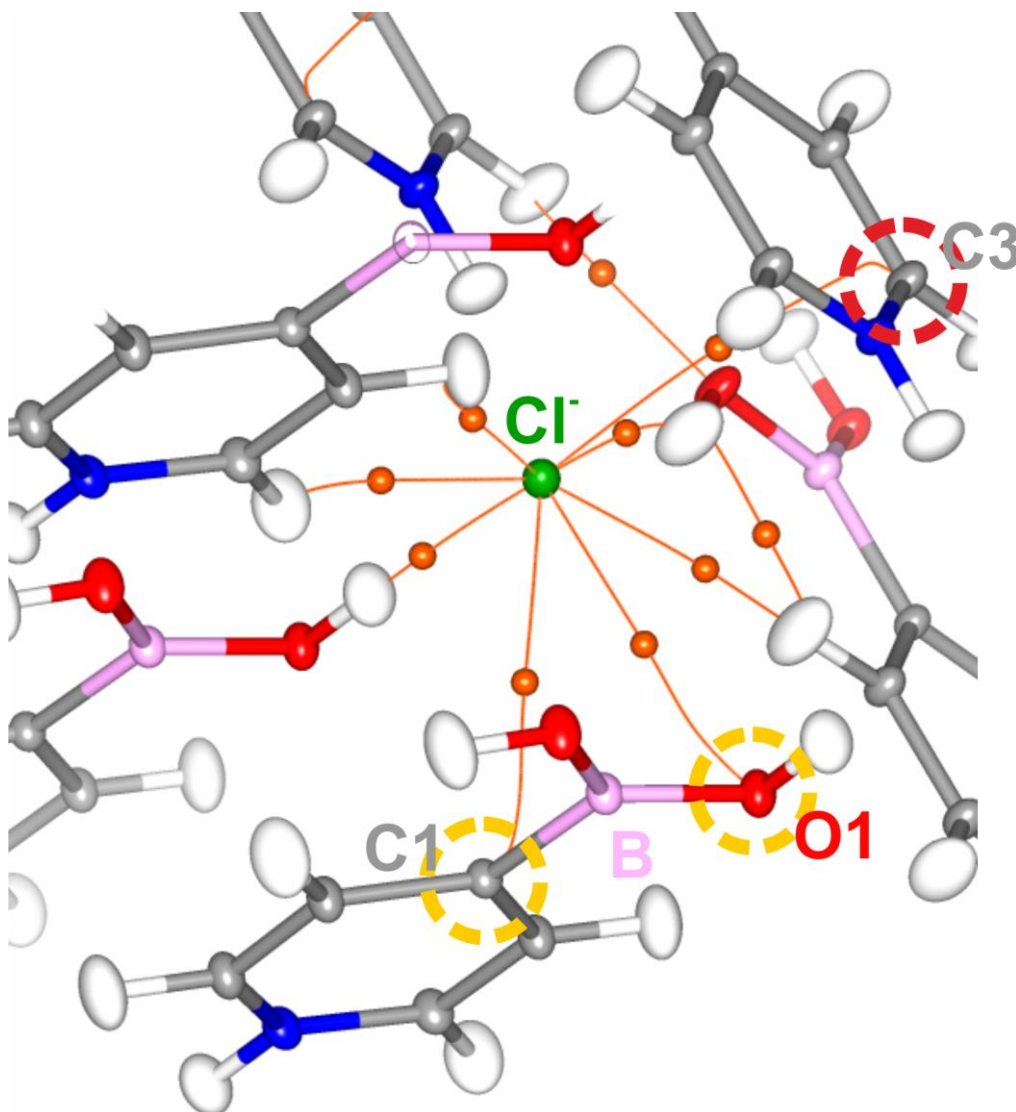
Figure 2. Bond paths starting at the chloride anion joining the carbon and oxygen atoms of an adjacent molecule. The π hole interaction does not display a bond path. Likewise, the bond path connecting the anion and the pyridinium ring takes place through the carbon alpha to the nitrogen atom. Bond paths are marked with a red lines.

The selected compound was the hydrochloride of 4-Pyridinylboronic acid, compound **1**. In the crystal structure of **1**, the chloride anion is located on top of the triel atom, Figure 1. For our astonishment, bond paths starting at the anion clearly avoid the region over the triel atom; instead, they were joining adjacent oxygen and carbon atoms, Figure 2. Bader states that the sufficient and necessary condition for a bond is a bond path of electronic

density.[9] This condition is fulfilled even in very weak interaction as weak hydrogen bonds,[10] halogen bonds[11] or tetrel bonds[6]. However, from Bader's theory point of view, the interaction $Cl^{-}\cdots$Boron is undetectable. Moreover, the bond paths and critical points between the chloride and the oxygen and carbon atoms define bonds in the Bader's nomenclature.

The absence of detectable bonds concerning boron atoms is not new. Antipin et al.[12] showed experimentally that despite the short B-B distance in the crystal structure of pentaethyl-1,5-dicarba-closo-pentaborane $[C_2B_3(Et)_5]$, no bond path or critical point were found between the boron atoms in the corresponding charge density study. However, in this latter example, the electron deficient regions of the two boron atoms point to each other justifying the lack of bond path. In contrast, compound **1** has an electron rich site at the anion. After the analysis of the MEP of **1**, the existence of an attractive interaction between the boron and the chloride atoms seems reasonable, Fig. 3.
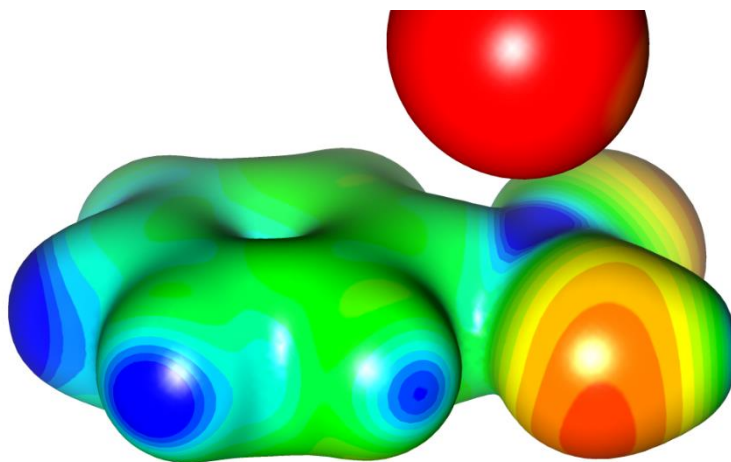
Figure 3. MEP calculated after multipolar refinement of the crystal structure of compound **1**. The red sphere represents the MEP of the anion, strongly negative, lying on top of the positive MEP region at the boron.

The MEP picture together with the absence of critical point is in line with the situation predicted by Pendás et al. [13] In the present system, the depletion of the charge density at the boron atom leads to a highly negative potential. However, the exchange of electronic density between electronic clouds takes place between the chloride and the oxygen and

carbon atoms bonded to the boron. In a similar manner, the bond path joining the chloride anion and the alpha carbon of the nitrogen in the pyridine ring deflects towards the C-C bond, despite the anion is located on top of the C-N bond. A plausible explanation can be related to the difference in the ellipticity of the two bonds, see table S1. While the electron densities are similar for the critical points of the CN and CC bonds, 2.31 and 2.24 eÅ^{-3}, the ellipticities at the bond's critical points are significantly different, 0.101 and 0.244, respectively, Fig 4.
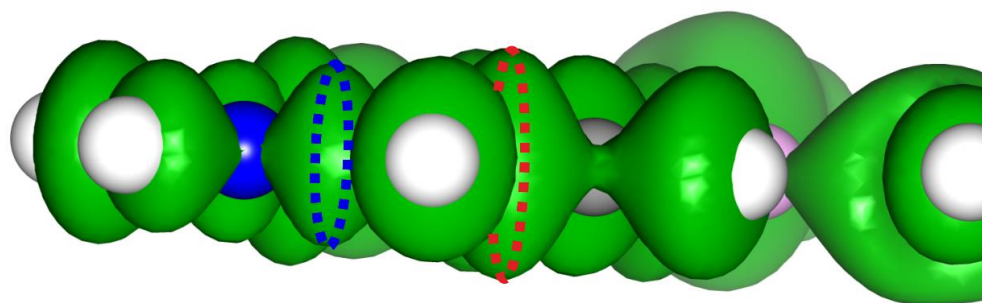
Figure 4. Comparison of the deformation at the NC bond, blue dotted ellipse, and CC bond, red dotted ellipse, of the pyridine ring.

At this point, we decided to analyze the nature of similar interactions. In particular, we explored the interaction in nitro and carboxylic groups, where the tetrel and pnicogen atom presented a π hole that can attract electronic rich sites like lone pairs or anions. We were able to crystallize a co-crystal of tartaric acid and 4,4'-bipyridine N-N'-dioxide, compound **2**. The crystal structure reveals a molecular arrangement displaying the interaction between both oxygen atoms of the N-oxide and the corresponding carbon atoms of the two carboxylic groups of the tartaric acid. The N-oxide oxygen atom arranges perpendicularly with respect to the C=O carbon. After the multipolar refinement, the critical points revealed the expected interaction between the oxygen and the carbon atoms (despite the bond path deflects towards to the oxygen at the end), Figure 5a.
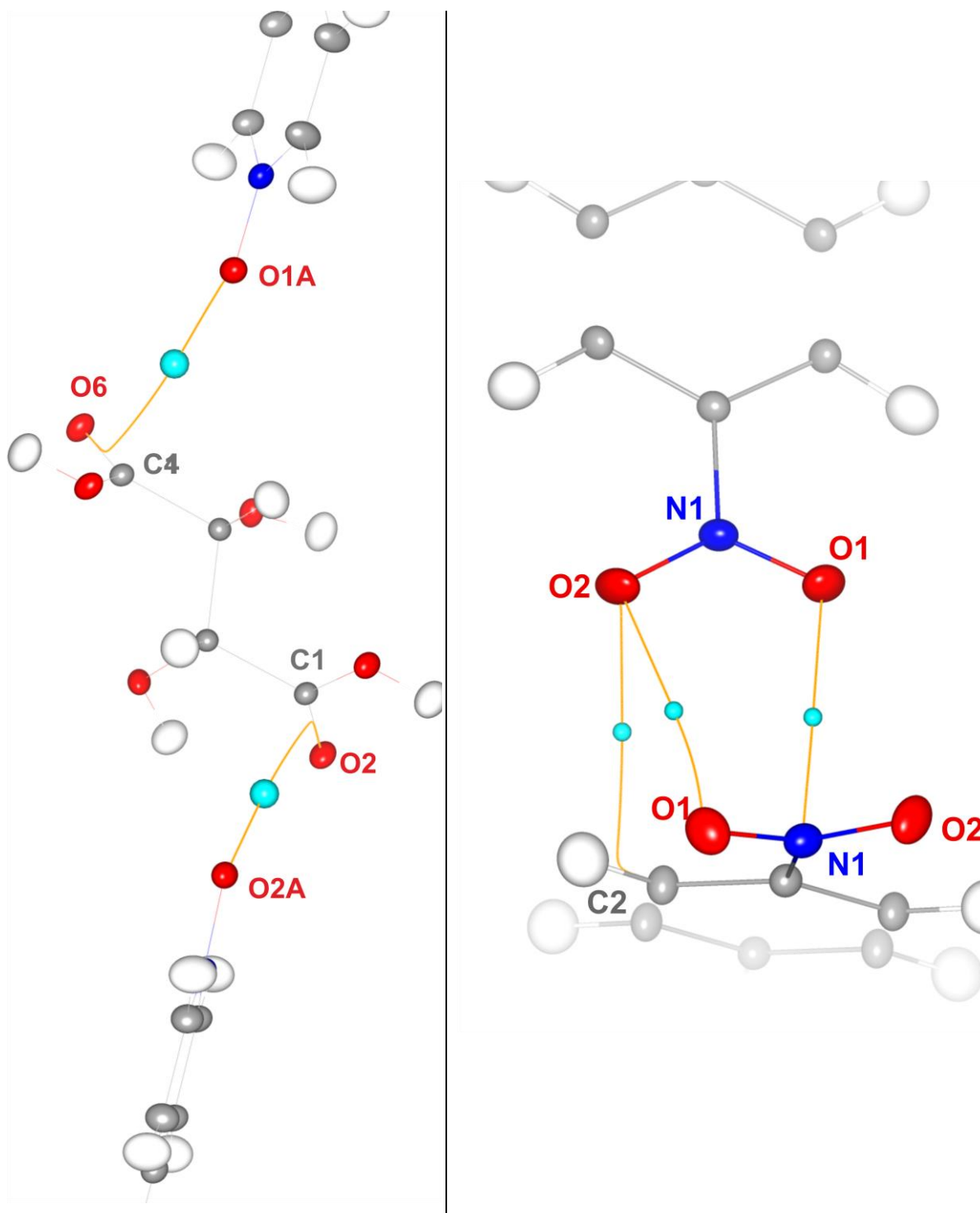
Figure 5. Bond paths and critical points between the oxygen lone pairs and the π holes in **2**, at carbon, a) and in **3**, at nitrogen b). In b) can be seen the bond path and critical point of the chalcogen interaction between the oxygen atoms.

Eventually, we were able to obtain suitable crystals for a charge density analysis involving a nitro group. The crystallization of 1,4-dinitrobenzene provided compound **3**. Crystal

structure of **3** suggests the searched interaction among the lone pair of the oxygen and the π hole of the nitrogen, pnicogen bond. At the same time, a chalcogen O···O interaction is likely to be present in the crystal structure. Both interactions were supported by the corresponding bond paths and (3,-1) critical points found in the topological analysis of the charge density obtained from the multipolar refinement.

The analysis of the three structures reveals that interactions, as weak as, chalcogen bonds can be substantiated using Bader's theory. π hole interactions, pnicogen and tetrel bond interactions presented likewise visible bond paths and critical points. However, in the case of the triel interaction, **1**, despite the high positive electrostatic potential at the boron atom, the calculated bond paths exclusively link the neighboring carbon and oxygen atoms to the anion. This finding experimentally supports the scenario described by Pendás et al.[13], in which the presence of a deep potential hole does not imply the presence of a bond path of electron density nor a critical point. Moreover, Bader's sufficient and necessary condition for a chemical bond is the existence of a bond path and (3,-1) critical point. Paradoxically, in **1**, the bond paths from the electron rich anion go to electron richer sites, oxygen and carbon atoms, instead to the boron electron deficient site. In addition, the electron rich atoms are further away from the anion. To illustrate this fact, it is worth comparing the tetrel and triel atoms involved. From the refined multipolar parameters, the net charge associated to the boron is around +0.3 e while the carbon has an associated charge of -0.04 e. Additionally, the negative value of the P_{20} quadrupolar projection, -0.37 e for the boron and -0.21 e for the carbon leading to a larger electron depletion at the boron atom. Eventually, the Cl^-···B distance is 3.28 Å while the Cl^-···C distance is 3.54 Å. Taken together, these results indicate that Cl^-···B interaction should be attractive and more intense than the corresponding Cl^-···C and Cl^-···O. There are theoretical studies demonstrating that atoms that should not interact attractively present bond paths due to confinement.[14,15] Thus, in the present example, the existence of bond paths between the Cl^-···C and Cl^-···O atoms raises a question about its attractive nature.

Another relevant detail of the Cl^-···O and Cl^-···C interactions is that the calculated energies associated to the observed critical points, using the Abramov expression[16], are quite weak.

In all three systems, the π hole interaction can be understood as a result of an empty π*-orbital of a sp^2-hybridized atom interacting with electron-rich regions of molecules. However, the electronic depletion in the π hole region is very intense in the boron atom, moderate in the carbon and less significant in the nitrogen atom. The lack of electron density in the boron atom emerges as the main reason for the absence of a (3, -1) bond critical point in the topological analysis of the charge density of **1**.

3. Experimental

Crystals of **1** were obtained by slow evaporation of phenylpyridine-4-boronic acid in an aqueous solution of hydro-chloride at 35%. Crystals of **2** were obtained by reflux of one equivalent of tartaric acid and one equivalent of bis-phenyl-N-oxide in methanol at 45°C. Crystals of compound **3** were obtained by slow evaporation in benzonitrile. The selected crystals of each compound were large enough to diffract until resolutions with $\sin(\theta)/\lambda >$ 1.2 Å^{-1}. Data collection were carried out at 90K using an Oxford Cryostream 700 plus cooling device in a Rigaku MHF007 rotating anode equipped with a Pilatus 200K hybrid pixel detector (especially recommended for charge density studies)[17,18]. Strategy in the data collection was chosen using only omega scans at chi angles between 40° and 55°. Data reduction and absorption correction was performed using CrysAlisPro 1.171.39.12b.[19] A second absorption correction using the program SADABS[20] was performed. Structure solution was obtained with SIR2014[21]. Structure refinement of the spherical atoms model was done with SHELXL-2014[22] using SHELXE[23]. The multipolar refinement was done using MOPRO[24]. The refined multipolar parameters were expanded until the octupolar level, using restrains according with the coordination of each atom.

In **1**, refinement until the hexadecapolar level was tried for the chloride anion but since no significant populations were refined at this level, the octupolar level was finally used. No symmetry restrain was fruitfully applied to the anion multipolar populations. We refined

reliable Anharmonic thermal motion parameters (Grad-Chamlier coefficients[25]) until the third order, for the Cl⁻ anion and O1.

In the multipolar refinement of **3**, we used the hydrogen atoms bond distance from the neutron diffraction data published by Tonogaki et al.[26]

The hydrogen thermal motion parameters were calculated with SHADE SERVER3.[27]

The quality of the multipolar refinements were verified with the help of the programs XDRKplot[28] and jnk2RDA v1.5 - 2013/10[29].

4. DFT study

DFT calculations by means of the TURBOMOLE 7.0 software at the M06-2X/def2-TZVP have been used to further analyze the strength of the triel bonding interaction. We have used the crystallographic coordinates to evaluate the binding energy of the Cl···B interaction using the system shown in Fig. 6a. The interaction energy is large and negative (−28.7 kcal/mol) due to the cationic nature of the boronic acid (protonated N atom of pyridine). As commented above, the presence of the O atoms directly bonded to the B atom likely weakens the interaction due to a dual effect. First, the electrostatic repulsion between the lone pairs of the O atoms and the negative chloride anion and, second, the Lewis acidity of B is reduced due to the donation of charge from the O atoms to the empty p_z orbital of B. In order to roughly estimate this effect, we have computed a theoretical model by replacing the OH groups of the boronic acid substituent by H-atoms, Fig. 6b. The position of the atoms has not been optimized (apart from the H-atoms) for comparison purposes. As a result, the interaction energy becomes more favorable in 13 kcal/mol, thus confirming that the presence of the O atoms overlaps the triel bonding interaction. We have also carried out the natural bond orbital analysis (NBO) using Gaussian 0.9-NBO 3.0, of both complexes focusing our attention to the second order perturbation analysis, since it is very useful to evaluate donor-acceptor interaction from an orbital point of view. In

the real complex (Fig. 6a) there is an orbitalic contribution between a filled lone pair of the

Cl atom to the empty p_z orbital of B with a concomitant stabilization energy of 5.54

kcal/mol that is the orbital contribution to the triel bond. In the model complex where the

OH groups have been replaced by H atoms, the same orbital contribution is present.

However, in this case it is considerably more favorable (15.17 kcal/mol of stabilization),

clearly confirming that the B atom is significantly more acidic in this model. It is also

important to note that in the boronic acid, there is an intramolecular orbital contribution

from the LP(O) to the unfilled p_z orbital of B that is 12.6 kcal/mol, also confirming the

electron donation from the O atoms to the B, thus reducing the π-acidity at B.
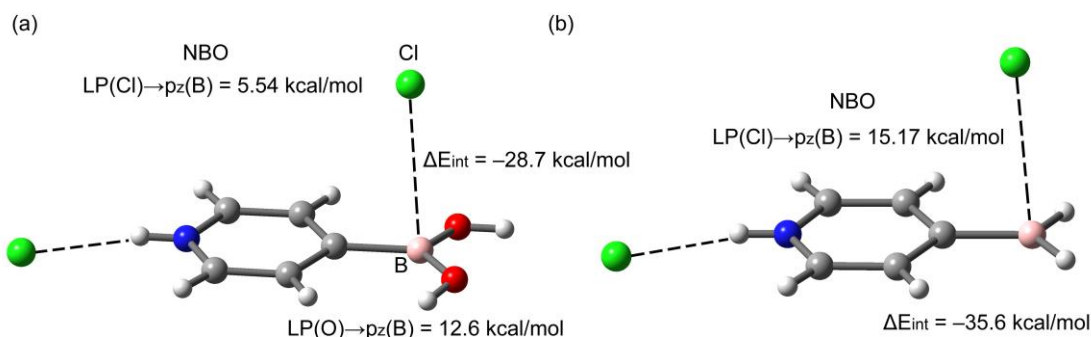
Figure 6. Theoretical models used to evaluate the triel bonding interaction at the M06-2X/def2-TZVP level of theory. a) structure model based on experimental single crystal structure. b) theoretical model created for comparison purposes.

5. Conclusions

Bader's theory demonstrated its use during the last decades. Weak interactions have been

well-described using this theory. In the recent years, many research groups payed

attention to these weak interactions due to its fundamental roles in catalysis, biological

processes, solvation, crystallization and co-crystallization, etc. The detailed description of

the interactions in the solid state is an excellent opportunity for analyzing, not only

attractive interactions, but also a priori not so favored interactions that can be frozen as a

consequence of the crystal packing. In the case of compound **1** of this work, an attractive interaction, the triel bonding remains hidden to the Bader's analysis. In contrast, apparently non-attractive interactions exhibit electronic interchange channels, considered as bonds in Bader's theory. DFT studies of a homologous model to **1**, where oxygen atoms where replaced by hydrogen atoms support this hypothesis. Additional NBO calculations further evidence the attractive Cl^--B interaction and the weakening provoked by the oxygen atoms.

We also compare the nature of the triel bonding with related π hole interactions. In the other two studied cases, compounds **2** and **3**, bond paths corresponding to the attractive interactions, tetrel bonding and pnicogen bonding, respectively, were evidence using Bader's theory. The comparison of the three studied π hole interactions, triel, tetrel and pnicogen bonding, allows us to conclude that in addition to the bond distance and strength of the interaction, the intensity of the π hole determines the presence of a bond path.

The analysis of isolated interaction within the crystal structure must be performed with great care. One must be aware that short interatomic distances present in the crystals could be a consequence of the crystal packing and not of the existence of attractive interactions between the involved atoms. The role of weak interactions is well appreciated in many chemical processes. The accurate assessment of weak interactions requires an in depth analysis of all involved intermolecular forces. In the present work, we demonstrated that the presence of reasonable attractive interactions can be accompanied by "non-expected" bonds. The latter are revealed through an accurate electron density analysis. In contrast, the former, that is the main attractive interaction i.e. the triel bonding, could not be revealed from the electron density analysis.

Closed shell attractive interactions featuring a very poor electron density site i.e. boron atom, can lead to the absence of a chemical bond base on Bader's definition. The typical presence of electron rich sites near the electron hole tend to reinforce this effect. This

observation seems to contradict the chemical intuition of bonds and attractive interactions.

6. References

(1)   Robertson, C. C.; Wright, J. S.; Carrington, E. J.; Perutz, R. N.; Hunter, C. A.; Brammer, L. *Chemical Science* **2017**, *8*, 5392.

(2)   Trujillo, C.; Sanchez-Sanz, G.; Alkorta, I.; Elguero, J. *New Journal of Chemistry* **2015**, *39*, 6791.

(3)   Politzer, P.; Murray, J. S.; Clark, T. *Physical Chemistry Chemical Physics* **2013**, *15*, 11178.

(4)   Brammer, L. *Faraday Discussions* **2017**, *203*, 485.

(5)   Omoto, K.; Fujimoto, H. *Journal of Organic Chemistry* **1998**, *63*, 8331.

(6)   Escudero-Adán, E. C.; Bauzá, A.; Frontera, A.; Ballester, P. *ChemPhysChem* **2015**, *16*, 2530.

(7)   Grabowski, S. *Molecules* **2015**, *20*, 11297.

(8)   Jelsch, B. F. B. G. C. E. C. E.-A. C. *Iucrj* **2018**.

(9)   Bader, R. F. W. *Journal of Physical Chemistry A* **1998**, *102*, 7314.

(10)   Espinosa, E.; Lecomte, C.; Molins, E. *Chemical Physics Letters* **1999**, *300*, 745.

(11)   Bui, T. T. T.; Dahaoui, S.; Lecomte, C.; Desiraju, G. R.; Espinosa, E. *Angewandte Chemie-International Edition* **2009**, *48*, 3838.

(12)   Antipin, M.; Boese, R.; Bläser, D.; Maulitz, A. *Journal of the American Chemical Society* **1997**, *119*, 326.

(13)   Pendás, A. M.; Francisco, E.; Blanco, M. A.; Gatti, C. *Chemistry – A European Journal* **2007**, *13*, 9362.

(14)   Haaland, A.; Shorokhov, D. J.; Tverdova, N. V. *Chemistry – A European Journal* **2004**, *10*, 4416.

(15)   Grimme, S.; Mück-Lichtenfeld, C.; Erker, G.; Kehr, G.; Wang, H.; Beckers, H.; Willner, H. *Angewandte Chemie International Edition* **2009**, *48*, 2592.

(16)   Abramov, Y. A. *Acta Crystallographica Section A* **1997**, *53*, 264.

(17)   Stalke, D. *Acta Crystallographica Section B-Structural Science Crystal Engineering and Materials* **2014**, *70*, 781.

(18)   Allé, P.; Wenger, E.; Dahaoui, S.; Schaniel, D.; Lecomte, C. *Phys. Scr.* **2016**, *91*, 063001.

(19)   Rigaku 2015.

(20)   Krause, L.; Herbst-Irmer, R.; Sheldrick, G. M.; Stalke, D. *Journal of Applied Crystallography* **2015**, *48*, 3.

(21)   Burla, M. C.; Caliandro, R.; Carrozzini, B.; Cascarano, G. L.; Cuocci, C.; Giacovazzo, C.; Mallamo, M.; Mazzone, A.; Polidori, G. *J. Appl. Cryst.* **2015**, *48*, 306.

(22)   Sheldrick, G. M. *Acta Crystallographica Section C-Structural Chemistry* **2015**, *71*, 3.

(23)   Hubschle, C. B.; Sheldrick, G. M.; Dittrich, B. *Journal of Applied Crystallography* **2011**, *44*, 1281.

(24)   Jelsch, C.; Guillot, B.; Lagoutte, A.; Lecomte, C. *Journal of Applied Crystallography* **2005**, *38*, 38.

(25)   *International Tables for Crystallography, Vol. D: Physical properties of crystals.*; Authier, A., Ed.; Kluwer Academic Publishers: Dordrecht/Boston/London, 2003.

(26)   Tonogaki, M.; Kawata, T.; Ohba, S.; Iwata, Y.; Shibuya, I. *Acta Crystallographica Section B* **1993**, *49*, 1031.

(27)   Madsen, A. O. *J. Appl. Cryst.* **2006**, *39*, 757.

(28)   Zhurov, V. V.; Zhurova, E. A.; Pinkerton, A. A. *Journal of Applied Crystallography* **2008**, *41*, 340.

(29)   Meindl, K.; Henn, J. *Acta Cryst. A* **2008**, *64*, 404.

7. Supporting information

a)
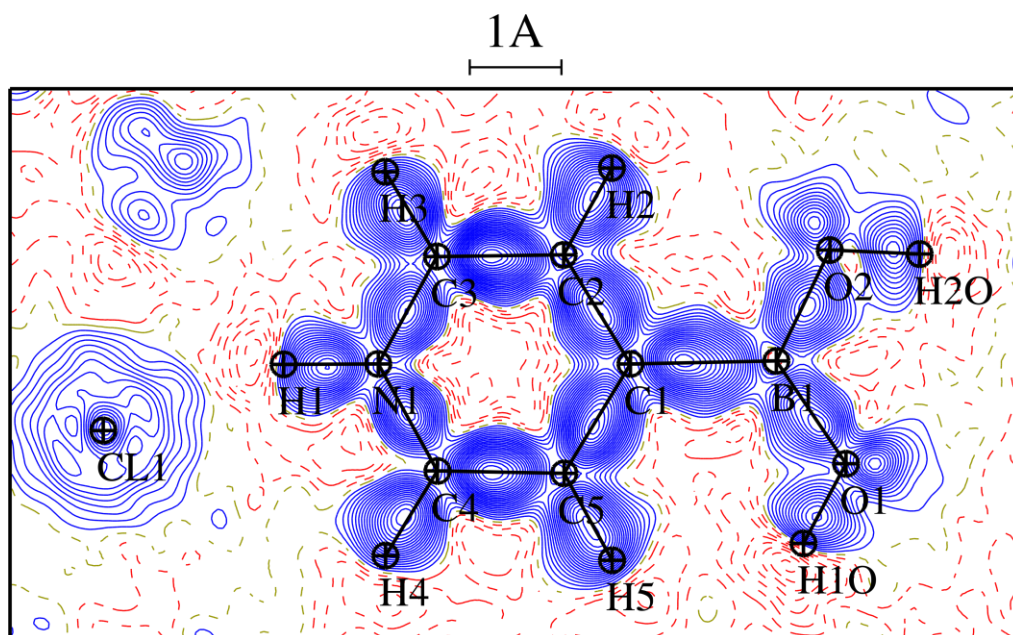
b)
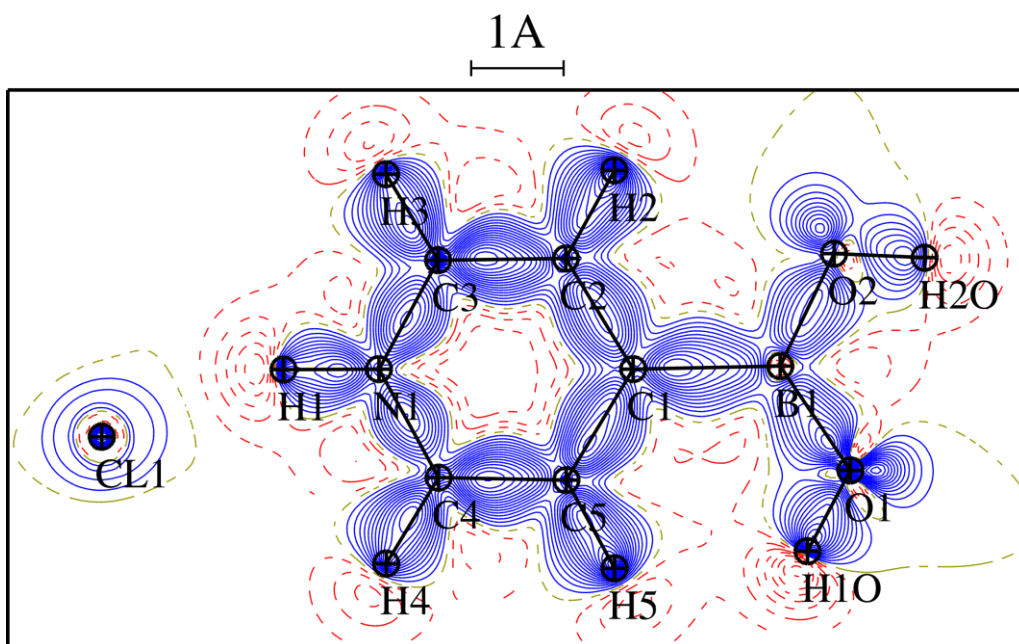
S 1. Dynamic deformation density a) and .static electron density deformation maps b) of compound **2** on the pyridinium ring plane. Contours levels at 0.05 e/Å^3.

b)
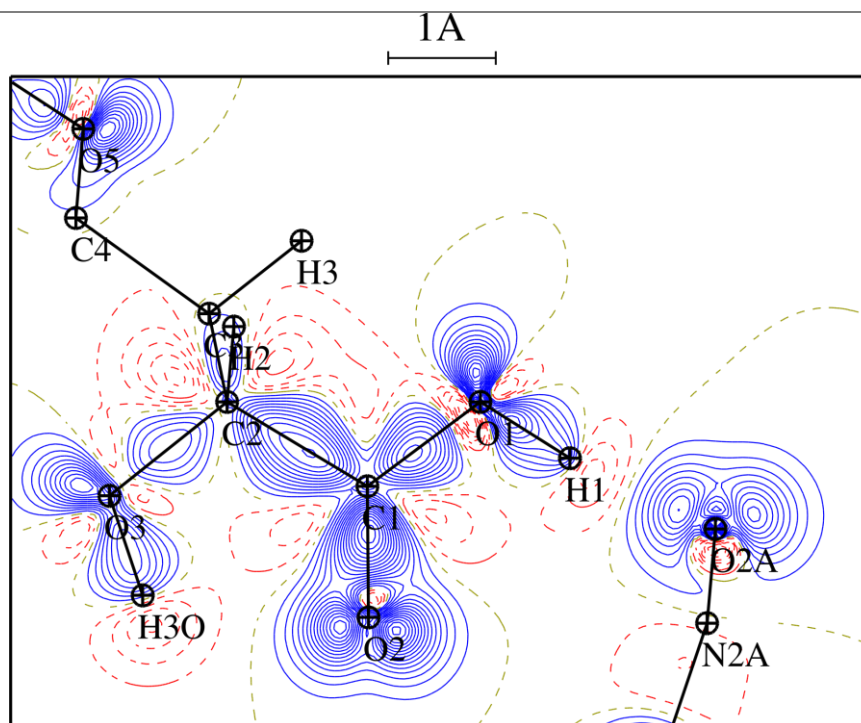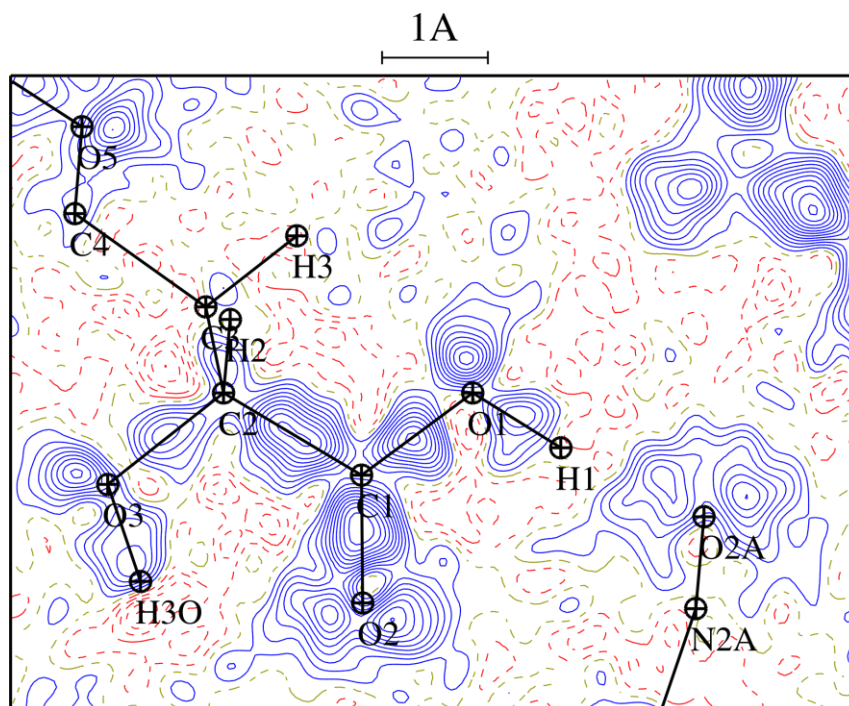
S 2. Dynamic deformation density a) and .static electron density deformation maps b) of compound **2** in the plane defined by C1, O1 and O2. Contours levels at 0.05 e/Å^3

a)
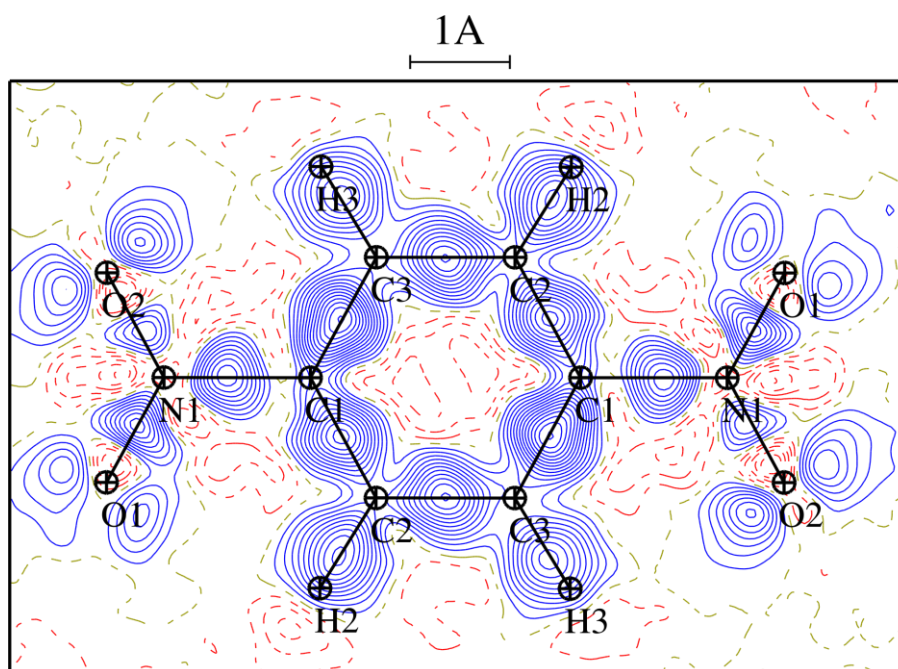
b)
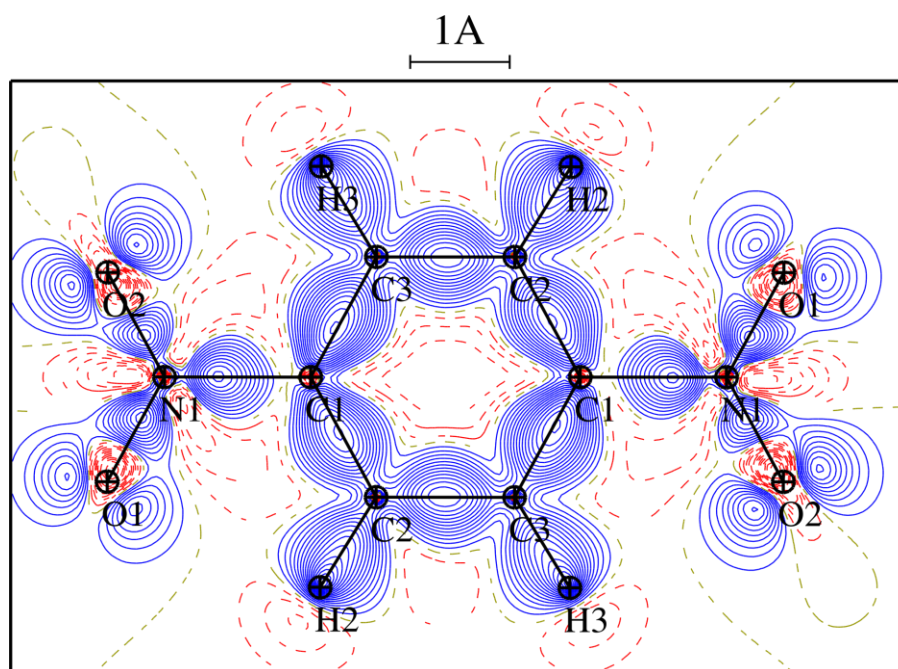
S 3. Dynamic deformation density a) and .static electron density deformation maps b) of compound **3** on the phenyl ring plane. Contours levels at 0.05 e/Å³

a)

0.42 <d< 5.95 (A)   1A

b)

fractal dimension (d^f) *vs.* residual density (ρ_0)

c)
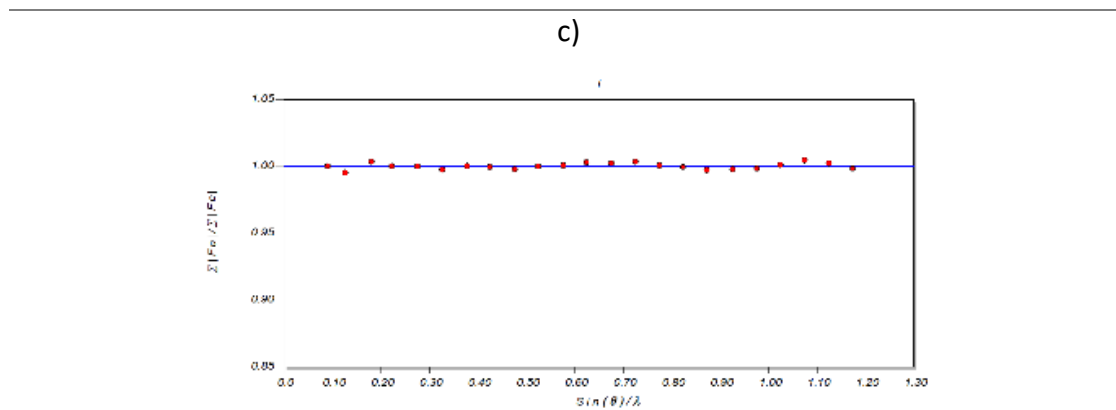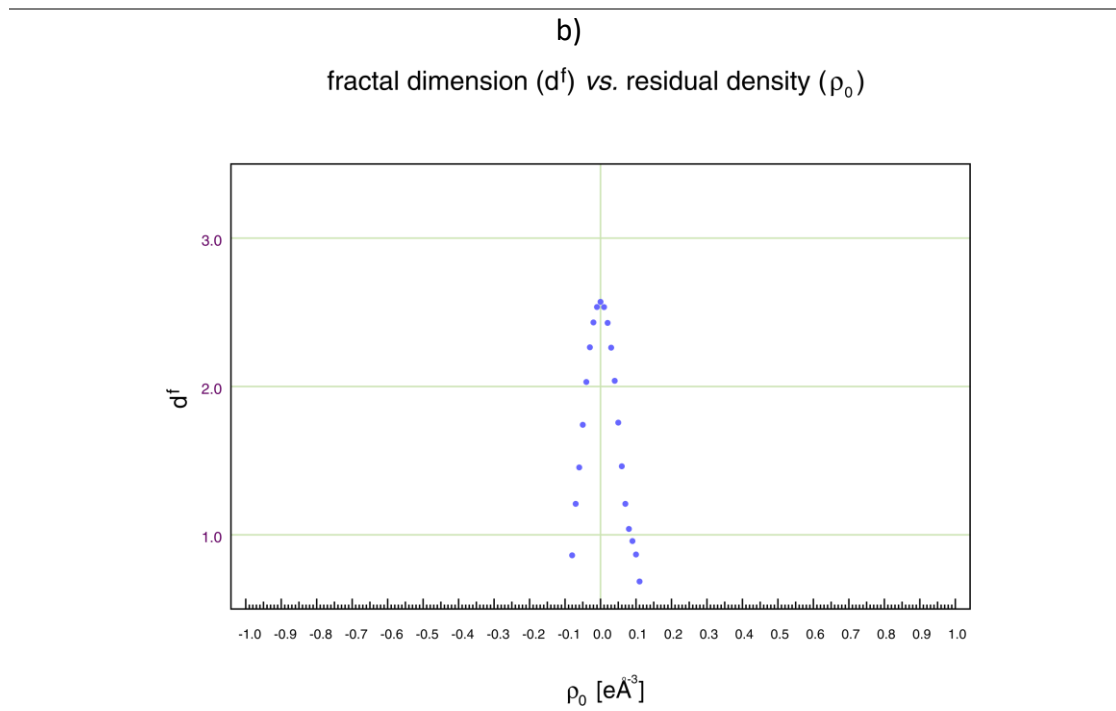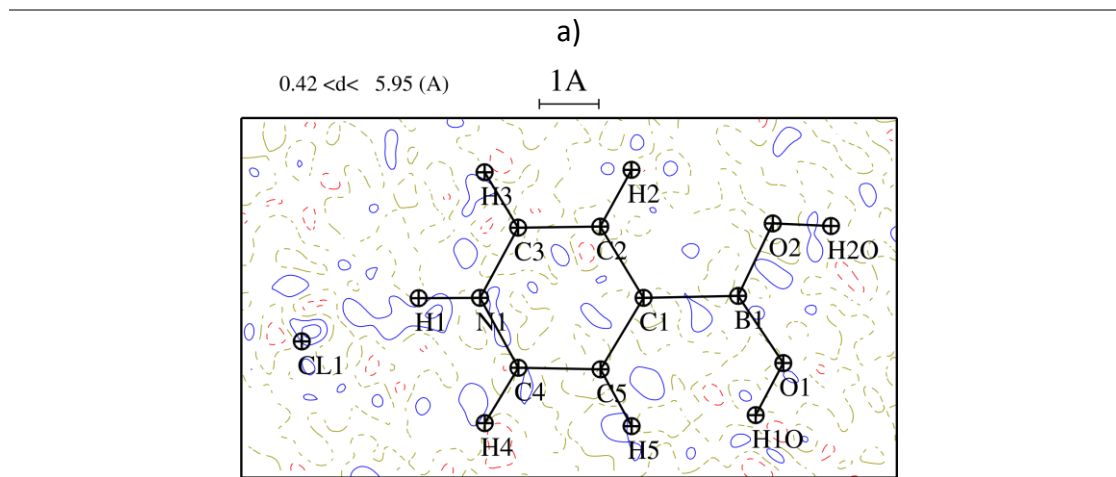
S 4. Fourier residual maps at the pyridinium ring (Contours levels at 0.05 e/Å^3), fractal dimension test and scaling factor plots of compound **1** a), b) and c) respectively.

a)

b)
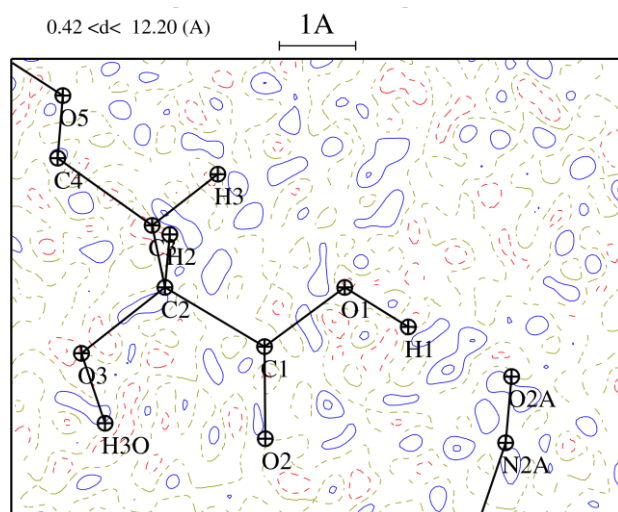
fractal dimension (d^f) *vs.* residual density (ρ_0)
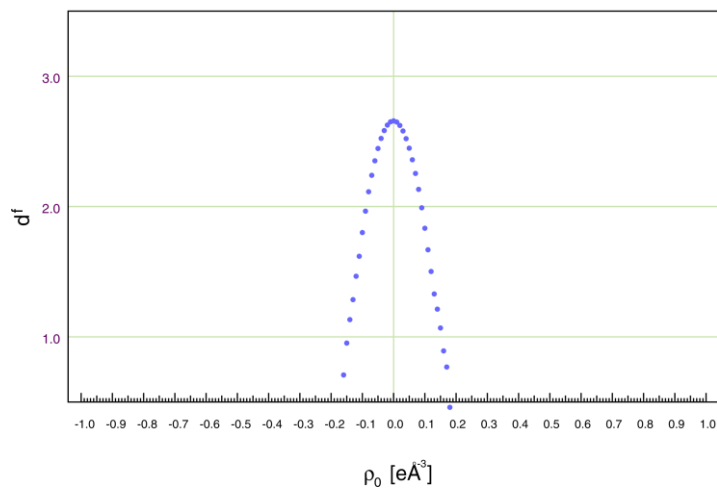
c)
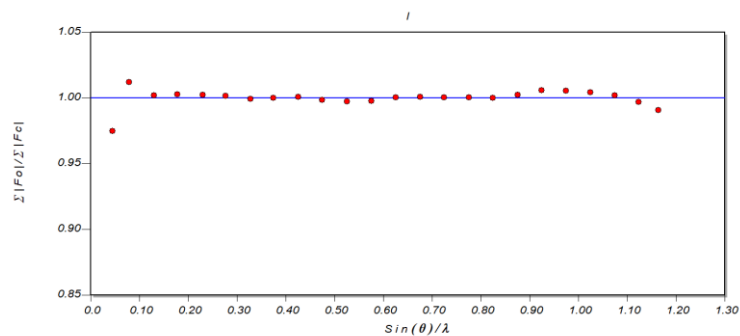
S 5. Fourier residual maps (Contours levels at 0.05 e/Å^3), fractal dimension test and scaling factor plots of compound **2** a), b) and c) respectively.

a)

d)
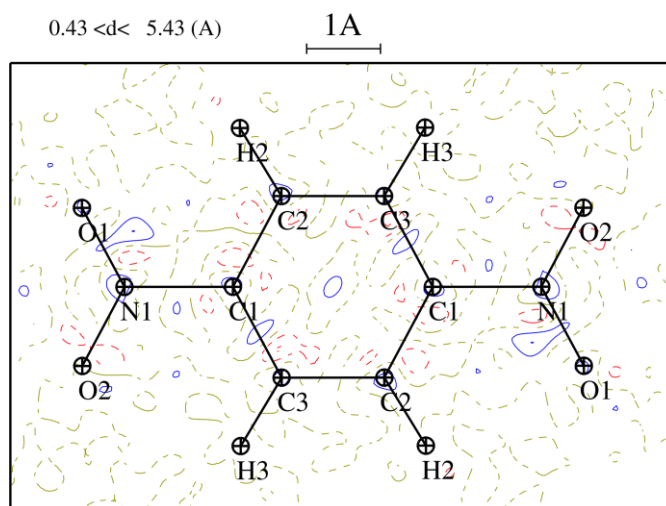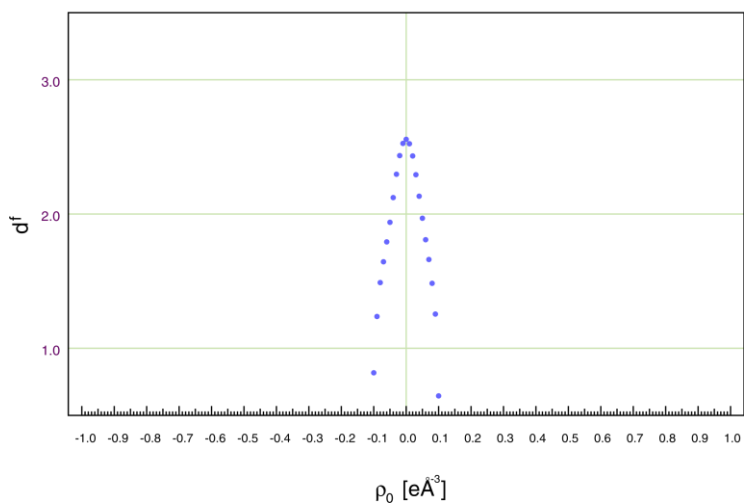
g)
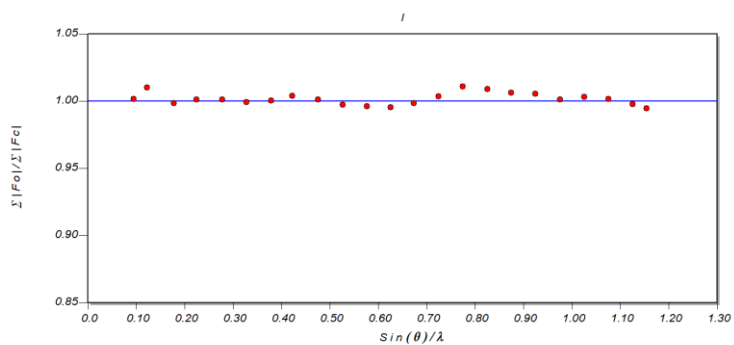
S 6. Fourier residual maps (Contours levels at 0.05 e/Å³), fractal dimension test and scaling factor plots of compound **3** a), b) and c) respectively.

Table S 1. Compound **1.** Bond energies calculated using the Abramov expression[16], bond distances and distances from the atom to the critical point, in Å. Electron density at the critical point in e/Å^3. Eigen values of the Hessian matrix and ellipticy at the critical point.

Atom1	Atom2	Hartree/Bohr^3		kJ/mol/Bohr^3		DISTIJ	DCPI	DCPJ	DEN	LAPL	3-EIGEN-VALUES			ELLIPTIC	TYPE
		Gcp	Vcp	Gcp	Vcp										
O1	B1	0.3099	-0.4847	813.7	-1272.7	1.361	0.907	0.456	1.44	13.0	-14.33	-13.47	40.83	0.064	(3,-1)
O1	H1O	0.2211	-0.8179	580.5	-2147.3	0.991	0.753	0.239	2.28	-36.2	-34.38	-34.27	32.43	0.003	(3,-1)
O2	B1	0.3141	-0.5158	824.6	-1354.4	1.356	0.901	0.455	1.52	10.8	-15.06	-14.70	40.59	0.025	(3,-1)
O2	H2O	0.2139	-0.7824	561.5	-2054.1	0.982	0.748	0.234	2.22	-34.2	-33.33	-33.27	32.41	0.002	(3,-1)
N1	C3	0.3041	-0.8756	798.4	-2298.9	1.343	0.813	0.530	2.31	-25.8	-18.04	-16.38	8.64	0.101	(3,-1)
N1	C4	0.2695	-0.8141	707.6	-2137.4	1.342	0.836	0.506	2.23	-26.5	-17.89	-15.53	6.90	0.152	(3,-1)
N1	H1	0.2066	-0.6669	542.5	-1751.0	1.033	0.774	0.259	1.99	-24.5	-26.65	-25.80	28.00	0.033	(3,-1)
C1	C2	0.2827	-0.7504	742.2	-1970.2	1.402	0.706	0.697	2.09	-17.8	-15.56	-13.51	11.23	0.152	(3,-1)
C1	C5	0.2878	-0.7577	755.7	-1989.4	1.403	0.687	0.715	2.10	-17.6	-16.12	-13.42	11.99	0.201	(3,-1)
C1	B1	0.1051	-0.3050	275.9	-800.7	1.593	1.080	0.514	1.23	-9.1	-9.49	-9.33	9.68	0.017	(3,-1)
C2	C3	0.3085	-0.8382	810.0	-2200.7	1.384	0.648	0.736	2.24	-21.3	-17.52	-14.08	10.28	0.244	(3,-1)
C2	H2	0.2118	-0.6117	556.0	-1605.9	1.089	0.718	0.371	1.87	-18.1	-17.71	-16.68	16.26	0.062	(3,-1)
C3	H3	0.1879	-0.5774	493.3	-1516.0	1.089	0.758	0.331	1.82	-19.4	-18.55	-17.37	16.48	0.068	(3,-1)
C4	C5	0.2997	-0.8245	786.9	-2164.7	1.384	0.733	0.651	2.22	-21.7	-17.50	-14.13	9.93	0.239	(3,-1)
C4	H4	0.1852	-0.5705	486.1	-1497.8	1.089	0.761	0.329	1.80	-19.3	-18.38	-17.03	16.12	0.080	(3,-1)
C5	H5	0.2165	-0.6252	568.3	-1641.3	1.089	0.727	0.362	1.89	-18.5	-18.44	-17.53	17.43	0.052	(3,-1)
Non covalent interactions															
CL1	H1	0.0236	-0.0219	62.0	-57.4	2.100	1.465	0.646	0.178	2.5	-0.67	-0.60	3.71	0.123	(3,-1)
CL1	H2O	0.0202	-0.0188	53.0	-49.3	2.137	1.509	0.633	0.163	2.1	-0.41	-0.40	2.90	0.019	(3,-1)
CL1	H1O	0.0178	-0.0170	46.7	-44.6	2.149	1.504	0.692	0.156	1.8	-0.62	-0.41	2.83	0.492	(3,-1)
O1	H5	0.0082	-0.0059	21.5	-15.4	2.765	1.598	1.178	0.063	1.0	-0.19	-0.05	1.26	3.211	(3,-1)
H3	O1	0.0079	-0.0057	20.7	-14.9	2.432	1.058	1.420	0.062	1.0	-0.23	-0.21	1.41	0.094	(3,-1)
CL1	H3	0.0064	-0.0045	16.7	-11.9	2.680	1.726	0.979	0.053	0.8	-0.18	-0.13	1.11	0.355	(3,-1)
CL1	H5	0.0059	-0.0040	15.6	-10.6	2.701	1.799	0.964	0.046	0.8	-0.12	-0.06	0.93	1.129	(3,-1)
CL1	C1	0.0041	-0.0033	10.7	-8.5	3.537	1.833	1.725	0.050	0.5	-0.12	-0.08	0.67	0.477	(3,-1)
CL1	O2	0.0037	-0.0028	9.8	-7.4	3.557	1.891	1.683	0.043	0.5	-0.10	-0.07	0.62	0.496	(3,-1)
CL1	C3	0.0035	-0.0026	9.1	-6.7	3.575	1.892	1.721	0.040	0.4	-0.06	-0.02	0.50	2.723	(3,-1)
CL1	H2	0.0026	-0.0017	6.9	-4.6	3.216	1.928	1.316	0.027	0.3	-0.05	-0.05	0.44	0.026	(3,-1)
C4	O1	0.0025	-0.0017	6.5	-4.4	3.527	1.786	1.754	0.027	0.3	-0.05	-0.04	0.40	0.325	(3,-1)

Table S 2. Compound **2.** Bond energies calculated using the Abramov expression[16], bond distances and distances from the atom to the critical point, in Å. Electron density at the critical point in e/Å^3. Eigen values of the Hessian matrix and ellipticy at the critical point.

Atom1	Atom2	Hartree/Bohr^3 Gcp	Vcp	kJ/mol/Bohr^3 Gcp	Vcp	DISTIJ	DCPI	DCPJ	DEN	LAPL	3-EIGEN-VALUES			ELLIPTIC	TYPE
O1	C1	0.2990	-0.8997	785.0	-2362.1	1.310	0.816	0.494	2.365	-29.08	-20.56	-19.23	10.71	0.070	(3,-1)
H1A	C1A	0.1909	-0.5867	501.1	-1540.2	1.084	0.340	0.744	1.834	-19.76	-18.63	-17.55	16.42	0.062	(3,-1)
C1	O2	0.5109	-1.3512	1341.4	-3547.5	1.216	0.425	0.791	2.968	-31.75	-30.09	-26.87	25.22	0.120	(3,-1)
C1	C2	0.2126	-0.5572	558.3	-1463.0	1.522	0.775	0.747	1.742	-12.72	-12.84	-11.28	11.40	0.139	(3,-1)
H2A	C2A	0.1853	-0.5503	486.6	-1444.7	1.082	0.341	0.741	1.758	-17.31	-17.02	-16.35	16.05	0.041	(3,-1)
H2	C2	0.2080	-0.5776	546.2	-1516.4	1.095	0.368	0.727	1.794	-15.57	-17.00	-16.56	17.99	0.026	(3,-1)
C2	O3	0.2544	-0.6306	668.0	-1655.6	1.408	0.588	0.820	1.861	-11.73	-13.79	-13.78	15.84	0.001	(3,-1)
C2	C3	0.1948	-0.4922	511.3	-1292.2	1.543	0.770	0.773	1.609	-9.90	-11.10	-10.53	11.73	0.054	(3,-1)
O3	H3O	0.1725	-0.7575	452.8	-1988.8	0.976	0.761	0.215	2.212	-39.77	-35.80	-34.95	30.98	0.024	(3,-1)
H3	C3	0.2084	-0.5748	547.1	-1509.2	1.096	0.372	0.724	1.788	-15.24	-17.01	-16.34	18.11	0.041	(3,-1)
C3	C4	0.2133	-0.5631	560.1	-1478.3	1.527	0.749	0.779	1.755	-13.15	-13.15	-11.39	11.39	0.155	(3,-1)
C3	O4	0.2457	-0.6198	645.1	-1627.2	1.402	0.580	0.822	1.847	-12.38	-13.64	-13.60	14.86	0.003	(3,-1)
C4	O6	0.5118	-1.3681	1343.6	-3591.9	1.211	0.423	0.788	2.995	-33.21	-31.57	-27.55	25.91	0.146	(3,-1)
C4	O5	0.2841	-0.8587	745.9	-2254.4	1.325	0.510	0.815	2.301	-28.00	-20.11	-18.36	10.47	0.095	(3,-1)
H4A	C4A	0.1900	-0.5639	498.9	-1480.5	1.082	0.340	0.742	1.784	-17.72	-17.36	-16.75	16.39	0.037	(3,-1)
H4	O4	0.2092	-0.8305	549.2	-2180.4	0.978	0.227	0.751	2.319	-39.73	-36.59	-35.61	32.47	0.027	(3,-1)
O5	H5O	0.1933	-0.6434	507.5	-1689.1	0.980	0.772	0.208	1.956	-24.75	-30.64	-30.48	36.38	0.005	(3,-1)
H5A	C5A	0.1932	-0.5879	507.2	-1543.6	1.082	0.345	0.738	1.835	-19.43	-18.38	-17.41	16.35	0.056	(3,-1)
O2A	N2A	0.5747	-1.0920	1508.9	-2867.1	1.332	0.657	0.675	2.466	5.54	-19.69	-18.55	43.78	0.062	(3,-1)
C3A	C4A	0.2796	-0.7458	734.1	-1958.1	1.402	0.714	0.688	2.081	-17.99	-16.43	-13.02	11.46	0.262	(3,-1)
C3A	C6A	0.2381	-0.6109	625.0	-1603.8	1.476	0.742	0.734	1.836	-12.99	-14.17	-11.85	13.03	0.196	(3,-1)
C3A	C2A	0.2827	-0.7547	742.3	-1981.4	1.399	0.713	0.686	2.096	-18.24	-16.43	-13.20	11.38	0.245	(3,-1)
C4A	C5A	0.2948	-0.7989	773.9	-2097.6	1.385	0.674	0.711	2.173	-20.18	-17.24	-13.39	10.44	0.287	(3,-1)
C5A	N1A	0.2839	-0.8135	745.3	-2135.9	1.352	0.476	0.876	2.213	-23.69	-18.29	-14.72	9.32	0.243	(3,-1)
C6A	C7A	0.2820	-0.7586	740.5	-1991.6	1.404	0.702	0.702	2.104	-18.75	-16.71	-13.46	11.42	0.242	(3,-1)
C6A	C10A	0.2815	-0.7489	739.0	-1966.3	1.399	0.708	0.691	2.085	-17.93	-16.30	-13.33	11.70	0.223	(3,-1)
C7A	C8A	0.3031	-0.8197	795.9	-2152.2	1.382	0.694	0.688	2.206	-20.58	-17.79	-13.68	10.89	0.301	(3,-1)
C7A	H7A	0.1950	-0.5908	511.9	-1551.0	1.083	0.750	0.333	1.839	-19.36	-18.46	-17.70	16.80	0.043	(3,-1)

Table S2 Continuation.

Atom1	Atom2	Hartree/Bohr^3		kJ/mol/Bohr^3		DISTIJ	DCPI	DCPJ	DEN	LAPL	3-EIGEN-VALUES			ELLIPTIC	TYPE
		Gcp	Vcp	Gcp	Vcp										
C8A	N2A	0.2885	-0.8232	757.3	-2161.4	1.354	0.495	0.859	2.228	-23.74	-17.66	-15.17	9.09	0.164	(3,-1)
C8A	H8A	0.2000	-0.5891	525.0	-1546.6	1.082	0.734	0.348	1.830	-18.23	-18.08	-17.18	17.03	0.053	(3,-1)
C9A	C10A	0.3043	-0.8181	799.0	-2147.9	1.383	0.707	0.676	2.202	-20.19	-17.51	-13.86	11.17	0.263	(3,-1)
C9A	N2A	0.2939	-0.8296	771.7	-2178.2	1.348	0.482	0.866	2.235	-23.31	-17.65	-15.22	9.56	0.159	(3,-1)
C9A	H9A	0.1955	-0.5864	513.4	-1539.6	1.082	0.734	0.348	1.829	-18.83	-18.23	-17.27	16.68	0.055	(3,-1)
C10A	H10A	0.2058	-0.5984	540.4	-1571.0	1.081	0.722	0.359	1.844	-18.00	-17.68	-16.96	16.64	0.043	(3,-1)
C2A	C1A	0.2992	-0.8139	785.7	-2136.8	1.379	0.667	0.712	2.198	-20.76	-17.64	-13.60	10.48	0.297	(3,-1)
O1A	N1A	0.5791	-1.1131	1520.4	-2922.3	1.326	0.658	0.668	2.501	4.35	-20.12	-18.81	43.28	0.069	(3,-1)
C1A	N1A	0.2872	-0.8253	754.0	-2166.9	1.350	0.480	0.870	2.233	-24.19	-18.87	-14.51	9.19	0.301	(3,-1)
Non covalent interactions															
H5O	O1A	0.0653	-0.0786	171.4	-206.3	1.546	0.496	1.050	0.443	5.01	-2.75	-2.69	10.45	0.021	(3,-1)
O3	H4	0.0409	-0.0335	107.3	-87.8	1.707	1.181	0.529	0.208	4.66	-0.72	-0.71	6.09	0.013	(3,-1)
H3O	O2	0.0164	-0.0140	43.0	-36.8	2.022	0.778	1.263	0.128	1.80	-0.55	-0.50	2.86	0.095	(3,-1)
O6	H10A	0.0115	-0.0079	30.2	-20.8	2.224	1.372	0.856	0.071	1.45	-0.25	-0.25	1.95	0.020	(3,-1)
H4A	O4	0.0089	-0.0063	23.5	-16.6	2.340	0.942	1.416	0.065	1.11	-0.23	-0.23	1.58	0.013	(3,-1)
O4	H9A	0.0085	-0.0062	22.3	-16.3	2.418	1.416	1.039	0.067	1.04	-0.24	-0.23	1.50	0.050	(3,-1)
O5	H3	0.0067	-0.0047	17.5	-12.2	2.515	1.476	1.073	0.053	0.83	-0.16	-0.14	1.13	0.177	(3,-1)
H5A	O6	0.0065	-0.0046	17.0	-12.1	2.556	1.167	1.446	0.054	0.80	-0.17	-0.16	1.13	0.084	(3,-1)
H2	O1	0.0058	-0.0040	15.2	-10.6	2.602	1.151	1.503	0.048	0.73	-0.13	-0.11	0.96	0.131	(3,-1)
O3	H9A	0.0050	-0.0035	13.2	-9.2	2.744	1.548	1.240	0.044	0.63	-0.11	-0.09	0.84	0.217	(3,-1)
C4A	C10A	0.0045	-0.0034	11.7	-8.9	3.230	1.608	1.625	0.049	0.53	-0.07	-0.04	0.64	0.744	(3,-1)
O6	H4A	0.0035	-0.0022	9.1	-5.8	2.784	1.579	1.237	0.029	0.45	-0.08	-0.06	0.59	0.355	(3,-1)
O2	O2A	0.0033	-0.0022	8.7	-5.7	3.373	1.878	1.594	0.030	0.43	-0.07	-0.04	0.54	0.739	(3,-1)
O6	C5A	0.0033	-0.0021	8.7	-5.6	3.335	1.607	1.735	0.029	0.43	-0.06	-0.03	0.53	1.059	(3,-1)
H10A	O4	0.0032	-0.0021	8.3	-5.5	2.944	1.348	1.651	0.030	0.41	-0.08	-0.05	0.54	0.579	(3,-1)
O6	O1A	0.0030	-0.0020	8.0	-5.2	3.390	1.912	1.581	0.028	0.39	-0.06	-0.03	0.49	0.819	(3,-1)
N1A	C3A	0.0023	-0.0016	6.2	-4.1	3.587	1.784	1.813	0.026	0.30	-0.03	-0.01	0.34	2.200	(3,-1)
O2	H4	0.0005	-0.0003	1.4	-0.7	3.542	1.956	1.594	0.005	0.07	-0.01	0.00	0.09	1.768	(3,-1)

Table S 2. Compound **3.** Bond energies calculated using the Abramov expression[16], bond distances and distances from the atom to the critical point, in Å. Electron density at the critical point in e/Å^3. Eigen values of the Hessian matrix and ellipticy at the critical point.

Atom1	Atom2	Hartree/Bohr^3 Gcp	Vcp	kJ/mol/Bohr^3 Gcp	Vcp	DISTIJ	DCPI	DCPJ	DEN	LAPL	3-EIGEN-VALUES			ELLIPTIC	TYPE
N1	O1	0.8322	-1.8173	2184.99	-4771.27	1.227	0.591	0.635	3.44	-14.73	-31.61	-28.84	45.72	0.096	(3,-1)
N1	O2	0.7900	-1.6957	2074.08	-4452.05	1.224	0.592	0.632	3.29	-11.16	-28.93	-27.52	45.29	0.051	(3,-1)
N1	C1	0.2129	-0.5602	559.00	-1470.83	1.470	0.893	0.578	1.75	-12.95	-12.48	-10.66	10.19	0.170	(3,-1)
C1	C2	0.2862	-0.7846	751.52	-2059.86	1.389	0.708	0.681	2.15	-20.44	-16.03	-13.38	8.97	0.199	(3,-1)
C1	C3	0.3028	-0.8277	794.88	-2173.24	1.391	0.732	0.660	2.22	-21.42	-16.47	-13.82	8.87	0.192	(3,-1)
C2	C3	0.2822	-0.7770	740.99	-2040.11	1.391	0.701	0.691	2.14	-20.49	-15.54	-13.28	8.33	0.170	(3,-1)
C2	H2	0.2116	-0.6276	555.58	-1647.72	1.077	0.707	0.370	1.90	-19.70	-17.88	-17.11	15.30	0.045	(3,-1)
C3	H3	0.2035	-0.5957	534.18	-1564.08	1.077	0.708	0.369	1.84	-18.20	-16.83	-16.40	15.03	0.026	(3,-1)
Non covalent interactions															
N1	O1	0.0067	-0.0046	17.45	-12.11	2.965	1.487	1.488	0.05	0.84	-0.14	-0.05	1.02	1.904	(3,-1)
C2	O2	0.0040	-0.0027	10.58	-7.15	3.278	1.752	1.554	0.04	0.51	-0.10	-0.09	0.70	0.203	(3,-1)
O1	O2	0.0032	-0.0020	8.51	-5.27	3.271	1.650	1.636	0.03	0.43	-0.06	-0.04	0.53	0.419	(3,-1)

Table S4. Crystallographic table of the refinements of **1**, **2** and **3**. Data collected at 90K.

Compound	1		2		3	
Empirical formula	$C_5 H_7 B Cl N O_2$		$C_{14} H_{14} N_2 O_8$		$C_6 H_4 N_2 O_4$	
Chemical name	4-Pyridinylboronic acid hydrochloride		tartaric acid + 4,4'-bipyridine N-N'-dioxide		1,4-dinitrobenzene	
Formula weight	159.38		142.13		168.11	
Crystal system /	Monoclinic		Orthorhombic		Monoclinic	
Space group	Pc		$P2_12_12_1$		$P2_1/n$	
Friedif$_{stat}$	124		7		-	
Unit cell dimensions	$a = 6.20620(5)$Å $\alpha= 90°$ $b = 5.25334(4)$Å $\beta = 105.5034(8)°$ $c = 11.18373(9)$Å $\gamma = 90°$		$a = 4.54400(10)$Å $\alpha= 90°.$ $b = 15.2652(2)$Å $\beta = 90°.$ $c = 20.3342(2)$Å $\gamma = 90°.$		$a = 5.66357(3)$Å $\alpha= 90°$ $b = 5.37326(3)$Å $\beta = 92.0201(5)°$ $c = 10.91612(7)$Å $\gamma = 90°$	
Volume	$351.359(5)$ Å^3		$1409.47(3)$ Å^3		$331.991(3)$ Å^3	
Z	2		4		2	
Density (calc.)	1.506 Mg/m^3		1.594 Mg/m^3		1.682 Mg/m^3	
Abs. coefficient	0.467 mm^{-1}		0.133 mm^{-1}		0.145 mm^{-1}	
F(000)	164		704		172	
Crystal size	0.3 x 0.25 x 0.2 mm^3		0.3 x 0.2 x 0.2 mm^3		0.35 x 0.3 x 0.2 mm^3	
Refls. collected	32802		90175		33917	
Abs. correction/Max-Min transmision	Multi-scan/0.75-0.73		Multi-scan//1.0-0.72		Multi-scan//0.75-0.70	
Refinement model	Spherical	Multipolar	Spherical	Multipolar	Spherical	Multipolar
Theta range	3.24 to 66.55°	3.24 to 58.52°	1.67 to 64.15°	3.24 to 55.53°	3.74 to 65.41°	3.74 to 55.52°
$\sin\theta/\lambda_{max}$	1.29Å^{-1}	1.2Å^{-1}	1.27Å^{-1}	1.16Å^{-1}	1.28Å^{-1}	1.16Å^{-1}
Weighting schem	$1/[\sigma^2(F_o^2)+(aP)^2+bP]$; a=0.0317, b=0.0002	$1/[a\sigma^2(I)]$; a=2.25	$1/[\sigma^2(F_o^2)+(aP)^2]$; a=0.0497	$1/[a\sigma^2(I)]$; a=1.15	$1/[\sigma^2(F_o^2)+(aP)^2+bP]$; a=0.0697, b=0.008	$1/[a\sigma^2(I)]$; a=4.9
Indep. reflections	8362[R_{int} = 0.0125]		19571[R_{int} = 0.0338]		5766[R_{int} = 0.0251]	
Completeness	87.9%		86.6%		99.0%	
Data / restraints / parameters	8184/ 2/ 119	7501/ 154/ 334	19571/ 0/ 273	18682/361/747	5766/ 0/ 63	4276/ 80/ 207
GOOF on F^2	1.113	0.997	0.994	1.036	1.109	1.008
R indices (all data)*	R_1 = 0.0136 wR^2 = 0.0405	R_1 = 0.0063 wR^2 = 0.0139	R_1 = 0.0399 wR^2 = 0.0839	R_1 = 0.0215 wR^2 = 0.0306	R_1 = 0.0319 wR^2 = 0.1110	R_1 = 0.0107 wR^2 = 0.0244
Hooft/Parsons parameter	y = 0.003(5) z=0.005(4)	y =0.009(5)	y =0.07(10) z=0.09(12)	y =-0.03(7)	-	-
Largest diff. peak and hole	0.40/-0.19 e.Å^{-3}	0.12/-0.09 e.Å^{-3}	0.57/-0.22 e.Å^{-3}	0.18/-0.16 e.Å^{-3}	0.57/-0.63 e.Å^{-3}	0.10/-0.10 e.Å^{-3}
RBT (non H)		2.4 x 10^{-4}		2.0 x 10^{-4}		1.4 x 10^{-4}

* I/σ(I)=0.1 for the multipolar refinement.

Experimental quantification of the quadrupole moment and the MEP maps of di- and triethynylbenzene: is the ethynyl substituent paradoxical?
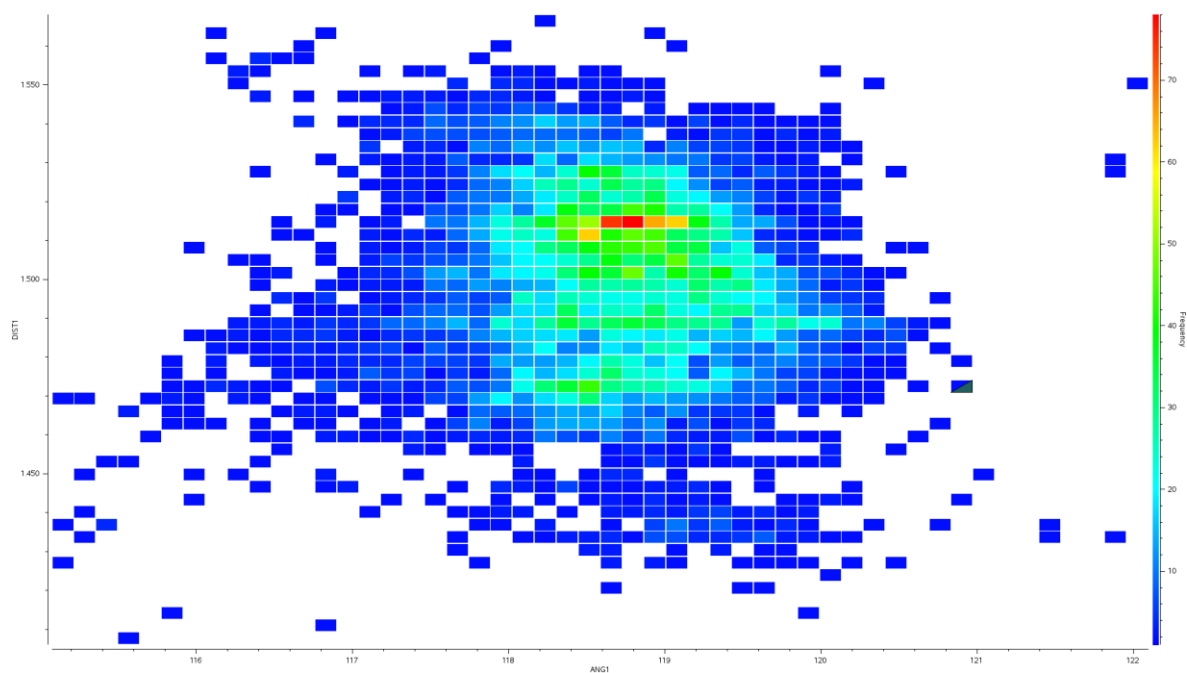
1. Introduction.

In this chapter, we describe the experimental determination of the quadrupole moments (Q) and the molecular electrostatic potentials (MEP) of diethynylbenzene, triethynylbenzene, tricyanobenzene and p-aminoaniline using high-resolution X-ray single crystal diffraction data. Based on DFT calculations, 1,3,5-triethynyl benzene presents a negative Q_{zz} value. Its magnitude is similar to the one calculated for the electron rich p-aminoaniline and twice that of the benzene. However, the calculated MEP value over the aromatic ring center is, unexpectedly, half that of benzene. In agreement with this latter result, triethynylbenzenes interact favorably with anions and cations because the interaction is dominated by ion-induced polarization. High-level ab initio calculation indicate that the progressively increase of the number of ethynyl substituents, from two to six, strengthens the ion–π interaction with anions and weakens the corresponding one with cations.

The fast development of supramolecular chemistry has a significant impact on the growing efficacy and success of constructing molecular assemblies of different sizes, shapes and functionalities.[1] Chemists working on this discipline mostly depend on the understanding of the non-covalent forces that govern molecular recognition phenomena.[2] Among these forces, those involving π-systems are very relevant for molecular interactions.[3] For instance, C–H/π, π–π and ion–π interactions are important in host-guest systems, catalysis and biological systems.[4-6]
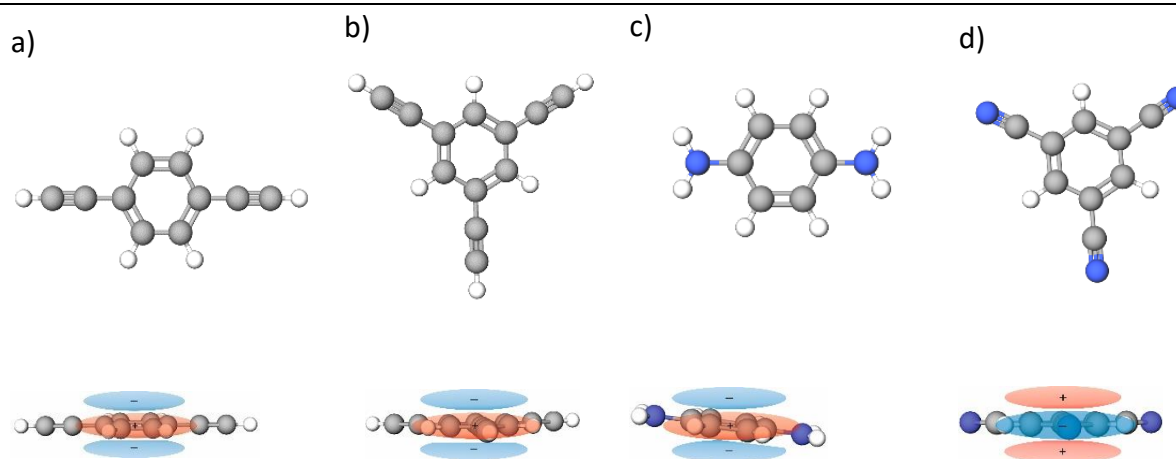
Figure 1. Schemes of the charges distribution corresponding to the quadrupole moment of a) 1,4-ethynilbenzene, b) 1,3,5-triethynilbenzene, c) p-Phenylenediamine and d) 1, 3, 5-tricyanobenzene.

The physical nature of ion–π interactions[7-12] (both cation–π and anion–π) have been studied and rationalized using high level ab initio calculations and several partition energy schemes. [13-16] The general assumption is that ion-induced polarization and electrostatic interactions are the main forces contributing to ion–π interactions. Regarding the polarization term, the π-cloud on an aromatic compound is readily polarized by the ion, leading to an 'induced dipole' (see scheme 1). The cation/anion can then interact with this induced dipole. This polarization contribution to the total interaction energy can be substantial. Regarding the electrostatic contribution, it correlates well with the permanent quadrupole moment perpendicular to the ring plane (Q_{zz} in Buckinghams, B)[17]. This physical property is a measure of the electron richness/deficiency of an aromatic system. As one might expect a more electron poor aromatic ring tends to display stronger binding to anions and an electron rich one to cations. The magnitude and sign of Q_{zz} depend on the substitution pattern on a given aromatic ring. For example, the negative Q_{zz} found for benzene (Q_{zz} = −8.48 B) predicts an attractive interaction with cations. If, however, H is replaced by F (i.e. hexafluorobenzene) the Q_{zz} turns into positive (9.50 B) and the interaction becomes attractive with anions.

The role of the substituents on the strength of ion–π interactions is of big interest and has been object of study by various groups. [12,17-19] In general, the different trends observed in

the interaction energies depending on the substituents of the arene have been reproduced using either their local dipoles or using the Q_{zz} of the arene, which is directly influenced by the magnitude of the local dipoles. A close examination of previous work present in the literature reveals that ethynyl-substituted arenes do not follow the expected trend regarding their π-binding ability toward cations and anions.
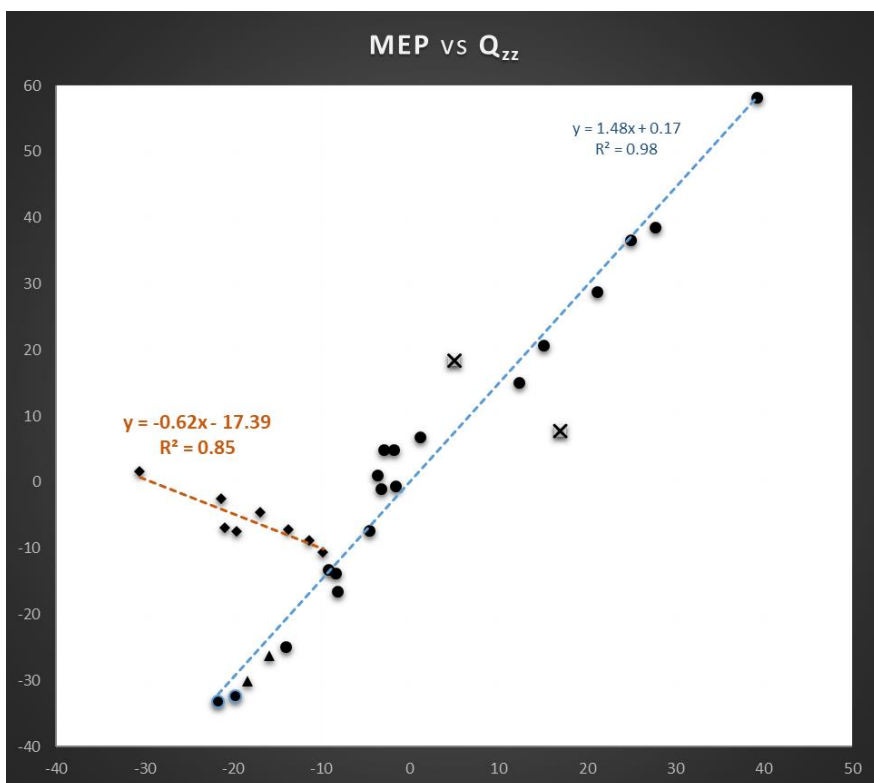
Figure 2. Plot of the MEP values versus the component values of the quadrupolar moment perpendicular to the phenyl ring, Q_{zz}, of a set of phenyl rings with different substituents at (1,4 and 1,3,5) symmetrical sites. The linear correlation of the ethynyl, methyl, SH and CF_3 substituted phenyl rings (diamonds) presents a negative slope.
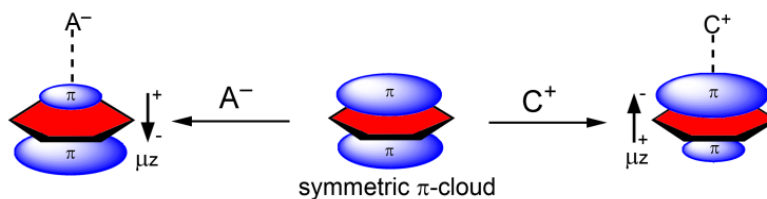
Figure 3. Schematic representation of the π-cloud polarization upon complexation of the ion with the aromatic ring.

Compound	Q_{zz}	α_{zz}	MEP
$C_6H_5(CCH)$	−11.5	47.1	−10.9
$C_6H_4(CCH)_2$	−13.8	55.2	−7.2
$C_6H_3(CCH)_3$	−17.0	63.5	−4.5
$C_6H_2(CCH)_4$	−21.4	71.7	−2.5
$C_6(CCH)_6$	−30.6	87.8	+1.6
Benzene[a]	−8.6 (−8.5)	63.8 (63.8)	−15.1

[a] Experimental values in parenthesis

Table 1. Theoretical Q_{zz} (B) and polarizability, α_{zz} (a.u.) values of ethynylbenzenes retrieved from the literature at the M06-2X/6-31+G*. MEP values (kcal·mol^{-1}) from this work at the MP2/aug-cc-pVTZ level of theory measured at the van der Waals surface over the ring center.

The ethynyl group can be considered an electron-withdrawing group (EWG) taking into consideration its Hammett's substituent constants[18] (σ_m = 0.20 and σ_p = 0.23) in line with the strong s character of the sp-hybridized C atom. Moreover, it has been shown experimentally that the ethynyl group also exerts an electron-withdrawing (EW) resonance effect.[19] In fact, the redox properties of alkynyl-substituted flavins have been studied and the reduction potential of ethynyl substituted flavins moves toward more positive values[20] in sharp agreement with the EW character of ethynyl based on the Hammett σ values. Similarly, the effect of the alkynyl substitution in benzoquinones has been studied using cyclic voltammetry confirming the EW nature of the ethynyl group.[21] These experimental investigations are in deep contrast with the Q_{zz} values obtained theoretically for a series of ethynyl-benzenes (see Table 1). It can be clearly observed that the Q_{zz} value becomes more negative as the number of CCH substituents increases. Actually, the hexaethynylbenzene presents a Q_{zz} value that is almost four times the value of benzene. Also unexpectedly, the molecular electrostatic potential value over the center of the ring becomes progressively less negative on going from the diethynyl to the tetraethynyl-benzene and finally becomes positive for hexaethynyl-benzene (see Table 1), in sharp disagreement with the Q_{zz} trend. It should be mention that the existence of linear correlation with positive slope between the Q_{zz} and MEP values, in a relevant set of

benzene derivatives (MEP = $1.48Q_{zz} + 0.17$, $R^2 = 0.98$), was previously demonstrated,[17] Fig. 2. In fact, the MEP value of benzene is larger than that if the hexaethynyl-benzene. The tendency observed for the MEP values reported in Table 1 agrees well with the previously mentioned EW nature of the ethynyl group.

At this point, we decided to calculate the MEP and Q_{zz} values of other phenyl rings in which the substituent was connected through a carbon atom to the ring. The investigated compounds include: p-xylene and mesitylene, containing $-CH_3$ groups and 1,4-bis(trifluoromethyl)benzene and 1,3,5-tris(trifluoromethyl)benzene, containing $-CF_3$ groups. When the calculated MEP and Q_{zz} values were plotted, we observed that both set of date presented a linear correlation with a negative slope and appeared in different quadrant of the Q_{zz} vs MEP plot. That is, while the set of phenyl rings substituted with methyl groups followed the same trend observed for the ethylnyl substituted phenyl groups, at the 3rd quadrant (- , -), the 1,4-bis(trifluoromethyl)benzene and 1,3,5-tris(trifluoromethyl)benzene appear clearly in the positive quadrant, (+ , +). With this new set of data, it is possible to group together in a single linear correlation the ethynyl, methyl and thiol substituted phenyl groups (MEP = $-0.62Q_{zz} + 17.39$, $R^2 = 0.85$), Fig. 2.

In order to shed some light into this matter, we undertook the experimental measurement of the Q_{zz} and MEP values of diethynyl- and triethynyl-benzene derived from high-resolution X-ray diffraction data aiming at assessing the reliability of the computational study and the theoretically determined quadrupole moments. For comparison purposes, we also determined the experimental values of tricyanobenzene (a well-known electron deficient aromatic ring) and 1,4-diaminobenzene (electron rich aromatic ring). We combined the experimental results with high level ab initio calculations (MP2/aug-cc-pVTZ) to further analyze the behavior of the different groups as substituents of the phenyl ring.
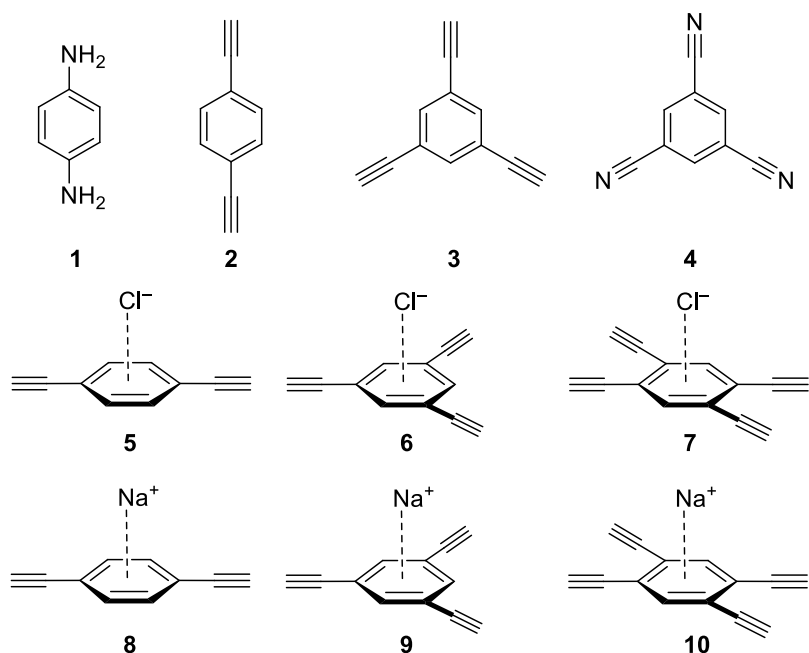
Figure 3. Molecular structures of compounds and complexes **1**–**10**.

The calculated interaction energies for complexes **5**–**10** can be used to instantiate the striking behavior of ethynylbenzenes in terms of Q_{zz} values. In short, anion–π interactions strengthens as the number of CCH substituents increases (complexes **5**–**7**) and the opposite is true for the cation–π interaction (complexes **8**–**10**). Therefore, the trend of the interaction energies, which are summarized in Table 2, is in agreement with the calculated MEP values but it does not correlate with the corresponding Q_{zz} magnitudes. To understand further this behavior, we performed a partitioning of the interaction energy into individual components using the SAPT method. The results are summarized in Table 3 and some interesting conclusions can be drawn from them. First, the electrostatic term is surprisingly favorable in all complexes (anion and cation–π). In the anion–π complexes, the polarization (E_{ind}) and dispersion (E_{disp}) contributions equally dominate the interaction and the electrostatic term increases as the number of CCH substituents increases. The large interaction energies obtained for the cation–π complexes are due to the contribution of the induction term (> 20 kcal·mol^{-1} in absolute value). This is due to the short cation–π distances that provokes a significant polarization of the π-cloud. The dispersion term is modest in the cation–π complexes. At this point, it is worth mentioning

120

that the results presented in Table 2 clearly demonstrate that the electrostatic picture of the ion–π interaction is totally incomplete. It is also surprising that the E_{ele} term for both tetraethynyl-benzene cation–π and anion–π complexes is approximately the same, which is −6.3 kcal·mol^{-1} for **7** and −6.8 kcal·mol^{-1} for **10**. A likely explanation for this behavior is the crucial contribution of the ion-induced dipole interaction in the total E_{ele} (see Scheme 1).

a)			b)			
Complex	E	d_z	E_{ele}	E_{ex}	E_{ind}	E_{disp}
5	−3.2	3.272	−2.9	12.7	−6.5	−6.6
6	−4.6	3.193	−5.0	15.3	−7.6	−7.5
7	−5.8	3.131	−6.3	17.7	−8.5	−8.2
8	−17.2	2.185	−10.3	16.3	−22.8	−1.5
9	−15.7	2.161	−7.9	17.1	−24.8	−1.6
10	−14.9	2.160	−6.8	17.0	−25.7	−1.6

Table 2. a) Interaction energies with BSSE correction (E, kcal·mol^{-1} and equilibrium distances (d, Å) of complexes 4–9. at the MP2/aug-cc-pVTZ level of theory. b) SAPT interaction energies (E_{total}, kcal·mol^{-1}) and their partitioning into the electrostatic, exchange, induction and dispersion contributions (E_{ele}, E_{ex}, E_{ind}, E_{disp}, respectively, kcal·mol^{-1}) at the RI-DFT/aug-cc-pVQZ level of theory using the DF-DFT-SAPT approach.

2. Experimental.

An appropriated manner to experimentally validate the theoretically calculated Q_{zz} and MEP values is based on the charge density distribution (CDD) analysis derived from high resolution X-ray diffraction data.[22-24] Suitable single crystals for X-ray charge density experiments were obtained for all four compounds 1-4 using different procedures. Single crystals of **1** were grown from a solution in nitrobenzene. Crystals of compounds **2** and **3**

were obtained by sublimation using a Kofler heating bench and crystals of compound **4** correspond to a solvate of nitrobenzene obtained from a nitrobenzene solution. Crystals of 1,4-dicyanobenzene, compound **11**, obtained under a variety of conditions, always presented small domains affecting low resolution reflections. Because of this, no reliable CDD studies of this compound based on experimental data are reported. High-resolution X-ray diffraction data were collected at 100K on a Rigaku XtaLab P200 Mo Kα rotating anode equipped with a Pilatus 200K detector (a hybrid pixel detector recommended for charge density studies[25-27]). Data reduction and absorption correction was performed using CrysAlisPro 1.171.39.12b.19[28] A second absorption correction using the program SADABS-2014/5[29] was performed. Structure solution was obtained with SIR2014[30]. Structure refinement of the spherical atoms model was done with SHELXL-2014[31] using SHELXE[32]. The MEP calculations and Q_{zz} derived from the X-ray data were performed using the program MOPRO.[33] An optimization of the used restrains based on free R factors was performed.[34,35] The thermal motion of the hydrogen atoms were calculated using SHADE SERVER3.[36]

The quality of the multipolar refinements was verified with the help of the programs XDRKplot27 and jnk2RDA v1.5 - 2013/1028.

The quadrupole moments of compounds 1-4 were calculated by performing a multipolar refinement of their high-resolution diffraction data. In order to evaluate the reliability of the multipolar refinements, the corresponding Fourier residual maps were inspected. No substantial residual densities were found in any of the maps, Figure 4.

In the same manner, the distribution of the residual densities and the behavior of the scaling factor were also analyzed. All together, the obtained results confirmed the consistency of the multipolar model. In CDD studies, the Gaussian distribution of residual electron density must exhibit a parabolic shape[37]. Figure 5 a), b) c) and d) show a parabolic curve (Gaussian) with slight deviations at the base. Likewise, the behavior of the scale factors, Figures 5 e, f, g, h, show an almost constant value throughout the full resolution range. These results warrant that the refined model are sound for all four structures.
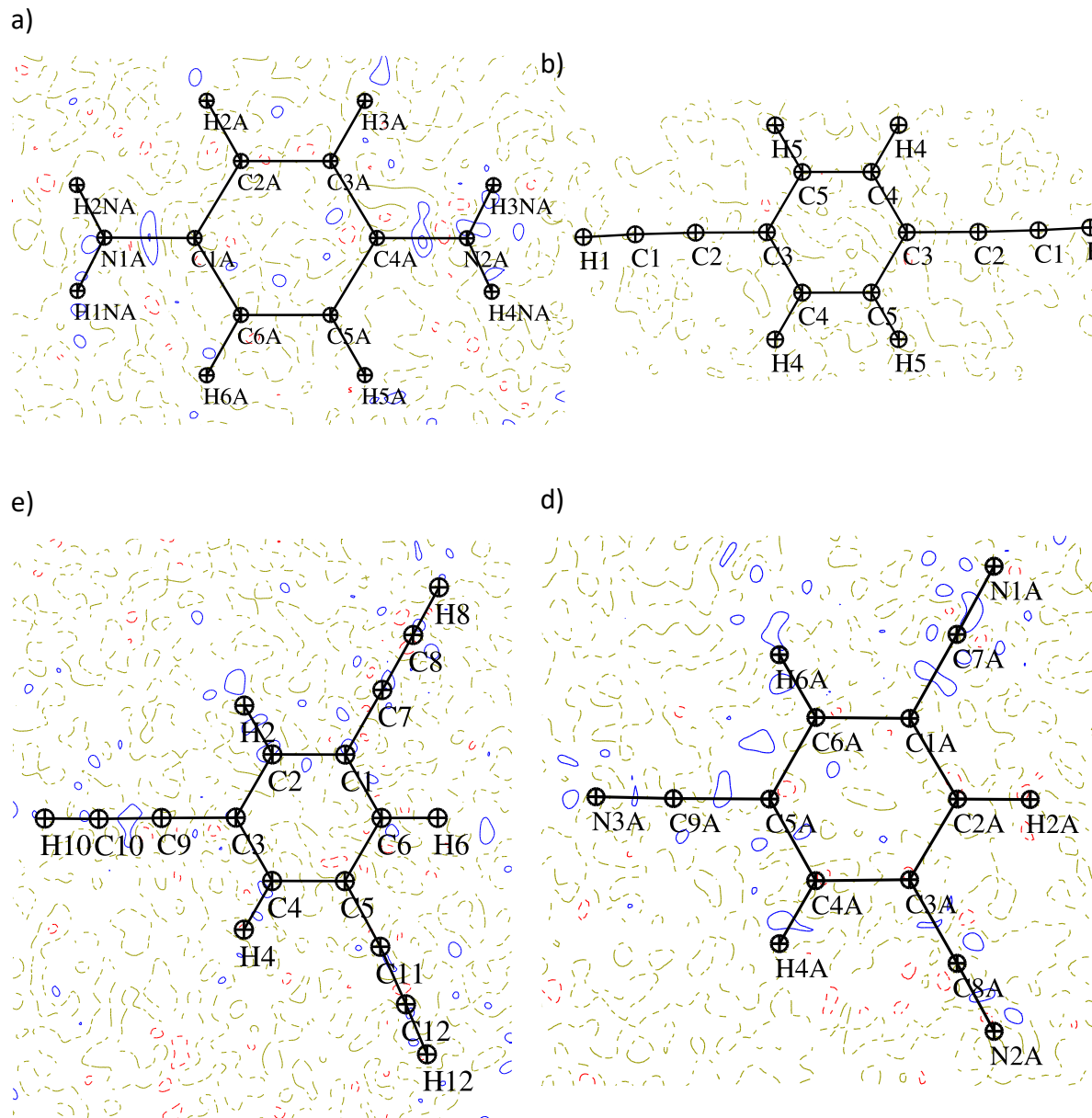
Figure 4. Fourier residual maps on the planes containing the phenyl ring of the compounds at 0.05 e/A³.
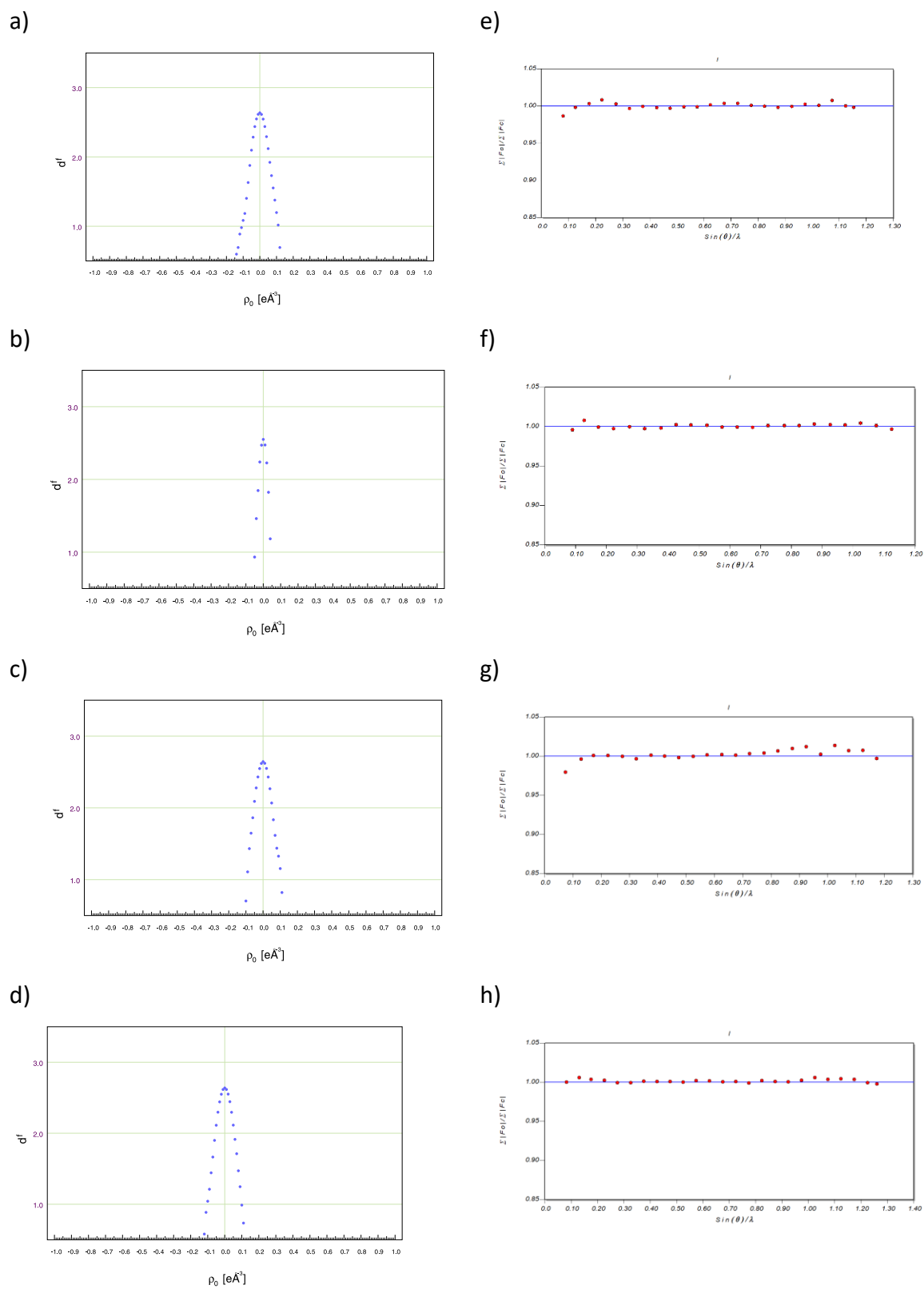
Figure 5. Fractal dimension test and scaling factor behavior plotted against resolution shells for compounds **1**, **2**, **3** and **4**.

3. Results and Discussion.

The multipolar refinements provided multipolar models showing sensible charge density deformation maps. The obtained maps exhibited electron rich areas associated with covalent bonds and lone pairs, and electron deficient regions, Fig. S1. In relation to the geometry of the molecules, small distortions of the phenyl rings were observed as a function of the substituents. The observed distortions are dissimilar for the different substituents. For example, compounds **3** and **4** show an identical distribution of residuals in the phenyl ring. However, the phenyl ring of compound **4** is somewhat distorted with respect to an ideal hexagonal shape. In contrast, the phenyl ring of compound **3** defines a regular hexagon. Although the diffraction data set of **11** does not allow a reliable multipolar refinement, we did collect high-resolution data. It is well known that the information contained at high resolution data is mainly related with the thermal motion and the atomic positions.[38] Therefore, the acquired data allowed the accurate estimation of the molecular geometry. The same geometrical alterations observed in the phenyl ring of **4** were observed in the case of **11**, Table 3. An analogous analysis of CDD performed on the crystal of compound **2**, revealed that its phenyl ring was distorted in an opposite manner with respect to the one measured for **11**. This result confirmed that the geometry of the phenyl ring is differently affected as a function of the nature of the substituents and their relative positioning.
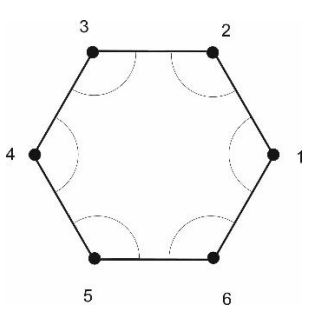
	Angle at					
Compound	1	2	3	4	5	6
1	117.820(6)	121.138(6)	121.079(6)	117.821(6)	121.116(6)	121.022(6)
2	119.430(4)	120.147(4)	120.423(5)	-	-	-
3	120.052(6)	119.950(6)	120.059(7)	119.941(6)	120.119(5)	119.880(6)
4	121.133(6)	118.695(6)	121.342(6)	118.674(5)	121.215(5)	118.925(5)
11	121.401(16)	119.349(17)	119.251(16)	-	-	-

Table 3. Angles at different sites of the phenyl rings of the studied compounds.

Figure 6. CSD search plots of the distance of substituted residuals in a phenyl ring against the C-C-C angle value of the substituted carbon.

We decide to investigate if the phenyl ring deformations were responsible of the different correlations obtained for the MEP and Q_{zz} values against the binding energies of the ion-complexes of the different phenyl substituted rings. We analyzed the geometry of phenyl rings as a function of the different substituents by performing an exhaustive search in the Cambridge Structural Data Base. We found that there is a clear linear correlation between the C-C-C angle of the phenyl ring and the bond distance of the substituent when the covalent connection takes place through an oxygen or nitrogen atom. Similarly, we detected the existence of a linear correlation between these parameters having an inverse slope when the substituent is connected through a boron atom. In contrast, phenyl

substituents connected through a carbon atom do not display a linear relationship between the same parameters, Figure 6. In the studied compounds, the cyano group clearly distorted the ideal geometry of a phenyl ring (identical bond lengths and 120° C-C-C angles). It behaves as a strong electron-withdrawing group. This behavior is in contrast with the ethynyl substituent, Table 1. Moreover, the cyano group is a clear outlier with respect to other carbon-connected substituents of the phenyl ring. The C-C(CN)$_{substitued}$-C angle is > 121°. In contrast, the C$_{phenyl}$-C$_{substituent}$ distances are very similar: 1.431 Å for the ethynyl substituted group and 1.434 Å for the cyano groups. Previous work showed that in monosustituted benzene derivates, the geometry distortion of the phenyl ring (C-C$_{substitued}$-C angle) and the electronegativity of the substituent were linearly correlates.[39] The putative linear correlations of the MEP and the Q$_{zz}$ values with the electronegativities of the substituents were also analyzed. Unfortunately, the observed trends do not show clear signs of any correlation and thus do not shed any light on the problem, Fig 7. In addition, the observed geometry distortions of the phenyl rings are not correlated with the MEP or the Q$_{zz}$ values.

Using the multipolar models of **2** and **3** we determined their Q$_{zz}$ values. For comparison purposes, we also determined, using the same methodology, the Q$_{zz}$ values of two additional substituted phenyls rings featuring an opposite electronic nature: the π-electron rich **1** and the π-electron poor **4**. The calculated Q$_{zz}$ values are summarized in Table 4. Using the charge density distribution of compounds **1–4**, we also determined the MEP value over the center of the rings at the VdW surface. From the inspection of the results (Table 4), several interesting aspects arise. First, the experimentally determined Q$_{zz}$ values demonstrate that the ethynyl substituents strongly change its value to more negative magnitudes in comparison to benzene (–16.2 B for **2** and –23.4 B for **3**). This result confirms the theoretical predictions. In fact, the experimentally calculated Q$_{zz}$ values of **1** and **3** are very similar. Second, the experimentally determined MEP values support the paradoxical behavior of the ethynyl group, since the MEP value of **3** is significantly less negative than that of **1**. Third, **4** exhibits the expected behavior since both Q$_{zz}$ and MEP values are large and positive.
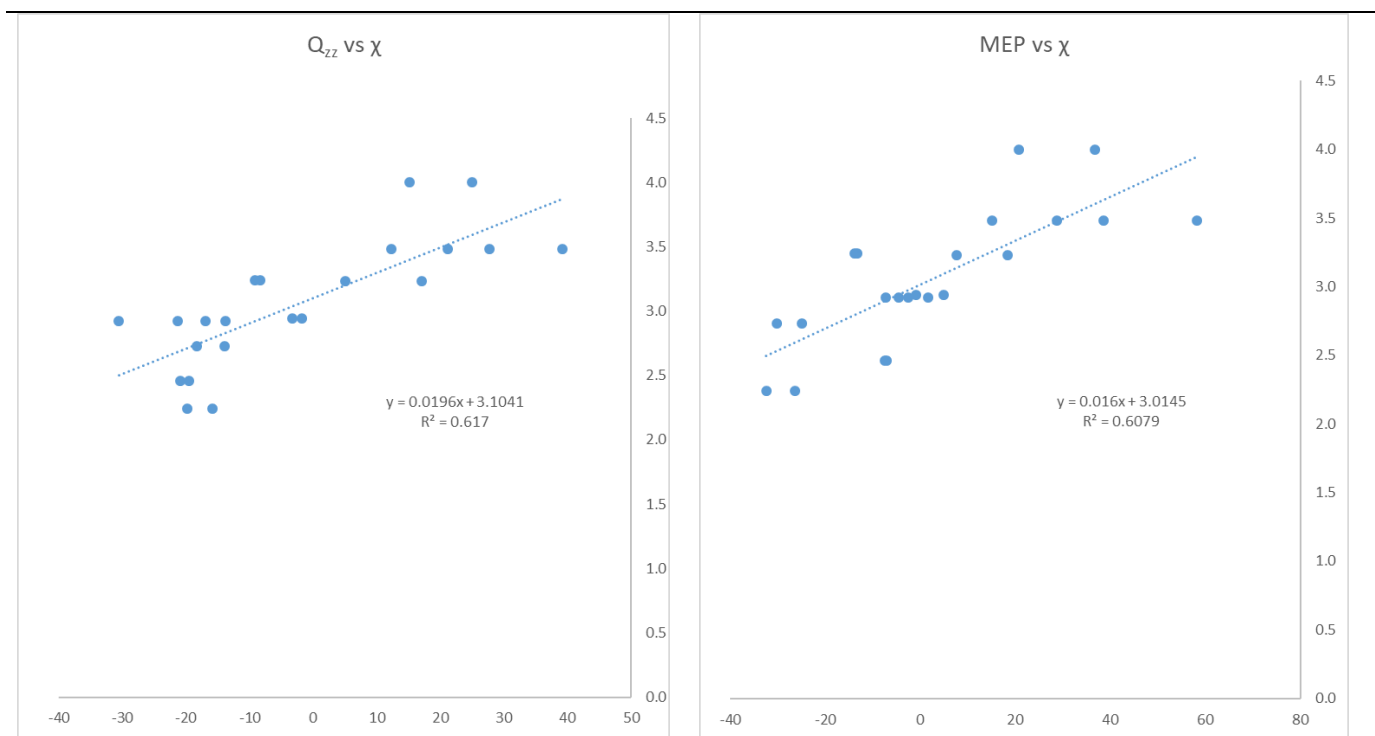
Figure 7. Correlation between the electronegativity of the substituted chemical groups vs Q_{zz} and MEP respectively.

Compound	Q_{zz}	MEP
1	−19.7 (−13.2)	−6.5 (−20.4)
2	−16.2 (−12.5)	−5.2 (−7.2)
3	−23.4 (−15.7)	−6.0 (−4.5)
4	+17.2 (+20.0)	+5.6 (+23.8)

Table 4. Experimental Q_{zz} (B) and MEP values (kcal·mol^{-1}) along the main symmetry axis at the van der Waals surface for compounds 1–4. Theoretical values using the MP2/aug-cc-pVTZ level are given in parenthesis**.**

The experimentally and theoretically calculated MEP surfaces are shown in Figure 8. We plotted the MEP values onto the van der Waals surface (iso-surface with electron density 0.001 a.u.). We found a good agreement between experimentally and theoretically

128

calculated values. The highest positive potential is located at the terminal hydrogen atom of the Csp–H bonds and the highest negative potential over the C≡C triple bonds.
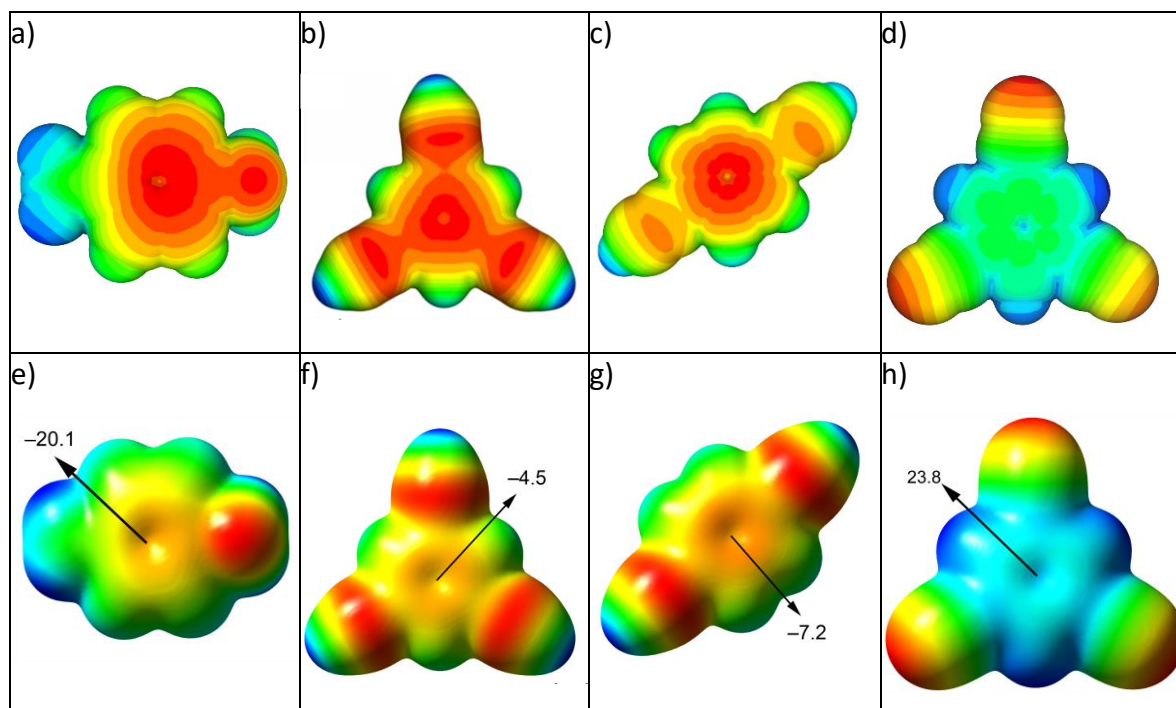
Figure 8. Experimental (top) and theoretical (bottom) MEP surfaces of substituted benzenes. The MEP values at selected points are indicated.

The analysis of the experimental results confirms the initial hypothesis, that is, the ethylnyl substituted phenyl rings have a paradoxical behavior regarding the correlation between MEP and Q_{zz} values.

The similarities encountered between compounds **3** and **4** gave us an excellent opportunity to gain further insight in the analysis of their CDD using multipolar refinements. In spite of the geometry distortion observed for the phenyl ring of **4**, we did not detect substantial differences in the electron density deformations of the two compounds. We paid special attention to the multipolar parameters perpendicular to the plane containing the phenyl ring. In particular, the p_{20} projection has almost identical deformations in **3** and **4**, tables S3 and S4.

4. Influence of substituents bearing terminal hydrogen atoms

a)

b)
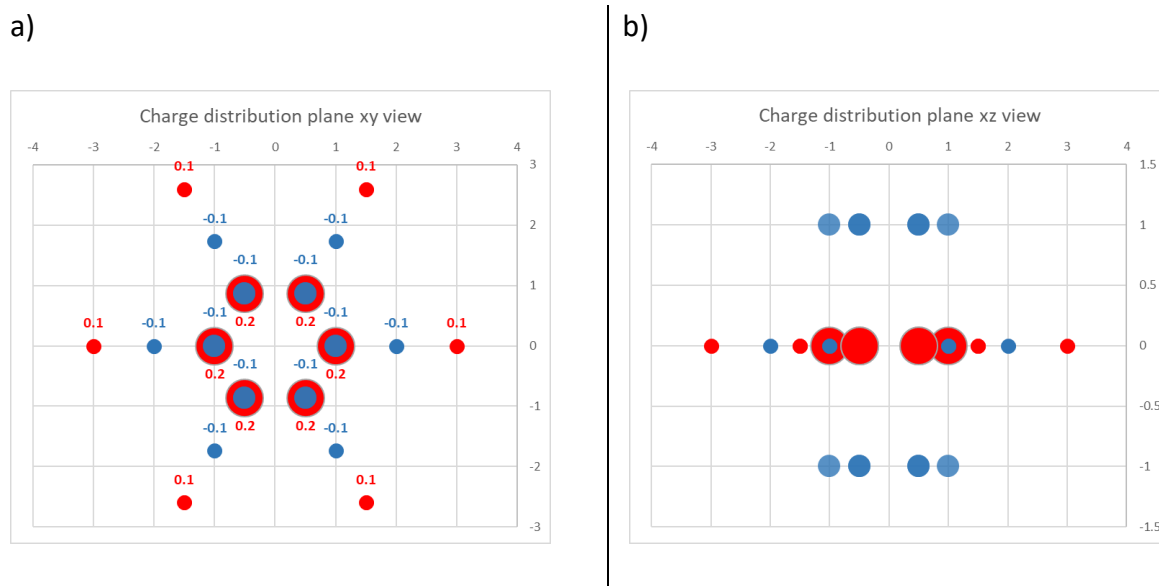
Figure 9. Charge distribution model of point charges. a) Charge distribution along the xy plane. b) Charge distribution along xz plane. Red point represents a positive charge; blue point represents a negative charge.

After having analyzed the charge density models, the electronegativity of the substituents and the geometry of the phenyl rings, we undertook a study of the in plane dissimilarities between cyano and ethynyl substituted phenyl rings. The ethynyl and cyano groups have clear differences with respect to charge distribution. The positive charge distribution at the end of the ethylnyl group is shared by the terminal carbon and hydrogen atoms, while the cyano group presents an electron rich distribution at its end, the nitrogen lone pair. The effect of this charge distribution difference was tested using a simple point charge model. Assuming that the sp^2 carbon atoms of the phenyl ring are contained on a plane, their electron clouds are responsible of the net negative quadruple moment, Q_{zz}. For example, six hexagonally distributed positive charges (+0.2) on the plane xy, with also twelve hexagonally distributed negative charges distributed (-0.1) on top and below the plane atoms, Fig. 9, results in a negative quadrupole component perpendicular to the plane xz, Q_{zz}=-2.4. The quadrupole moment of the system at the center of the ring would be notably increased, Q_{zz} = -5.4, if the dipoles were positioned at the edge of the ring, forming concentrically regular hexagons, Fig. 9 and Table S5. The dipole moments of the terminal hydrogens of the ethylnyl groups can play a similar role, making Q_{zz} significantly

more negative. This hypothesis is supported by the fact that other carbon substituted phenyl rings, in which the substituents feature terminal hydrogen atoms, experience a similar behavior. In addition, the increase of the number of ethynyl substituents shows a linear regression with respect to the Q_{zz} value. In contrast, the changes in Q_{zz} values that are assigned to an increase of substituents of the phenyl rings having a negative charge distribution at their ends, i.e. lone pairs, show a positive linear correlation with the MEP values. In any case, the strong influence exerted by substituents featuring an electron positive distribution at their ends on the corresponding Q_{zz} values of the six-membered aromatic system advise against its use in the analysis of ion-π interactions.

5. Conclusion.

In conclusion, we have provided both experimental and theoretical evidence of the paradoxical behavior of ethynyl group as phenyl substituent, since the Q_{zz} becomes more negative and the MEP value more positive as the number of CCH substituent increases. Thus, the EW nature of the CCH group agrees with the MEP value over the center of the ring and disagrees with the Q_{zz} value. Moreover, we have shown that other substituents present a similar behavior. An in-depth analysis of charge density distribution using high-resolution X-ray diffraction data does not serve to reveal the origin of the different trends followed by the Q_{zz} and MEP values of the phenyl-substituted rings. We also show that in these cases the quadrupole moment is not suitable to explain the nature of electrostatic interaction in both cation and anion–π complexes. All substituted phenyl rings displaying a behavior of their quadrupole moments similar to the one observed for the ethynyl substituted phenyl rings feature terminal hydrogen atoms in the substituents. This finding led us to consider the effect of the terminal hydrogen atoms, that is, the presence of a positive charge distribution at the end of the substituent, as the origin of the observed trend. The results obtained with a simple model of point charge distributions supports this hypothesis. Further investigation is needed to provide a more rigorous physical

explanation for the opposed trends observed in MEP and Q_{zz} values in certain phenyl substituted aromatic rings. In any case, our results indicate that the use of Q_{zz} values to analyzed and predict ion–π interaction is not recommended.

6. References

(1)   Schneider, H.-J. *Angewandte Chemie International Edition* **2009**, *48*, 3924.

(2)   Schneider, H.-J. Y., Anatoly *Principles and methods in supramolecular chemistry*; Wiley: Chichester, 2000.

(3)   Meyer, E. A.; Castellano, R. K.; Diederich, F. *Angewandte Chemie International Edition* **2003**, *42*, 1210.

(4)   SCRUTTON, N. S.; RAINE, A. R. C. *Biochem. J.* **1996**, *319*, 1.

(5)   Ma, J. C.; Dougherty, D. A. *Chem. Rev. (Washington, DC, U. S.)* **1997**, *97*, 1303.

(6)   Zacharias, N.; Dougherty, D. A. *Trends Pharmacol. Sci.* **2002**, *23*, 281.

(7)   Hay, B. P.; Bryantsev, V. S. *Chem. Commun.* **2008**, 2417.

(8)   Schottel, B. L.; Chifotides, H. T.; Dunbar, K. R. *Chem. Soc. Rev.* **2008**, *37*, 68.

(9)   Frontera, A.; Gamez, P.; Mascal, M.; Mooibroek, T. J.; Reedijk, J. *Angewandte Chemie International Edition* **2011**, *50*, 9564.

(10)   Frontera, A.; Quiñonero, D.; Deyà, P. M. *Wiley Interdisciplinary Reviews: Computational Molecular Science* **2011**, *1*, 440.

(11)   Giese, M.; Albrecht, M.; Rissanen, K. *Chem. Rev. (Washington, DC, U. S.)* **2015**, *115*, 8867.

(12)   Bauza, A.; Mooibroek, T. J.; Frontera, A. *CrystEngComm* **2016**, *18*, 10.

(13)   Garau, C.; Frontera, A.; Quiñonero, D.; Ballester, P.; Costa, A.; Deyà, P. M. *ChemPhysChem* **2003**, *4*, 1344.

(14)   Kim, D.; Tarakeshwar, P.; Kim, K. S. *The Journal of Physical Chemistry A* **2004**, *108*, 1250.

(15)   Kim, D. Y.; Singh, N. J.; Lee, J. W.; Kim, K. S. *J. Chem. Theory Comput.* **2008**, *4*, 1162.

(16)   Bauza, A.; Deya, P. M.; Frontera, A.; Quinonero, D. *Phys. Chem. Chem. Phys.* **2014**, *16*, 1322.

(17)   Bauzá, A.; Quiñonero, D.; Deyà, P. M.; Frontera, A. *Chemical Physics Letters* **2013**, *567*, 60.

(18)   Landgrebe, J. A.; Rynbrandt, R. H. *The Journal of Organic Chemistry* **1966**, *31*, 2585.

(19)   Eaborn, C.; Thompson, A. R.; Walton, D. R. M. *Journal of the Chemical Society B: Physical Organic* **1969**, 859.

(20)   Choy, N.; Russell, K. C.; Alvarez, J. C.; Fider, A. *Tetrahedron Lett.* **2000**, *41*, 1515.

(21)   Hammershøj, P.; Reenberg, T. K.; Pittelkow, M.; Nielsen, C. B.; Hammerich, O.; Christensen, J. B. *Eur. J. Org. Chem.* **2006**, *2006*, 2786.

(22)   Spackman, M. A. *Chemical Reviews (Washington, DC, United States)* **1992**, *92*, 1769.

(23)   Spackman, M. A.; Byrom, P. G. *Acta Crystallographica Section B-Structural Science* **1996**, *52*, 1023.

(24)   Koritsanszky, T. S.; Coppens, P. *Chemical Reviews* **2001**, *101*, 1583.

(25)   Stalke, D. *Acta Crystallographica Section B-Structural Science Crystal Engineering and Materials* **2014**, *70*, 781.

(26)   Allé, P.; Wenger, E.; Dahaoui, S.; Schaniel, D.; Lecomte, C. *Phys. Scr.* **2016**, *91*, 063001.

(27)   Wenger, E.; Dahaoui, S.; Alle, P.; Parois, P.; Palin, C.; Lecomte, C.; Schaniel, D. *Acta Crystallographica Section B* **2014**, *70*, 783.

(28)   Rigaku 2015.

(29)   Sheldrick, G. M. **2014**.

(30)   Burla, M. C.; Caliandro, R.; Carrozzini, B.; Cascarano, G. L.; Cuocci, C.; Giacovazzo, C.; Mallamo, M.; Mazzone, A.; Polidori, G. *Journal of Applied Crystallography* **2015**, *48*, 306.

(31)   Sheldrick, G. M. *Acta Crystallographica a-Foundation and Advances* **2015**, *71*, 3.

(32)   Hubschle, C. B.; Sheldrick, G. M.; Dittrich, B. *Journal of Applied Crystallography* **2011**, *44*, 1281.

(33)   Zarychta, B.; Pichon-Pesme, V.; Guillot, B.; Lecomte, C.; Jelsch, C. *Acta Crystallographica Section A* **2007**, *63*, 108.

(34)   Paul, A.; Kubicki, M.; Jelsch, C.; Durand, P.; Lecomte, C. *Acta Crystallographica Section B* **2011**, *67*, 365.

(35)   Brünger, A. T. *Nature* **1992**, *355*, 472.

(36)   Madsen, A. O. *J. Appl. Cryst.* **2006**, *39*, 757.

(37)   Meindl, K.; Henn, J. *Acta Crystallographica Section A* **2008**, *64*, 404.

(38)   Parsons, S.; Wagner, T.; Presly, O.; Wood, P. A.; Cooper, R. I. *J. Appl. Cryst.* **2012**, *45*, 417.

(39)   Campanelli, A. R.; Domenicano, A.; Ramondo, F.; Hargittai, I. *The Journal of Physical Chemistry A* **2004**, *108*, 4940.

6. Supporting information

ATOM	AXES	Ax	Ay	Az	KP1	KP2	Pval 0	Plms	Px(P11)	Py(P1-1)	Pz(P10)	2 0	2 1	2 -1	2 2	2 -2	3 0	3 1	3 -1	3 2	3 -2	3 3	3 -3
C1A	bXY	C2A	C6A		0.9856 (14)	0.931 (7)	4.021 (11)		**0.075 (3)**	-0.002 (3)	-0.012 (3)	**-0.181 (4)**	0.002 (3)	-0.004 (3)	**-0.047 (3)**	0.001 (3)	-0.004 (3)	**0.028 (3)**	0.001 (3)	0.001 (3)	0.005 (3)	**-0.301 (6)**	0.002 (3)
C2A	bXY	C1A	C3A		0.9831 (12)	0.975 (6)	4.174 (8)		-0.004 (3)	0.004 (3)	0.004 (2)	**-0.167 (3)**	0.002 (2)	-0.005 (2)	-0.009 (3)	0.006 (2)	0.003 (3)	**0.023 (3)**	0.001 (2)	-0.001 (3)	0.000 (2)	**-0.244 (4)**	-0.002 (2)
C3A	bXY	C4A	C2A		0.9833 (13)	0.971 (7)	4.181 (9)		-0.011 (3)	-0.001 (3)	0.000 (3)	**-0.169 (3)**	-0.003 (3)	0.002 (3)	-0.001 (3)	0.002 (3)	0.007 (3)	**0.022 (3)**	0.005 (3)	-0.005 (3)	0.002 (3)	**-0.243 (4)**	-0.001 (3)
C4A	bXY	C3A	C5A		0.9872 (14)	0.935 (7)	4.029 (11)		**0.071 (3)**	-0.001 (3)	-0.011 (3)	**-0.180 (4)**	0.005 (3)	0.003 (3)	**-0.047 (3)**	-0.005 (3)	-0.006 (3)	**0.037 (3)**	-0.001 (3)	0.001 (3)	-0.002 (3)	**-0.305 (6)**	0.007 (3)
C5A	bXY	C4A	C6A		0.9821 (13)	0.971 (7)	4.175 (9)		-0.005 (3)	0.000 (3)	0.001 (3)	**-0.166 (3)**	-0.006 (2)	0.001 (2)	-0.007 (3)	0.003 (2)	0.004 (3)	**0.022 (3)**	-0.004 (3)	-0.001 (3)	0.003 (3)	**-0.247 (4)**	-0.003 (3)
C6A	bXY	C1A	C5A		0.9834 (13)	0.977 (7)	4.174 (9)		-0.008 (3)	0.006 (3)	-0.001 (3)	**-0.164 (3)**	0.001 (2)	-0.002 (3)	-0.003 (3)	0.009 (3)	-0.003 (3)	**0.022 (3)**	0.000 (3)	0.010 (3)	-0.006 (3)	**-0.245 (4)**	0.000 (3)
C1B	bXY	C2B	C3B		0.9889 (14)	0.928 (7)	4.026 (11)		**0.070 (3)**	0.002 (3)	-0.001 (3)	**-0.192 (4)**	-0.012 (3)	-0.004 (3)	**-0.043 (3)**	0.005 (3)	0.005 (3)	**0.039 (3)**	0.003 (3)	0.001 (3)	0.002 (3)	**-0.302 (6)**	-0.003 (3)
C2B	bXY	C1B	C3B_SYM-		0.9834 (13)	0.980 (7)	4.173 (9)		-0.003 (3)	0.002 (3)	-0.003 (3)	**-0.171 (3)**	0.002 (3)	0.003 (3)	-0.003 (3)	0.010 (3)	-0.005 (3)	**0.017 (3)**	0.002 (3)	0.006 (3)	0.005 (3)	**-0.251 (4)**	-0.009 (3)
C3B	bXY	C1B	C2B_SYM-		0.9832 (13)	0.979 (7)	4.178 (9)		-0.008 (3)	0.003 (3)	-0.010 (3)	**-0.179 (3)**	0.003 (3)	-0.005 (3)	-0.004 (3)	0.008 (3)	0.006 (3)	**0.024 (3)**	0.001 (3)	-0.006 (3)	0.003 (3)	**-0.247 (5)**	-0.006 (3)
C1C	bXY	C2C	C3C_SYM-		0.9870 (14)	0.954 (7)	4.025 (11)		**0.071 (3)**	0.016 (3)	0.010 (3)	**-0.189 (4)**	-0.009 (3)	0.000 (3)	**-0.038 (3)**	0.005 (3)	0.000 (3)	**0.029 (3)**	-0.005 (3)	-0.008 (3)	-0.002 (3)	**-0.300 (4)**	0.012 (3)
C2C	bXY	C1C	C3C		0.9812 (13)	0.994 (7)	4.171 (9)		0.001 (3)	-0.003 (3)	0.005 (3)	**-0.171 (3)**	0.005 (3)	-0.002 (3)	-0.003 (3)	0.011 (3)	0.000 (3)	**0.028 (3)**	0.001 (3)	-0.001 (3)	-0.005 (3)	**-0.242 (4)**	-0.001 (3)
C3C	bXY	C1C_SYMC2C	-		0.9828 (13)	0.974 (8)	4.183 (9)		-0.010 (3)	0.015 (3)	-0.004 (3)	**-0.169 (3)**	0.000 (3)	0.008 (3)	-0.006 (3)	0.004 (3)	0.001 (3)	**0.029 (2)**	-0.002 (3)	-0.001 (3)	0.001 (3)	**-0.238 (4)**	-0.001 (3)
N1A	ZX	C1A	H2NA		0.9748 (8)	0.993 (9)	5.355 (10)		0.001 (2)	**-0.030 (2)**	-0.054 (3)	**-0.038 (2)**	0.002 (2)	0.004 (2)	-0.015 (2)	0.012 (2)	**0.151 (3)**	-0.006 (2)	-0.004 (2)	-0.038 (2)	0.038 (2)	**0.064 (2)**	-0.007 (2)
N2A	ZX	C4A	H4NA		0.9734 (8)	0.997 (9)	5.354 (10)		0.000 (2)	**0.029 (2)**	-0.054 (3)	**-0.043 (2)**	0.002 (2)	-0.003 (2)	-0.006 (2)	-0.010 (2)	**0.145 (3)**	-0.011 (2)	0.005 (2)	-0.038 (2)	-0.041 (2)	**0.060 (2)**	0.008 (2)
N1B	ZX	C1B	H1NB		0.9744 (8)	0.978 (9)	5.364 (10)		**-0.023 (3)**	-0.019 (3)	-0.063 (3)	**-0.023 (2)**	0.004 (2)	-0.003 (2)	-0.016 (2)	0.008 (2)	**0.150 (3)**	-0.002 (3)	-0.008 (2)	-0.043 (2)	0.045 (2)	**0.054 (3)**	-0.007 (2)
N1C	ZX	C1C	H2NC		0.9734 (9)	0.946 (10)	5.368 (10)		**-0.025 (3)**	0.008 (3)	-0.062 (3)	**-0.022 (3)**	0.001 (3)	0.003 (3)	-0.002 (3)	-0.019 (3)	**0.150 (3)**	-0.005 (3)	0.003 (3)	-0.036 (3)	-0.033 (3)	**0.041 (3)**	0.014 (3)
H2A	ZX	C2A	C1A		1.185 (5)	1.68 (3)	0.865 (6)		**0.073 (3)**															
H3A	ZX	C3A	C4A		1.189 (5)	1.68 (3)	0.868 (7)		**0.075 (3)**															
H5A	ZX	C5A	C4A		1.190 (6)	1.68 (3)	0.867 (7)		**0.071 (3)**															
H6A	ZX	C6A	C1A		1.185 (5)	1.69 (3)	0.870 (7)		**0.072 (3)**															
H2B	ZX	C2B	C1B		1.164 (5)	1.68 (3)	0.871 (7)		**0.069 (3)**															
H3B	ZX	C3B	C1B		1.165 (6)	1.68 (3)	0.867 (8)		**0.071 (3)**															
H2C	ZX	C2C	C1C		1.167 (5)	1.68 (3)	0.866 (7)		**0.074 (3)**															
H3C	ZX	C3C	C2C		1.159 (6)	1.67 (3)	0.869 (8)		**0.069 (3)**															
H1NA	ZX	N1A	C1A		1.208 (6)	1.81 (2)	0.763 (6)		**0.075 (2)**															
H2NA	ZX	N1A	C1A		1.204 (6)	1.81 (2)	0.759 (6)		**0.069 (3)**															
H3NA	ZX	N2A	C4A		1.212 (6)	1.81 (2)	0.766 (6)		**0.076 (3)**															
H4NA	ZX	N2A	C4A		1.204 (6)	1.81 (2)	0.759 (6)		**0.072 (3)**															
H1NB	ZX	N1B	C1B		1.178 (6)	1.80 (2)	0.763 (6)		**0.07 (3)**															
H2NB	ZX	N1B	C1B		1.195 (6)	1.80 (2)	0.764 (6)		**0.075 (3)**															
H1NC	ZX	N1C	C1C		1.167 (6)	1.80 (2)	0.762 (6)		**0.069 (2)**															
H2NC	ZX	N1C	C1C		1.187 (7)	1.81 (3)	0.769 (8)		**0.074 (3)**															

TS 1. Multipolar parameters of belonging to the crystals structure of compound 1.

ATOM	AXES	Ax	Ay	Az	KP1	KP2	Pval	Plms Px(P11)	Py(P1-1)	Pz(P10)	2 0	2 1	2 -1	2 2	2 -2	3 0	3 1	3 -1	3 2	3 -2	3 3	3 -3
C1	ZX	C2	C4		1.0075 (18)	0.981 (12)	4.11 (3)	0.003 (2)	0.007 (3)	**0.071 (5)**	**0.259 (8)**	0.03 (2)	-0.009 (2)	-0.01 (2)	0.021 (2)	**-0.047 (3)**	0.009 (3)	0.004 (3)	0.012 (2)	0.001 (2)	0.003 (2)	-0.007 (2)
C2	ZX	C1	C4		1.0058 (16)	0.912 (9)	4.09 (2)	0.001 (2)	0.001 (2)	**0.121 (7)**	**0.304 (7)**	-0.032 (3)	-0.008 (2)	-0.009 (2)	-0.023 (2)	**-0.066 (4)**	0.005 (3)	-0.003 (3)	0.002 (3)	-0.001 (3)	0.001 (2)	0.002 (2)
C3	bXY	C4	C2		1.0009 (15)	0.972 (7)	4.037 (17)	**-0.030 (3)**	**-0.049 (3)**	-0.006 (2)	**-0.160 (3)**	0.023 (2)	0.000 (2)	-0.002 (2)	**-0.043 (2)**	-0.004 (2)	-0.007 (2)	-0.020 (2)	0.004 (2)	-0.005 (2)	**-0.271 (6)**	0.003 (2)
C4	bXY	C3	C5		0.9992 (12)	0.977 (6)	4.123 (12)	0.007 (3)	0.013 (3)	0.007 (2)	**-0.179 (3)**	-0.025 (2)	0.000 (2)	**-0.036 (3)**	-0.002 (2)	-0.001 (2)	0.014 (2)	0.006 (2)	0.002 (2)	0.005 (2)	**-0.239 (4)**	-0.003 (2)
C5	bXY	C4	H5		1.0001 (12)	0.967 (6)	4.124 (12)	0.013 (3)	0.000 (3)	0.004 (2)	**-0.173 (3)**	-0.025 (2)	-0.005 (2)	-0.027 (2)	-0.002 (2)	-0.001 (2)	0.001 (2)	-0.015 (2)	-0.006 (2)	-0.004 (2)	**-0.241 (4)**	-0.006 (3)
H1	ZX	C1	C4		1.188 (10)	1.64 (4)	0.822 (15)			**0.077 (4)**												
H4	ZX	C4	C3		1.275 (16)	1.74 (4)	0.842 (11)			**0.101 (4)**												
H5	ZX	C5	C4		1.267 (15)	1.74 (4)	0.852 (11)			**0.087 (4)**												

TS 2 Multipolar parameters of belonging to the crystals structure of compound 2.

ATOM	AXES	Ax	Ay	Az	KP1	KP2	Pval	Plms Px(P11)	Py(P1-1)	Pz(P10)	2 0	2 1	2 -1	2 2	2 -2	3 0	3 1	3 -1	3 2	3 -2	3 3	3 -3
C1	XY	C7	C2		0.997 (14)	0.986 (8)	3.981 (15)	**-0.032 (3)**	0.001 (3)	-0.009 (2)	**-0.167 (3)**	0.008 (2)	0.004 (2)	-0.026 (3)	0.004 (2)	0.001 (3)	**-0.024 (3)**	0.004 (2)	0.001 (3)	0.003 (3)	**0.250 (5)**	0.004 (3)
C2	bXY	C3	C1		0.989 (14)	0.944 (8)	4.186 (15)	**-0.017 (3)**	0.004 (3)	-0.004 (2)	**-0.211 (3)**	-0.004 (2)	0.008 (2)	0.007 (3)	0.010 (2)	0.002 (3)	**0.030 (2)**	0.001 (2)	-0.005 (3)	-0.001 (2)	**-0.270 (5)**	-0.001 (3)
C3	XY	C9	C2		0.997 (14)	0.985 (7)	3.986 (17)	**-0.035 (3)**	0.007 (3)	0.005 (3)	**-0.167 (4)**	0.005 (2)	-0.010 (2)	-0.012 (3)	0.005 (3)	0.001 (3)	**-0.025 (3)**	0.002 (3)	-0.001 (3)	0.004 (3)	**0.250 (5)**	-0.007 (3)
C4	bXY	C3	C5		0.989 (13)	0.948 (9)	4.178 (15)	**-0.015 (3)**	-0.002 (3)	0.000 (5)	**-0.212 (5)**	-0.015 (3)	0.000 (3)	-0.002 (3)	0.002 (2)	-0.006 (3)	**0.028 (3)**	0.000 (3)	0.005 (3)	0.001 (3)	**-0.278 (2)**	0.001 (2)
C5	XY	C11	C6		0.996 (14)	0.985 (18)	3.979 (18)	**-0.037 (3)**	0.001 (3)	-0.005 (5)	**-0.170 (5)**	-0.005 (3)	0.007 (3)	-0.012 (3)	0.005 (2)	0.003 (3)	**-0.023 (3)**	0.000 (3)	0.001 (3)	-0.005 (3)	**0.251 (3)**	-0.006 (3)
C6	bXY	C5	C1		0.988 (13)	0.949 (9)	4.18 (15)	**-0.024 (3)**	0.003 (3)	0.009 (5)	**-0.207 (6)**	-0.002 (3)	-0.005 (3)	0.009 (2)	0.007 (2)	-0.001 (3)	**0.030 (3)**	0.000 (3)	0.007 (3)	-0.001 (3)	**-0.272 (2)**	0.000 (2)
C7	ZX	C8	C6		1.004 (14)	0.975 (18)	4.133 (18)	0.000 (3)	0.010 (3)	**0.136 (5)**	**0.284 (5)**	-0.008 (3)	-0.011 (3)	0.000 (3)	-0.004 (2)	**-0.054 (3)**	-0.006 (3)	-0.002 (3)	0.006 (2)	0.000 (3)	0.009 (2)	0.003 (2)
C8	ZX	C7	C2		1.006 (13)	1.020 (9)	4.039 (15)	-0.002 (3)	0.000 (3)	**0.091 (5)**	**0.243 (5)**	-0.008 (3)	0.018 (2)	-0.001 (2)	0.001 (2)	**-0.068 (3)**	0.01 (3)	-0.01 (3)	0.004 (3)	-0.004 (3)	-0.016 (2)	0.007 (2)
C9	ZX	C10	C4		1.004 (15)	0.979 (14)	4.139 (18)	0.005 (3)	-0.011 (3)	**0.130 (5)**	**0.300 (5)**	-0.011 (3)	-0.012 (3)	0.002 (2)	-0.009 (2)	**-0.046 (3)**	0.002 (3)	-0.001 (3)	0.009 (2)	-0.007 (2)	0.003 (2)	0.005 (3)
C10	ZX	C9	C4		1.009 (13)	1.035 (7)	4.046 (17)	0.003 (3)	0.013 (3)	**0.097 (3)**	**0.257 (4)**	0.009 (3)	-0.007 (3)	-0.002 (3)	0.006 (3)	**-0.051 (3)**	-0.004 (3)	0.002 (3)	-0.001 (3)	-0.006 (3)	0.006 (5)	-0.005 (3)
C11	ZX	C12	C4		1.004 (14)	0.992 (8)	4.136 (15)	0.006 (3)	0.010 (3)	**0.138 (2)**	**0.289 (3)**	-0.017 (2)	0.007 (2)	0.005 (3)	0.006 (3)	**-0.053 (3)**	0.013 (2)	0.001 (2)	0.006 (2)	-0.001 (3)	0.004 (6)	0.003 (3)
C12	ZX	C11	C4		1.008 (14)	1.019 (7)	4.042 (17)	0.002 (4)	-0.003 (3)	**0.087 (3)**	**0.254 (4)**	0.004 (2)	0.004 (2)	0.000 (3)	-0.008 (3)	**-0.065 (3)**	0.014 (3)	0.004 (3)	-0.003 (3)	0.002 (3)	0.005 (5)	-0.002 (3)
H2	ZX	C2	C3		1.235 (7)	1.321 (14)	0.787 (9)			**0.094 (3)**												
H4	ZX	C4	C3		1.236 (7)	1.333 (14)	0.784 (10)			**0.092 (4)**												
H6	ZX	C6	C5		1.233 (7)	1.326 (14)	0.789 (10)			**0.091 (4)**												
H8	ZX	C8	C2		1.115 (7)	1.195 (14)	0.872 (10)			**0.130 (4)**												
H10	ZX	C10	C2		1.133 (7)	1.198 (14)	0.876 (9)			**0.129 (4)**												
H12	ZX	C12	C4		1.135 (7)	1.201 (14)	0.867 (9)			**0.122 (3)**												

TS 3. Multipolar parameters belonging to the crystal structure of compound **3**.

ATOM	AXES	Ax	Ay	Az	KP1	KP2	Pval	Plms Px(P11)	Py(P1-1)	Pz(P10)	2 0	2 1	2 -1	2 2	2 -2	3 0	3 1	3 -1	3 2	3 -2	3 3	3 -3
C1A_1	XY	C7A	C6A	-	1.0137 (17)	0.954 (8)	4.04 (2)	**-0.074 (4)**	0.005 (3)	0.003 (3)	**-0.161 (4)**	-0.014 (3)	-0.002 (3)	**-0.049 (4)**	0.005 (3)	0.004 (3)	**-0.023 (4)**	0.003 (3)	0.001 (4)	0.002 (3)	**0.287 (7)**	0.001 (4)
C2A_1	bXY	C3A	C1A	-	1.0114 (17)	0.962 (9)	4.05 (2)	**-0.040 (4)**	0.006 (3)	-0.003 (3)	**-0.223 (5)**	0.000 (3)	0.006 (3)	0.016 (4)	0.008 (3)	0.006 (4)	**0.026 (4)**	0.005 (3)	0.005 (3)	0.007 (3)	**-0.252 (7)**	0.005 (4)
C3A_1	XY	C8A	C4A	-	1.0140 (17)	0.962 (8)	4.03 (2)	**-0.072 (4)**	-0.005 (3)	0.006 (3)	**-0.162 (4)**	-0.008 (3)	-0.019 (3)	**-0.046 (3)**	0.001 (3)	0.004 (3)	**-0.026 (3)**	0.001 (3)	-0.001 (3)	0.003 (3)	**0.289 (7)**	-0.004 (3)
C4A_1	bXY	C5A	C3A	-	1.0153 (17)	0.964 (8)	4.04 (2)	**-0.042 (4)**	0.002 (3)	0.006 (3)	**-0.237 (5)**	0.003 (3)	0.011 (3)	0.015 (4)	-0.002 (3)	-0.004 (3)	**0.029 (4)**	0.001 (3)	-0.002 (3)	0.002 (3)	**-0.258 (7)**	0.004 (3)
C5A_1	XY	C9A	C4A	-	1.0126 (17)	0.954 (8)	4.04 (2)	**-0.080 (4)**	-0.007 (3)	0.002 (3)	**-0.173 (4)**	0.007 (3)	0.008 (3)	**-0.046 (3)**	-0.002 (3)	0.003 (3)	**-0.031 (3)**	0.003 (3)	0.000 (3)	0.003 (3)	**0.283 (7)**	-0.005 (3)
C6A_1	bXY	C1A	C5A	-	1.0151 (17)	0.968 (8)	4.05 (2)	**-0.036 (4)**	-0.010 (3)	-0.010 (3)	**-0.228 (5)**	-0.003 (3)	-0.010 (3)	0.016 (3)	0.001 (3)	0.006 (3)	**0.029 (3)**	0.000 (3)	-0.008 (3)	-0.002 (3)	**-0.253 (6)**	0.003 (3)
C7A_1	ZX	N1A	C6A	-	1.0219 (16)	0.907 (8)	4.130 (15)	0.012 (3)	0.002 (3)	**0.183 (6)**	**0.389 (8)**	-0.002 (3)	-0.019 (3)	0.010 (3)	0.003 (3)	**-0.038 (5)**	-0.008 (4)	0.001 (4)	-0.005 (4)	0.002 (4)	-0.002 (3)	0.005 (3)
C8A_1	ZX	N2A	C4A	-	1.0192 (16)	0.929 (8)	4.127 (15)	0.002 (3)	0.001 (3)	**0.182 (6)**	**0.370 (7)**	-0.003 (3)	-0.007 (3)	0.001 (3)	-0.006 (3)	**-0.041 (5)**	0.004 (4)	0.000 (4)	0.004 (4)	-0.010 (4)	0.002 (3)	0.004 (3)
C9A_1	ZX	N3A	C4A	-	1.0247 (16)	0.927 (8)	4.127 (15)	0.001 (3)	-0.003 (3)	**0.182 (6)**	**0.378 (7)**	-0.001 (3)	0.005 (3)	0.008 (3)	0.007 (3)	**-0.042 (5)**	-0.003 (4)	-0.005 (4)	0.003 (4)	0.004 (4)	0.004 (3)	0.002 (3)
N1A_1	ZX	C7A	C6A	-	1.0025 (12)	1.023 (11)	5.023 (15)	0.008 (3)	-0.002 (4)	**-0.042 (4)**	**0.204 (4)**	-0.004 (3)	-0.016 (3)	-0.002 (3)	0.001 (3)	**0.046 (4)**	-0.004 (3)	-0.005 (3)	0.016 (3)	-0.004 (3)	0.007 (3)	-0.009 (3)
N2A_1	ZX	C8A	C4A	-	1.0041 (11)	1.032 (11)	5.016 (15)	-0.018 (3)	0.002 (3)	**-0.042 (4)**	**0.203 (3)**	0.009 (3)	-0.011 (3)	0.011 (3)	0.007 (3)	**0.048 (3)**	0.012 (3)	-0.001 (3)	0.020 (3)	-0.011 (3)	-0.002 (3)	-0.005 (3)
N3A_1	ZX	C9A	C6A	-	1.0020 (12)	1.056 (11)	5.017 (15)	-0.015 (3)	-0.017 (4)	**-0.052 (4)**	**0.193 (3)**	-0.002 (3)	-0.013 (3)	0.009 (3)	0.003 (3)	**0.046 (4)**	0.010 (3)	0.001 (3)	0.015 (3)	0.005 (3)	-0.001 (3)	0.002 (3)
H2A_1	ZX	C2A	C3A	-	1.189 (9)	1.62 (3)	0.824 (14)			**0.079 (4)**												
H4A_1	ZX	C4A	C5A	-	1.213 (9)	1.63 (3)	0.838 (14)			**0.077 (4)**												
H6A_1	ZX	C6A	C1A	-	1.218 (9)	1.63 (3)	0.806 (13)			**0.083 (4)**												
C1B_1	bXY	C6B	C2B	-	1.016 (2)	0.931 (11)	3.91 (3)	**0.161 (7)**	-0.005 (4)	0.000 (3)	**-0.134 (6)**	0.016 (3)	-0.009 (3)	**-0.157 (6)**	-0.006 (4)	-0.006 (4)	0.009 (4)	-0.005 (4)	-0.004 (4)	-0.011 (4)	**-0.282 (11)**	0.004 (4)
C2B_1	bXY	C1B	C3B	-	1.009 (2)	0.959 (10)	4.10 (3)	**-0.035 (5)**	0.022 (5)	-0.001 (3)	**-0.214 (6)**	0.002 (3)	-0.004 (3)	0.010 (4)	0.026 (4)	-0.008 (4)	0.021 (4)	0.009 (4)	0.006 (4)	0.000 (4)	**-0.266 (8)**	0.015 (4)
C3B_1	bXY	C2B	C4B	-	1.005 (2)	0.947 (10)	4.14 (3)	**-0.025 (5)**	0.008 (5)	-0.014 (4)	**-0.223 (6)**	0.008 (3)	0.016 (4)	0.001 (4)	0.010 (4)	0.004 (4)	0.012 (4)	-0.004 (4)	-0.002 (4)	0.015 (4)	**-0.268 (8)**	-0.008 (4)
C4B_1	bXY	C5B	C3B	-	1.007 (3)	0.972 (13)	4.11 (3)	**-0.038 (5)**	0.006 (4)	-0.008 (4)	**-0.225 (7)**	0.012 (3)	0.009 (4)	-0.001 (5)	-0.006 (4)	-0.009 (4)	**0.028 (4)**	-0.011 (4)	-0.006 (4)	0.005 (4)	**-0.268 (10)**	0.007 (5)
C5B_1	bXY	C6B	C4B	-	1.005 (2)	0.953 (10)	4.14 (3)	**-0.025 (5)**	0.010 (5)	-0.001 (3)	**-0.220 (6)**	0.010 (3)	0.009 (3)	-0.002 (4)	0.005 (3)	-0.003 (4)	**0.026 (4)**	-0.003 (4)	-0.008 (4)	0.009 (4)	**-0.264 (8)**	-0.003 (4)
C6B_1	bXY	C1B	C5B	-	1.009 (2)	0.956 (9)	4.10 (3)	**-0.031 (5)**	0.022 (5)	0.006 (3)	**-0.219 (6)**	-0.003 (3)	-0.013 (3)	0.014 (4)	0.030 (4)	-0.005 (4)	0.021 (4)	0.008 (4)	0.013 (4)	0.003 (4)	**-0.275 (8)**	0.000 (4)
N1B_1	bXY	O2B	O1B	-	0.9920 (15)	0.805 (7)	5.033 (18)	-0.013 (5)	0.009 (4)	0.018 (3)	**-0.255 (6)**	-0.002 (3)	0.007 (3)	**-0.029 (4)**	0.004 (4)	-0.009 (4)	0.019 (4)	-0.009 (4)	-0.001 (4)	0.002 (4)	**-0.400 (9)**	0.006 (4)
O1B_1	XY	N1B	O2B	-	0.9942 (9)	0.995 (12)	6.154 (13)	**-0.099 (4)**	0.001 (3)	-0.009 (3)	**-0.085 (3)**	-0.011 (3)	0.001 (3)	**-0.137 (3)**	0.001 (3)	0.004 (3)	**-0.025 (3)**	0.003 (3)	0.002 (3)	-0.004 (3)	**0.037 (3)**	0.005 (3)
O2B_1	XY	N1B	O1B	-	0.9972 (10)	0.969 (13)	6.138 (13)	**-0.075 (4)**	-0.002 (5)	-0.006 (3)	**-0.087 (4)**	-0.014 (3)	-0.008 (3)	**-0.132 (3)**	0.000 (3)	-0.001 (4)	**-0.030 (4)**	-0.009 (4)	0.002 (3)	-0.002 (3)	**0.039 (3)**	0.004 (3)
H2B_1	ZX	C2B	C1B	-	1.190 (11)	1.59 (5)	0.817 (17)			**0.079 (5)**												
H3B_1	ZX	C3B	C2B	-	1.189 (10)	1.62 (3)	0.786 (15)			**0.076 (4)**												
H4B_1	ZX	C4B	C5B	-	1.190 (10)	1.63 (3)	0.799 (16)			**0.078 (4)**												
H5B_1	ZX	C5B	C6B	-	1.189 (10)	1.62 (3)	0.815 (15)			**0.069 (4)**												
H6B_1	ZX	C6B	C1B	-	1.181 (11)	1.59 (5)	0.826 (17)			**0.082 (5)**												

TS 4. Multipolar parameters belonging to the crystal structure of compound **4**.
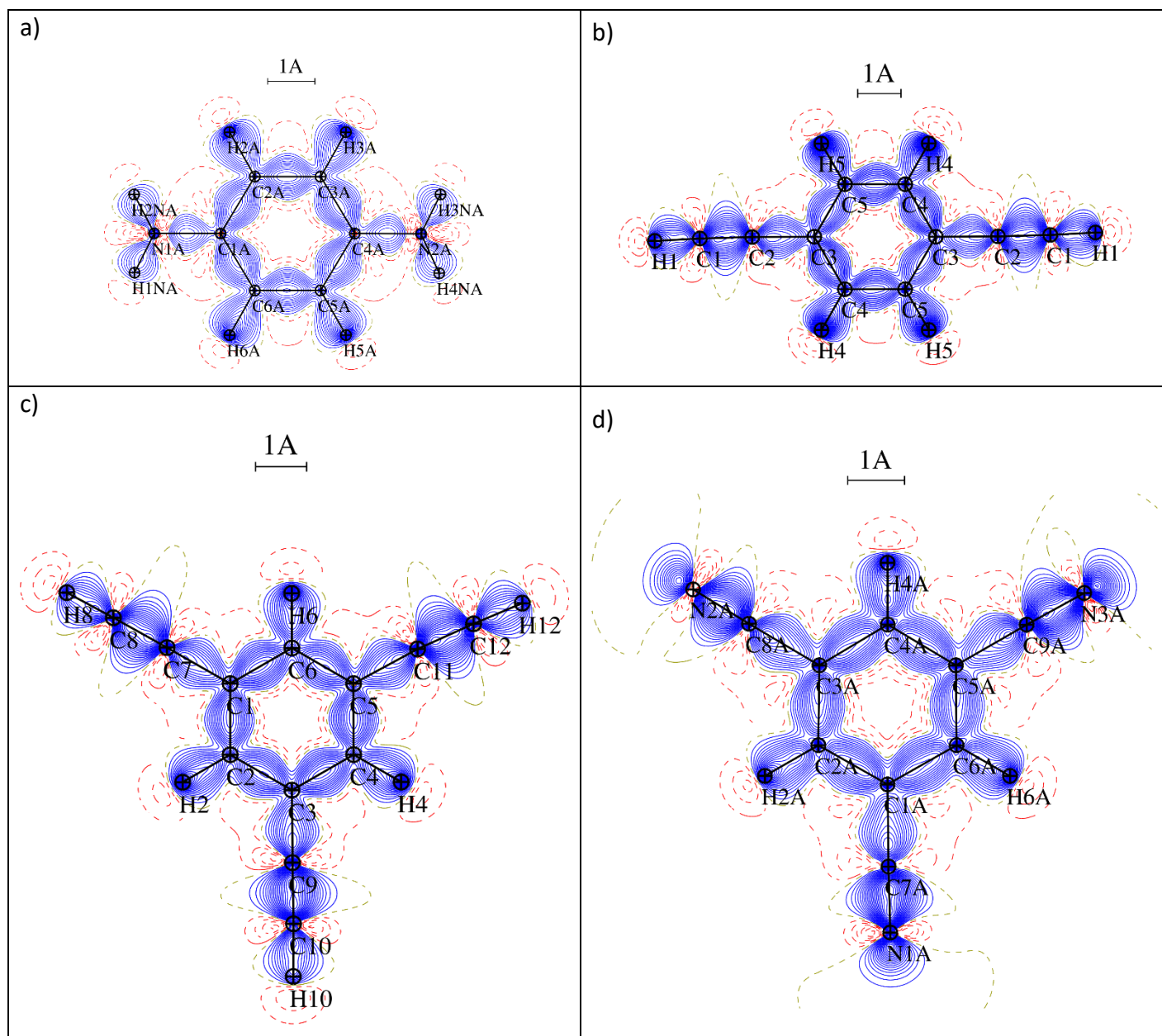
S 1. SED of compounds 1, a) 2, b) 3, c) and 4, d) at 0.05 e/Å^3.

TS 5. Coordinates of the charge distribution (Fig. 9) for the calculation of the quadrupole moment:

$$Q_{ij} = \sum_{l} q_l \left(3 r_{il} r_{jl} - r^2 \delta_{ij}\right)$$

x	y	z	q	r^2
-1	0	1	-0.1	2
-0.5	-0.86603	1	-0.1	2
0.5	-0.86603	1	-0.1	2
1	0	1	-0.1	2
0.5	0.866025	1	-0.1	2
-0.5	0.866025	1	-0.1	2
-1	0	-1	-0.1	2
-0.5	-0.86603	-1	-0.1	2
0.5	-0.86603	-1	-0.1	2
1	0	-1	-0.1	2
0.5	0.866025	-1	-0.1	2
-0.5	0.866025	-1	-0.1	2
-1	0	0	0.2	1
-0.5	-0.86603	0	0.2	1
0.5	-0.86603	0	0.2	1
1	0	0	0.2	1
0.5	0.866025	0	0.2	1
-0.5	0.866025	0	0.2	1
1.5	2.598076	0	0.1	9
1.5	-2.59808	0	0.1	9
-3	0	0	0.1	9
3	0	0	0.1	9
-1.5	-2.59808	0	0.1	9
-1.5	2.598076	0	0.1	9
1	1.732051	0	-0.1	4
1	-1.73205	0	-0.1	4
-2	0	0	-0.1	4
2	0	0	-0.1	4
-1	-1.73205	0	-0.1	4
-1	1.732051	0	-0.1	4

<div align="right">

Chapter 5

</div>

The use of Mo *Kα* radiation in the assignment of the absolute configuration of light-atom molecules. The importance of high resolution data.
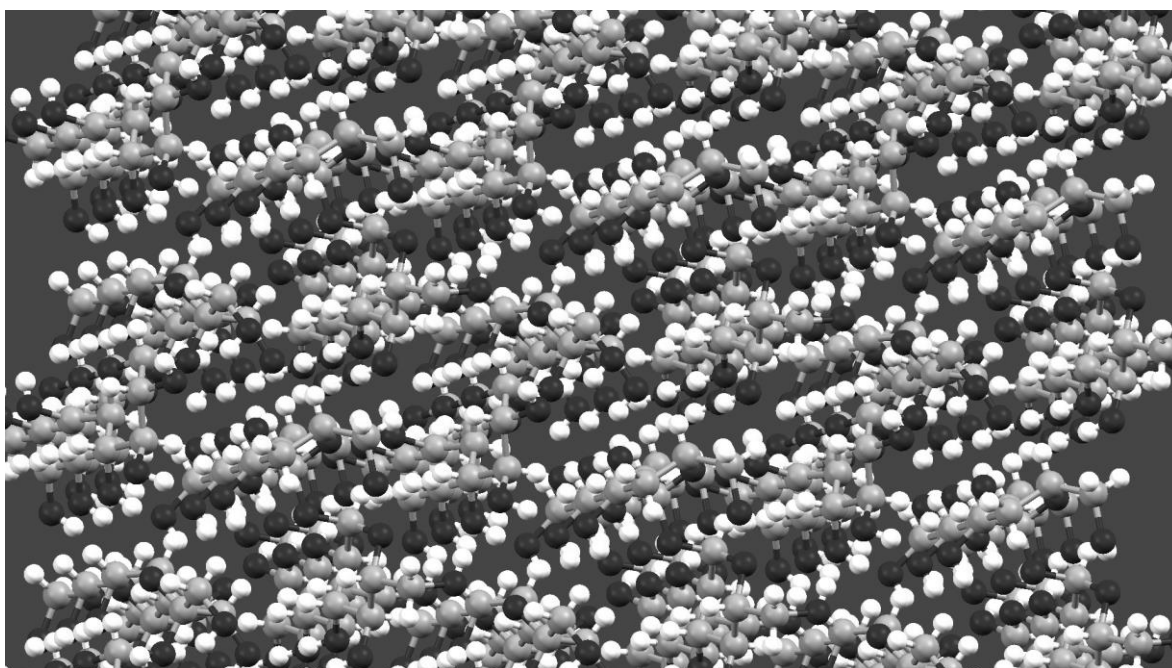
1. Introduction.

Recent studies have confirmed the usefulness of the Hooft and Parsons methodologies for determination of the absolute crystal structures of enantiopure light-atom compounds using Cu $K\alpha$ radiation. While many single crystal diffractometers used for small-molecule structure determination are equipped with molybdenum anodes, use of data from such instruments for the absolute structure determination of light-atom crystal structures is rarely documented and has often been found to be unsuccessful. The Hooft and Parsons methodologies have been applied to 44 data sets obtained from single crystals containing light-atom molecules of known chirality using Mo $K\alpha$ radiation. Several factors influencing the calculation of accurate and precise values for the Hooft and Parsons parameters obtained from these data sets have been identified, inclusion of high resolution diffraction data being particularly important. The correct absolute structure was obtained in all cases, with the standard uncertainties of the final absolute structure parameters below 0.1 for the great majority.

The use of X-ray crystallography for determination of the absolute configuration of molecules made up of atoms no heavier than oxygen (so-called light-atom molecules) constitutes a difficult task. However, this objective has many important implications. For example, many active pharmaceutical ingredients (APIs) are chiral light-atom compounds, and the assignment of the absolute configuration to these materials is of great concern to drug manufacturers and drug authorization authorities because different enantiomers can have different physiological properties. Examples include the tragic results of the use of thalidomide that took place in the late 1950s and early 1960s, and the formation of toxic metabolites derived from (S)-benoxaprofen that lead to the suspension of sales in the 1990s and the reduced pain-killing capabilities and liver poisoning properties of the (R)-naproxen enantiomer.

New methodologies were recently introduced which, when applied to crystals of enantiopure light-atom compounds, enable precise absolute structure determination to be carried out using standard X-ray single crystal diffraction data sets, thus leading to the unequivocal assignment of the absolute structure.[1,2] In principle, Cu $K\alpha$ radiation has a distinct advantage over Mo $K\alpha$ radiation[1,3] on account of its larger resonant scattering factors which lead to more significant Bijvoet intensity differences. Indeed, the use of Cr $K\alpha$ radiation, with its still greater resonant scattering effects, has even been suggested.[2]

The resonant scattering effects of a crystal structure can be quantified through the Friedif$_{stat}$ parameter[4] and it tends to be about six-times smaller for Mo $K\alpha$ radiation than for Cu $K\alpha$. A recent study involving 150 data sets[5] demonstrated the difficulty of determining the absolute structure of light-atom crystals using data collected with Mo $K\alpha$ radiation and thus the assignment of absolute configuration to their chiral molecular components.
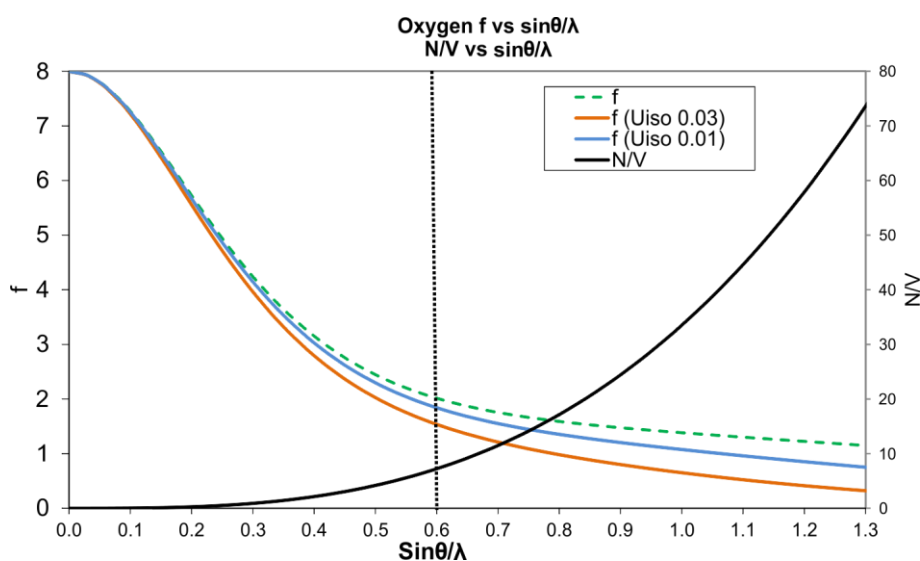
Figure 1. (Left vertical axis) Plots of the difference in atomic scattering factor, f, for an oxygen atom *vs* $\sin\vartheta/\lambda$: dotted green line without thermal motion, orange and blue lines are for U_{iso} 0.03 Å^2 and 0.01 Å^2, respectively. (Right vertical axis) Plot of the number of reflections per cell volume, *N/V*, *vs* resolution (black line). The vertical black dotted line represents the maximum resolution in $\sin\vartheta/\lambda$ achieved with Cu $K\alpha$ radiation, 0.6Å^{-1} for a goniometer geometry that achieves a maximum resolution in $\sin\vartheta/\lambda$ of 1.3Å^{-1} with Mo $K\alpha$ radiation.

The absolute structure determination of single crystals containing atoms no heavier than oxygen is based on statistical methods, and the ability to distinguish unambiguously between enantiomorphic arrangements of atoms increases with the number of independent reflections measured during data collection. The number of reflections that can be collected using Mo $K\alpha$ radiation is ten times larger than using Cu $K\alpha$ radiation for the same 2θ range without a massive increment in data acquisition time. Consequently, the limitation of the weaker resonant scattering of Mo $K\alpha$ radiation can be compensated by a substantial increase in the number of reflections (Fig. 1). In addition, because the effect of the resonant scattering is angle independent, the relative contribution to the intensity differences ($\Delta f/f$) increases (following the f"/f trend) at very high resolution accessible with Mo $K\alpha$ radiation (Fig. S1), though collection at low temperature is mandatory (Fig. 1) to obtain acceptable counting statistics.

This paper describes the methodology used to determine unambiguously the absolute structure of crystals constituted exclusively by light-atoms using X-ray diffraction data obtained with instruments equipped with molybdenum anodes. Because the crystal structures are composed of light-atom enantiopure organic molecules their absolute configuration can therefore also be assigned.

2. Experimental

A total of 21 enantiopure organic compounds were investigated, Table S1, yielding 44 single crystal data collections. The crystals were made up of compounds for which the absolute configuration is well established. All data were collected using Mo $K\alpha$ radiation to a maximum resolution of 1.3 Å^{-1}. Friedif$_{stat}$ was in the range of 5.6 to 7.1. The single crystals of all the compounds were obtained by slow evaporation of aqueous solutions, except for the crystal producing the data set 6802, which was obtained by slow evaporation of a methanol solution. Some compounds were measured several times using crystals of different size and quality. Several data collections using the same crystal were

performed for D-threonine, L-Threonine and L-Hydroxyproline. The data collections were carried out at 100 K with a strategy that included φ and ω scans and was the same for all the samples (Table S2). The data collection strategy ensures a redundancy greater than 5 for the full data set for an orthorhombic structure; the redundancy is ~ 6 between 0 and 1.0 Å^{-1}, and ~ 3 between 1.0 and 1.3 Å^{-1}. Data were acquired to the physical limit of the instrument at a detector distance of 40 mm. The total measurement time was about 24 hours for each crystal. The Friedel pair coverage for the full data sets were over 90% in all cases.

Three different instruments were used for the data collections:

Diffractometer (a): Bruker-Nonius FR591 rotating anode equipped with a CCD-Apex II 4K detector, Montel multilayer optics, a Kappa 4-axis goniometer and a Kryoflex low temperature device. This instrument was used for all but four data collections.

Diffractometer (b): Apex DUO diffraction system equipped with a CCD-Apex II 4K detector, Microfocus E025 IμS X-ray source, Quazar MX multilayer optics, a Kappa 4-axis goniometer and an Oxford Cryosystems 700 plus. Three samples, 5008, 5212 and 5214, were measured on this device.

Diffractometer (c): D8 Venture diffraction system equipped with a PHOTON 100 Detector, a Microfocus E025 IμS X-ray source, Helios multilayer optics, a Kappa 4-axis goniometer and a Kryoflex II low temperature device. The sample 5215 was measured on this device.

Data reduction was carried out using SAINT V6.0A and V8.30C. The multi-scan absorption correction was accomplished with SADABS.[6,7] In all cases equivalent data were identified using the crystal point group, though similar results were obtained using the Laue group.

The crystal structures were solved with SIR2011[8] or SHELXS[9] and refined with the program SHELXL2013.[10] The non-H atoms were refined in all cases with anisotropic displacement parameters. For most of the structures, H atoms were located in Fourier maps and their positions and Uiso refined; for structures modelled with disorder the U_{iso}, position and angles of the H atoms were constrained to ideal values. For the refinements performed

omitting different data ranges, H atoms were fixed to the parameters obtained from the refinement with the full data set. Both refined (using the TWIN/BASF commands) and post-refinement values of the Flack parameter,[11] x, were calculated with SHELXL2013. Values of the likelihood of having the correct absolute structure as defined by Hooft et al.[1] [P2(right)], the Hooft parameter, y, and Flack parameter using the Parsons method,[2] that we will refer as Parsons parameter, z, were calculated with PLATON[1,12] via BIJVOET routine from CIF and FCF files obtained without refining the Flack parameter. The student-t distribution[13] was used for the calculation of y. Values of the optimized number of degrees of freedom for a t-distribution are listed in table S3.

For the leverage analysis of x the crystal structures were refined with CRYSTALS[14] and the program HATTIE was used as described by Parsons et al.[15]

Crystallographic information files containing unmerged intensity data for all structures are available as supplementary material to this paper.

2.1 Reproducibility of the experiments

In order to check the reproducibility of the experiments a total of twelve measurements were performed with two L-Threonine and one D-Threonine single crystals. Two data collections of one crystal of L-Hydroxyproline were also performed with the same goal.

In all the threonine structures the U_{iso} and the positions of the H-atoms were refined. One crystal of D-Threonine was measured a total of seven times, re-mounting the crystal each time. The data collection was performed six times on Diffractometer (a), achieving different redundancies each time; in three cases the redundancy was around 5.5, in two below 4 and in one case the redundancy was 11.6. For the last, extra φ and ω scans were added to the strategy, doubling the total measurement time. Conversely, in the data-sets with redundancy below 4 the measurement was aborted before the end of the data collection strategy. The seventh data collection of the D-Threonine crystal was performed

using diffractometer (b) achieving a redundancy of 5.7. A second crystal of D-Threonine was also measured with the three different diffractometers. The redundancies were 8.2 for the data collected on diffractometer (c) and 5.9 for the data sets collected on the other two diffractometers. The resolution of the data set collected on diffractometer (c) was increased to 1.35 Å^{-1}. Finally, a crystal of L-Threonine was measured twice yielding redundancies of 5.6 and 2.6 on diffractometer (a).

The data collection of the crystal of L-Hydroxyproline was performed twice achieving redundancies of 5.2 and 11.5.

Table 1. Calculated values of the absolute structure parameters obtained using Mo $K\alpha$ radiation.

The x, y and z columns contain the calculated values of the Flack parameter x, Hooft parameter y and Parsons parameter z, respectively. Other relevant crystallographic parameters for the different crystal structures are also included in the table.

Compound	Sample	Friedif$_{stat}$	N$_{ind}$(I>4σ)	Redundan	R_1(I>4σ)	x (Flack)	y (Hooft)	z (Parsons)	Rint(Rsigma) at sin(ϑ/λ)=0.5Å
L-Alanine	5001 [a]	6.5	6209	4.5	0.0254	-0.08(28)	0.05(8)	0.06(8)	0.035(0.019)
	5002 [a]	6.5	6575	5.0	0.0299	-0.07(29)	-0.09(9)	-0.06(10)	0.047(0.036)
D-Alanine	5006 [a]	6.5	6549	5.1	0.0196	0.05(22)	-0.02(5)	0.02(5)	0.017(0.015)
	5008 [b]	6.5	6169	4.8	0.0238	0.02(23)	-0.01(5)	-0.01(4)	0.014(0.013)
L-Serine	5101 [a]	6.5	7308	5.2	0.0270	0.03(28)	0.05(5)	0.07(5)	0.021(0.013)
D-Threonine	5201 [a]	6.7	8832	5.2	0.0210	0.12(22)	0.04(5)	0.05(5)	0.027(0.013)
	5202 [a]	6.7	8389	5.2	0.0202	-0.01(21)	-0.03(6)	-0.03(5)	0.025(0.015)
	5203 [a]	6.7	8124	5.8	0.0219	0.01(24)	0.06(6)	0.07(6)	0.030(0.018)
	5204 [a]	6.7	8324	11.6	0.0221	0.03(24)	0.02(6)	0.02(6)	0.040(0.021)
	5205 [I,a]	6.7	7711	3.7	0.0266	0.02(29)	0.00(9)	-0.01(10)	0.039(0.033)
	5206 [I,a]	6.7	6401	3.2	0.0237	0.29(32)	0.10(7)	0.10(8)	0.028(0.026)
	5212 [b]	6.7	8758	5.7	0.0241	0.08(26)	0.01(9)	-0.01(10)	0.042(0.021)
	5213 [a]	6.7	8952	5.9	0.0196	-0.12(19)	-0.03(5)	-0.03(4)	0.021(0.010)
	5214 [b]	6.7	8883	5.9	0.0229	0.09(24)	0.06(7)	0.07(7)	0.032(0.013)
	5215 [c]	6.7	9543	8.2	0.0224	0.00(21)	-0.02(5)	-0.03(5)	0.027(0.012)
L-Threonine	5210 [a]	6.7	8473	5.6	0.0223	0.11(23)	0.09(4)	0.09(3)	0.018(0.010)
	5211 [a]	6.7	8060	2.6	0.0235	0.07(25)	0.05(8)	0.05(8)	0.026(0.020)
L-Aspartate	5301 [a]	6.5	8234	2.6	0.0263	-0.06(23)	0.02(9)	-0.01(8)	0.025(0.020)
L-Hydroxyproline	5401 [a]	6.8	9535	5.2	0.0230	0.06(26)	0.03(3)	0.03(3)	0.015(0.009)
	5402 [a]	6.8	9311	11.5	0.0239	0.07(26)	0.05(3)	0.06(3)	0.026(0.010)
L-Glutamine	5501 [a]	6.7	9418	5.2	0.0205	0.15(20)	0.07(5)	0.08(5)	0.027(0.014)
L-Histidine	5602 [a]	5.7	10624	5.1	0.0299	0.14(40)	0.07(7)	0.09(6)	0.025(0.016)
	5603 [a]	5.7	10721	5.0	0.0360	-0.10(45)	0.08(8)	0.08(11)	0.073(0.035)
	5604 [a]	5.7	11241	5.1	0.0314	0.09(42)	0.01(7)	0.00(7)	0.026(0.016)
L-Valine	5701 [a]	6.6	18138	2.5	0.0295	0.11(19)	0.10(9)	0.12(8)	0.045(0.036)
L-Isoleucine	5801 [a]	6.4	19689	2.6	0.0315	-0.20(20)	-0.05(9)	-0.04(8)	0.038(0.031)
Methyl-α-L-rhamnopyranoside	6001 [a]	7.1	13309	5.3	0.0217	-0.08(16)	-0.05(5)	-0.04(4)	0.032(0.016)
	6002 [a]	7.1	12004	5.3	0.0233	0.03(17)	0.07(4)	0.07(4)	0.022(0.011)
	6003 [a]	7.1	11628	5.5	0.0238	0.14(18)	0.11(4)	0.11(4)	0.021(0.012)
Methyl-α-D-mannopyranoside	6101 [a]	7.0	13431	4.9	0.0208	-0.08(17)	-0.06(4)	-0.07(3)	0.024(0.014)
Methyl-α-D-glucopyranoside	6201 [a]	7.0	13732	5.2	0.0239	0.03(18)	0.02(4)	0.02(4)	0.024(0.014)
	6202 [a]	7.0	13666	5.2	0.0273	0.07(21)	0.02(6)	0.00(6)	0.046(0.022)
ß-D-Galactose pentaacetate	6301 [a]	7.0	24645	5.2	0.0367	-0.04(21)	0.01(5)	0.03(6)	0.124(0.070)
ß-D-Lactose monohydrate	6401 [a]	6.9	23466	2.6	0.0347	-0.02(22)	-0.02(5)	0.01(5)	0.032(0.027)
α-D-glucopyranosyl-(1→2)-β-D-fructofuranoside	6501 [a]	6.9	20204	2.4	0.0198	-0.06(12)	0.03(5)	-0.01(5)	0.018(0.018)
	6502 [a]	6.9	20110	2.9	0.0197	0.04(11)	0.05(4)	0.06(3)	0.017(0.017)
	6503 [a]	6.9	21902	2.6	0.0207	-0.09(12)	-0.04(4)	-0.04(5)	0.019(0.016)
	6504 [a]	6.9	20599	4.7	0.0190	0.04(11)	0.04(3)	0.05(3)	0.017(0.012)
	6507 [I,a]	6.9	9994	1.2	0.0239	-0.20(20)	0.07(8)	0.04(8)	0.013(0.022)
ß-D-Maltose octaacetate	6601 [a]	7.0	40462	4.8	0.0629	0.02(33)	-0.03(8)	0.04(10)	0.203(0.119)
β-D-Allose	6802 [a]	6.9	9528	6.6	0.0267	-0.17(25)	-0.08(8)	-0.04(8)	0.022(0.031)
L-Tartaric acid	7001 [a]	6.3	8734	2.5	0.0225	0.04(20)	0.02(8)	0.04(10)	0.031(0.028)
$C_{15}H_{26}O_2$ [16]	7701 [a]	5.6	26783	3.1	0.0393	-0.01(32)	-0.02(10)	-0.04(11)	0.116(0.149)
$C_{11}H_{14}O_6$ [17]	7801 [a]	7.0	14435	3.8	0.0364	0.09(31)	-0.02(8)	-0.04(7)	0.083(0.063)

Superscript I = Incomplete data set, a= rotating anode Bruker FR591 + APEX II, b = μ-source APEX II DUO, c = μ-source Bruker Venture + Photon 100. L-Hydroxyproline (5401 and 5402) crystallizes disordered over two positions with an occupation ratio of around 0.50:0.50. ß-D-Maltose octaacetate (6601) crystallizes highly disordered, showing acetate residues in different orientations and the partial presence of a water molecule.

3. Results and discussion

Table 1 summarizes the values for the absolute structure parameters (x^1, y and z). We did not obtain any bizarre or outlandish value. The values of the standard uncertainties of the x parameter are dispersed in the range of 0.11 to 0.45, and in no case below that recommended for materials of known enantiopurity, $u_x \leq 0.1$.[18] It is notable that although the values determined for the standard uncertainty of the x parameter are high, the use of the known absolute structure in the refinement model returns value of the x parameter close to zero. In all cases, the calculated values for y and z were also very close to 0 when the correct absolute structure of the crystal was used in refinement. Their standard uncertainties were within the limits defined by Flack and Bernardinelli, $u_y \leq 0.10$ and $u_z \leq 0.11$. All the probabilities calculated using the Bayesian two-way test assuming an enantiopure compound [P2(right)] were 1.0. As already pointed out by Thompson & Watkin,[5] the values for the y and z parameters showed a linear correlation with a slope close to unity (Fig. 2). The results indicate that it is possible to determine the absolute structure of crystals containing only light-atoms using Mo $K\alpha$ radiation provided that the diffraction data sets extend to high resolution. In the following sections, we will analyze the different features of the data sets that potentially play important roles in attainment of accurate and precise values for the absolute crystal structure parameters. In this way, we aim to validate the idea that the inclusion of high resolution data is mandatory for absolute crystal structure determination of most of the crystals containing only light-atom molecules when using Mo $K\alpha$ radiation.

---

[1] Post-refinement calculation of *x* and refinement of *x* provided identical results.
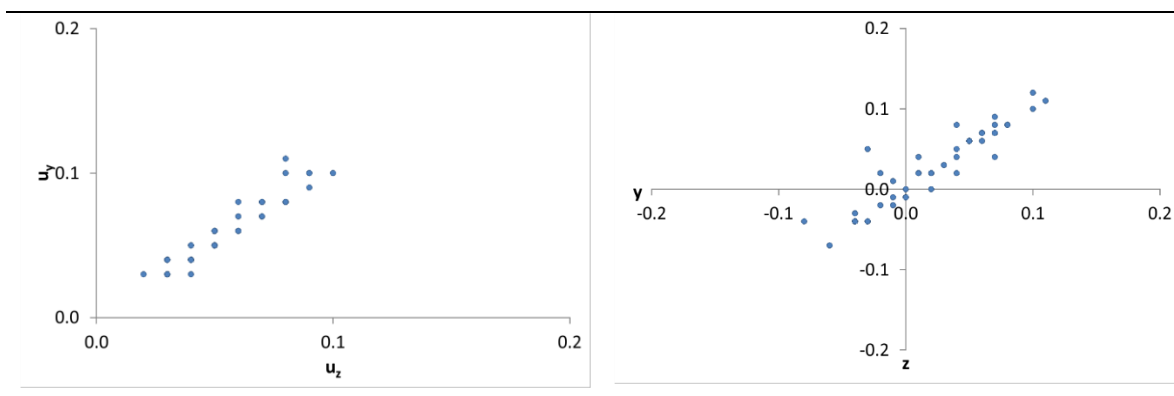
Figure 2. (a) Plot of the Hooft *y* parameter *vs*. the Parsons *z* parameter. (b) Plot of the standard uncertainties of *y vs* the standard uncertainties of *z*.

3.1 Influence of the redundancy and R_1 factor.

As indicated in Section 2.1, one single crystal of D-Threonine was measured seven times (data sets 5201-5206 and 5212) in order to check the consistency of the measurements. For all the data sets the values of the three absolute structure parameters are close to zero; the standard uncertainties of the y and z parameters are significantly smaller than those of x. For the data set 5206 the x Flack parameter achieves a maximum value 0.29. The standard uncertainties values of the y and z parameters are directly correlated with the value of R_1 for the fully refined model (Fig. 3). The standard uncertainty of x also follows the trend of R_1, however for the data set 5206 in which the number of reflections is reduced compared to the others the magnitude of u_x increases noticeably.

151
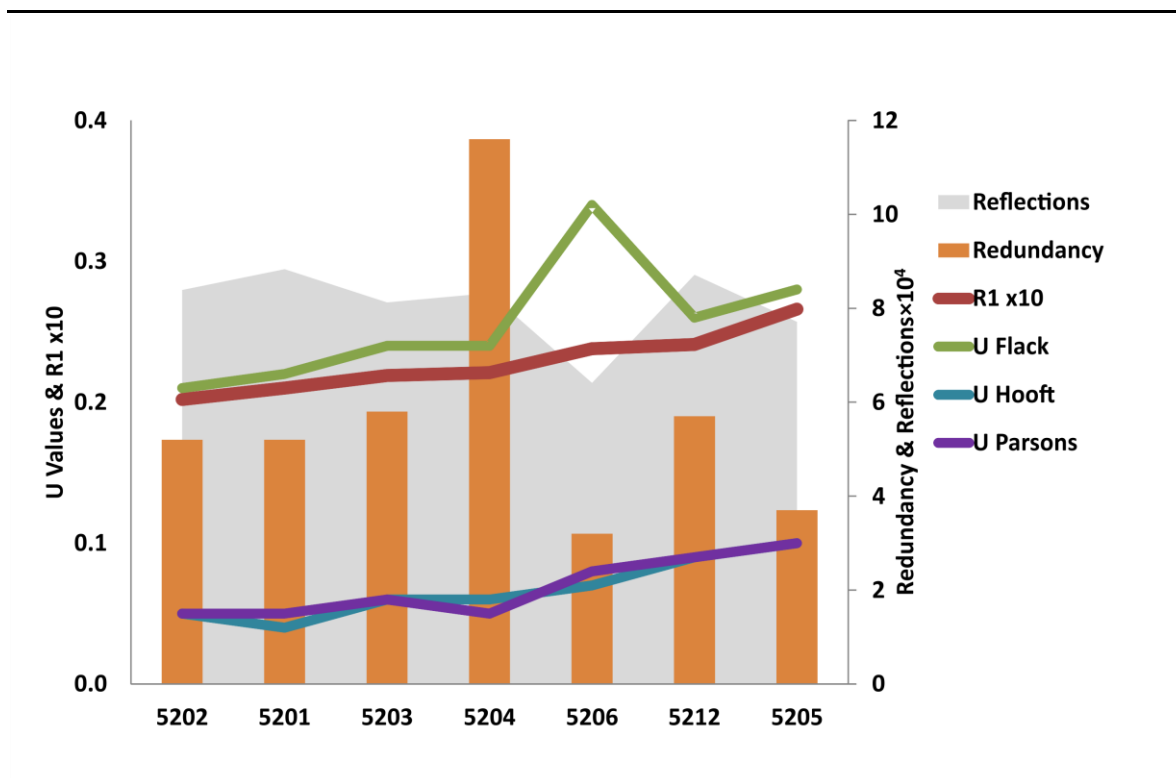
Figure 3. Plots of some properties of the seven data sets collected using the same single crystal and the results obtained during the refinement. Data sets 5201 to 5206 were collected on a Bruker FR591 rotating anode. Data set 5212 was collected on a Bruker Duo system equipped with a μ-source.

Several conclusions can be drawn from the results obtained in these measurements. The increase of redundancy to a value of 11.6 does not improve significantly the precision of any of the absolute structure parameters. The low redundancy obtained for data sets 5205 and 5206 slightly increases both the R1 factor and the standard uncertainties of the absolute structure parameters. Finally, the data collected with diffractometer (b) (5212, $<I/\sigma(I)> \sim 42$) provides slightly worse values of R1, magnitudes of absolute structure parameters and their uncertainties than those obtained with data sets 5201, 5202 and 5203 ($<I/\sigma(I)> \sim 67$) collected on diffractometer (a) although all data sets have similar redundancy and number of reflections.

Data sets 5213, 5214 and 5215, were obtained by diffracting one crystal of D-Threonine on the three different diffractometers (a), (b) and (c), respectively. The data set collected

with the diffractometer (a) has a better R_1 factor than the other two data sets, 1.96% vs 2.31% and 2.23%. The data set collected with diffractometer (c) has the largest number of independent reflections due to the increase achieved in resolution. For these three data sets, very similar values of the absolute structure parameters and their standard uncertainties were obtained. The y and z parameters clearly fulfil the requirements proposed by Flack & Bernardinelli[18] for an unequivocal absolute structure determination of an enantiopure compound. The standard uncertainties of x follow an analogous trend to the values of the R_1 factor.

3.2 Variables influencing the accuracy of the absolute structure parameters

The magnitude of the standard uncertainties of the refined absolute structure parameters, assuming a normal distribution of measurement errors, is related to the number of reflections by $1/\sqrt{(N-P)}$, where N and P are the numbers of reflections and refined parameters, respectively. In addition, the standard uncertainty also depends on other elements including the R_1 factor, $Friedif_{stat}$ and the redundancy of the data (Fig. S2). In order to quantify the influence of these entire variables on the magnitudes of the standard uncertainties of the absolute structure parameters we empirically defined a parameter η (Equation 1).

$$\eta = \frac{R_1}{\sqrt{N} \cdot \tan^{-1}(Redun) \cdot (Friedif_{stat})^{3/2}} \cdot 10^5 \quad (1)$$

η is directly proportional to the R_1 factor and inversely proportional to $Friedif_{stat}$ to the power of 3/2. η is almost independent of the redundancy, and this factor is incorporated in the denominator of the formula through the arctangent function of redundancy. Finally the dependency of η with the number of reflections is included in the formula as $1/\sqrt{N}$, since $N \gg P$ (Table S4). This definition was made such that η can be seen as a measure of the absolute structure resolving power of the data set. Fig. 4(a), (c) and (e) depict plots of

u_x, u_y and u_z against η. A linear correlation of u_x with η is found. Linear relationships of η and the standard uncertainties of the y and z parameters are also observed but the spread of the data points is significantly smaller. The plots of the values of the absolute structure parameters versus η show that the magnitudes of the x parameter vary slightly as the value of η increases, Fig. 4 (b). Conversely, the magnitudes of the y and z parameters are much less sensitive to changes in the value of η, Fig. 4(d) and 4(f).
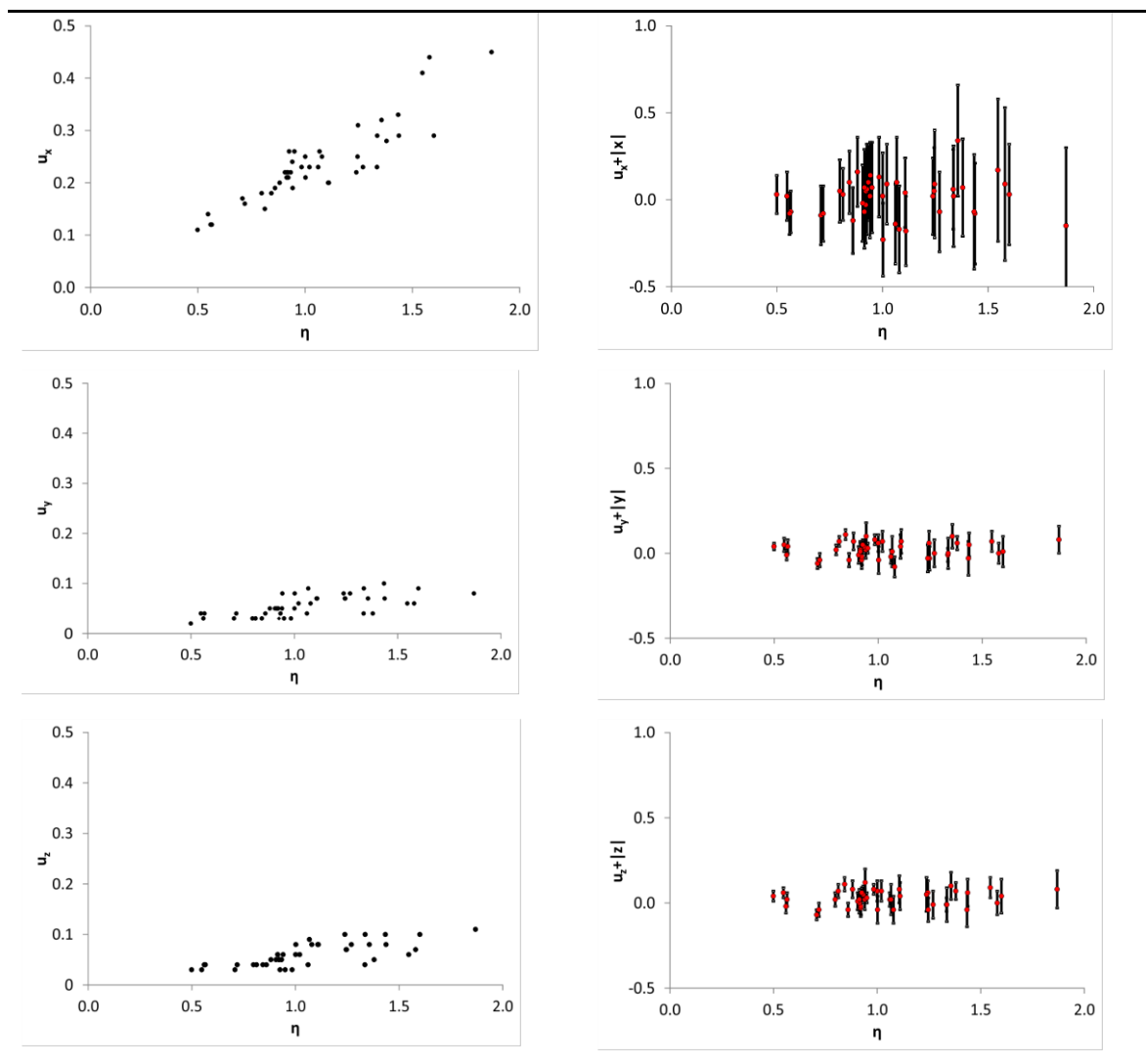
Figure 4. Plots of the standard uncertainties determined for the *x* (a), *y* (c) and *z* (e) parameters versus $\eta \times 10^5$, and of $x \pm u_x$ (b), $y \pm u_y$ (d) and (f) $z \pm u_z$ versus $\eta \times 10^5$.

The visual analysis of the plots of the absolute structure parameters and their uncertainties vs η reveals a trend that might be considered obvious: good data quality that result in a good R_1 factor is needed to determine accurately the absolute structure of the crystal. Even though the magnitudes of Friedif$_{stat}$ are quite similar, as shown by Flack & Shmueli,[4] higher values of Friedif$_{stat}$ still tend to yield lower standard uncertainties of the absolute structure parameters. Because of the relationship that exists between the number of reflections and the uncertainties values of the structural parameters it must play an important role in determining the absolute structure of the crystal, see Table S4. This fact indicates that the increase in the resolution range (increase in number of reflections) favours the accuracy of the absolute structure parameters. For the same reason, provided data to sufficiently high resolution can be measured, big molecules, or more general, big asymmetric units, have a significant advantage for determining the absolute structure of a crystal.

Number of structures that fulfil the requirement at different data resolution cut-offs of a total of 44 structures.

Table 2. Number of structures (and its percentage) that fulfil the requirement at different data resolution cut-offs of a total of 44 structures.

% of Theoretical reflections	Requirement Cut-off (Å^{-1})	$|y| \leq 0.1$	$u_y \leq 0.1$	$|z| \leq 0.1$	$u_z \leq 0.1$	$|y|, u_y \leq 0.1$	$|z|, u_z \leq 0.1$
100%	No cut-off	44(100%)	44(100%)	43(98%)	43(98%)	44(100%)	42(95%)
48%	1.0	40(91%)	43(98%)	39(89%)	39(89%)	39(89%)	33(75%)
34%	0.9	38(86%)	39(89%)	39(89%)	33(75%)	34(77%)	31(70%)
25%	0.8	35(80%)	33(75%)	35(80%)	32(73%)	29(66%)	34(36%)
15%	0.7	23(52%)	17(39%)	23(52%)	16(37%)	13(30%)	11(25%)
10%	0.6	22(50%)	7(16%)	21(48%)	5(89%)	7(16%)	3(7%)

3.3 Refinements at low resolution ranges.

We performed the refinement of all the data sets at different resolution cut-offs i.e. 0.6, 0.7, 0.8, 0.9 and 1.0 Å^{-1}, Table S5. The values of the absolute structure parameters were calculated at each resolution cut-off. The standard uncertainties of x are far too high to permit any interpretation. At lowest resolution, the spread of the y and z parameters is also increased. Moreover, the wrong absolute structures were implied in some cases. However, the use of the lowest resolution cut-offs also caused a dramatic increase in the standard uncertainties, consistent with the increased spread of values of the parameters. In particular, for data sets refined with the minimum resolution required by the IUCr, $\sin(\theta/\lambda) = 0.6$ Å^{-1}, we observed that of a total of 44 structure refinements the corresponding absolute magnitudes calculated for $|y|$ and $|z|$ are smaller than 0.1 in 22 (50%) and 21 (48%) cases, respectively. In addition, the uncertainty values determined for the y and z parameters was smaller than 0.1 in only 7 (16%) and 5 (11%) cases, respectively. Examining the magnitudes of the parameters for absolute structure determination in combination with their standard uncertainties, we concluded that 7 (16%) data sets of the 44 analyzed featured values of $|y|$ or u_y that are larger than 0.1 for a 0.6 Å^{-1} cut-off. The corresponding figure for z and u_z is 3 (7%). The number of data sets fulfilling the requirement of $|y|$ or u_y and $|z|$ or $u_z < 0.1$ increases to 29 (66%) and 28 (64%) respectively for a 0.8 Å^{-1} cut-off. All the data sets fulfil the above requirement when no-cut off resolution is considered for $|y|$ or u_y with 95% for $|z|$ or u_z. (See Table 2 and S5)

3.4. High resolution data

We have shown above that the values of the standard uncertainties of the absolute structure parameters decrease as data of higher resolution are used in structure refinement, Fig. 5. However, Parsons et al.[19] has suggested, on the basis of leverage analyses, that the inclusion of very high resolution data may have a weak influence when

determining the x parameter. It is therefore sensible to consider that the observed diminution in the uncertainty values is simply owed to the increase in the number of data points associated with data sets acquired at higher resolution. If the high resolution data do not contain information about absolute structure, their consideration during structure refinement should not significantly affect the magnitudes calculated for the absolute structure parameters of the crystal. The effect of the high resolution reflections was analyzed using two different methodologies.
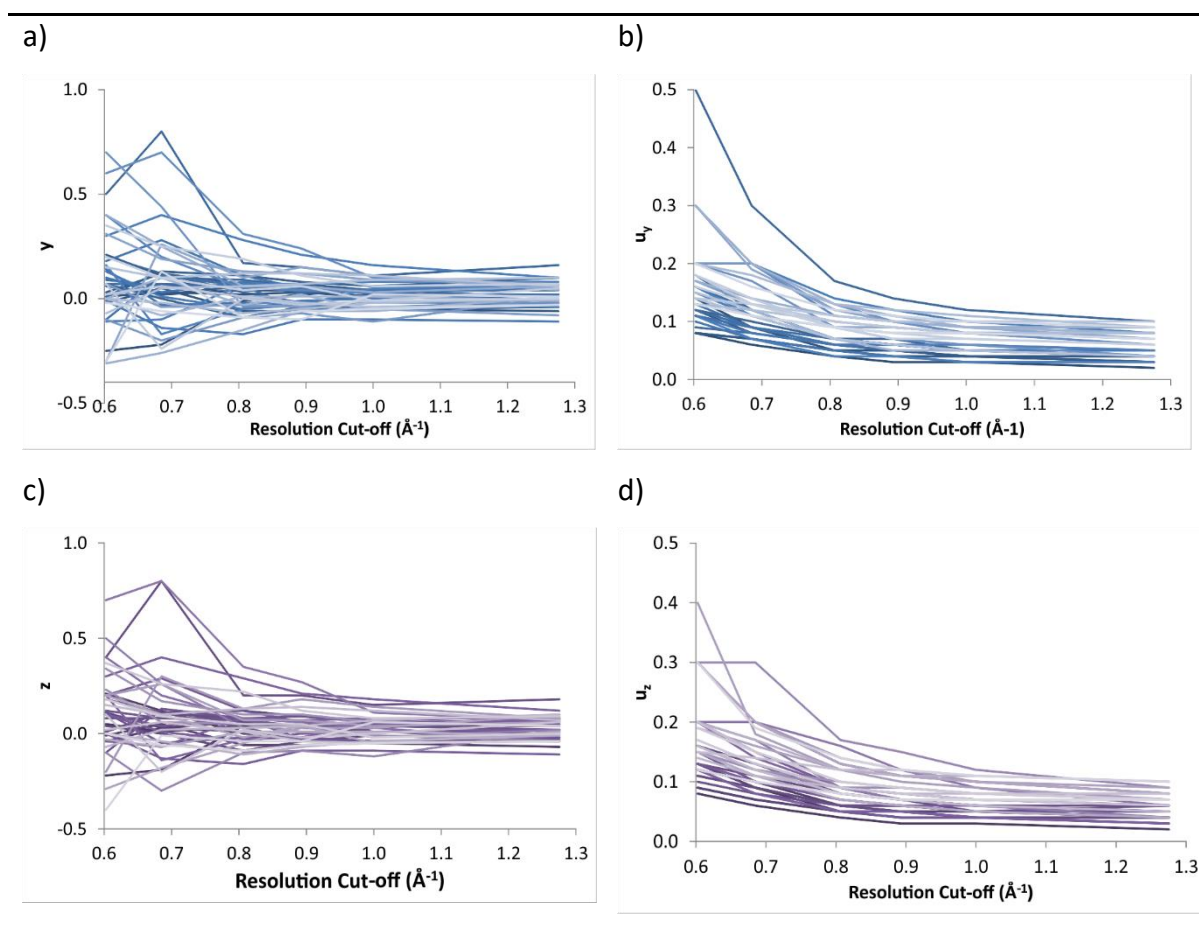
Figure 5. Evolution of the y, a) and z, c) parameters and their standard uncertainties, u_y, b) and u_z, d) along different resolution cut-offs.

3.4.1 Refinements using Friedel opposites in high resolution shells.

Data sets were modified by inverting the indices of the reflections in high-resolution shells as defined in (2).

$$\begin{cases} h \rightarrow h \ \ for \ \ \frac{sin\theta}{\lambda} < resolution \ limit \\ h \rightarrow \overline{h} \ \ for \ \ \frac{sin\theta}{\lambda} \geq resolution \ limit \end{cases} \quad (2)$$

The values for the absolute structure parameters x, y and z obtained on refinement are summarized in Table S6. The different values correspond to data sets in which the indexes were inverted above $\sin(\theta/\lambda)$ = 0.6, 0.7, 0.8, 0.9 and 1.0 Å^{-1}. The data in Table S6 show that the calculated x, y and z parameters are significantly influenced by the value chosen for the resolution limit. In particular, for $\sin(\theta/\lambda)$ =0.8 Å^{-1} the calculated average values for the Hooft and Parsons parameters are close to 0.55 and that of the Flack parameter is near to 0.65. This result indicates that the data acquired at resolution values larger than $\sin(\theta/\lambda)$ =0.8 Å^{-1} must contain significant information with respect to the resonant scattering. When the inversion is performed with the data at higher resolutions than $\sin(\theta/\lambda)$ =0.7 Å^{-1} the calculated values for the x parameter differ substantially from those obtained for y and z (Fig. 6). In short, the inclusion of high resolution data has a stronger effect in the calculated values of x than in y and z. This effect is analysed further in Section 3.5.
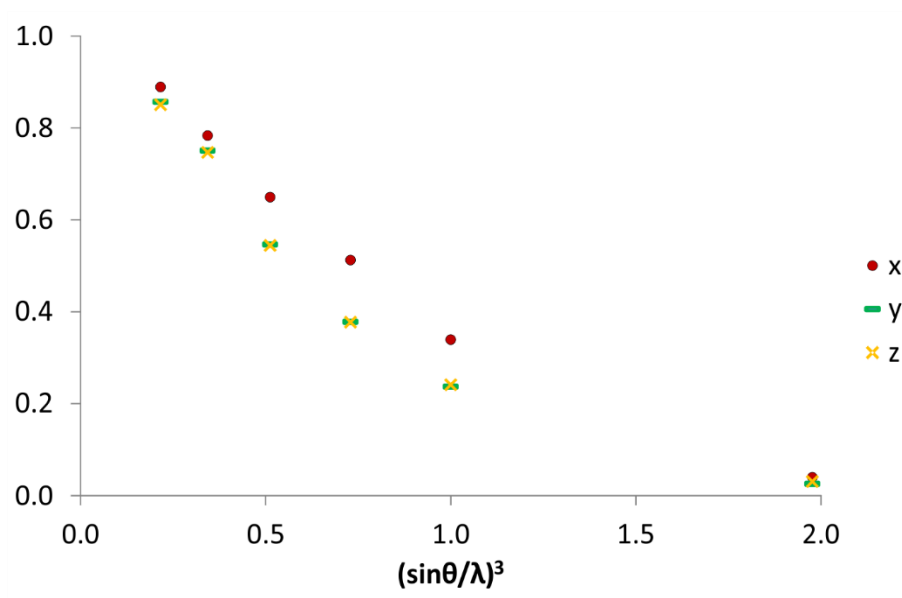
Figure 6. Changes in the absolute structure parameters values as a function of inverted Friedel pairs from different high resolution ranges. The Y axis values correspond to the arithmetic mean of the parameters calculated for all the data sets at each $(\sin\vartheta/\lambda)^3$ value. $(\sin\vartheta/\lambda)^3 \sim N/V$

Most data-sets listed in Table 1 were collected out to the physical resolution limit of the diffractometer, about 1.25 Å^{-1}. However, in four cases, 6301, 6601, 7701 and 7801, the resolution range was limited by the diffracting power of the crystals: these data sets featured very weak reflections beyond 1.0 Å^{-1} ($<I/\sigma(I)> < 8$) Thus, the inversion of indexes for reflections beyond a resolution of 1.0 Å^{-1} had a negligible effect for these structures.

3.4.2 Calculation of absolute structure parameters in different resolution shells

For five data sets, the absolute structure parameters were calculated using four resolution shells, 0-0.7 Å^{-1}, 0.7-0.9 Å^{-1}, 0.9-1.1 Å^{-1} and 1.1-1.3 Å^{-1} which contain 17%, 19%, 16% and 36% of the theoretical number reflections up to a resolution of 1.3 Å^{-1}. The selected five data sets form a heterogeneous set in terms of data quality. Data sets 5101 and 6504 have $<I/\sigma(I)>$ of 51.1 and 50.7 respectively in the highest shell whereas data sets 6301, 5001

and 5602 respectively have, $<I/\sigma(I)> = 7.5$, $<I/\sigma(I)> = 27.1$ and $<I/\sigma(I)> = 41.2$ in the same range. To visualize the y and z parameters together, the calculated values for $|y|+u_y$ and $|z|+u_z$ are depicted in Fig. 7a and 7b, respectively. As shown in the figures, all resolution shells contain meaningful information with respect to the structural parameters except the highest resolution shell of 6301. This result indicates that there is important information related to the absolute structure of the crystal available at high resolution ranges and that the y and z parameters constitute an appropriate means to extract this information.
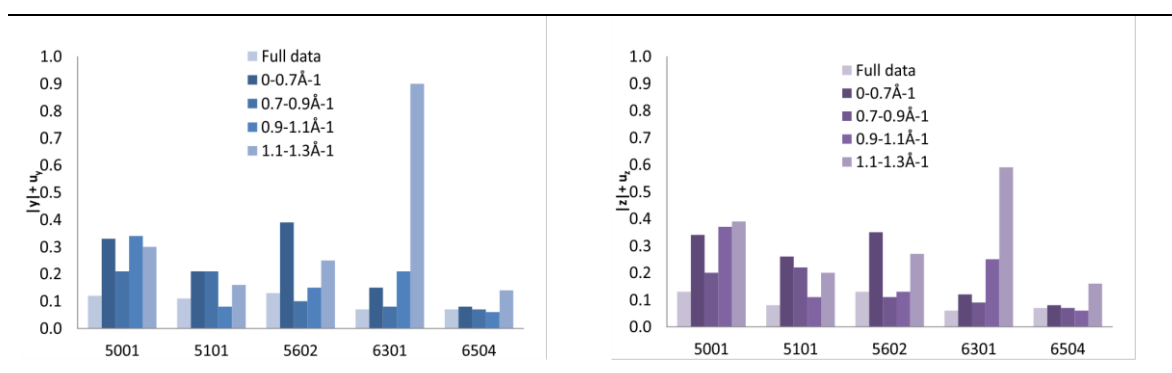
Figure 7. Calculated values of $|y|+u_y$, (a) and $|z|+u_z$ (b) for selected data sets at different resolution shells. Data sets 5101 and 6504 are of very good quality at ultrahigh resolution. For 5602 the ultrahigh resolution data quality is good, medium for 5001 and poor for 6301.

3.5 The Influence of spherical scattering factors and T^2 analysis of x

In previous sections, we demonstrated that the inclusion of high resolution reflection data in structure analysis is an important factor for achieving accuracy and precision in absolute structure parameters. On the basis of a leverage analysis of the absolute structure refinement of L-Alanine Parsons et al.[19] suggested that, while inclusion of Bijvoet ratios at high resolutions was important, their efficacy in increasing the precision of x was questionable because of the weak intensities typically associated with high resolution

range reflections. The value of the standard uncertainty of the Flack parameter x is very sensitive to errors in the structural model used in the refinement process. By contrast, the methodologies applied for the calculation of the y and z parameters provide information about absolute structure even in early stages of the refinement process, for example using an isotropic atomic displacement model. To illustrate this significant difference, we used the results obtained with the data set 5213. The values of the y and z parameters and their standard uncertainties determined for this data set remained almost constant either using the isotropic or anisotropic model, -0.01(5) vs -0.03(5) for y and 0.03(4) vs -0.03(4) for z, respectively. In striking contrast, depending on the use of the isotropic or anisotropic model the value of the R_1 factor changed from 9.27% to 1.96% and the Flack parameter x and its standard uncertainty shifted from -0.09(99) to -0.12(19). (It should be noted that a drop in the value of R_1 leads to a drop in the standard uncertainties of all refined parameters, included x). By the same token, the precision in the values of x is expected to improve slightly with the application of models that correct for the errors associated with the spherical model, models that use databases[20,21] or the multipolar atomic model. The corrections applied to the spherical model of atoms have the largest effect on the reflections at low resolution.[22] Thus, the contribution to the accuracy of x provided by the low resolution reflections is affected by systematic errors derived from the use of the spherical-atom model. This is specially the case for crystals composed of molecules with only light-atoms. For crystals of light-atom compounds diffracted with Mo $K\alpha$ radiation these corrections become even more important when trying to determine absolute structure due to the small resonant scattering effects associated with this energy.

The leverage analysis does not take into consideration the systematic errors associated with the use of the spherical-atom model, and this limitation can result in an underestimation of the real leverage provided by the high resolution range reflections in the calculation of x. In order to evaluate this hypothesis, the structures of this work were refined using exclusively the high resolution reflections, $\sin(\theta/\lambda) > 0.8$ Å^{-1}, instead of performing a much more time consuming multipolar refinement. Though the precision of y and z are relatively unaffected for most data sets, the exclusive use of high resolution

data provides a significant improvement in the precision of x (Fig. 8 and Fig. S5). This observation is also relevant because the number of reflections used is reduced by 25% when high resolution data are exclusively considered. It is in accordance with the behavior of the absolute structure parameters observed in Fig. 6. Even though there is an improvement in the precision of x the precision is still far from being adequate for unequivocal absolute structure determination. As shown by Parsons et al.[15,19] to obtain accurate values of the Flack parameter a weighting scheme based on the Bijvoet differences needs to be applied for the calculation of x.
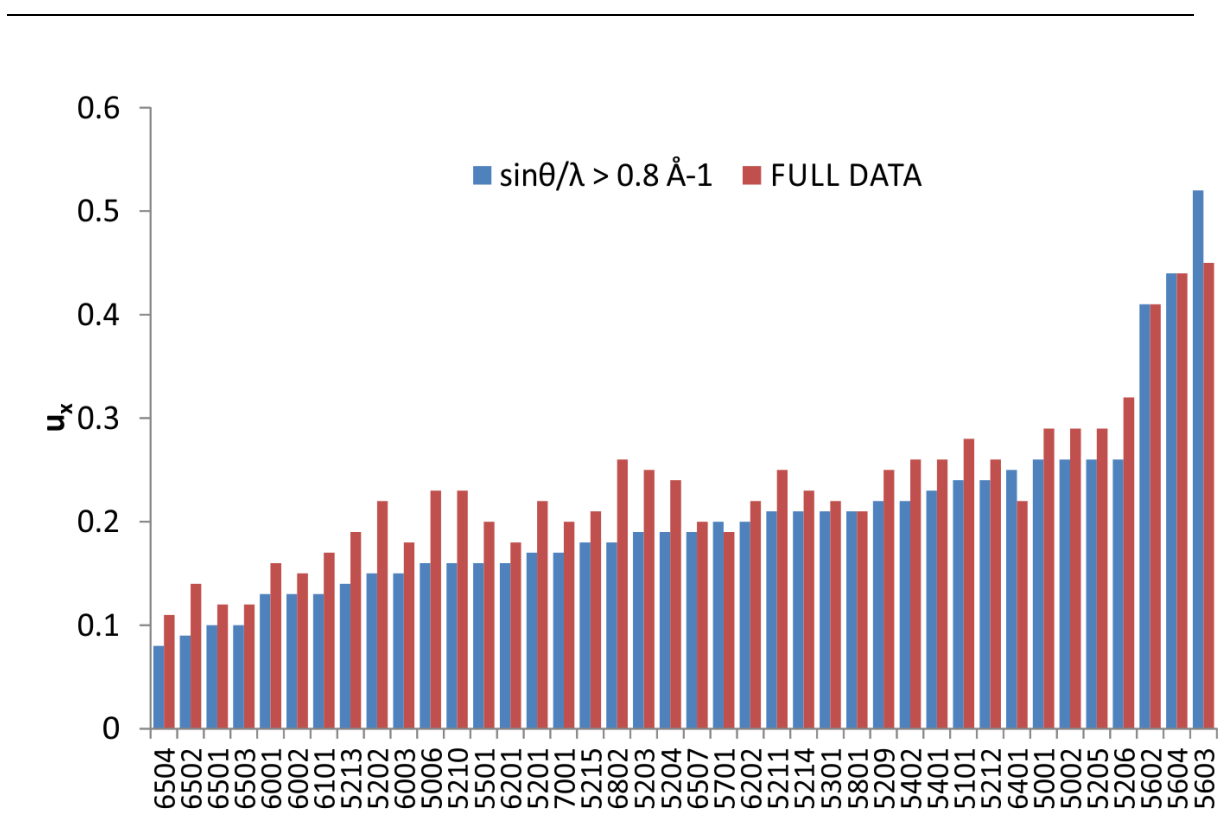
Figure 8. Plot of the standard uncertainties of *x* with and without low-resolution data included in refinement. The red bars represent the values of u_x with full data sets and blue dots with high resolution data sets, $\sin\vartheta/\lambda > 0.8$ Å^{-1}.

In addition to the leverage analysis of L-Alanine, we also performed leverage analyses on other data sets. We observed different distributions of the T^2 values with respect to the resolution ranges. In most of the data sets, the decay of the T^2 value at high resolution is

more pronounced and takes place at a lower resolution than in L-Alanine. Fig. 9 illustrates these observations using data sets of 5213 (D-threonine) and 6504 (sucrose); other examples are available in Fig. S4. Both data sets are of very good quality data with R_{int} < 0.02 and <I/σ(I)> > 30 up to 1.25 Å^{-1}; they also have similar values of Friedif$_{stat}$, 6.7 and 6.9 for 5213 and 6504 respectively. The largest values of T^2 and <T^2> are displaced to higher resolution than for L-alanine for 5213 and to lower resolution for 6504. The improvement in the precision of x resulting from omission of data with sin(θ)/λ < 0.8 Å^{-1} seen for 6504 seems to be inconsistent with the leverage analysis, which suggests that, the inclusion of reflection data acquired at low resolution should improve the precision of x. Our interpretation of the systematic errors associated with the spherical-atom model serves to explain the different behavior, observed in Section 3.4.1 for the values of the x parameter in comparison with those of the y and z analogues. While the consideration of high resolution data had a rather marked effect on the values of the absolute structure parameter x, the y and z parameters were less sensitive to the inclusion of high resolution data. In other words, the y and z parameters, which depend mainly on the Bijvoet ratios or differences, are not significantly influenced by the $||Fo|^2-|Fc|^2|$ differences of the full data set including the low resolution range.
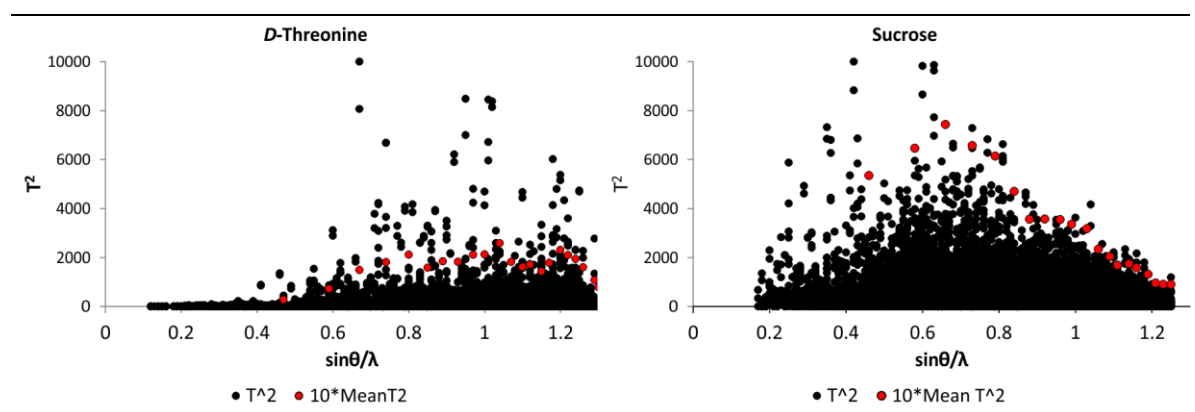
Figure 9. *T* analysis of the Flack parameter. T^2 versus sinϑ/λ for *D*-Threonine, sample 5213, (a) and sucrose, sample 6504, (b). The quantity *T* measures the influence of an observation of the Flack parameter, *x*.

4. Conclusion

A series of 44 high-resolution data sets collected using Mo *Kα* radiation have been used to determine the absolute structure parameters of enantiopure single crystals containing no atom heavier than oxygen. All the calculated absolute structure parameters assign the correct absolute configuration to the molecules; however, acceptable standard uncertainties are only obtained for the Hooft y and Parsons z parameters. The standard uncertainties determined for the Flack parameter are not sufficiently small to validate the assigned absolute configuration of any of the molecules except for sucrose.

In most of the tests the use of data limited to the IUCr minimum standard of resolution, $\sin(\theta)/\lambda \leq 0.6$ Å^{-1}, did not provide sufficiently accurate or precise absolute structure parameters. Accuracy and precision of the absolute structure parameter values is progressively improved by including data collected at higher resolution. All the structural parameter values benefit from the inclusion of data at high resolution ranges during structure refinement. The results of a T^2 analysis demonstrated that the distribution of resolution ranges influencing the accuracy of the Flack parameter, x, changes significantly in different structures. In spite of this generalization, the majority of absolute structure determinations based on the x value improve in accuracy when reflections at low resolution ranges are omitted. This finding demonstrates the sensitivity of the x parameter to systematic errors caused by exclusive consideration of diffraction data acquired at low resolution ranges using Mo *Kα* radiation in structure refinement. The y and z parameters seem to be less sensitive to this problem, though their accuracy is improved when diffraction data at the full range of resolution is considered. In general, when data sets of the same quality and Friedif$_{stat}$ are compared, the values and accuracies of their absolute structure parameters are better for crystals having larger asymmetric units. This fact is due to an increase in the number reflections used for their calculation.

In conclusion, reflection data acquired to high resolution with Mo *Kα* radiation can be used for the determination of the absolute configuration of light-atom molecules. The

proposed methodology consists on assigning the absolute structure of the crystal using the y (Hooft) and z (Parsons) parameters. Attending to the parameter defined in this work, η, values of $\eta \leq 2$ should lead to standard uncertainties of those parameters smaller than 0.1. The inclusion of high resolution data becomes especially important in crystals providing a small number of reflections. In the case of crystals with large asymmetric units, the consideration of reflection data acquired just at medium-high resolution suffices for the determination of accurate absolute structure parameters using the proposed methodology and Mo $K\alpha$ radiation.

5. References

(1)   Hooft, R. W. W.; Straver, L. H.; Spek, A. L. *J. Appl. Cryst.* **2008**, *41*, 96.

(2)   Parsons, S.; Flack, H. D.; Wagner, T. *Acta Cryst. B* **2013**, *69*, 249.

(3)   Thompson, A. L.; Watkin, D. J. *Tetrahedron: Asymmetry* **2009**, *20*, 712.

(4)   Flack, H. D.; Shmueli, U. *Acta Cryst. A* **2007**, *63*, 257.

(5)   Thompson, A. L.; Watkin, D. J. *J. Appl. Cryst.* **2011**, *44*, 1017.

(6)   Sheldrick, G. M. **2008**.

(7)   Blessing, R. H. *Acta Cryst. A* **1995**, *51*, 33.

(8)   Burla, M. C.; Caliandro, R.; Camalli, M.; Carrozzini, B.; Cascarano, G. L.; Giacovazzo, C.; Mallamo, M.; Mazzone, A.; Polidori, G.; Spagna, R. *J. Appl. Cryst.* **2012**, *45*, 357.

(9)   Sheldrick, G. M. *Acta Cryst. A* **2008**, *64*, 112.

(10)   Sheldrick, G. M. *SHELXL2013. University of Göttingen, Germany.* **2013**, .

(11)   Flack, H. D. *Acta Cryst. A* **1983**, *39*, 876.

(12)   Spek, A. L. *J. Appl. Cryst.* **2003**, *36*, 7.

(13)   Hooft, R. W. W.; Straver, L. H.; Spek, A. L. *Acta Cryst. A* **2009**, *65*, 319.

(14)   Betteridge, P. W.; Carruthers, J. R.; Cooper, R. I.; Prout, K.; Watkin, D. J. *J. Appl. Cryst.* **2003**, *36*, 1487.

(15)   Parsons, S.; Pattison, P.; Flack, H. D. *Acta Cryst. A* **2012**, *68*, 736.

(16)   Carreras, J.; Livendahl, M.; McGonigal, P. R.; Echavarren, A. M. *Angew Chem Int Edit* **2014**, *53*, 4896.

(17)   Nieto, N.; Molas, P.; Benet-Buchholz, J.; Vidal-Ferran, A. *J. Org. Chem.* **2005**, *70*, 10143.

(18)   Flack, H. D.; Bernardinelli, G. *J. Appl. Cryst.* **2000**, *33*, 1143.

(19)   Parsons, S.; Wagner, T.; Presly, O.; Wood, P. A.; Cooper, R. I. *J. Appl. Cryst.* **2012**, *45*, 417.

(20)   Jelsch, C.; Guillot, B.; Lagoutte, A.; Lecomte, C. *J. Appl. Cryst.* **2005**, *38*, 38.

(21)   Dittrich, B.; Strumpel, M.; Schafer, M.; Spackman, M. A.; Koritsanszky, T. *Acta Cryst. A* **2006**, *62*, 217.

(22)   Ruysink, A. F. J.; Vos, A. *Acta Cryst. A* **1974**, *A 30*, 503.

Note.

All the reported structures were measured using a CCD detector but 5215 whose data were collected using the first version of a CMOS detector (Photon 100 detector). The minimum Friedif$_{stat}$ of the reported compounds were 5.6 for compound 7701. For 7701, y=-0.02(10) and z=-0.04(11), i.e., the biggest reported standard deviation for the y and z parameters of this work. This may suggest that we are approximating to the distinguishing limit when using Mo $K\alpha$ radiation. However, in chapter 2, we reported the structure of a non-centrosymmetric crystal structure, crystalizing in $P2_12_12_1$. The crystallized compound has a Friedif$_{stat}$ = 2.9. For this crystal structure, the absolute structure parameters take values of 0.00 and 0.03 with standard deviations of 0.10-0.11, confirming the absolute structure determination. (see Table S1, Chapter 2)

5. Supporting information

Table S1 List of diffracted crystals including the chemical name of the enantiopure compound, the sample code of the diffraction data sets and the Chemical Abstracts Service Registry number assigned to each compound.

Compound	Sample code	Space Group	N of non H atoms in the asymmetric unit
L-Alanine	5001-5002	$P2_12_12_1$	*6*
D-Alanine	5006 and 5008	$P2_12_12_1$	*6*
L-Serine	5101	$P2_12_12_1$	*7*
D-Threonine	5201-5206, 5212-5215	$P2_12_12_1$	*8*
L-Threonine	5210-5211	$P2_12_12_1$	*8*
L-Aspartate	5301	$P2_1$	*9*
L-Hydroxyproline	5401- 5402	$P2_12_12_1$	*9*
L-Glutamine	5501	$P2_12_12_1$	*10*
L-Histidine	5602-5604	$P2_12_12_1$	*11*
L-Valine	5701	$P2_1$	*16*
L-Isoluecine	5801	$P2_1$	*18*
Methyl-α-*L*-rhamnopyranoside	6001-6003	$P2_12_12_1$	*12*
Methyl-α-*D*-mannopyranoside	6101	$P2_12_12_1$	*13*
Methyl-α-*D*-glucopyranoside	6201- 6202	$P2_12_12_1$	*13*
β-*D*-Galactose pentaacetate	6301	$P2_12_12_1$	*27*
β-*D*-Lactose monohydrate (milk sugar)	6401	$P2_12_12_1$	
β-*D*-Fructofuranosyl-α-*D*-glucopyranoside (sucrose)	6501-6504 and 6507	$P2_1$	*23*
β-*D*-Maltose octaacetate	6601	$P2_12_12_1$	*32*
β-*D*-Allose	6802	$P2_12_12_1$	*12*
L-Tartaric acid	7001	$P2_1$	*10*
C15H26O2	7701	$P2_12_12$	*17*
C11H14O6	7801	$P2_12_12_1$	*17*

Table S2 Measurement strategy

Operation	Distance (mm)	2θ (deg)	ω (deg)	φ (deg)	χ (deg)	Time (sec)	Width (deg)	Sweep (deg)
Omega Scan	40	-42.0	-42.0	0.0	54.74	2.0	0.3	104.0
Omega Scan	40	-42.0	-42.0	45.0	54.74	2.0	0.3	104.0
Omega Scan	40	-42.0	-42.0	90.0	54.74	2.0	0.3	104.0
Omega Scan	40	-42.0	-42.0	135.0	54.74	2.0	0.3	104.0
Omega Scan	40	-42.0	-42.0	180.0	54.74	2.0	0.3	104.0
Omega Scan	40	-42.0	-42.0	225.0	54.74	2.0	0.3	104.0
Omega Scan	40	-42.0	-42.0	270.0	54.74	2.0	0.3	104.0
Omega Scan	40	-42.0	-42.0	315.0	54.74	2.0	0.3	104.0
Phi Scan	40	-42.0	-146.0	0.0	54.74	2.0	0.3	360.0
Omega Scan	40	-94.0	-94.0	0.0	54.74	30.0	0.3	104.0
Omega Scan	40	-94.0	-94.0	45.0	54.74	30.0	0.3	104.0
Omega Scan	40	-94.0	-94.0	90.0	54.74	30.0	0.3	104.0
Omega Scan	40	-94.0	-94.0	135.0	54.74	30.0	0.3	104.0
Omega Scan	40	-94.0	-94.0	180.0	54.74	30.0	0.3	104.0
Omega Scan	40	-94.0	-94.0	225.0	54.74	30.0	0.3	104.0
Omega Scan	40	-94.0	-94.0	270.0	54.74	30.0	0.3	104.0
Omega Scan	40	-94.0	-94.0	315.0	54.74	30.0	0.3	104.0

Table S3. Values of the optimized number of degrees of freedom, v, for a t-distribution.

Sample code	v		Sample code	v
5001	99.4		6001	26.9
5002	99.4		6002	99.9
5006	99.6		6003	19.0
5008	99.7		6101	23.7
5101	99.9		6201	34.0
5201	99.4		6202	47.3
5202	62.0		6301	99.7
5203	37.8		6401	99.3
5204	99.0		6501	15.8
5205	100.0		6502	12.1
5206	99.6		6503	15.1
5210	29.5		6504	18.9
5211	28.6		6507	52.8
5212	99.7		6601	99.4
5213	99.0		6802	7.1
5214	99.5		7001	41.9
5215	99.4		7701	99.4
5301	32.4		7801	99.6
5401	99.5			
5402	99.8			
5501	98.9			
5602	99.6			
5603	62.3			
5604	26.9			
5701	49.1			
5801	18.9			

Table S4 Calculated values of the y and z parameters and their corresponding standard uncertainties after removing different percentages of random reflections for three data sets 5213, 5602 and 6601. N is the number of reflections, Nf is the number of Friedel pairs, R_1 is the R_1 factor, $Redun$ is the redundancy, $Tan^{-1}(Redun)$ is the arctangent of the redundancy, u_y and u_z are the calculated standard uncertainties. In order to show the influence of the number of reflections[1] two more theoretical standard uncertainties were calculated, u_{yn} and u_{zn} without considering N and $u_{yn'}$ and $u_{zn'}$ considering N, being $u_{y(100\%)}$ and $u_{z(100\%)}$ the standard uncertainties obtained from the refinement with the full data set, as follows:

$$u_{yn} = u_{y(100\%)} \cdot \frac{R_1}{R_1 all} \cdot \frac{\tan^{-1} Redun\ (all)}{\tan^{-1} Redun} \ ; \ u_{zy} = u_{y(100\%)} \cdot \sqrt{\frac{Nf(all)}{Nf}} \cdot \frac{R_1}{R_1 all} \cdot \frac{\tan^{-1} Redun\ (all)}{\tan^{-1} Redun} ; \ u_{zn} \text{ and } u_{zn'} \text{ analogous to } u_{yn} \text{ and } u_{zn'} \text{ respectively.}$$

5213

% of N	% of Friedel pairs	N	Nf	R_1	Redun	$Tan^{-1}(Redun)$	y	u_y	u_{yn}	$u_{yn'}$	z	u_z	u_{zn}	$u_{zn'}$
100%	100%	8775	3844	0.0196	5.9	1.40	-0.04	0.05	0.05	0.05	-0.03	0.04	0.04	0.04
96%	94%	8454	3612	0.0201	4.0	1.32	0.00	0.06	0.05	0.06	0.01	0.06	0.04	0.04
93%	88%	8126	3372	0.0206	3.0	1.25	0.03	0.07	0.06	0.06	0.01	0.07	0.05	0.05
84%	73%	7339	2798	0.0216	2.0	1.10	-0.04	0.09	0.07	0.08	-0.03	0.09	0.06	0.07
76%	61%	6693	2341	0.0215	1.5	0.98	-0.07	0.11	0.08	0.10	-0.07	0.10	0.06	0.08
69%	50%	6042	1929	0.0225	1.2	0.87	-0.13	0.12	0.09	0.13	-0.13	0.12	0.07	0.10

5602

% of N	% of Friedel pairs	N	Nf	R_1	Redun	$Tan^{-1}(Redun)$	y	u_y	u_{yn}	$u_{yn'}$	z	u_z	u_{zn}	$u_{zn'}$
100%	100%	10624	4658	0.0299	5.1	1.38	-0.03	0.08	0.08	0.08	0.05	0.07	0.07	0.07
25%	94%	10190	4376	0.0300	3.4	1.29	0.11	0.08	0.09	0.09	0.12	0.08	0.08	0.08
24%	86%	9687	4015	0.0302	2.6	1.20	0.16	0.09	0.09	0.10	0.16	0.09	0.08	0.09
76%	71%	8656	3311	0.0303	1.7	1.04	0.10	0.13	0.11	0.13	0.07	0.12	0.09	0.11
66%	57%	7630	2632	0.0299	1.3	0.91	0.07	0.16	0.12	0.16	0.03	0.14	0.11	0.14
59%	48%	6904	2241	0.0305	1.0	0.81	-0.09	0.18	0.14	0.20	-0.16	0.17	0.12	0.18

6601

% of N	% of Friedel pairs	N	Nf	R_1	Redun	$Tan^{-1}(Redun)$	y	u_y	u_{yn}	$u_{yn'}$	z	u_z	u_{zn}	$u_{zn'}$
100%	100%	40459	25547	0.0629	4.8	1.37	-0.03	0.08	0.08	0.08	0.05	0.10	0.10	0.10
93%	92%	37536	23593	0.0660	3.2	1.27	0.07	0.13	0.09	0.09	0.10	0.13	0.11	0.12
86%	82%	34921	20829	0.0671	2.4	1.18	0.09	0.16	0.10	0.11	0.13	0.15	0.12	0.14
76%	63%	30552	16068	0.0686	1.6	1.02	-0.20	0.20	0.12	0.15	-0.10	0.20	0.15	0.18
66%	49%	26771	12410	0.0700	1.2	0.88	-0.20	0.20	0.14	0.20	-0.10	0.20	0.17	0.25
59%	39%	23845	9972	0.0713	1.0	0.77	0.40	0.30	0.16	0.26	0.40	0.30	0.20	0.32

[1] When removing random reflections from the data set the number of Friedel pairs will decay faster than the number of total reflections.

Table S5. Values of the absolute structure parameters y and z and their corresponding standard deviations at different resolution cut-offs. First row contains the values of the η parameter.

	5001	5002	5006	5008	5101	5201	5202	5203	5204	5205	5206	5210	5211	5212	5213	5214	5215	5301	5401	5402	5501	5602
η	1.44	1.60	1.06	1.34	1.38	0.93	0.92	1.00	0.94	1.34	1.36	0.98	1.24	1.07	0.86	1.02	0.92	1.27	0.95	0.93	0.88	1.52
Y																						
1.28	0.05	0.01	-0.02	-0.01	0.06	0.04	-0.04	0.06	0.02	0.00	0.10	0.08	0.06	0.01	-0.04	0.07	-0.02	0.01	0.03	0.05	0.07	0.07
1.00	-0.01	0.02	-0.02	0.01	0.11	0.04	-0.05	0.05	0	0.06	0.06	0.08	0.03	-0.11	-0.01	0.1	-0.04	-0.06	0.03	0.04	0.02	0.06
0.89	-0.03	-0.1	-0.03	0.01	0.12	0.05	-0.05	-0.03	-0.01	0.04	0.04	0.07	0.06	-0.07	-0.04	0.24	-0.02	0.02	0.05	0.05	-0.02	0.11
0.81	0	-0.09	-0.04	0.01	0.12	0.11	0.06	-0.05	-0.05	0.03	0.03	0.07	0.06	-0.09	-0.09	0.31	-0.02	-0.03	0.04	0.08	0.03	0.19
0.68	-0.24	0.13	0.44	-0.08	0.1	0.28	0.11	-0.17	0.01	0.04	0.04	-0.1	0.25	-0.2	0	0.7	-0.03	0.1	-0.03	0.03	0.12	0.25
0.60	0.07	-0.3	0.7	0	0.15	0.18	-0.1	0.16	0.13	-0.19	-0.19	-0.11	0.4	-0.1	0.07	0.6	0.14	0	0.01	0.1	0.2	0.35
U(Y)																						
1.28	0.07	0.09	0.04	0.04	0.04	0.04	0.05	0.05	0.05	0.09	0.08	0.03	0.07	0.09	0.04	0.06	0.05	0.08	0.03	0.03	0.05	0.06
1.00	0.08	0.1	0.06	0.05	0.05	0.05	0.05	0.06	0.05	0.07	0.07	0.03	0.08	0.09	0.05	0.08	0.05	0.09	0.03	0.03	0.05	0.07
0.89	0.09	0.11	0.07	0.05	0.06	0.06	0.06	0.06	0.06	0.08	0.08	0.04	0.09	0.11	0.06	0.1	0.05	0.11	0.04	0.04	0.07	0.08
0.81	0.1	0.12	0.09	0.07	0.07	0.06	0.07	0.07	0.07	0.08	0.08	0.04	0.09	0.12	0.07	0.13	0.06	0.13	0.05	0.05	0.07	0.09
0.68	0.13	0.16	0.17	0.12	0.11	0.09	0.12	0.11	0.11	0.11	0.11	0.07	0.14	0.2	0.12	0.2	0.09	0.2	0.07	0.07	0.1	0.14
0.60	0.18	0.2	0.2	0.13	0.14	0.11	0.16	0.16	0.15	0.14	0.14	0.11	0.17	0.2	0.16	0.3	0.13	0.3	0.08	0.1	0.12	0.18
Z																						
1.28	0.06	0.04	0.02	-0.01	0.07	0.05	-0.03	0.07	0.02	-0.01	0.10	0.08	0.06	0.02	-0.04	0.07	-0.02	0.01	0.03	0.06	0.08	0.09
1.00	0	0.06	-0.02	0.01	0.12	0.05	-0.04	0.06	0.01	0.05	0.05	0.08	0.04	-0.12	-0.01	0.11	-0.04	-0.05	0.04	0.05	0.03	0.08
0.89	-0.02	-0.04	0.04	0.01	0.14	0.06	-0.03	-0.02	0	0.03	0.03	0.07	0.07	-0.09	-0.04	0.27	-0.02	0.04	0.07	0.06	-0.03	0.12
0.81	0.02	-0.04	0.03	0.01	0.13	0.12	0.08	-0.03	-0.04	0.02	0.02	0.08	0.07	-0.1	-0.09	0.35	-0.02	-0.02	0.05	0.08	0.03	0.22
0.68	-0.2	-0.01	0.26	-0.07	0.1	0.29	0.13	-0.14	0.01	0.04	0.04	-0.07	0.26	-0.3	0	0.8	-0.05	0.1	-0.02	0.04	0.11	0.26
0.60	0.1	-0.4	0.5	-0.03	0.15	0.2	-0.1	0.2	0.1	-0.18	-0.18	-0.04	0.2	-0.1	0.04	0.7	0.11	0.2	0	0.1	0.18	0.37
U(Z)																						
1.28	0.08	0.1	0.04	0.04	0.05	0.05	0.05	0.06	0.06	0.1	0.07	0.03	0.07	0.09	0.04	0.06	0.05	0.08	0.03	0.03	0.05	0.06
1.00	0.08	0.11	0.06	0.05	0.06	0.06	0.06	0.07	0.07	0.08	0.08	0.04	0.09	0.12	0.05	0.09	0.05	0.1	0.04	0.04	0.06	0.07
0.89	0.09	0.12	0.07	0.06	0.07	0.07	0.07	0.08	0.08	0.09	0.09	0.05	0.1	0.15	0.07	0.12	0.06	0.11	0.04	0.04	0.07	0.08
0.81	0.1	0.14	0.09	0.07	0.08	0.08	0.09	0.09	0.09	0.09	0.09	0.05	0.12	0.17	0.08	0.16	0.07	0.13	0.05	0.05	0.09	0.09
0.68	0.15	0.19	0.17	0.11	0.12	0.12	0.15	0.14	0.15	0.12	0.12	0.08	0.18	0.3	0.13	0.2	0.1	0.2	0.07	0.08	0.13	0.13
0.60	0.2	0.3	0.2	0.15	0.16	0.15	0.2	0.2	0.2	0.14	0.14	0.12	0.4	0.3	0.16	0.3	0.15	0.3	0.1	0.12	0.16	0.17

Table S5. Continuation.

	5603	5604	5701	5801	6001	6002	6003	6101	6201	6202	6301	6401	6501	6502	6503	6504	6507	6601	6802	7001	7701	7801
η	1.87	1.58	0.94	1.00	0.72	0.81	0.84	0.71	0.80	0.91	0.91	0.91	0.57	0.55	0.56	0.50	1.11	1.24	1.08	1.11	1.43	1.68
Y																						
1.28	0.08	0.00	0.10	-0.04	-0.04	0.07	0.11	-0.06	0.02	0.02	0.01	-0.01	0.04	0.05	-0.01	0.04	0.07	0.01	-0.08	0.04	-0.03	-0.03
1.00	0.1	-0.01	0.16	0.03	-0.05	0.04	0.06	-0.05	0.01	0.02	0.04	0.03	0.06	0.04	0.01	0.04	0.09	-0.06	-0.05	0.11	-0.04	-0.05
0.89	0.1	0.06	0.21	0.04	-0.06	0.07	0.08	-0.02	0.03	0.06	0.03	0.05	0.05	0.02	0.03	0.04	0.12	-0.06	-0.04	0.15	-0.02	-0.06
0.81	0.13	0.04	0.28	0.05	-0.06	0.07	0.11	0	0.06	0.09	0.06	0.06	0.03	-0.01	0.02	0.04	0.13	-0.15	-0.03	0.1	0.01	-0.09
0.68	0.13	0.1	0.4	0.2	0.05	0.12	0.13	0.11	0.02	0.1	0.07	0.006	-0.1	-0.22	0.03	0.02	0.19	-0.26	-0.04	0.26	0.06	-0.06
0.60	0.2	0.2	0.3	0.4	-0.02	0.03	0.01	0.21	0.1	0	0.07	0.09	-0.19	-0.25	0.01	0.06	0.31	-0.31	0.07	-0.3	0.02	-0.02
U(Y)																						
1.28	0.08	0.06	0.08	0.08	0.04	0.03	0.03	0.03	0.03	0.05	0.05	0.05	0.04	0.04	0.03	0.02	0.07	0.09	0.08	0.07	0.1	0.07
1.00	0.09	0.07	0.1	0.08	0.04	0.04	0.05	0.04	0.04	0.05	0.06	0.05	0.04	0.04	0.04	0.03	0.08	0.09	0.08	0.09	0.1	0.08
0.89	0.1	0.07	0.12	0.1	0.05	0.05	0.06	0.04	0.04	0.06	0.06	0.06	0.05	0.05	0.05	0.03	0.08	0.1	0.09	0.1	0.1	0.08
0.81	0.12	0.09	0.14	0.11	0.05	0.06	0.07	0.05	0.05	0.06	0.06	0.07	0.05	0.06	0.05	0.04	0.09	0.11	0.1	0.12	0.11	0.09
0.68	0.16	0.13	0.2	0.2	0.07	0.08	0.12	0.07	0.07	0.09	0.08	0.09	0.08	0.09	0.09	0.06	0.11	0.14	0.13	0.19	0.13	0.11
0.60	0.2	0.16	0.3	0.2	0.08	0.12	0.18	0.08	0.08	0.11	0.09	0.12	0.1	0.14	0.11	0.08	0.14	0.17	0.17	0.3	0.14	0.13
Z																						
1.28	0.08	0.00	0.12	-0.04	-0.04	0.07	0.11	-0.07	0.02	0.00	0.02	0.01	0.02	0.06	-0.02	0.04	0.04	0.10	-0.04	0.08	-0.04	-0.04
1.00	0.1	-0.02	0.18	0.03	-0.05	0.04	0.07	-0.05	0.01	0.01	0.04	0.06	0.04	0.06	0.01	0.04	0.06	0.03	-0.01	0.14	-0.05	-0.05
0.89	0.1	0.05	0.21	0.06	-0.06	0.07	0.09	-0.02	0.03	0.06	0.04	0.09	0.04	0.05	0.01	0.04	0.1	0.03	0.01	0.18	-0.04	-0.06
0.81	0.12	0.05	0.29	0.08	-0.06	0.07	0.12	0	0.06	0.08	0.07	0.08	0.01	0.04	0.01	0.04	0.1	-0.05	0.05	0.13	0.01	-0.09
0.68	0.03	0.09	0.4	0.2	0.05	0.11	0.11	0.12	0.03	0.11	0.08	0.08	-0.12	-0.19	0.03	0.01	0.17	-0.18	0.06	0.3	0.06	-0.06
0.60	0.1	0.18	0.3	0.4	-0.01	0.01	0.01	0.21	0.11	0.01	0.08	0.12	-0.21	-0.22	-0.04	0.05	0.34	-0.29	0.23	-0.2	0.02	0.00
U(Z)																						
1.28	0.11	0.07	0.08	0.08	0.04	0.04	0.04	0.03	0.04	0.06	0.06	0.05	0.04	0.03	0.04	0.02	0.07	0.09	0.08	0.08	0.1	0.07
1.00	0.12	0.08	0.10	0.10	0.05	0.05	0.05	0.04	0.04	0.06	0.05	0.05	0.04	0.04	0.04	0.03	0.08	0.1	0.08	0.1	0.11	0.07
0.89	0.13	0.09	0.11	0.11	0.06	0.05	0.06	0.04	0.04	0.07	0.06	0.06	0.05	0.05	0.05	0.03	0.09	0.11	0.09	0.12	0.12	0.07
0.81	0.14	0.10	0.13	0.13	0.06	0.06	0.06	0.05	0.05	0.08	0.06	0.07	0.06	0.05	0.06	0.04	0.10	0.12	0.09	0.14	0.12	0.08
0.68	0.18	0.15	0.2	0.2	0.09	0.09	0.09	0.07	0.07	0.11	0.08	0.10	0.09	0.09	0.10	0.06	0.12	0.16	0.12	0.2	0.14	0.10
0.60	0.2	0.19	0.3	0.2	0.11	0.13	0.13	0.09	0.09	0.13	0.10	0.12	0.11	0.13	0.12	0.08	0.15	0.19	0.16	0.3	0.15	0.12

Table S6. Absolute structure parameters x, y and z calculated using Friedel opposites from different high resolution cutoffs, 0.6, 0.7, 0.8, 0.9 and 1.0 and no cutoff data.

	u_x	x						u_y	y						u_z	z					
Sample code		0.6	0.7	0.8	0.9	1.0	Full		0.6	0.7	0.8	0.9	1.0	Full		0.6	0.7	0.8	0.9	1.0	Full
5001 salanin	0.29	0.99	0.68	0.52	0.33	0.23	-0.08	0.07	0.86	0.64	0.46	0.24	0.14	0.05	0.07	0.86	0.64	0.44	0.24	0.13	0.06
5002 Lalanine04	0.29	1.04	0.84	0.61	0.53	0.36	0.03	0.07	0.86	0.72	0.46	0.29	0.24	0.01	0.07	0.85	0.72	0.49	0.32	0.28	0.04
5006 Dalanina	0.23	1	0.89	0.71	0.54	0.38	-0.14	0.04	1.03	0.97	0.72	0.51	0.37	-0.02	0.04	1.00	0.97	0.72	0.51	0.40	0.02
5101 Lserin	0.28	0.88	0.81	0.77	0.66	0.51	0.07	0.04	0.87	0.79	0.70	0.56	0.45	0.06	0.04	0.86	0.78	0.70	0.57	0.46	0.07
5201 Dthreonin	0.22	0.88	0.9	0.78	0.64	0.45	0.10	0.05	0.90	0.87	0.62	0.44	0.28	0.04	0.05	0.90	0.86	0.62	0.44	0.28	0.05
5202 Dthreonin_0m	0.22	0.93	0.89	0.77	0.58	0.35	-0.03	0.05	0.98	0.94	0.77	0.51	0.27	-0.04	0.05	0.98	0.94	0.75	0.50	0.28	-0.03
5203 Dthreonin0126	0.25	0.88	0.73	0.6	0.5	0.36	0.02	0.05	0.86	0.69	0.51	0.37	0.26	0.06	0.05	0.85	0.67	0.50	0.36	0.25	0.07
5204 Dthreonin0216	0.24	0.9	0.8	0.65	0.51	0.35	0.02	0.05	0.92	0.78	0.59	0.43	0.26	0.02	0.05	0.92	0.78	0.59	0.44	0.28	0.02
5205 Dthreoninbr	0.29	0.83	0.58	0.34	0.24	0.15	0.02	0.09	0.82	0.55	0.12	0.12	0.06	0.00	0.10	0.81	0.53	0.21	0.11	0.05	-0.01
5206 Dthreoninbr	0.32	0.48	0.52	0.34	0.32	0.38	0.29	0.07	0.52	0.48	0.24	0.13	0.13	0.10	0.08	0.51	0.46	0.21	0.11	0.11	0.10
5210 L-Threo100k	0.23	0.8	0.7	0.62	0.54	0.39	0.13	0.03	0.82	0.69	0.56	0.43	0.29	0.08	0.03	0.82	0.68	0.55	0.43	0.29	0.08
5211 L-Threo100kb	0.25	0.96	0.9	0.73	0.54	0.34	0.13	0.07	0.94	0.87	0.58	0.40	0.20	0.06	0.07	0.93	0.87	0.59	0.42	0.22	0.06
5212 Dthreo_1	0.26	0.94	0.81	0.65	0.57	0.30	0.10	0.09	0.93	0.80	0.57	0.45	0.18	0.01	0.09	0.92	0.80	0.58	0.45	0.18	0.02
5213 Threonin_UB	0.19	1.01	0.89	0.73	0.63	0.45	0.05	0.04	0.98	0.89	0.65	0.48	0.32	-0.04	0.04	0.99	0.89	0.64	0.48	0.32	-0.04
5214 Dthrenin_UB_DUO	0.23	0.88	0.91	0.8	0.64	0.38	-0.12	0.06	0.93	0.95	0.75	0.61	0.39	0.07	0.06	0.94	0.96	0.76	0.62	0.40	0.07
5215 DthreoUBPho	0.21	0.92	0.77	0.66	0.58	0.43	0.09	0.05	0.95	0.77	0.57	0.41	0.24	-0.02	0.04	0.94	0.76	0.55	0.39	0.23	-0.02
5301 Laspat100k	0.22	0.9	0.91	0.8	0.71	0.35	0.05	0.08	0.90	0.82	0.63	0.46	0.25	0.01	0.08	0.91	0.84	0.64	0.46	0.26	0.01
5401 LHrdroxP	0.26	0.87	0.84	0.76	0.61	0.38	-0.07	0.03	0.86	0.78	0.59	0.43	0.25	0.03	0.03	0.86	0.79	0.60	0.44	0.26	0.03
5402 LHrdroxPb	0.26	0.87	0.74	0.64	0.49	0.33	0.07	0.03	0.89	0.79	0.62	0.43	0.25	0.05	0.03	0.87	0.76	0.61	0.42	0.25	0.06
5501 LGlutSa	0.2	0.76	0.69	0.6	0.45	0.39	0.06	0.05	0.84	0.76	0.61	0.40	0.30	0.07	0.05	0.83	0.75	0.60	0.40	0.31	0.08
5602 LHistidinB	0.41	0.77	0.73	0.73	0.54	0.46	0.17	0.06	0.85	0.82	0.65	0.44	0.29	0.07	0.06	0.86	0.81	0.64	0.42	0.29	0.09
5603 LHistidinC	0.45	1.03	0.82	0.7	0.48	0.24	-0.15	0.08	0.79	0.65	0.48	0.30	0.22	0.08	0.11	0.78	0.63	0.44	0.29	0.21	0.08
5604 Lhistidin	0.44	0.83	0.63	0.69	0.57	0.35	0.09	0.07	0.91	0.79	0.60	0.45	0.23	0.00	0.06	0.92	0.79	0.57	0.42	0.20	0.00
5701 LValin	0.19	0.85	0.94	0.84	0.71	0.51	0.14	0.08	0.85	0.90	0.72	0.56	0.45	0.10	0.08	0.80	0.85	0.69	0.53	0.46	0.12
5801 Lisoleucine	0.21	1.02	0.85	0.65	0.45	0.32	-0.23	0.08	0.99	0.96	0.73	0.54	0.41	-0.04	0.08	0.98	0.95	0.73	0.53	0.39	-0.04
6001 Malrpb	0.16	1.02	0.93	0.75	0.55	0.39	-0.08	0.04	0.91	0.83	0.56	0.34	0.18	-0.04	0.04	0.91	0.82	0.55	0.33	0.18	-0.04

Table S6. Continuation.

	u_x	x						u_y	y						u_z	z					
6002 Malr100ka	0.15	0.94	0.91	0.68	0.57	0.36	0.03	0.03	0.87	0.79	0.61	0.42	0.27	0.07	0.03	0.87	0.80	0.59	0.42	0.26	0.07
6003 Malr100kc	0.18	0.87	0.8	0.68	0.53	0.30	0.10	0.04	0.85	0.77	0.64	0.45	0.27	0.11	0.03	0.85	0.77	0.61	0.43	0.27	0.11
6101 MaDMan	0.17	1.03	0.94	0.8	0.63	0.33	-0.09	0.03	0.98	0.89	0.61	0.38	0.18	-0.06	0.03	0.98	0.89	0.60	0.37	0.17	-0.07
6201 MaDGlu	0.18	0.83	0.73	0.64	0.53	0.35	0.05	0.03	0.85	0.74	0.55	0.34	0.20	0.02	0.03	0.84	0.74	0.55	0.34	0.19	0.02
6202 aDHeptaL	0.22	0.87	0.79	0.75	0.64	0.44	0.07	0.05	0.81	0.74	0.56	0.37	0.19	0.02	0.05	0.82	0.74	0.56	0.36	0.18	0.00
6301 BDGalP	0.21	0.97	0.82	0.71	0.42	0.26	-0.07	0.05	0.71	0.58	0.38	0.18	0.12	0.01	0.05	0.69	0.58	0.38	0.18	0.11	0.02
6401 BDLactose	0.22	0.94	0.81	0.65	0.42	0.34	-0.02	0.05	0.88	0.76	0.53	0.32	0.22	-0.01	0.05	0.83	0.74	0.52	0.33	0.24	0.01
6501 aDGluBDFru	0.12	0.86	0.71	0.66	0.57	0.43	-0.07	0.04	0.82	0.73	0.64	0.52	0.37	0.04	0.03	0.83	0.74	0.65	0.49	0.35	0.02
6502 aDGlu-BDFruE	0.14	0.81	0.66	0.55	0.42	0.29	0.02	0.04	0.85	0.71	0.59	0.43	0.29	0.05	0.03	0.83	0.70	0.59	0.43	0.30	0.06
6503 azucar	0.12	0.98	0.91	0.79	0.58	0.39	-0.08	0.03	0.93	0.88	0.73	0.51	0.31	-0.01	0.03	0.92	0.87	0.71	0.48	0.29	-0.02
6504 adglubfru-a	0.11	0.93	0.91	0.77	0.65	0.45	0.03	0.02	0.89	0.81	0.63	0.47	0.31	0.04	0.02	0.88	0.80	0.61	0.46	0.30	0.04
6507 adGluBdFru_0m	0.2	1.03	0.73	0.51	0.36	0.28	-0.18	0.07	0.81	0.69	0.54	0.37	0.28	0.07	0.07	0.84	0.71	0.52	0.35	0.26	0.04
7001 Ltartaric	0.2	0.91	0.87	0.78	0.65	0.52	0.04	0.07	0.88	0.82	0.71	0.53	0.39	0.04	0.08	0.86	0.81	0.71	0.55	0.40	0.08
7701 JCP106	0.33	0.63	0.64	0.49	0.29	0.06	-0.07	0.10	0.54	0.44	0.24	0.04	-0.04	-0.03	0.10	0.54	0.44	0.24	0.01	-0.06	-0.04
7801 NN43a2ab	0.43	0.68	0.42	0.13	0.12	0.00	0.07	0.07	0.66	0.42	0.09	0.01	-0.04	-0.03	0.07	0.65	0.41	0.09	0.01	-0.03	-0.04
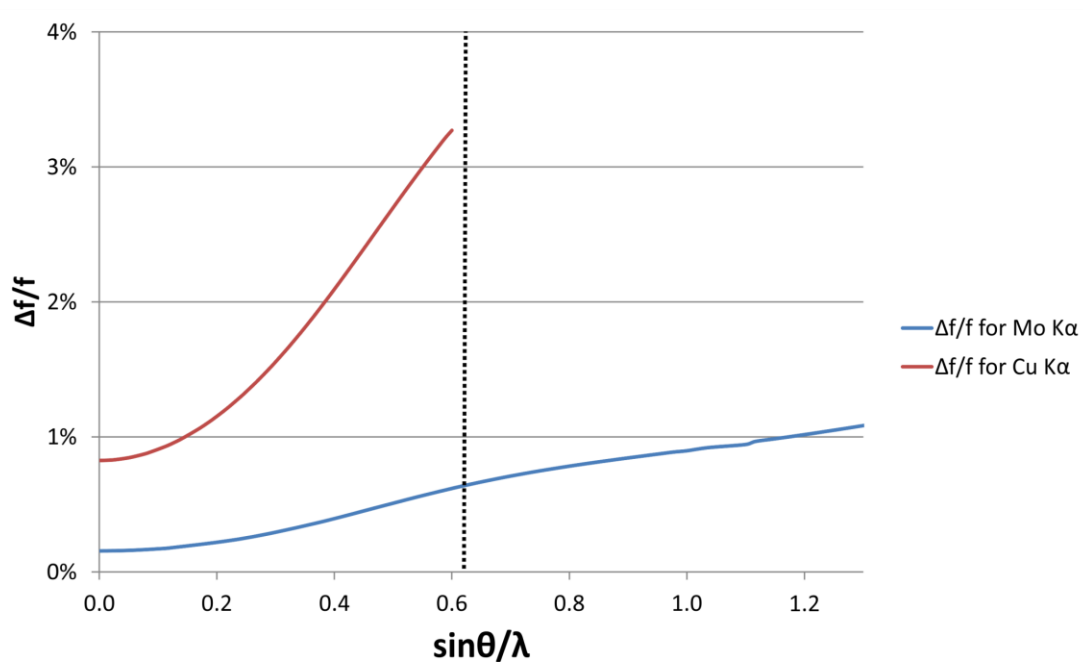
Figure S 1. Plots of the maximum relative difference between Friedel pairs in atomic scattering factor for an oxygen atom due to resonant scattering effects for Cu *Kα* radiation, red line and Mo *Kα* radiation, blue line. The dotted line represents the physical limit of the Cu *Kα* radiation.

a)   b)   c)

d)   e)   f)
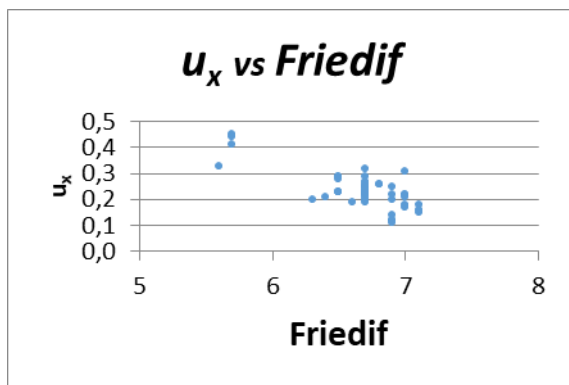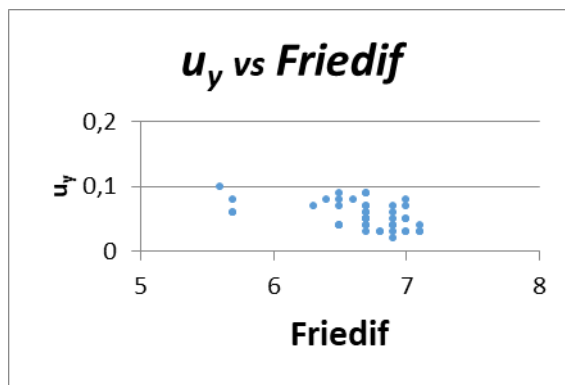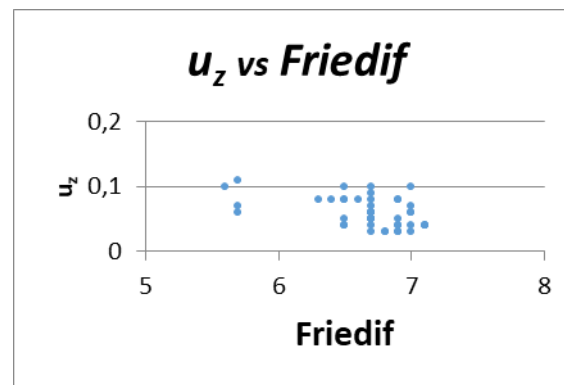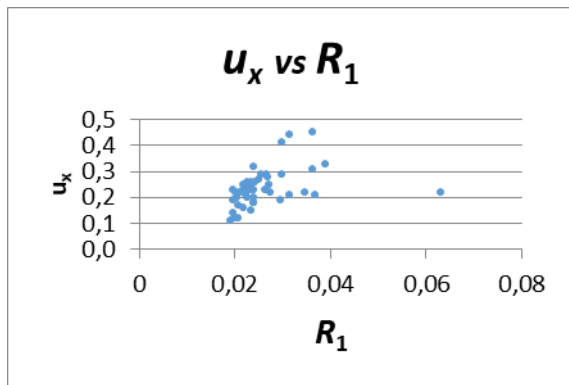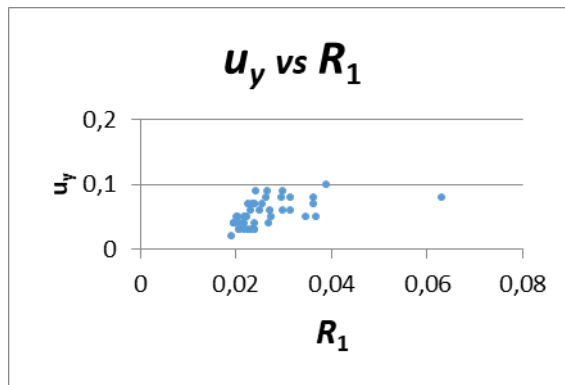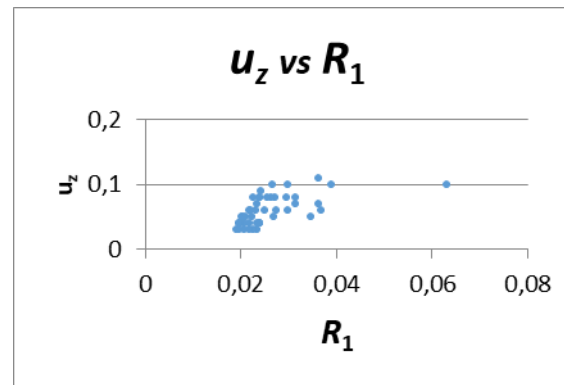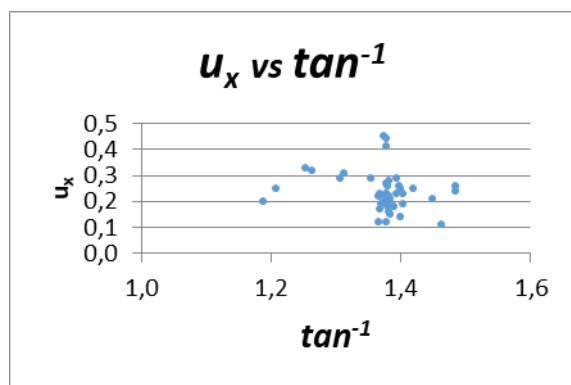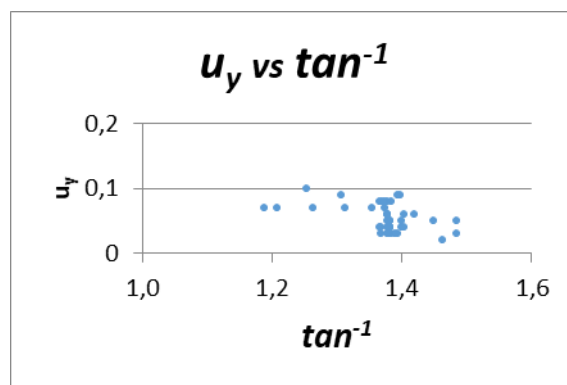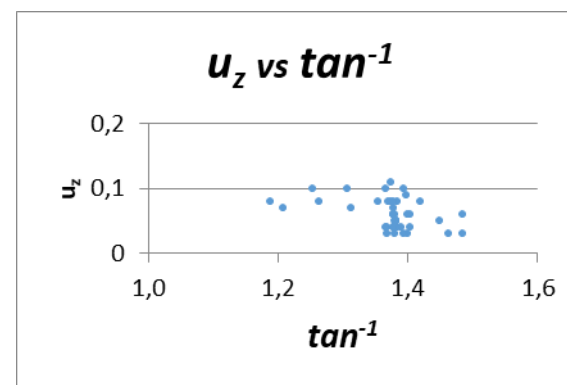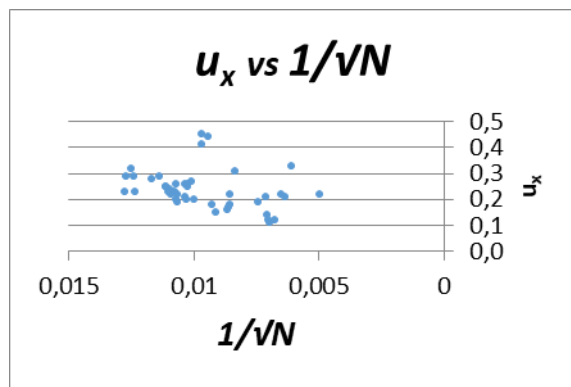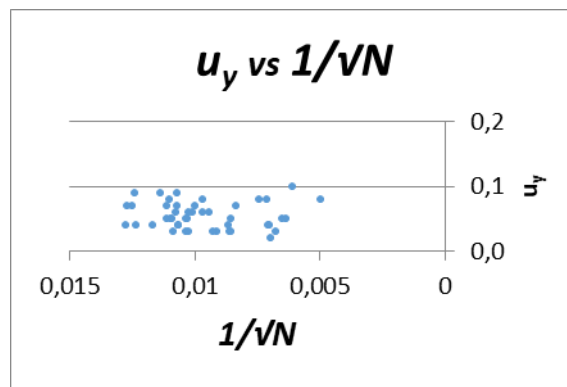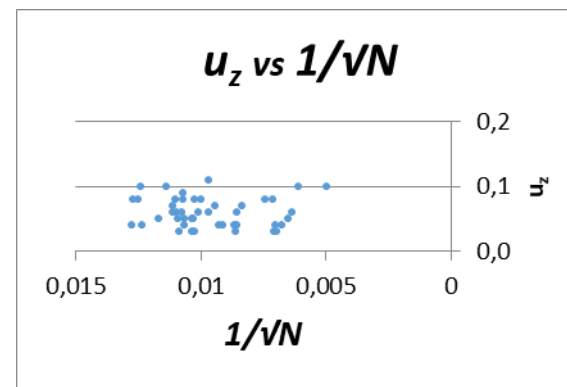
Figure S 2. Standard uncertainties of the absolute structure parameters *vs Friedif*$_{stat}$ (a), (b) and (c), *vs* R_1 (d), (e), and (f), *vs tan*$^{-1}$ (g), (h) and (l) and vs $1/\sqrt{N}$ (j), (k) and (l)

a)
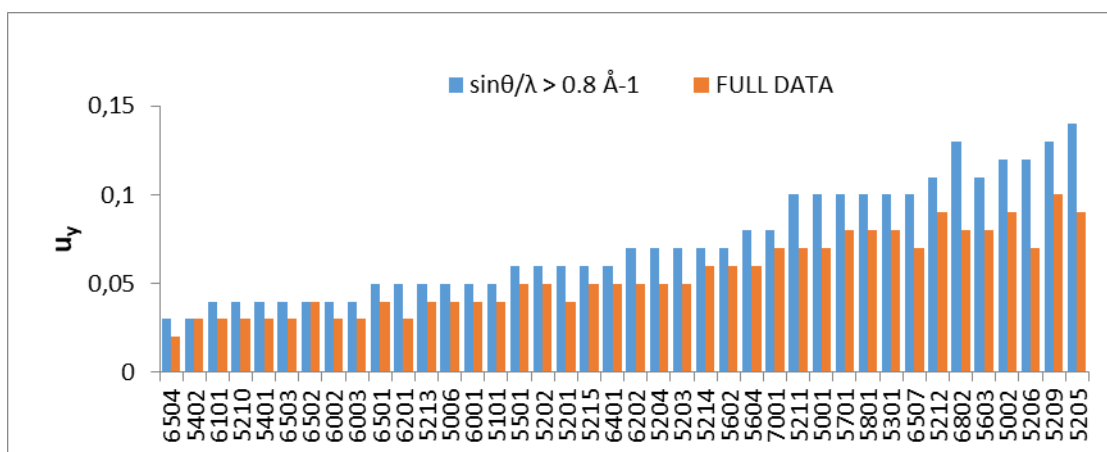
b)
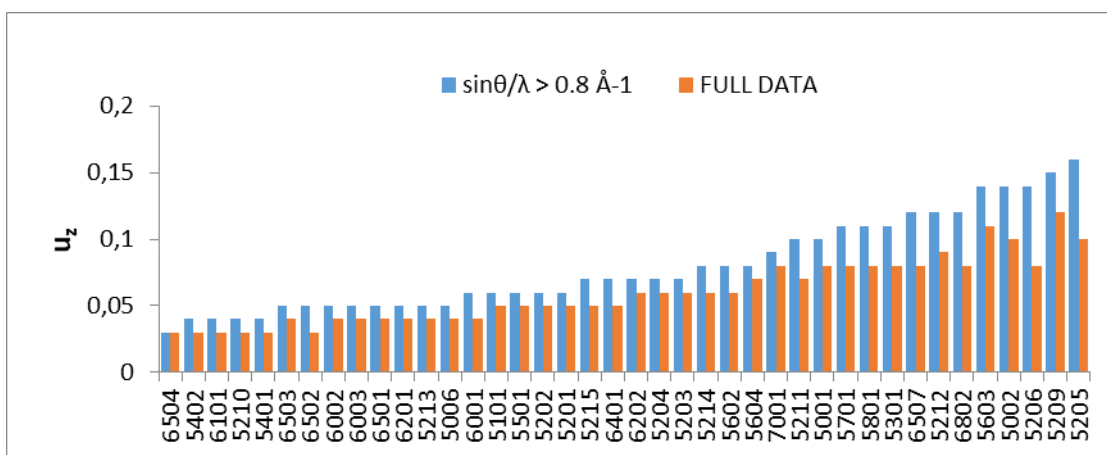
Figure S 3. Plots of the standard uncertainties of y, a) and z, b). The red dots represent the values of uy and uz with full data sets and blue dots with high resolution data sets, sinθ/λ > 0.8 Å⁻¹.

a)
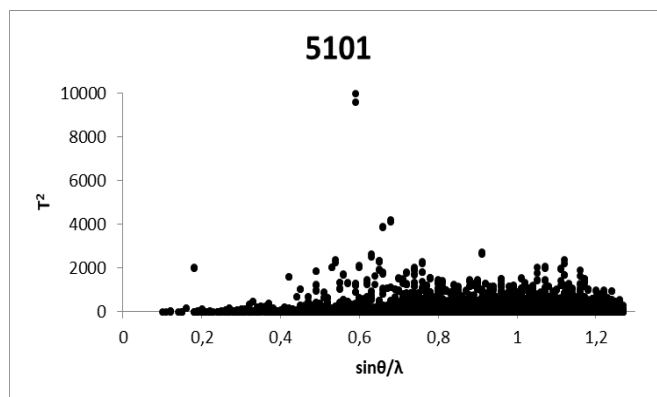
b)
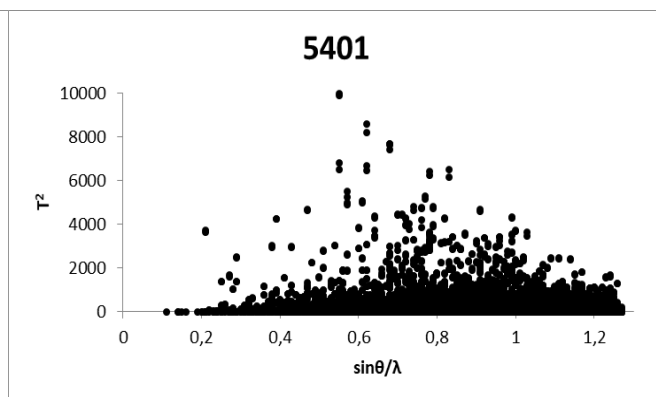
c)
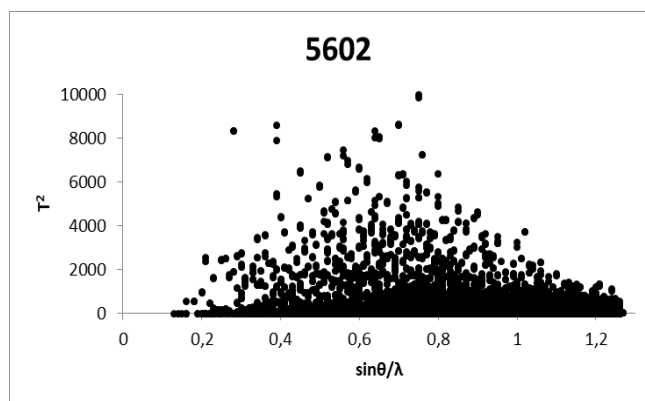
d)
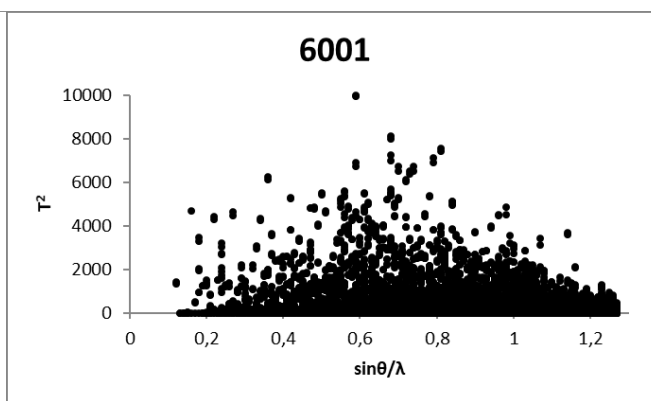
Figure S 4. T analysis for sample 5101, a), 5401, b), 5602, c) and 6001, d).

Chapter 6

Study of the electronic properties of the trifluoromethyl group
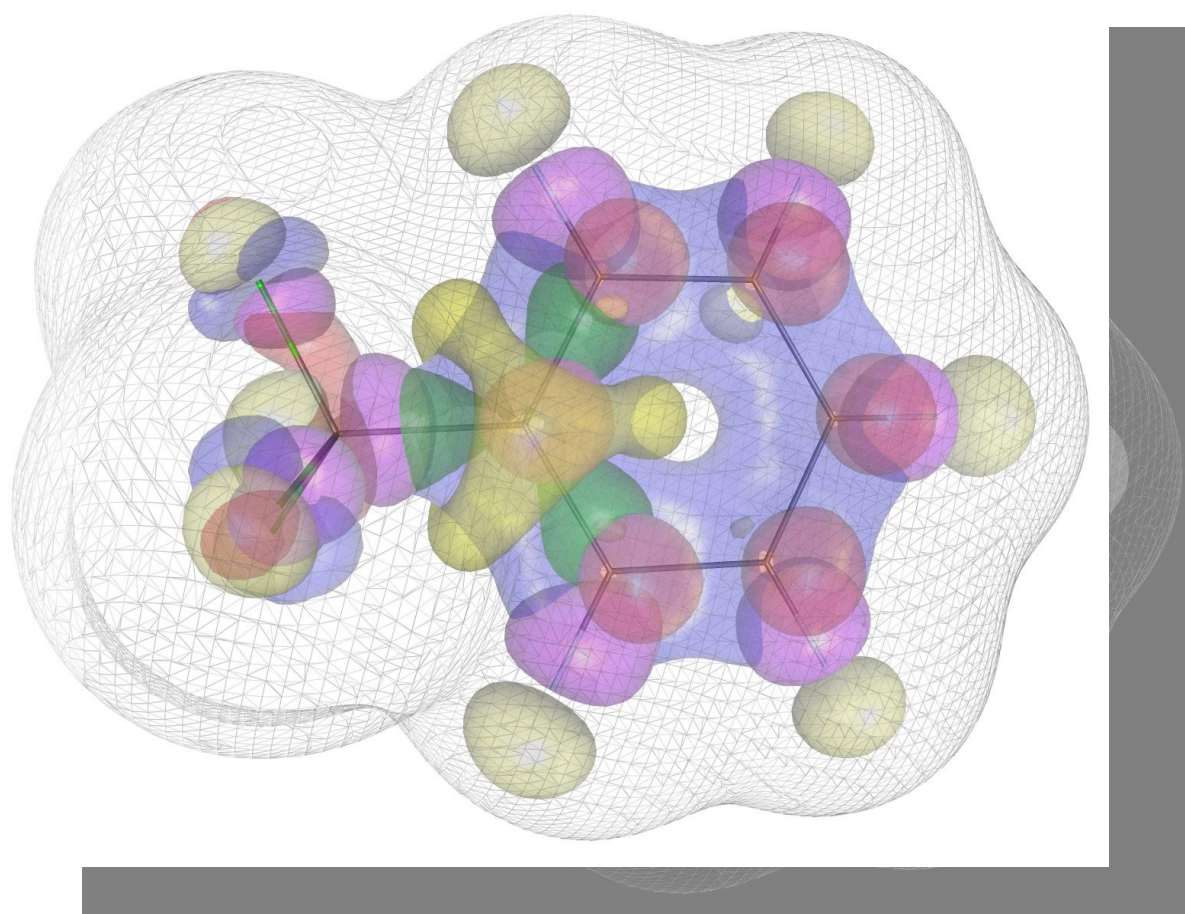
1. Introduction.

Many molecules used in the pharmaceutical and agrochemicals industries bear a trifluoromethyl group (CF_3). The biological activity of these compounds is well known.[1] In particular, aromatic rings with CF_3 substituents constitute an important set of above mentioned family.[2] The role of the CF_3 in the development of new materials is also relevant, such as the famous Teflon. Therefore, the chemistry involving this functional group is of great interest for the chemistry community.

On the basis of the high electronegativity of the fluorine atoms, the CF_3 group is considered an electron-withdrawing (EW) group. Regarding the electronegativity, the CF_3 group has a value of $\chi = 3.23^{3i}$ in Pauling units. This value is in agreement with those of other EW groups like cyano, CN, $\chi = 3.33$, chlorine atom, Cl, $\chi = 2.94$, the nitro group, NO_2, $\chi = 4.00$ or just fluorine atom, F, $\chi = 3.98$. Functional groups considered to be electron-donating have smaller values of χ. For instance, the methyl groups, CH_3, $\chi = 2.45$ or the amine group, NH_2, $\chi = 2.68$. As pointed out by Campanelli et al. the electronegativity of the CH_3 group increases as the H atoms are replaced by fluorine atoms.[4] The phenyl ring in trifluoromethyl-benzene, ($PhCF_3$) is more electron deficient that of toluene or benzene. This finding is supported by calculated values of MEP and Q_{zz} of 1,4-trifluoromethylbenzene and 1,3,5-trifluoromethybenzene in comparison to *p*-xylene and mesytilene. Other evidence include the calculated Hammett, Taft and modified Swain-Lupton constants which also substantiate the EW character of the CF_3 group.[5]

Some results reported along the last years are in contradiction with the above statements.[6] In particular, the results published by Holmes and Thomas[7] based on Electron Spectroscopy for Chemical Analysis (ESCA), indicate that in spite of the electron-withdrawing (EW) characteristics of the CF_3, the phenyl rings to which it is attached display a negative charge at the substituted carbon atom.

---

[i] This value was estimated for a trifluoromethyl group in a CF_3Cl molecule.
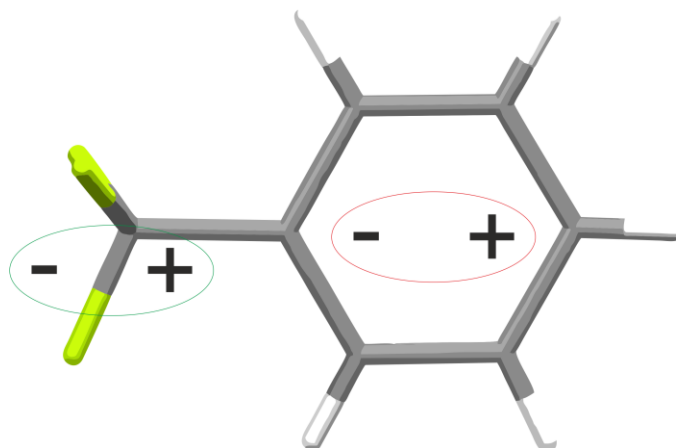
Figure 1. Induced dipole at the phenyl ring as consequence of the dipole at the CF_3 group.

Attempts to explain these contradictory results have been proposed. One focused on the dipole moment generated by the charge distribution at CF_3 substituent. The electronegative fluorine atoms concentrate negative charge leading to positive density at the carbon atom. As a consequence of the induced dipole by the CF_3, the α-carbon of the phenyl ring becomes negative,[8,9] Fig 1. This explanation is consistent with the Bond Valence Model[10] in which an atom distributes its electron valence as equally as possible between the bonds it forms.
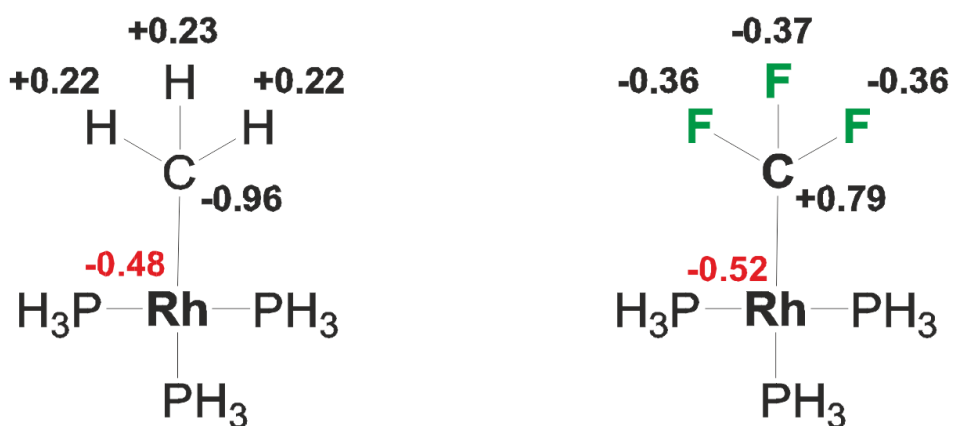
Figure 2. Calculated charge distribution of the CH_3 and CF_3 groups forming a Rhodium organometallic complex.

Many of the trifluoromethylation processes require an organometallic catalyst. Several organometallic compounds containing CF_3 groups have been reported. These compounds showed that the CF_3 groups behaves in a similar manner to the CH_3 group, in relation to the electron donating character.[11-15] In particular, the structural analysis

reported by Goodman et al.[13] was accompanied of theoretical calculations that supported the electron donor character of the CF_3 group, Fig. 2. In the same vein, recent reported studies describe equivalent outcomes.[16,17]

Some theoretical studies have been recently reported concerning the CF_3 group and its electron-donor/acceptor character. In organometallic compounds, the CF_3 group displays a strong trans ligand influence in spite of being weaker electron donor than the CH_3.[18]

The controversy generated by the reported results, dealing with the electronic properties of the CF_3 group, prompted us to consider an alternative approach for its analysis. The aim of this study is to compare the electronic properties of the methyl and trifluoromethyl groups using experimental data. X-ray charge density analysis (CDS), is an excellent tool for studying the charge distribution of crystalline compounds. CDS studies might be used to validate theoretical calculations as those reported for the CF_3 group.

2. Experimental.

For the charge density analysis, initial candidates were homologous molecules bearing CF_3 and CH_3 groups as well as other heavy atoms. Several Mn complexes were investigated. In spite of the good quality of the obtained crystals, only one compound bearing the CF_3 group did not present structural disorder, Fig. 5c. Eventually, two comparable palladium complexes containing CF_3 and CH_3 groups were obtained, which did not show structural complications, , Fig. 5a-b. The suitability of the crystals for charge density studies were tested. In order to obtain suitable data for an X-ray charge density single crystal analysis, several crystals were measured, varying the crystal size, detector distance and data collection strategies. The measured crystals lead to high quality structures regarding R_1 (1.45 and 1.47 %) and R_{int} (0.0147 and 0.0205) factors. The quality of every data set was tested together with their residual electron density map. After detailed analyses of the residual electron density maps, we considered that

the collected data were not suitable for obtaining reliable multipolar models for justifying the charge density maps.

Following the above attempts with organometallic compounds, we decided to move to simpler systems. In particular, we reduced the candidates to trifluoromethyl-benzene, compound **1** and toluene, compound **2**. The selected compounds, despite its simple structure, present evident difficulties when designing a single crystal experiment. Both compounds are liquids at room temperature with melting points, 244K for **1** and 178K for **2.**
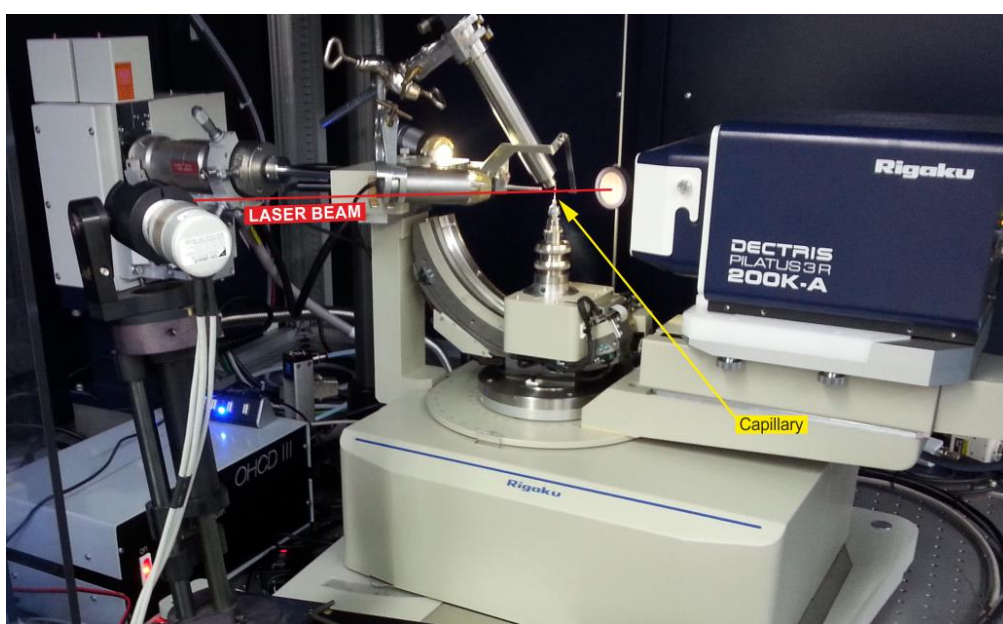
Figure 3. Laser setup of on a diffractometer for crystallizing compounds **1** and **2** under a N_2 cryostream.

For the crystallization process, a quartz-glass Lindemann capillary of 0.3mm with a wall thickness of 0.01 mm of diameter was filled with liquid compounds **1** and **2**. The corresponding capillary was aligned to be fully inside the N_2 stream produced by an Oxford 700 plus cooling system. The N_2 stream was programed to be at temperatures just below the compounds melting point. The capillary was monitored with a video-microscope, Fig. 3. The crystallization was immediately observed when placing the capillary inside the N_2 stream. However, crystal quality was far from producing suitable data for a single crystal analysis. At this point, an IR laser was set up in the following manner. The Laser beam is guided with a mirror setting equipped with a precision engine that allows its centering. Using this setting, the IR laser beam was focused on

the capillary. The beam laser was then aligned with the capillary so that when displacing the beam, it is focused on its axis. The IR laser heats up the capillary, melting its content on the focused region. The beam position and intensity are software controlled. In order to obtain suitable crystals for a single crystal experiment, the beam intensity is adjusted to just melting the content. At the same time, a couple of very slow melting scans along the capillary improve successively the crystal quality. The crystal quality was regularly checked along the capillary through X-ray diffraction. The total crystallization process takes 16-24h. In this manner, suitable single crystals were obtained for **1** and **2**. However, despite the crystals were good enough for attempting a high resolution data collection, the single crystal inside the capillary suffer some damage in the cooling process to 90K. Because of this shortcoming, the crystallization inside the capillary was directly attempted at the measurement temperature, 90K in both cases. At this temperature, the improvement of the crystal quality is more difficult. It is necessary to work at larger laser intensities while the rest of the capillary remains at 90 K. This provokes a large temperature gradient that recurrently leads into broken capillaries, especially for **2**. After several trials, a single crystal of **1** and **2**, suitable for high resolution experiment were obtained. For **1**, no single crystal structure was previously reported. After a low resolution experiment, no structural problems, such as disorder, twining, etc. were detected. Therefore, a high resolution data collection was carried out to resolutions beyond $\sin(\theta)/\lambda = 1.2$ Å^{-1}. The data collection strategy was optimized for reducing the differences in the scattering produced by the capillary depending on its orientations with respect to the X-ray beam, Fig. 4. Data collections where carried out on a Rigaku MHF007 rotating anode equipped with a Pilatus 200K hybrid pixel detector. For the data collection the software Rigaku CrystalClear-SM Expert 2.1 b29[19] was used. Data reduction was carried out using CrysAlisPro 1.171.12b[20]. The absorption correction were done using SADABS 2014/5[21]. The intensity of the reflections were analyzed using Wingx[22]. Structure solutions for both compounds were obtained with SIR2014[23] and refined with SHELXLE[24].

a)   b)
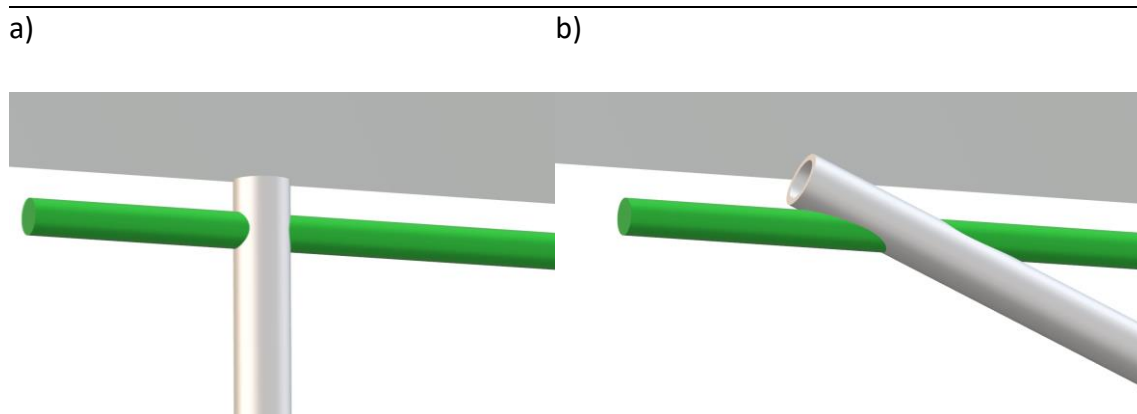
Figure 4. Scheme showing a X-ray beam (in green), going through a capillary, grey cylinder. It can be observed how the beam passes through a bigger capillary surface when sloped with respect to the beam, b) than when perpendicular, a).

Crystal structure of **2** was already published[25-27] corresponding to the α-phase polymorph of toluene.[28] Data were cut at a resolution of $\sin(\theta)/\lambda = 1.2$ Å^{-1} = 1.19. The final R_{int}=0.017 and the refined spherical model reports and R_1=4.58%. The observed residual density maps are located at the expected sites after the refinement of the spherical model. In a similar manner, the spherical model refinement of **1** confirms its suitability for a multipolar refinement, R_{int}=0.0121, R_1=3.65%. Data resolution to $\sin(\theta)/\lambda = 1.25$ Å^{-1}.

Multipolar refinement of **1** and **2** were therefore carried out using MOPRO[29]. Multipolar parameters were refined until the octupolar level. Estimation of the anisotropic thermal motion parameters of the hydrogen atoms were performed with SHADE3 SERVER[30]. Symmetry restrains and constrains were applied to the corresponding multipolar projections.[31] In the multipolar refinement of **2**, electron residual densities, intercalated between the hydrogen of the methyl group, were observed after the final model was imposed. These electron densities were understood as disordered positions of the methyl-hydrogen atoms. The new hydrogen positions were refined, fixing its occupancy to a disordered parts ratio of 75:25. Moreover, the symmetry applied to the multipolar projection of the methyl carbon, 3m, was disordered following the respective disordered hydrogen positions.

The scale factor and the residual density maps were inspected with the help of the programs XDRKplot27[32] and jnk2RDA v1.5-2013/1028[33].

3. Results and discussion.

Despite the unsuccessful attempts for getting suitable data sets of the aforementioned Pd and Mn complexes, three of these structures ($C_{10}H_{24}N_2F_6Pd_1$, $C_{10}H_{30}N_2Pd_1$ and $C_6O_5F_3Mn_1$) allowed an accurate estimation of their molecular geometries, Fig. 5.
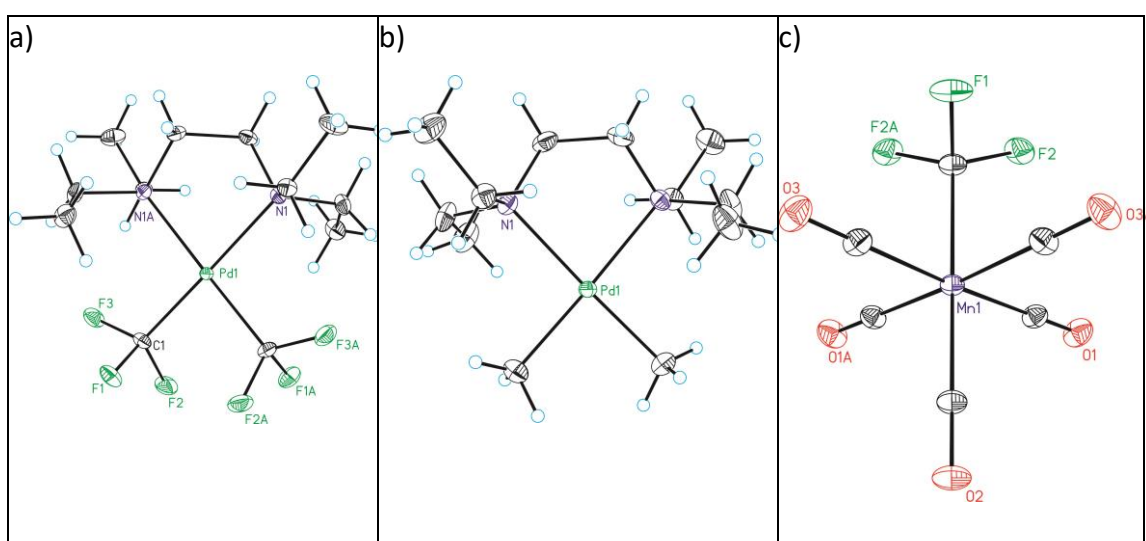
Figure 5. Organometallic compounds bearing CF_3 and CH_3 groups bonded to Pd, a), b) and Mn c). Ellipsoids at 50% probability.

Some relevant details were observed in these crystal structures: the bond distances and trans ligand effect of the CF_3 and CH_3 are slightly different, see Table 1. The Pd-CF_3 bond, as well as the trans distance, Pd-N, are shorter than in the homologous Pd-CH_3 complex. This result is in good agreement with the behavior observed in similar complexes of Rh, Mn and Pt.[12-15,18]

Another interesting detail is that the CF_3 geometry is distorted with respect to the calculated values for a covalently bound CF_3 group.[34] Moreover, this distortion points towards a CF_3 anion geometry.

191

Table 1. Comparison of Pd-CF$_3$ and Pd-CH$_3$ bond distances and the corresponding trans bond distance Pd-N.

	Bond distance (Å)	
R	Pd-R	Pd-N
CF$_3$	2.0193(3)	2.1949(2)
CH$_3$	2.0390(5)	2.2184(3)

Table 2. Bond distances and bond angles of the CF$_3$ group bonded to Pd, Mn and to the phenyl ring.

	Pd-CF$_3$		Mn-CF$_3$		Ph-CF$_3$	
Bond distances (Å)	C1 F1	1.3683(5)	F1-C4	1.3709(8)	C7-F1	1.3398(2)
	C1-F2	1.3689(5)	F2-C4	1.3737(5)	C7-F2	1.3440(2)
	C1-F3	1.3726(5)			C7-F3	1.3477(3)
Geometrical angles	F1-C1-F2	104.04(3)°	F2-C4-F2	103.27(4)°	F1-C7-F2	106.833(15)°
	F1-C1-F3	103.11(3)°	F1-C4-F2	103.26(4)°	F1-C7-F3	106.572(14)°
	F2-C1-F3	102.88(3)°	F2-C4-F2	102.95(5)°	F2-C7-F3	105.969(18)°

The multipolar parameters of **1** and **2** were analyzed in order to properly estimate the charge distribution in the phenyl ring carbon atoms. There is evidence to consider the CF$_3$ group as an electron withdrawing (EW) group. In chapter 4 for example, the calculated MEP of 1,3,5-trifluoromethyl-benzene increased with respect to the MEP of 1,4-trifluormethyl-benzene. This is the expected effect of an EW substituent group of a phenyl ring. Additionally, the geometrical parameters of **1** are in agreement with those observed by Campanelli et al.[4] for EW groups. For instance, the α-carbon displays a more obtuse angle, 120.893(10)°, than in the case of a regular hexagon (benzene). In contrast, **2**, shows more acute angles, 118.142(10)° and 118.200(9)°, for the two molecular entities present in the asymmetric unit, than benzene. The effect of a well-known nitro, NO$_2$, EW group, is also studied. In chapter 4, 1,3,5-tricyano-benzene co-crystallize together with a nitro-benzene molecule, compound **3**. In **3**, the nitro group also promotes the formation of a more obtuse angle than in benzene, 122.877(6)°. In spite of the clear relationship that exists between the magnitude of the angle at the substituted carbon and the electron character of the substituent, the calculated charge

distribution for **1** described by Holmes and Thomas[7] using Electron Spectroscopy for Chemical Analysis (ESCA) is in apparent contradiction with the EW character of the CF_3 group.
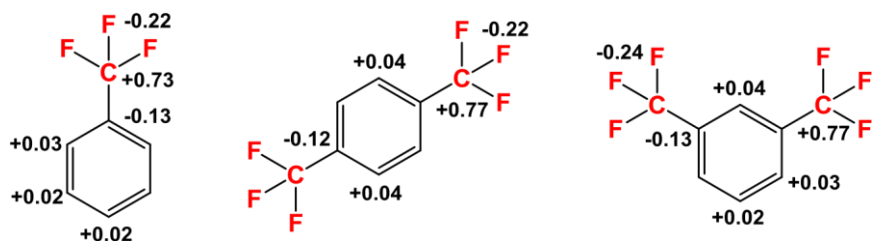
Figure 6. ESCA measured charges at the different atomic positions for benzene rings substituted with CF3 groups.

Fig. 6 shows that the α-carbon in trifluoromethyl-benzene, **1**, has formal charge of -0.13. The charge redistribution suggested by Pople and Gordon[6] would explain the charge observed at the α-carbon in this series of compounds. However, this explanation based on charge redistribution along the atoms forming the molecule was contested because it showed some inconsistencies for other families of compounds.[35,36] Additionally, it should be taking into account that even halogen atoms have their own charge distribution.
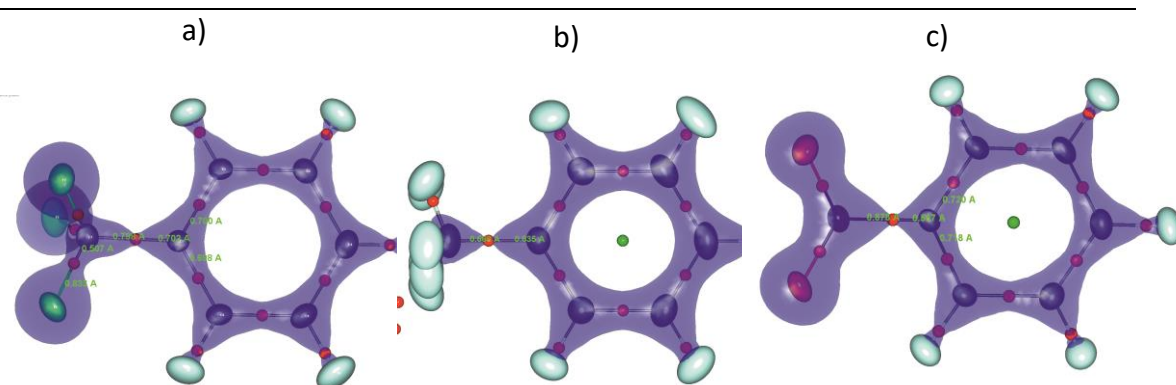
Figure 7. Electron density distribution at the bond critical point level between the α-carbon and the corresponding substituted group on the phenyl ring, 1.65, 1,75 and 1.7 $eÅ^{-3}$. The BCP is displaced towards the α-carbon in **1** and **3**, while the opposite behavior is observed in **2**.

3.1 Charge density study.

The charge density study described herein shows that the electronic distribution in the substituted benzenes **1**, **2** and **3**, are significantly different, Fig. 7.

The observed differences in the electron density translates into significant changes in the distances between the bond critical points and the α-carbons. Conversely, the distances from

Table 3. Bond critical points between α-carbon and substituted atoms of the phenyl ring.

Compound	Atom 1	Atom 2	d_{12} (Å)	$d_{1\text{-}cp}$ (Å)	$d_{2\text{-}cp}$ (Å)	ρ_{cp} (e Å^{-3})	$\Delta(\rho)$	λ_1	λ_2	λ_3	ε	bcp
1	C1A	C7A	1.503	0.770	0.734	1.702	-11.1	-11.7	-11.5	12.1	0.020	(3,-1)
	C1B	C7B	1.503	0.771	0.731	1.706	-11.1	-12.0	-11.3	12.1	0.061	(3,-1)
2	C1	C7	1.500	0.702	0.798	1.823	-12.2	-13.4	-12.4	13.5	0.081	(3,-1)
3	C1B	N1B	1.465	0.587	0.878	1.780	-13.1	-13.5	-11.3	11.7	0.193	(3,-1)

Table 4. Bond critical points between α-carbon and adjacent atoms of the phenyl ring.

Compound	Atom 1	Atom 2	d_{12} (Å)	$d_{1\text{-}cp}$ (Å)	$d_{2\text{-}cp}$ (Å)	ρ_{cp} (e Å^{-3})	$\Delta(\rho)$	λ_1	λ_2	λ_3	ε	bcp
1	C1A	C2A	1.396	0.699	0.698	2.146	-17.3	-17.3	-14.2	14.3	0.215	(3,-1)
	C1A	C6A	1.395	0.697	0.699	2.133	-17.2	-17.1	-14.2	14.0	0.202	(3,-1)
	C1B	C2B	1.398	0.698	0.700	2.169	-17.3	-17.7	-14.5	14.9	0.219	(3,-1)
	C1B	C6B	1.398	0.699	0.699	2.124	-16.7	-17.0	-14.2	14.4	0.200	(3,-1)
2	C1	C2	1.397	0.701	0.696	2.112	-18.7	-16.1	-13.5	11.0	0.196	(3,-1)
	C1	C6	1.394	0.698	0.696	2.111	-18.1	-16.3	-13.0	11.2	0.256	(3,-1)
3	C1B	C2B	1.392	0.718	0.674	2.164	-19.5	-17.0	-13.9	11.5	0.221	(3,-1)
	C1B	C6B	1.389	0.720	0.669	2.184	-19.9	-17.2	-14.0	11.3	0.230	(3,-1)

the α-carbon to critical points of the bonds with the adjacent neighbor carbon atoms in the phenyl ring remain unaltered, Table 1 & Table 2. When two atoms are covalently bonded, the BCP gets closer to the less electronegative atom, compressing the electron density towards the latter. This behavior is clearly observed in **3**. The BCP between the nitrogen and the alpha carbon atoms is located at 0.587 Å from the former and 0.878 Å from the latter. In **1**, the CF$_3$ substituted carbon atom (C1) behaves as a more electronegative nucleus than the corresponding methyl substituted carbon atom in **2**. The analysis of the refined multipolar parameters reveals also interesting data. The valence populations suggest negative charges on all atoms except in the CF$_3$ carbon atom, C7, and in all hydrogen atoms. C7 is bonded to three fluorine atoms, so it does not come as a surprise to have a positive charge value. The rest of the carbon atoms in the phenyl ring can extract charge from the covalently bonded hydrogen atoms. Finally, the CF$_3$ substituted carbon atom, C1, can only extract charge either

from the carbon adjacent carbon atoms of the phenyl ring or from its CF_3 substituent. Surprisingly, attending to its valence population, C1, becomes negative despite being bonded to the EW CF_3 group, Table 3. The calculated negative value is in good agreement with the one reported by Holmes and Thomas.[7] Nevertheless, the atomic valence populations should be considered with care. The kappa values of C1 in compound **1** indicate a spread of electron density deformation in the non-spherical terms, table S1. In order to validate the valence population of C1, the κ' parameter was restrained to contract the aspherical electron deformations of C1. Under these conditions, κ' took a value of 1.01, with C1 still displaying a negative charge of -0.08 e. The remaining carbon atoms of the phenyl ring compensate this charge decrease. In contrast, nitro-benzene, **3**, the substituted carbon is positively charged despite being modelled with one expanded deformation parameter, κ'. In compound **2**, toluene, the charge distribution in the carbon atoms of the phenyl ring is also unique. The *meta*-carbon atoms become more negative than its *ortho*-neighbors.

Table 5. Multipolar parameters of compound **1**

ATOM	KP1	KP2	Pval	Charge	P11	P1-1	P10	P20	P21	P2-1	P22	P2-2	P30	P31	P3-1	P32	P3-2	P33	P3-3
C1_1	1.003	0.90	**4.16**	-0.16	**0.033**	-0.014	-0.002	**-0.198**	0.005	0.006	**-0.042**	0.000	0.015	**0.024**	**-0.033**	0.011	-0.010	**-0.298**	-0.019
C2_1	1.000	1.01	4.09	-0.09	**-0.026**	0.015	-0.010	**-0.188**	0.005	0.008	0.007	0.015	0.007	**0.037**	0.006	0.000	-0.016	**-0.242**	-0.011
C3_1	1.001	0.98	4.16	-0.16	**-0.031**	0.002	0.001	**-0.211**	-0.009	-0.006	0.000	-0.005	0.004	**0.030**	-0.002	-0.003	-0.020	**-0.247**	-0.002
C4_1	0.994	0.99	4.25	-0.25	-0.008	-0.005	0.005	**-0.201**	-0.014	-0.004	-0.005	-0.001	-0.010	**0.023**	-0.007	-0.013	0.006	**-0.277**	-0.004
C5_1	1.001	0.98	4.16	-0.16	**-0.040**	-0.007	0.002	**-0.205**	0.004	0.005	0.014	0.001	0.004	**0.033**	0.002	-0.010	-0.008	**-0.242**	0.009
C6_1	0.998	1.02	4.09	-0.09	**-0.025**	0.017	-0.014	**-0.197**	-0.007	0.003	0.001	0.012	0.007	**0.035**	-0.003	0.006	-0.011	**-0.237**	-0.005
C7_1	1.010	1.14	**3.62**	0.38	0.001	0.002	**0.097**	**0.101**	-0.007	0.004	-0.007	0.019	**0.233**	0.017	-0.002	-0.008	-0.006	**0.180**	-0.007
F1_1	0.990	0.81	7.23	-0.23	0.000	0.010	**0.040**	**-0.055**	0.008	-0.002	0.020	-0.004	**0.056**	-0.001	-0.007	0.006	-0.004	-0.017	-0.007
F2_1	0.990	0.82	7.23	-0.23	-0.001	0.010	**0.040**	**-0.055**	0.008	-0.001	0.019	-0.004	**0.056**	0.000	-0.007	0.005	-0.004	-0.016	-0.007
F3_1	0.990	0.82	7.23	-0.23	-0.001	0.011	**0.041**	**-0.055**	0.008	-0.001	0.019	-0.004	**0.056**	-0.001	-0.007	0.005	-0.004	-0.016	-0.007
H2_1	1.34	1.34	0.77	0.23	**0.092**														
H3_1	1.32	1.33	0.75	0.25	**0.074**														
H4_1	1.32	1.33	0.73	0.27	**0.091**														
H5_1	1.33	1.33	0.74	0.26	**0.070**														
H6_1	1.32	1.33	0.77	0.23	**0.087**														

Another way for estimating the charge of an atom in a molecule is through the atomic basin. In this manner, the charge of the α-carbon in **1** becomes positive, +0.08 e. This result is in striking contrast with the one discussed above. Moreover, the *ortho*- and *meta*-carbon atoms also become positive, remaining the *para*-carbon only negative.

The magnitude range of the integrated basin values is considerable, Tables S1, S2 and S3, which suggest that these values should be considered with caution. The same calculations performed with compounds **2** and **3** assigned neutral charge to the α-carbon in **2** and negative charge for the counterpart in **3**. Only in the case of **3**, the values of the valence population and the atomic basin charge are in good agreement for the α-carbon, Table 6.

Table 6. Integrated atomic basin populations of α-carbons.

Compound	Atom	Population (e^-)	Charge (e^-)
1	C1	5.92	0.08
2	C1A	6.02	-0.02
2	C1B	6.00	0.00
3	C1B	5.87	0.13

3.2 Theoretical calculations.

To support the observations of the X-ray charge density study, we performed theoretical structure calculations (**B3LYP/6-31+G***.) The molecular electrostatic potential maps (MEP) of trifluoromethyl-benzene, 1,3,5-trifluoromethyl-benzene and hexa-trifluoromethyl-benzene were analyzed. All of them supported the EW character of the CF_3 group. The electrostatic potential value became more positive as the number of CF_3 substituents was increased, Fig. 8. This observation was previously noted in the calculated MEPs in chapter 4, for 1,4-trifluoromethyl-benzene and 1,3,5-trifluoromethyl-benzene. It is also interesting to note that the region over the α-carbon in **1** has a negative value of the MEP. An additional detail reveals that the MEP value at the fluorine atoms becomes less negative as the number of CF_3 groups increases. This finding indicates the existence of an electron distribution involving all CF_3 group. This polarizability of the CF_3 group was already pointed out by True et al.[3]
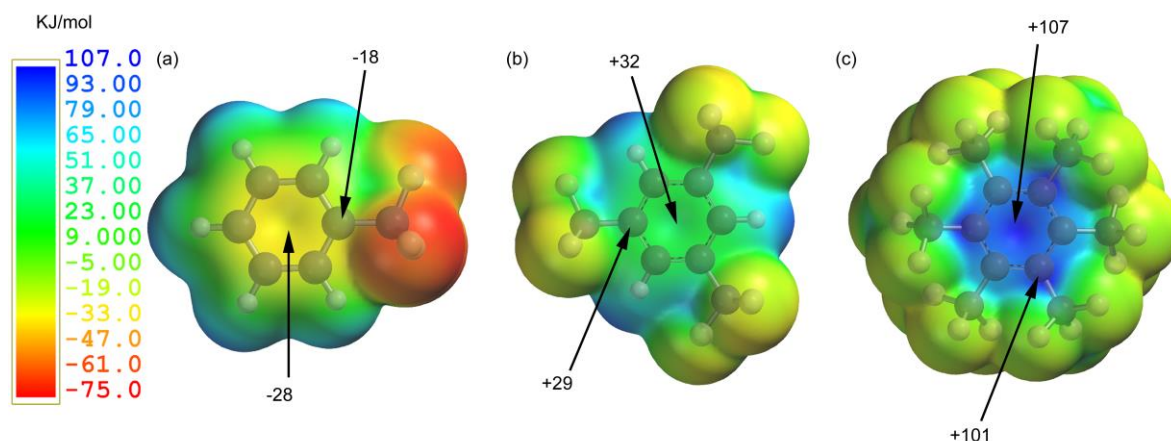
Figure 8. Calculated MEP surfaces of trifluoromethyl-benzene, 1,3,5-trifluromethyl-benzene and hexa-trifluoromethyl-benzene at B3LYP/6-31G* level (isovalue used for the surfaces is 0.001 a.u.).

Calculations at a higher level of theory were carried out to compare MEPs of benzene, toluene, **2** and trifluoromethyl-benzene, **1**, Fig. 9 and 10 a).
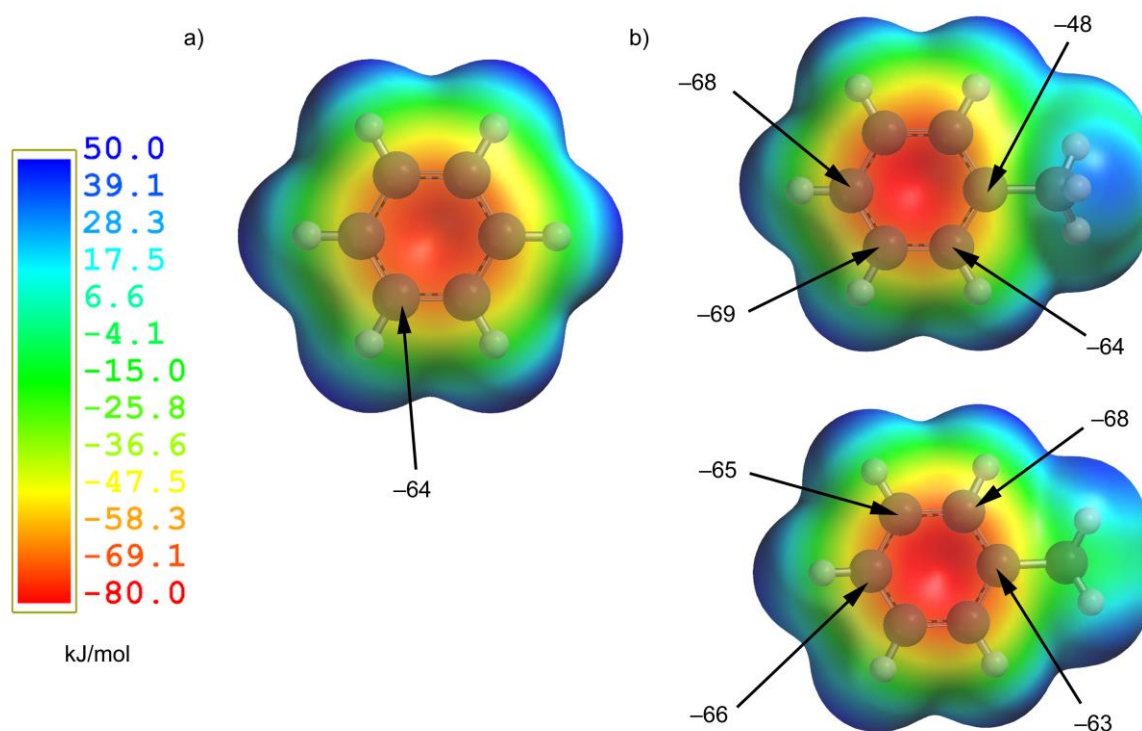
Figure 9. MEP surfaces of benzene (a) and toluene (b) (isovalue = 0.001 a.u.). The MEP at the different sites of the molecule are labeled in KJ/mol units. The toluene molecule has the methyl group with one hydrogen pointing perpendicularly to the plane containing phenyl ring. Therefore, the two sides of the toluene are not equivalent and both are displayed in the picture.

197
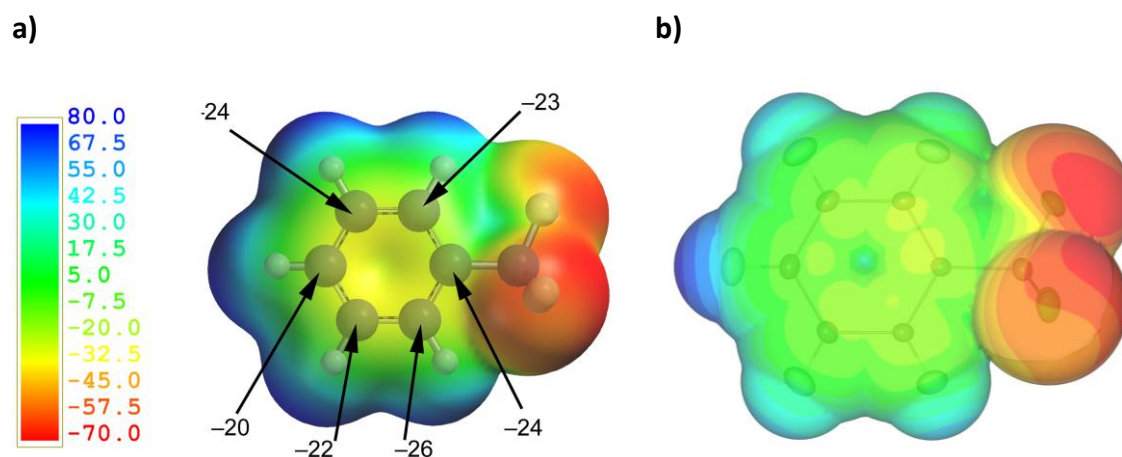
Figure 10. a) MEP of **1** plotted onto the Van der Waals surface (isovalue = 0.001 a.u.). Values in KJ/mol. b) MEP calculated from the experimental charge density distribution.

For **1**, the MEPs calculated values show a positive increase for all the carbon atoms of the phenyl ring substituted with the CF_3 group when compared to benzene. This is the expected behavior for an EW group. In addition, the calculated MEP values display almost identical magnitudes for all carbon atoms in the phenyl ring including the substituted one. For **2**, toluene, the substituted-carbon is assigned a less negative value in the side having the hydrogen atom of the methyl group perpendicularly oriented with respect to the phenyl ring plane. This is due to the influence of the hydrogen in the MEP. In **1**, the analogous effect of the fluorine atom should also make the MEP to display a more negative magnitude in the substituted carbon. However, this effect is not observed in the MEP calculations of 1,3,5-trifluoromethyl-benzene and hexa-trifluoromethyl-benzene, most likely due to different conformation of the substituent controlled by an intramolecular interaction CH-F.
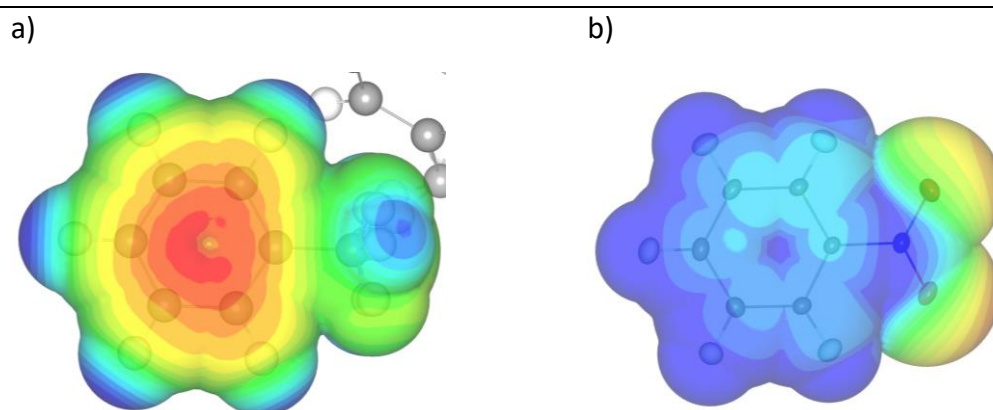
Figure 11. Calculated MEP from experimental charge density of **2** and **3**.

4. Conclusions

The electronic properties of the CF_3 group has been studied through an X-ray charge density study and computational methods. Successful charge density studies based on X-ray high resolution diffraction experiments were carried out for compound **1**, **2** and **3**, despite being a liquid under standard conditions. The use of an "in situ" crystallization methodology, using an IR laser, has been proven very effective in the crystallization of **1** and **2**, providing single crystals of enough quality to perform this kind of experiments.

In contrast, the efforts for performing charge density studies of organometallic compounds bearing coordinated CF_3 groups were unsuccessful. However, the solved structures revealed a distortion in the CF_3 geometry, when coordinated to a metal, with respect to the same functional group covalently bonded. The CF_3 displays an ionic character when coordinated to a metal owing to its resemblance with the CF_3 anion.

Computational methods described substantial changes in the MEP of phenyl substituted rings having an increasing number of CF_3 groups. These results are in agreement with the EW character of the CF_3 substituent. Conversely, neither the charge density study, nor the MEP values indicate a diminution of the electronic population promoted by the CF_3 group at the *ipso*-carbon. In contrast, for the NO_2 group, the charge density analysis displays a slight diminution of the electron population in the *ipso*-carbon. In spite of the charge decrease, the MEP map does not display a significant depletion of the value at the *ipso*-carbon. Remarkably, the MEP value at the *ipso*-carbon is not the less positive.

The ionic character observed for CF_3 group coordinated to metals together with the MEP variations observed by increasing the number of CF_3 substituents in a phenyl ring indicate that CF_3 features an efficient charge redistribution.

199

5. References

(1)   Lehmann, F. *Naunyn-Schmiedebergs Archiv Fur Experimentelle Pathologie Und Pharmakologie* **1928**, *130*, 250.

(2)   Tomashenko, O. A.; Grushin, V. V. *Chemical Reviews* **2011**, *111*, 4475.

(3)   True, J. E.; Thomas, T. D.; Winter, R. W.; Gard, G. L. *Inorganic Chemistry* **2003**, *42*, 4437.

(4)   Campanelli, A. R.; Domenicano, A.; Ramondo, F.; Hargittai, I. *Journal of Physical Chemistry A* **2004**, *108*, 4940.

(5)   Hansch, C.; Leo, A.; Taft, R. W. *Chemical Reviews* **1991**, *91*, 165.

(6)   Pople, J. A.; Gordon, M. *Journal of the American Chemical Society* **1967**, *89*, 4253.

(7)   Holmes, S. A.; Thomas, T. D. *Journal of the American Chemical Society* **1975**, *97*, 2337.

(8)   Bromilow, J.; Brownlee, R. T. C.; Topsom, R. D.; Taft, R. W. *Journal of the American Chemical Society* **1976**, *98*, 2020.

(9)   Levy, J. B. *Structural Chemistry* **1999**, *10*, 121.

(10)   Brown, I. D. *Chemical Reviews* **2009**, *109*, 6858.

(11)   Coan, P. S.; Folting, K.; Huffman, J. C.; Caulton, K. G. *Organometallics* **1989**, *8*, 2724.

(12)   Grushin, V. V.; Marshall, W. J. *Journal of the American Chemical Society* **2006**, *128*, 4632.

(13)   Goodman, J.; Grushin, V. V.; Larichev, R. B.; Macgregor, S. A.; Marshall, W. J.; Roe, D. C. *Journal of the American Chemical Society* **2009**, *131*, 4236.

(14)   Goodman, J.; Grushin, V. V.; Larichev, R. B.; Macgregor, S. A.; Marshall, W. J.; Roe, D. C. *Journal of the American Chemical Society* **2010**, *132*, 12013.

(15)   Tomashenko, O. A.; Escudero-Adan, E. C.; Belmonte, M. M.; Grushin, V. V. *Angewandte Chemie-International Edition* **2011**, *50*, 7655.

(16)   Algarra, A. G.; Grushin, V. V.; Macgregor, S. A. *Organometallics* **2012**, *31*, 1467.

(17)   Romine, A. M.; Nebra, N.; Konovalov, A. I.; Martin, E.; Benet-Buchholz, J.; Grushin, V. V. *Angewandte Chemie-International Edition* **2015**, *54*, 2745.

(18)   Knovalov, A., Universitat Rovira i Virgili, 2017.

(19)   Rigaku **2013**.

(20)   Diffraction, R. O. **2015**.

(21)   Sheldrick, G. M. **2014**.

(22)   Farrugia, L. *J. Appl. Cryst.* **2012**, *45*, 849.

(23)   Burla, M. C.; Caliandro, R.; Carrozzini, B.; Cascarano, G. L.; Cuocci, C.; Giacovazzo, C.; Mallamo, M.; Mazzone, A.; Polidori, G. *J. Appl. Cryst.* **2015**, *48*, 306.

(24)   Hubschle, C. B.; Sheldrick, G. M.; Dittrich, B. *J. Appl. Cryst.* **2011**, *44*, 1281.

(25)   Anderson, M.; Bosio, L.; Bruneauxpoulle, J.; Fourme, R. *Journal De Chimie Physique Et De Physico-Chimie Biologique* **1977**, *74*, 68.

(26)   Ibberson, R. M.; David, W. I. F.; Prager, M. *J. Chem. Soc.-Chem. Commun.* **1992**, 1438.

(27)   Nayak, S. K.; Sathishkumar, R.; Row, T. N. G. *Crystengcomm* **2010**, *12*, 3112.

(28)   Andre, D.; Fourme, R.; Bruneauxpoulle, J.; Bosio, L. *Journal of Molecular Structure* **1982**, *81*, 253.

(29)   Jelsch, C.; Guillot, B.; Lagoutte, A.; Lecomte, C. *J. Appl. Cryst.* **2005**, *38*, 38.

(30)   Madsen, A. O. *J. Appl. Cryst.* **2006**, *39*, 757.

(31)   Domagala, S.; Jelsch, C. *J. Appl. Cryst.* **2008**, *41*, 1140.

(32)   Zhurov, V. V.; Zhurova, E. A.; Pinkerton, A. A. *J. Appl. Cryst.* **2008**, *41*, 340.

(33)   Meindl, K.; Henn, J. *Acta Crystallographica Section A* **2008**, *64*, 404.

(34)   Harlow, R. L. B.-B., Jordi ; Miloserdov, Fedor M. ; Konovalov, Andrey I. ; Marshall, William J. ; Escudero-Adán, Eduardo C. ; Martin, Eddy ; Lishchynskyi, Anton; Grushin, Vladimir V. *Submitted.* **2018**.

(35)   Stolow, R. D.; Samal, P. W.; Giants, T. W. *Journal of the American Chemical Society* **1981**, *103*, 197.

(36)   Sardella, D. J. *Journal of the American Chemical Society* **1972**, *94*, 5206.

6. Supporting information.

Table S 1. Atomic charges from the atomic basins integration for **1**.

Atom	Electrons	Net charge
C1B	5.87	0.13
C2B	6.09	-0.09
C3B	6.33	-0.33
C4B	6.05	-0.04
C5B	6.15	-0.15
C6B	6.42	-0.42
N1B	7.56	-0.56
O1B	9.00	-1.00
O2B	8.63	-0.63
H2B	1.04	-0.04
H3B	0.74	0.26
H4B	1.12	-0.12
H5B	1.06	-0.06
H6B	0.76	0.24

Table S 2. Atomic charges from the atomic basins integration for **2**.

Atom	Electrons	Net charge
C1A	6.02	-0.02
H2A	0.90	0.10
C2A	6.16	-0.16
H3A	0.95	0.05
C3A	6.12	-0.12
H4A	0.93	0.07
C4A	6.00	-0.00
H5A	0.89	0.12
C5A	6.19	-0.19
H6A	0.95	0.06
C6A	6.10	-0.10
C1B	6.00	0.00
H2B	0.90	0.10
C2B	6.18	-0.18
H3B	0.98	0.02
C3B	5.96	0.04
H4B	0.90	0.10
C4B	5.98	0.02
H5B	0.87	0.13
C5B	6.11	-0.11
H6B	1.01	-0.01
C6B	5.98	0.02

Table S 3. Atomic charges from the atomic basins integration for **3**.

Atom	Electrons	Net charge
F1	10.34	-1.34
F2	9.51	-0.51
F3	9.50	-0.50
C1	5.92	0.08
C2	5.93	0.07
C3	5.86	0.14
C4	6.26	-0.26
C5	5.98	0.02
C6	5.85	0.15
C7	4.31	1.69
H2	0.96	0.05
H3	1.05	-0.05
H4	0.72	0.28
H5	0.91	0.09
H6	1.01	-0.01

Table S1. Multipolar parameters of **1**.

ATOM	KP1	KP2	Pval	Plms	P10	P11	P1-1	20	21	P2-1	P22	P2-2	P30	P31	P3-1	P32	P3-2	P33	P3-3
C1_1	1.003	0.90	**4.161**		**0.033**	-0.014	-0.002	**-0.198**	0.005	0.006	**-0.042**	0.000	0.015	**0.024**	**-0.033**	0.011	-0.010	**-0.298**	-0.019
C2_1	1.000	1.01	4.094		**-0.026**	0.015	-0.010	**-0.188**	0.005	0.008	0.007	0.015	0.007	**0.037**	0.006	0.000	-0.016	**-0.242**	-0.011
C3_1	1.001	0.98	4.164		**-0.031**	0.002	0.001	**-0.211**	-0.009	-0.006	0.000	-0.005	0.004	**0.030**	-0.002	-0.003	-0.020	**-0.247**	-0.002
C4_1	0.994	0.99	4.25		-0.008	-0.005	0.005	**-0.201**	-0.014	-0.004	-0.005	-0.001	-0.010	**0.023**	-0.007	-0.013	0.006	**-0.277**	-0.004
C5_1	1.001	0.98	4.16		**-0.040**	-0.007	0.002	**-0.205**	0.004	0.005	0.014	0.001	0.004	**0.033**	0.002	-0.010	-0.008	**-0.242**	0.009
C6_1	0.998	1.02	4.09		**-0.025**	0.017	-0.014	**-0.197**	-0.007	0.003	0.001	0.012	0.007	**0.035**	-0.003	0.006	-0.011	**-0.237**	-0.005
C7_1	1.010	1.14	**3.62**		0.001	0.002	**0.097**	**0.101**	-0.007	0.004	-0.007	0.019	**0.233**	0.017	-0.002	-0.008	-0.006	**0.180**	-0.007
F1_1	0.990	0.81	7.23		0.000	0.010	**0.040**	**-0.055**	0.008	-0.002	0.020	-0.004	**0.056**	-0.001	-0.007	0.006	-0.004	-0.017	-0.007
F2_1	0.990	0.82	7.23		-0.001	0.010	**0.040**	**-0.055**	0.008	-0.001	0.019	-0.004	**0.056**	0.000	-0.007	0.005	-0.004	-0.016	-0.007
F3_1	0.990	0.82	7.23		-0.001	0.011	**0.041**	**-0.055**	0.008	-0.001	0.019	-0.004	**0.056**	-0.001	-0.007	0.005	-0.004	-0.016	-0.007
H2_1	1.34	1.34	0.77		**0.092**														
H3_1	1.32	1.33	0.75		**0.074**														
H4_1	1.32	1.33	0.73		**0.091**														
H5_1	1.33	1.33	0.74		**0.070**														
H6_1	1.32	1.33	0.77		**0.087**														

Table S2. Multipolar parameter of **2**.

ATOM	KP1	KP2	Pval	Plms	P10	P11	P1-1	20	21	P2-1	P22	P2-2	P30	P31	P3-1	P32	P3-2	P33	P3-3
C1A_1	**1.0269**	**1.0530**	**3.89**	**0**	**0.056**	**0.000**	**-0.001**	**-0.173**	**-0.005**	**0.002**	**-0.025**	**0.010**	**0.006**	**0.023**	**0.004**	**-0.001**	**0.013**	**-0.216**	**-0.005**
C1B_2	**1.0291**	**1.0652**	**3.89**	**0**	**0.060**	**0.002**	**0.002**	**-0.174**	**-0.007**	**0.005**	**-0.025**	**0.014**	**0.009**	**0.022**	**0.003**	**-0.001**	**0.014**	**-0.217**	**0.000**
C2A_1	1.0185	1.0404	4.05	0	0.012	-0.012	0.007	-0.180	0.001	0.005	-0.016	-0.007	0.001	0.017	-0.004	-0.002	-0.001	-0.227	0.005
C2B_2	1.0209	1.0593	4.05	0	0.013	-0.015	0.009	-0.187	-0.001	0.004	-0.013	-0.014	-0.001	0.028	-0.002	0.000	0.000	-0.227	-0.002
C3A_1	1.0053	0.9582	4.16	0	0.009	-0.011	-0.004	-0.219	-0.001	-0.003	-0.008	-0.004	0.002	0.021	0.014	0.000	0.009	-0.265	0.001
C3B_2	1.0059	0.9609	4.16	0	0.008	-0.009	-0.005	-0.226	-0.001	-0.002	-0.010	0.000	-0.002	0.020	0.016	0.001	0.008	-0.262	0.005
C4A_1	1.0093	0.9597	4.05	0	-0.009	0.008	-0.008	-0.195	0.002	-0.006	-0.003	0.009	-0.009	0.037	0.005	0.002	0.002	-0.250	0.010
C4B_2	1.0101	0.9598	4.05	0	-0.007	0.010	-0.002	-0.190	0.007	-0.003	-0.006	0.001	-0.008	0.037	-0.003	0.007	0.003	-0.238	0.008
C5A_1	1.0048	0.9594	4.17	0	0.008	-0.013	-0.002	-0.222	-0.002	0.000	-0.012	-0.001	0.007	0.016	0.013	-0.004	0.009	-0.263	0.006
C5B_2	1.0065	0.9572	4.16	0	0.009	-0.011	-0.001	-0.223	-0.001	0.001	-0.014	0.000	-0.005	0.020	0.013	0.000	0.009	-0.263	0.003
C6A_1	1.0161	1.0373	4.05	0	0.011	-0.013	0.007	-0.186	-0.001	0.006	-0.015	-0.005	0.002	0.021	-0.004	0.004	0.002	-0.226	0.001
C6B_2	1.0192	1.0380	4.05	0	0.011	-0.017	0.005	-0.188	0.003	0.001	-0.011	-0.007	-0.003	0.026	-0.004	-0.002	0.006	-0.220	0.005
C7A_1	**1.0079**	**0.8478**	**4.06**	**0**	**0**	**0**	**-0.044**	**0.007**	**0**	**0**	**0**	**0**	**0.380**	**0**	**0**	**0**	**0**	**0.073**	**0**
C7Aa_1	1.0079	0.8478	4.06	0	0	0	-0.044	0.007	0	0	0	0	0.380	0	0	0	0	0.073	0
C7B_2	**1.0052**	**0.8449**	**4.06**	**0**	**0**	**0**	**-0.037**	**0.014**	**0**	**0**	**0**	**0**	**0.374**	**0**	**0**	**0**	**0**	**0.082**	**0**
C7Bb_2	1.0052	0.8449	4.06	0	0	0	-0.037	0.014	0	0	0	0	0.374	0	0	0	0	0.082	0

Table S2. continuation. Multipolar parameters of hydrogen atoms in compound **2**.

ATOM	KP1	KP2	Pval	P10
H2A	1.114	1.168	0.98	0.124
H2B	1.097	1.104	0.98	0.124
H3A	1.157	1.167	0.91	0.115
H3B	1.125	1.164	0.91	0.115
H4A	1.179	1.167	0.89	0.114
H4B	1.144	1.176	0.89	0.114
H5A	1.121	1.170	0.89	0.115
H5B	1.150	1.161	0.89	0.114
H6A	1.119	1.166	0.98	0.124
H6B	1.140	1.173	0.98	0.123
H71A	1.041	1.087	0.98	0.152
H71B	1.060	1.085	0.98	0.156
H72A	1.028	1.084	0.97	0.163
H72B	1.056	1.095	0.97	0.165
H73A	1.036	1.081	0.97	0.162
H73B	1.042	1.094	0.95	0.178
H74A	1.029	1.065	0.98	0.147
H74B	1.060	1.085	1.00	0.133
H75A	1.097	1.104	0.99	0.126
H75B	1.056	1.095	0.99	0.150
H76A	1.021	1.059	1.00	0.170
H76B	1.042	1.094	1.01	0.123

Table S3. Multipolar parameters of the nitrobenzene molecule, compound **3**.

ATOM	AXES	Ax	Ay	Az	KP1	KP2	Pval	Plms Px(P11)	Py(P1-1)	Pz(P10)	2 0	2 1	2 -1	2 2	2 -2	3 0	3 1	3 -1	3 2	3 -2	3 3	3 -3
C1B_1	bXY	C6B	C2B	-	1.016 (2)	0.931 (11)	3.91 (3)	**0.161 (7)**	-0.005 (4)	0.000 (3)	**-0.134 (6)**	0.016 (3)	-0.009 (3)	**-0.157 (6)**	-0.006 (4)	-0.006 (4)	0.009 (4)	-0.005 (4)	-0.004 (4)	-0.011 (4)	**-0.282 (11)**	0.004 (4)
C2B_1	bXY	C1B	C3B	-	1.009 (2)	0.959 (10)	4.10 (3)	**-0.035 (5)**	0.022 (5)	-0.001 (3)	**-0.214 (6)**	0.002 (3)	-0.004 (3)	0.010 (4)	0.026 (4)	-0.008 (4)	0.021 (4)	0.009 (4)	0.006 (4)	0.000 (4)	**-0.266 (8)**	0.015 (4)
C3B_1	bXY	C2B	C4B	-	1.005 (2)	0.947 (10)	4.14 (3)	**-0.025 (5)**	0.008 (5)	-0.014 (4)	**-0.223 (6)**	0.008 (3)	0.016 (4)	0.001 (4)	0.010 (4)	0.004 (4)	0.012 (4)	-0.004 (4)	-0.002 (4)	0.015 (4)	**-0.268 (8)**	-0.008 (4)
C4B_1	bXY	C5B	C3B	-	1.007 (3)	0.972 (13)	4.11 (3)	**-0.038 (6)**	0.006 (4)	-0.008 (4)	**-0.225 (7)**	0.012 (3)	0.009 (4)	-0.001 (5)	-0.006 (4)	-0.009 (4)	**0.028 (4)**	-0.011 (4)	-0.006 (4)	0.005 (4)	**-0.268 (10)**	0.007 (5)
C5B_1	bXY	C6B	C4B	-	1.005 (2)	0.953 (10)	4.14 (3)	**-0.025 (5)**	0.010 (5)	-0.001 (3)	**-0.220 (6)**	0.010 (3)	0.009 (3)	-0.002 (4)	0.005 (4)	-0.003 (4)	**0.026 (4)**	-0.003 (4)	-0.008 (4)	0.009 (4)	**-0.264 (8)**	-0.003 (4)
C6B_1	bXY	C1B	C5B	-	1.009 (2)	0.956 (9)	4.10 (3)	**-0.031 (5)**	0.022 (5)	0.006 (3)	**-0.219 (6)**	-0.003 (3)	-0.013 (3)	0.014 (4)	0.030 (4)	-0.005 (4)	0.021 (4)	0.008 (4)	0.013 (4)	0.003 (4)	**-0.275 (8)**	0.000 (4)
N1B_1	bXY	O2B	O1B	-	0.9920 (15)	0.805 (7)	5.033 (18)	-0.013 (5)	0.009 (4)	0.018 (3)	**-0.255 (6)**	-0.002 (3)	0.007 (3)	**-0.029 (4)**	0.004 (4)	-0.009 (4)	0.019 (4)	-0.009 (4)	-0.001 (4)	0.002 (4)	**-0.400 (9)**	0.006 (4)
O1B_1	XY	N1B	O2B	-	0.9942 (9)	0.995 (12)	6.154 (13)	**-0.099 (4)**	0.001 (3)	-0.009 (3)	**-0.085 (3)**	-0.011 (3)	0.001 (3)	**-0.137 (3)**	0.001 (3)	0.004 (3)	**-0.025 (3)**	0.003 (3)	0.002 (3)	-0.004 (3)	**0.037 (3)**	0.005 (3)
O2B_1	XY	N1B	O1B	-	0.9972 (10)	0.969 (13)	6.138 (13)	**-0.075 (4)**	-0.002 (5)	-0.006 (5)	**-0.087 (4)**	-0.014 (3)	-0.008 (3)	**-0.132 (3)**	0.000 (3)	-0.001 (4)	**-0.030 (4)**	-0.009 (4)	0.002 (3)	-0.002 (3)	**0.039 (3)**	0.004 (3)
H2B_1	ZX	C2B	C1B	-	1.190 (11)	1.59 (5)	0.817 (17)			**0.079 (5)**													
H3B_1	ZX	C3B	C2B	-	1.189 (10)	1.62 (3)	0.786 (15)			**0.076 (4)**													
H4B_1	ZX	C4B	C5B	-	1.190 (10)	1.63 (3)	0.799 (16)			**0.078 (4)**													
H5B_1	ZX	C5B	C6B	-	1.189 (10)	1.62 (3)	0.815 (15)			**0.069 (4)**													
H6B_1	ZX	C6B	C1B	-	1.181 (11)	1.59 (5)	0.826 (17)			**0.082 (5)**													

Table S4. Bond critical points of compound **2**.

			Hartree	/Bohr3	kJ/mo	l/Bohr^3										
Atom1	Atom2	CP	Gcp	Vcp	Gcp	Vcp	DISTIJ	DCPI	DCPJ	DEN	LAPL	3-E	IGEN-V	ALUES	ELLIPTIC	TYPE
F1	C7	cp1	0.239	-0.690	626.8	-1812.2	1.340	0.833	0.507	2.007	-20.5	-18.1	-17.1	14.6	0.057	(3,-1)
F2	C7	cp2	0.246	-0.701	646.3	-1841.3	1.344	0.828	0.517	2.023	-20.1	-18.5	-17.0	15.3	0.086	(3,-1)
F3	C7	cp3	0.231	-0.657	606.2	-1726.2	1.348	0.839	0.509	1.946	-18.9	-17.1	-15.8	14.1	0.080	(3,-1)
C1	C2	cp4	0.285	-0.764	748.5	-2005.2	1.397	0.701	0.696	2.112	-18.7	-16.1	-13.5	11.0	0.196	(3,-1)
C1	C6	cp5	0.289	-0.765	758.0	-2009.2	1.394	0.698	0.696	2.111	-18.1	-16.3	-13.0	11.2	0.256	(3,-1)
C1	**C7**	**cp6**	**0.240**	**-0.606**	**628.8**	**-1591.1**	**1.500**	**0.702**	**0.798**	**1.823**	**-12.2**	**-13.4**	**-12.4**	**13.5**	**0.081**	**(3,-1)**
C2	C3	cp7	0.293	-0.777	768.2	-2040.8	1.392	0.699	0.693	2.132	-18.5	-16.6	-13.6	11.7	0.225	(3,-1)
C2	H2	cp8	0.230	-0.623	604.7	-1636.7	1.081	0.700	0.381	1.872	-15.7	-18.6	-17.7	20.6	0.048	(3,-1)
C3	C4	cp9	0.298	-0.796	781.7	-2090.1	1.395	0.688	0.707	2.164	-19.3	-16.9	-13.8	11.4	0.224	(3,-1)
C3	H3	cp10	0.222	-0.598	583.6	-1569.6	1.078	0.710	0.368	1.824	-14.8	-17.9	-17.3	20.5	0.034	(3,-1)
C4	C5	cp11	0.295	-0.790	773.2	-2074.5	1.395	0.708	0.687	2.156	-19.4	-16.8	-13.9	11.3	0.210	(3,-1)
C4	H4	cp12	0.219	-0.607	575.1	-1594.1	1.079	0.711	0.369	1.849	-16.3	-18.6	-17.5	19.8	0.065	(3,-1)
C5	C6	cp13	0.286	-0.760	751.8	-1996.4	1.397	0.687	0.710	2.104	-18.1	-16.3	-13.5	11.7	0.210	(3,-1)
C5	H5	cp14	0.225	-0.601	591.5	-1578.8	1.079	0.712	0.367	1.829	-14.5	-18.1	-17.5	21.1	0.034	(3,-1)
C6	H6	cp15	0.224	-0.609	588.3	-1598.6	1.080	0.707	0.374	1.847	-15.5	-18.3	-17.8	20.5	0.028	(3,-1)

Table S5. Bond critical points of compound **2**.

Atom1		Atom2		CP	Hartree/Bohr3 Gcp	Vcp	kJ/mol/Bohr^3 Gcp	Vcp	DISTIJ	DCPI	DCPJ	DEN	LAPL	3-E	IGEN-V	ALUES	ELLIPTIC	TYPE
C1A	1	C2A	1	cp1	0.306	-0.791	803.3	-2076.5	1.396	0.699	0.698	2.146	-17.3	-17.3	-14.2	14.3	0.215	(3,-1)
C1A	1	C6A	1	cp2	0.302	-0.783	793.1	-2054.7	1.395	0.697	0.699	2.133	-17.2	-17.1	-14.2	14.0	0.202	(3,-1)
C1A	**1**	**C7A**	**1**	**cp3**	**0.212**	**-0.540**	**556.8**	**-1416.5**	**1.503**	**0.770**	**0.734**	**1.702**	**-11.1**	**-11.7**	**-11.5**	**12.1**	**0.020**	**(3,-1)**
H2A	1	C2A	1	cp5	0.204	-0.577	535.0	-1513.6	1.083	0.353	0.731	1.797	-16.3	-17.4	-16.6	17.7	0.050	(3,-1)
C2A	1	C3A	1	cp6	0.298	-0.787	783.3	-2065.4	1.392	0.706	0.685	2.145	-18.3	-16.8	-14.0	12.5	0.204	(3,-1)
H3A	1	C3A	1	cp7	0.209	-0.586	547.6	-1539.0	1.083	0.357	0.726	1.813	-16.3	-17.0	-16.7	17.5	0.018	(3,-1)
C3A	1	C4A	1	cp8	0.296	-0.786	778.3	-2064.2	1.393	0.712	0.680	2.146	-18.6	-16.4	-13.9	11.6	0.181	(3,-1)
H4A	1	C4A	1	cp9	0.209	-0.582	548.1	-1527.5	1.083	0.362	0.722	1.803	-15.8	-17.0	-16.6	17.8	0.022	(3,-1)
C4A	1	C5A	1	cp10	0.303	-0.803	796.1	-2107.4	1.391	0.684	0.707	2.172	-18.9	-16.6	-14.0	11.7	0.188	(3,-1)
H5A	1	C5A	1	cp11	0.192	-0.556	503.2	-1460.5	1.083	0.342	0.741	1.764	-16.7	-16.9	-16.5	16.7	0.024	(3,-1)
C5A	1	C6A	1	cp12	0.297	-0.782	779.8	-2054.1	1.395	0.690	0.706	2.137	-18.2	-16.7	-13.9	12.5	0.197	(3,-1)
H6A	1	C6A	1	cp13	0.206	-0.582	540.8	-1526.8	1.083	0.354	0.729	1.806	-16.3	-17.3	-16.8	17.8	0.031	(3,-1)
C7A	1	H71A	1	cp14	0.132	-0.409	346.3	-1074.0	1.077	0.783	0.295	1.479	-14.0	-14.6	-11.9	12.5	0.230	(3,-1)
C7A	1	H72A	1	cp15	0.124	-0.401	325.8	-1052.6	1.077	0.790	0.288	1.468	-14.7	-14.7	-12.0	11.9	0.230	(3,-1)
C7A	1	H73A	1	cp16	0.130	-0.409	340.2	-1072.6	1.077	0.785	0.293	1.481	-14.4	-14.7	-12.0	12.3	0.224	(3,-1)
C7A	1	H74A	1	cp17	-0.203	-0.055	-531.9	-144.9	1.077	1.007	0.072	0.923	-44.4	-27.4	-24.6	7.6	0.113	(3,-1)
C7A	1	H75A	1	cp18	-0.051	-0.152	-134.9	-399.1	1.077	0.958	0.122	0.997	-24.6	-18.6	-15.2	9.3	0.220	(3,-1)
C7A	1	H76A	1	cp19	-0.242	-0.036	-636.2	-94.3	1.077	1.013	0.066	0.925	-50.2	-30.0	-27.3	7.1	0.100	(3,-1)
C1B	2	C2B	2	cp25	0.313	-0.806	821.7	-2115.8	1.398	0.698	0.700	2.169	-17.3	-17.7	-14.5	14.9	0.219	(3,-1)
C1B	2	C6B	2	cp26	0.303	-0.779	794.3	-2044.2	1.398	0.699	0.699	2.124	-16.7	-17.0	-14.2	14.4	0.200	(3,-1)
C1B	**2**	**C7B**	**2**	**cp27**	**0.213**	**-0.542**	**559.6**	**-1422.7**	**1.503**	**0.771**	**0.731**	**1.706**	**-11.1**	**-12.0**	**-11.3**	**12.1**	**0.061**	**(3,-1)**
H2B	2	C2B	2	cp29	0.197	-0.563	518.0	-1478.3	1.083	0.337	0.746	1.774	-16.2	-17.5	-16.8	18.0	0.042	(3,-1)
C2B	2	C3B	2	cp30	0.300	-0.789	788.2	-2071.2	1.392	0.707	0.686	2.147	-18.2	-16.9	-14.0	12.8	0.207	(3,-1)
H3B	2	C3B	2	cp31	0.198	-0.568	519.4	-1492.0	1.083	0.345	0.738	1.785	-16.6	-17.2	-16.4	16.9	0.045	(3,-1)
C3B	2	C4B	2	cp32	0.296	-0.782	778.3	-2054.4	1.392	0.713	0.679	2.138	-18.3	-16.2	-13.8	11.7	0.179	(3,-1)
H4B	2	C4B	2	cp33	0.197	-0.558	516.1	-1465.6	1.083	0.352	0.731	1.763	-15.9	-16.7	-16.2	17.0	0.032	(3,-1)
C4B	2	C5B	2	cp34	0.300	-0.792	788.9	-2078.5	1.393	0.684	0.709	2.153	-18.4	-16.3	-13.9	11.8	0.176	(3,-1)
H5B	2	C5B	2	cp35	0.201	-0.569	527.0	-1492.9	1.083	0.351	0.732	1.782	-16.1	-17.1	-16.3	17.3	0.045	(3,-1)
C5B	2	C6B	2	cp36	0.297	-0.779	779.6	-2045.0	1.394	0.691	0.703	2.131	-17.8	-16.6	-13.9	12.6	0.196	(3,-1)
H6B	2	C6B	2	cp37	0.214	-0.595	562.0	-1563.0	1.083	0.360	0.723	1.828	-16.1	-17.6	-16.9	18.4	0.041	(3,-1)
C7B	2	H71B	2	cp38	0.156	-0.451	409.2	-1184.5	1.077	0.764	0.316	1.556	-13.4	-14.7	-10.8	12.0	0.363	(3,-1)
C7B	2	H72B	2	cp39	0.153	-0.450	401.9	-1182.4	1.077	0.766	0.314	1.557	-13.9	-14.8	-10.9	11.7	0.357	(3,-1)
C7B	2	H73B	2	cp40	0.144	-0.441	377.9	-1158.8	1.077	0.774	0.305	1.546	-14.8	-14.9	-11.1	11.2	0.342	(3,-1)
H72B	2	H74B	2	cp41	-0.487	0.013	-1279.3	33.2	0.506	0.475	0.045	1.166	-92.7	-53.5	-48.9	9.7	0.096	(3,-1)
H71B	2	H75B	2	cp42	-0.750	0.147	-1967.9	385.8	0.506	0.484	0.033	1.157	******	-72.0	-67.4	9.0	0.068	(3,-1)
H73B	2	H76B	2	cp43	-0.665	0.110	-1745.7	289.7	0.506	0.483	0.035	1.139	******	-65.5	-61.2	9.2	0.070	(3,-1)

209

Table S6. Bond critical points of compound **3.**

		Hartree/Bohr3		kJ/mol/Bohr^3													
Atom1	Atom2	Gcp	Vcp	Gcp	Vcp	DISTIJ	DCPI	DCPJ	RHO	LAPL	3-EIGEN-VALUES			ELLIP	Type
C1A	C2A	0.64200	-5.91150	1685.57	-15520.64	1.3978	0.7103	0.6875	2.1400	-18.51	11.96	-13.68	-16.79	0.23	(3,-1)
C1A	C6A	0.64470	-5.91440	1692.66	-15528.26	1.3964	0.7056	0.6907	2.1490	-18.50	12.13	-13.76	-16.87	0.23	(3,-1)
C1A	C7A	0.56370	-4.40490	1479.99	-11565.06	1.4354	0.6914	0.7440	1.8790	-13.11	12.74	-12.36	-13.49	0.09	(3,-1)
C2A	C3A	0.63870	-5.90240	1676.91	-15496.75	1.3983	0.6814	0.7169	2.1290	-18.50	11.89	-13.70	-16.69	0.22	(3,-1)
C2A	H2A	0.56250	-5.55250	1476.84	-14578.09	1.0826	0.7103	0.3723	1.8750	-17.71	18.73	-17.85	-18.58	0.04	(3,-1)
C3A	C4A	0.64170	-5.92590	1684.78	-15558.45	1.3980	0.7085	0.6895	2.1390	-18.57	12.13	-13.79	-16.90	0.23	(3,-1)
C3A	C8A	0.56490	-4.47230	1483.14	-11742.02	1.4347	0.6939	0.7408	1.8830	-13.37	12.79	-12.43	-13.74	0.11	(3,-1)
C4A	C5A	0.64350	-5.93950	1689.51	-15594.16	1.3959	0.6899	0.7061	2.1450	-18.61	12.05	-13.81	-16.85	0.22	(3,-1)
C4A	H4A	0.57360	-5.55970	1505.99	-14596.99	1.0820	0.7046	0.3773	1.9120	-17.65	19.60	-18.28	-18.97	0.04	(3,-1)
C5A	C6A	0.64170	-5.88340	1684.78	-15446.87	1.3978	0.7103	0.6875	2.1390	-18.40	12.10	-13.77	-16.73	0.22	(3,-1)
C5A	C9A	0.56670	-4.49840	1487.87	-11810.55	1.4330	0.6879	0.7451	1.8890	-13.46	12.81	-12.60	-13.66	0.08	(3,-1)
C6A	H6A	0.57000	-5.59750	1496.53	-14696.24	1.0822	0.7056	0.3766	1.9000	-17.83	19.41	-18.28	-18.96	0.04	(3,-1)
C7A	N1A	1.02990	-8.92230	2704	-23425.50	1.1557	0.4207	0.7350	3.4330	-27.45	28.75	-27.98	-28.22	0.01	(3,-1)
C8A	N2A	1.03050	-9.23600	2705.58	-24249.12	1.1561	0.4232	0.7330	3.4350	-28.70	27.67	-27.95	-28.42	0.02	(3,-1)
C9A	N3A	1.03440	-9.84380	2715.82	-25844.90	1.1551	0.4283	0.7267	3.4480	-31.10	25.08	-27.78	-28.40	0.02	(3,-1)
C1B	C2B	0.64920	-6.17340	1704.47	-16208.26	1.3916	0.7178	0.6739	2.1640	-19.50	11.45	-13.93	-17.02	0.22	(3,-1)
C1B	C6B	0.65520	-6.28790	1720.23	-16508.88	1.3892	0.7202	0.6691	2.1840	-19.91	11.34	-14.01	-17.23	0.23	(3,-1)
C1B	N1B	0.53400	-4.35300	1402.02	-11428.80	1.4647	0.5868	0.8779	1.7800	-13.14	11.72	-11.33	-13.52	0.19	(3,-1)
C2B	C3B	0.64410	-6.01320	1691.08	-15787.66	1.3923	0.7074	0.6850	2.1470	-18.90	11.52	-13.84	-16.58	0.2	(3,-1)
C2B	H2B	0.55950	-5.54900	1468.97	-14568.90	1.0824	0.7137	0.3688	1.8650	-17.72	18.51	-17.64	-18.58	0.05	(3,-1)
C3B	C4B	0.64560	-6.09370	1695.02	-15999.01	1.3971	0.6968	0.7003	2.1520	-19.21	11.58	-14.16	-16.63	0.17	(3,-1)
C3B	H3B	0.54720	-5.40940	1436.67	-14202.38	1.0828	0.7139	0.3689	1.8240	-17.26	17.97	-17.15	-18.07	0.05	(3,-1)
C4B	C5B	0.64470	-6.03440	1692.66	-15843.32	1.3933	0.6966	0.6967	2.1490	-18.98	11.63	-13.88	-16.73	0.2	(3,-1)
C4B	H4B	0.56040	-5.66080	1471.33	-14862.43	1.0827	0.7160	0.3667	1.8680	-18.16	18.57	-18.09	-18.65	0.03	(3,-1)
C5B	C6B	0.64770	-6.07290	1700.54	-15944.40	1.3921	0.6851	0.7071	2.1590	-19.11	11.55	-13.89	-16.77	0.21	(3,-1)
C5B	H5B	0.54900	-5.33050	1441.4	-13995.23	1.0826	0.7132	0.3695	1.8300	-16.93	18.31	-17.24	-18.00	0.04	(3,-1)
C6B	H6B	0.56400	-5.69300	1480.78	-14946.97	1.0825	0.7137	0.3688	1.8800	-18.26	18.28	-17.77	-18.77	0.06	(3,-1)
N1B	O1B	1.01550	-5.08100	2666.2	-13340.17	1.2279	0.5938	0.6342	3.3850	-12.20	47.51	-28.96	-30.74	0.06	(3,-1)
N1B	O2B	1.01730	-5.14210	2670.92	-13500.58	1.2267	0.5869	0.6398	3.3910	-12.43	47.85	-29.10	-31.18	0.07	(3,-1)

Table S7. Comparison of the multipolar parameters with restrained $k'>1$ for compound **2**. A column including the valence population of the atoms with respect to the minimized model was added, ΔP_v.

Atom k	K'	P_{val}	ΔP_v	P_{10}	P_{11}	P_{1-1}	P_{20}	P_{21}	P_{2-1}	P_{22}	P_{2-2}	P_{30}	P_{31}	P_{3-1}	P_{32}	P_{3-2}	P_{33}	P_{3-3}
C1	1.011	1.01	4.08	**0.12**	0.029	-0.012	-0.004	-0.163	0.006	0.008	-0.037	-0.001	0.010	0.020	-0.026	0.010	-0.006	-0.226	-0.014
C2	1.008	1.01	4.06	**-0.11**	-0.001	0.003	-0.010	-0.176	0.008	0.010	0.000	0.012	0.011	0.039	0.009	0.000	-0.016	-0.237	-0.014
C3	1.008	0.97	4.09	**0.05**	-0.011	0.001	0.003	-0.207	-0.015	-0.009	-0.018	-0.007	0.005	0.025	-0.002	-0.003	-0.023	-0.248	-0.001
C4	1.001	1.01	4.15	**-0.02**	0.012	-0.001	0.008	-0.187	-0.013	-0.005	-0.014	0.002	-0.011	0.018	-0.006	-0.019	0.002	-0.263	0.002
C5	1.010	1.00	4.08	**0.05**	-0.014	-0.009	0.002	-0.190	0.004	0.004	0.003	-0.002	0.002	0.029	-0.001	-0.013	-0.011	-0.227	0.012
C6	1.005	1.03	4.07	**-0.11**	-0.001	0.010	-0.017	-0.187	-0.006	0.005	-0.012	0.008	0.010	0.033	-0.008	0.007	-0.013	-0.233	-0.008
C7	1.012	1.11	3.65	**-0.06**	-0.003	-0.002	0.112	0.109	-0.007	0.005	-0.006	0.025	0.250	0.019	0.000	-0.011	-0.010	0.188	-0.006
F1	0.994	0.84	7.18	**0.01**	0.007	0.037	-0.004	-0.051	0.008	-0.009	0.029	0.008	0.071	0.004	0.005	0.007	-0.005	-0.024	0.008
F2	0.993	0.87	7.19	**0.01**	0.014	0.018	0.021	-0.053	0.011	0.008	0.015	-0.009	0.056	-0.001	-0.004	0.006	-0.010	-0.005	-0.006
F3	0.995	0.88	7.18	**0.01**	0.008	0.024	0.033	-0.052	0.006	0.006	0.017	-0.007	0.054	-0.002	-0.014	0.000	-0.004	-0.006	-0.005
H2	1.249	1.24	0.88	**0.02**			0.091												
H3	1.231	1.24	0.86	**0.00**			0.054												
H4	1.233	1.24	0.83	**0.00**			0.078												
H5	1.243	1.24	0.85	**0.00**			0.058												
H6	1.234	1.24	0.88	**0.01**			0.085												

General conclusions.

In summary, in this thesis, high resolution data were used in single crystal X-ray diffraction experiments. Some of these data were collected on a state of the art diffractometer. In particular, these collected data took advantage of novel X-ray detector technology, hybrid pixel detectors also known as photon counting detectors. This new technology improves the dynamic range of the detectors as well as the signal to noise ratio, leading to more reliable data. Parameters like the scale factor become more homogenous when using these detectors. In the same manner, weak intensities become more precise and accurate. As a consequence, the thermal parameters can be better estimated, as well as the atomic positions, which results in more defined residual maps. These residual maps are fitted through a multipolar model that can be refined in a very stable way providing reliable electron densities from which valuable information can be derived.

The high resolution data have been successfully used in the characterization of weak interactions through the multipolar refinement applying Bader's theory. In contrast, with the help of computational methods, they have been exposed the limitations of Bader's theory for the characterization of weak interactions under certain environments. The calculation of electrostatic moments through the experimental charge density distribution was efficiently accomplished. The synergy of the experimental X-ray charge density studies with computational methods resulted in an increase of the reliability of both methodologies.

Eventually, the usability of molybdenum radiation has been demonstrated in the determination of the absolute structure of molecules containing no atom heavier than oxygen.

In particular, in the analysis of weak interactions, we started by studying the tetrel bond interactions (chapter 2). We report a combined experimental and calculated electron density study of 1,1,2,2-tetracyanocyclopropane accompanied with the corresponding accurate topological analyses to characterize qualitatively the non-

covalent carbon bonding in the crystal packing. The N···C intermolecular bond can be classified as a closed-shell interaction and its electrostatic nature is demonstrated by the mapped $\Delta\rho(r)$ distribution. The interaction occurs between a nucleophilic (or Lewis base) region (δ^-) of a nitrogen atom and an electrophilic (or Lewis acid) region (δ^+) of the carbon atoms in the (CN)2C–C(CN)2 motif of the three-membered ring. The region of positive electrostatic potential (σ-hole) is readily accessible making non-covalent 'carbon-bonding' a viable supramolecular interaction in the solid-state. This finding is in sharp agreement with a recent thorough CSD analysis, providing strong support to carbon-bonding interactions in (CN)2C–C(CN)2 motifs. The interaction is highly directional in structures having (CN)CC(CN) dihedral angles of ≤ 15°. The experimental demonstration of the existence of a σ-hole in a X-ray charge density analysis, by means of the representation of the static deformation of the electron density *iso*-surface is very relevant and supports the theoretically proposed existence of σ-hole based interactions involving carbon, the lighter tetrel atom.

A similar study has been done in order to quantify the triel bond interactions involving boron atoms (chapter 3). The detailed description of the interactions in the solid offers an excellent opportunity for analyzing, not only attractive interactions, but also a priori not so favored interactions that can be frozen as a consequence of the crystal packing. In the crystal structure of 4-Pyridinylboronic acid hydrochloride, an attractive interaction, the triel bonding, remains hidden to the Bader's analysis. In contrast, non-attractive interactions exhibit electronic interchange channels, considered as bonds in Bader's theory. DFT studies of a homologous model, where oxygen atoms where replaced by hydrogen atoms support this hypothesis. Additional NBO calculations further evidence the attractive Cl$^-$-B interaction and the weakening provoked by the oxygen atoms.

We also compare the nature of the triel bonding with related π hole interactions. In other two studied cases, a co-crystal of tartaric acid and 4,4'-bipyridine N-N'-dioxide and 1,4-dinitrobenzene, the bond paths and critical points corresponding to the attractive interactions, tetrel bonding and pnicogen bonding, respectively, were evident using Bader's theory. Moreover, in 1,4-dinitrobenzene it was possible to characterize a chalcogen bond between the electron rich site of the oxygen to the

electron poor region of the other oxygen of the nitro group. The comparison of the three studied π hole interactions, triel, tetrel and pnicogen bonding, allows us to conclude that in addition to the bond distance and strength of the interaction, the intensity of the π hole determines the presence of a bond path.

In the charge density study of the triel bond we observe that short interatomic distances present in the crystals that are consequence of the crystal packing and not of the existence of attractive interactions between the involved atoms could display bond paths in the Bader's sense. The theoretical calculations confirmed this hypothesis. In the present work, we demonstrated that a reasonable attractive interaction as the triel bond can be accompanied by "non-expected" bonds that overlap its trace in the charge density. The latter are revealed through an accurate electron density analysis. In contrast, the former, that is the main attractive interaction i.e. the triel bonding, could not be supported by an electron charge density study neither theoretical nor experimental.

Close shell attractive interactions featuring a very poor electron density site i.e. boron atom, can lead to the absence of a chemical bond based on Bader's definition. The typical presence of electron rich sites near the electron hole tend to reinforce this effect. This observation seems to contradict the chemical intuition of bonds and attractive interactions

In chapter 4 we have provided both experimental and theoretical determination of the quadrupolar moment for a set of substituted phenyl rings. The ethynyl group as substituent is included in the study due to its observed paradoxical behavior; the Q_{zz} becomes more negative and the MEP value more positive as the number of CCH substituent increases. Thus, the EW nature of the CCH group agrees with the MEP value over the center of the ring and disagrees with the Q_{zz} value. Moreover, we have shown that other substituents present a similar behavior. An in-depth analysis of charge density distribution using high resolution X-ray diffraction data does not serve to reveal the origin of the different trends followed by the Q_{zz} and MEP values of the phenyl substituted rings. We also show that in these cases the quadrupole moment is not suitable to explain the nature of electrostatic interaction in both cation and anion–

215

π complexes. All substituted phenyl rings displaying a behavior of their quadrupole moments similar to the one observed for the ethynyl substituted phenyl rings feature terminal hydrogen atoms in the substituents. This finding led us to consider the effect of the terminal hydrogen atoms, which is the presence of an electron positive distribution at the end of the substituent, as the origin of the observed trend. The results obtained with a simple model of point charge distributions support this hypothesis. Further investigations are needed to provide a more rigorous physical explanation for the opposed trends observed in MEP and Q_{zz} values in certain phenyl substituted aromatic rings. In any case, our results indicate that the use of Q_{zz} values to analyzed and predict ion–π interaction is not consistent.

Eventually, in chapter 5, a series of 44 high-resolution data sets collected using Mo *Kα* radiation have been used to determine the absolute structure parameters of enantiopure single crystals containing no atom heavier than oxygen. All the calculated absolute structure parameters assign the correct absolute configuration to the molecules; however, acceptable standard uncertainties are only obtained for the Hooft y and Parsons z parameters.

The standard uncertainties determined for the Flack parameter are not sufficiently small to validate the assigned absolute configuration of any of the molecules except for sucrose.

In most of the tests the use of data limited to the IUCr minimum standard of resolution, $\sin\theta/\lambda \leq 0.6$ Å^{-1}, did not provide sufficiently accurate or precise absolute structure parameters. Accuracy and precision of the absolute structure parameter values are progressively improved by including data collected at higher resolution. All the structural parameter values benefit from the inclusion of data at high resolution ranges during structure refinement. The results of a T^2 analysis demonstrated that the distribution of resolution ranges influencing the accuracy of the Flack parameter, x, changes significantly in different structures. In spite of this generalization, the majority of absolute structure determinations based on the x value improve in accuracy when reflections at low resolution ranges are omitted. This finding demonstrates the sensitivity of the x parameter to systematic errors caused by exclusive consideration of

diffraction data acquired at low resolution ranges using Mo $K\alpha$ radiation in structure refinements. The y and z parameters are not sensitive to this problem, though their accuracy is improved when diffraction data at the full range of resolution is considered. In general, when data sets of the same quality and Friedif$_{stat}$ are compared, the values and accuracies of their absolute structure parameters are better for crystals having larger asymmetric units. This fact is due to an increase in the number reflections used for their calculation.

Therefore, it has been demonstrated that reflection data acquired to high resolution with Mo $K\alpha$ radiation can be used for the determination of the absolute configuration even for light-atom molecules. The proposed methodology consists on assigning the absolute structure of the crystal using the y (Hooft) and z (Parsons) parameters. Attending to the parameter defined in this work, η, values of $\eta \leq 2$ should lead to standard uncertainties of those parameters smaller than 0.1. The inclusion of high resolution data becomes especially important in crystals providing a small number of reflections. In the case of crystals with large asymmetric units, the consideration of reflection data acquired just at medium-high resolution suffices for the determination of accurate absolute structure parameters using the proposed methodology and Mo $K\alpha$ radiation.

Eventually, it is expected that the capability of hybrid pixel detectors (and other new technologies as CMOS detectors) demonstrated for precise measurements of weak intensities will increase the success of determining the absolute structure of light atom molecules with nitrogen as the heaviest atom even when using Molybdenum as X-ray radiation source.

UNIVERSITAT ROVIRA I VIRGILI
HIGH RESOLUTION X-RAY SINGLE CRYSTAL DIFFRACTION
Eduardo Carmelo Escudero Adán

UNIVERSITAT
ROVIRA i VIRGILI

ICIQ

Institut
Català
d'Investigació
Química